SCUOLA DI SCIENZE
Corso di Laurea Magistrale in Astrofisica e Cosmologia
Dipartimento di Fisica e Astronomia

Investigating the AGN-starburst connection in a nearby Seyfert galaxy with ALMA and multiwavelength data

Tesi di Laurea Magistrale

Candidata:
Matilde Mingozzi

Relatore:
Chiar.mo Prof.
Andrea Cimatti

Co-relatori:
Dott.ssa Francesca Pozzi
Dott. Arturo Mignano
Dott.ssa Livia Vallini

Sessione II - I seduta
Anno Accademico 2015-2016

Ai miei genitori,
alle mie care amiche,
Marta, Lisa, Anna e Bebè,
a Carlo

"It all just disappears, doesn't it? Everything you are, gone in moment. Like breath on a mirror. Any moment now, he's a coming. We all change when you think about it. We're all different all through our lives. And that's okay, that's good. You've got to keeping moving. As long as you remember all the people that you used to be. I will not forget one line of this, not one day. I swear. I will always remember when the Doctor was me."

Contents

Sommario

Il contesto astrofisico all'interno del quale si inserisce il presente lavoro di tesi riguarda la comprensione della mutua interazione fra l'accrescimento attorno ai buchi neri supermassivi (SMBH) e la formazione stellare all'interno delle galassie che li ospitano. Tale tema è uno dei maggiori campi di ricerca dell'astronomia extragalattica moderna, in quanto è ormai chiaro che per comprendere la fisica di una galassia non si può prescindere dal considerare anche come l'AGN centrale la influenzi. Dato che la radiazione elettromagnetica in continuo ed in riga è prodotta da diversi processi astrofisici in bande differenti dello spettro, per avere la visione più completa possibile di tali oggetti complessi è necessario un approccio multibanda che permetta di discriminare quale sia il contributo relativo dei due processi all'energetica globale e di capire come si influenzino reciprocamente.

Lo scopo di questo progetto di tesi è la comprensione dei fenomeni fisici di una Seyfert dell'Universo vicino, NGC 34. Tale oggetto è stato scelto poiché presenta una vasta collezione di dati multibanda in letteratura e, inoltre, è stato recentemente osservato dall'interferomentro submm ALMA in banda 9, i cui dati si trovano in archivio. La tesi si è sviluppata principalmente in due parti: in primo luogo, sono stati calibrati e analizzati i dati di archivio ottenuti con ALMA e sono state prodotte mappe in continuo a 435 μm e mappe e profili di riga della transizione del monossido di carbonio CO(6-5) ($\nu_{rest-frame} = 691.473\,\mathrm{GHz}$); successivamente, si è cercato di dare una possibile interpretazione coerente dell'oggetto. Particolare attenzione è stata rivolta allo studio del mezzo interstellare (ISM) per capire quali sono le sue proprietà fisiche in termini di densità, composizione chimica e tipo di radiazione dominante (da formazione stellare o accrescimento). Tale studio è stato possibile analizzando la distribuzione spettrale di diverse transizioni del CO (CO SLED), ottenuta unendo i dati relativi all'osservazione ALMA con altri presenti in letteratura. In particolare, la CO SLED osservata è stata confrontata con modelli dell'ISM che includono sia "Photo-Dissociation Regions" (PDRs), regioni dominate dalla radiazione ultravioletta prodotta da fotoni di origine stellare (6-13.6 eV), sia "X-ray Dominated Regions" (XDRs), la cui componente prevalente è data da fotoni di alta energia (1-100 keV) prodotti dall'AGN. Tali modelli sono stati prodotti utilizzando il codice di fotodissociazione CLOUDY. In tale contesto, i dati della CO SLED sono stati messi in relazione con altre proprietà fisiche della sorgente, come il tasso di formazione stellare, la massa di gas e la luminosità X, per avere un quadro complessivo dell'oggetto. Per riprodurre i dati osservati della CO SLED, abbiamo preso in considerazione

due diversi approcci: in primo luogo, si è ipotizzato che il contributo dato dalla formazione stellare fosse dominante, utilizzando solo modelli di PDR (*Modello 1*); successivamente, si è ipotizzato che le transizioni del CO più energetiche fossero prodotte dalla radiazione X proveniente dall'AGN centrale, utilizzando anche modelli di XDR (*Modello 2*). Infine, è stato effettuato il test statistico "*F-test*" per testare quale dei modelli analizzati riproducesse meglio i dati osservati. Dall'analisi del "*F-test*" abbiamo trovato che il *Modello 2*, che prende in considerazione anche il contributo dell'AGN, risulta più affidabile del *Modello 1*. Per un'analisi più approfondita sul contributo delle XDR sarebbero necessarie osservazioni ALMA ad alta risoluzione della regione nucleare della galassia, dove l'influenza dell'AGN può risultare dominante. Un'altra possibilità è quella di analizzare l'emissione di molecole caratterizzate da un'alta densità critica (p.e., HCN), in grado di tracciare le regioni più dense.

Questo lavoro mostra quale sia l'importanza cruciale di ALMA per aprire una nuova finestra di indagine sulle componenti delle galassie e AGN, in quanto, grazie alla sua alta risoluzione angolare e sensibilità, permette di esplorare le condizioni fisiche e la cinematica del mezzo interstellare freddo e di definire nuovi diagnostici.

Questo lavoro di tesi è così strutturato:

- nel Capitolo 1 viene presentata una panoramica sulla problematica scientifica, descrivendo le proprietà principali di NGC 34, tratte dalla letteratura.

- nel Capitolo 2 vengono introdotti i principi di base dell'interferometria e le caratteristiche principali dello strumento ALMA. Inoltre, vengono presentate la descrizione del processo di calibrazione dei dati ALMA, le immagini prodotte e, infine, discussi i risultati ottenuti.

- nel Capitolo 3 vengono riassunte le principali caratteristiche del mezzo interstellare, introducendo PDRs e XDRs.

- nel Capitolo 4 vengono presentati i modelli di CLOUDY utilizzati, i risultati derivanti dal confronto con i dati osservativi e l'analisi statistica effettuata.

- nel Capitolo 5 sono riassunti i risultati principali e presentate le prospettive future.

Abstract

The astrophysical context in which this thesis project lies concerns the comprehension of the mutual interaction between the accretion onto a Super Massive Black Hole (SMBH) and the Star Formation (SF), that take place in the host galaxy. This is one of the key topic of the modern extragalactic astrophysical research. Indeed, it is widely accepted that to understand the physics of a galaxy, the contribution of a possible central AGN must be taken into account. Since line and continuum radiation are due to several astrophysical processes in different bands of the electromagnetic spectrum, a multiwavelength approach has to be adopted in order to distinguish which is the global role of the SF and the accretion activities and to understand how they influence eachother.

The aim of this thesis is the study of the physical processes of the nearby Seyfert galaxy NGC 34. This source was selected because of the wide collection of multiwavelength data available in the literature. In addition, recently, it has been observed with the Atacama Large Submillimeter/Millimeter Array (ALMA) in Band 9. This project is divided in two main parts: first of all, we reduced and analyzed the ALMA data, obtaining the 435 μm and CO(6-5) maps ($\nu_{rest-frame} = 691.473$ GHz); then, we looked for a coherent explaination of NGC 34 physical characteristics. In particular, we focused on the ISM physics, in order to understand its properties in terms of density, chemical composition and dominant radiation field (SF or accretion). This work has been done through the analysis of the spectral distribution of several CO transitions as a function of the transition number (CO SLED), obtained joining the CO(6-5) line with other transitions available in the literature. More precisely, the observed CO SLED has been compared with ISM models, including Photo-Dissociation Regions (PDRs), regions whose physics and chemistry are dominated by stellar UV radiation (6-13.6 eV), and X-ray-Dominated Regions (XDRs), whose characteristics are mainly influenced by X-ray photons (1-100 keV) due to the central AGN. These models have been obtained through the state-of-the-art photoionization code CLOUDY. Along with the observed CO SLED, we have taken into account other physical properties of NGC 34, such as the Star Formation Rate (SFR), the gas mass and the X-ray luminosity. In order to reproduced the observed CO transitions, we have considered two different approaches: initially, we have hypothesized that the star formation contribution was dominant, using only PDR models (*Model 1*); then, we have used also XDR models, hypothesising that the more energetical CO transitions were due to the AGN (*Model 2*). Finally, we have

carried out a statistical analysis, through the *F-test*, to test which model best-fitted the observed data. We found that *Model 2*, that requires the presence of a central AGN, is more reliable than *Model 1*. Overall, ALMA high resolution observations of NGC 34 nuclear region, where the influence of the accretion could dominate, are needed to determine the real contribution of the AGN activity. Another possibility could be the study of high critical density molecules, such as the HCN, which trace the ISM densest regions.

This thesis project points out the crutial role played by ALMA in shedding light on AGN and SF galaxy components, since, thanks to its high angular and spatial resolution, allows to investigate the ISM physical properties and kinematics and to define new diagnostics.

This thesis is organized as follows.

- Chapter 1 deals with an overview of the scientific background, focusing on the main properties of NGC 34, available in the literature;

- In Chapter 2, the basic principles of interferometry and the main ALMA features are introduced. Furthermore, the ALMA data reduction and the relative results are presented.

- In Chapter 3, a general overview on ISM properties is proposed, introducing PDRs and XDRs.

- In Chapter 4, CLOUDY models are presented, illustrating the results obtained by the comparison with observed data and the statistical analysis carried out.

- In Chapter 5, we summarize the main results, focusing on the future perspectives.

Chapter 1

The AGN-starburst connection: an intriguing case, NGC 34

1.1 Introduction

In the last decade, intensive observational and theoretical investigations have demonstrated how the Star Formation Rates (SFRs) of galaxies and the Active Galactic Nuclei (AGN) phenomena are deeply connected. There are many observational pieces of evidence that support this connection, such as the tight relations between the Super Massive Black Hole (SMBH) mass and the host galaxy properties (bulge mass and luminosity, velocity dispersion) or the similar shape of the star formation and the BH accretion density as a function of the cosmic time. The understanding of the physical processes relating the growth of the SMBH and its interplay with the host galaxy is one of the key topic of the modern astrophysics.

This is the general context of the work presented in this thesis. In particular, a detailed study of a local IR Luminous Seyfert galaxy, NGC 34, where the two phenomena co-exist, will be presented, trying to gain a coherent picture of this galaxy, using all the available information. The multi-band data presented in the literature will be "joined" with new ALMA data. In particular, the analysis of the raw ALMA data corresponding to the Carbon-Monoxide (CO) molecule will be presented. The CO is a very good tracer of the gas mass, and its emission as a function of the rotational level can give important contraints on the physical properties of the gas, such as density, temperature and the types of excitation source (SF or accretion).

In the following, we describe the scientific background of this study, providing a brief overview of AGN and starburst activity. In addition, we focus on the Seyfert galaxy NGC 34, showing its multiwavelength properties.

1

1.2 A panchromatic view of Active Galactic Nuclei

AGN are among the brightest sources in the sky, shining over a broad range of frequencies, from the radio to the gamma rays. They are characterized by a very powerful emission ($L \approx 10^{42} - 10^{48} \, \mathrm{erg \, s^{-1}}$), located into the central region ($\approx 2 - 10$ pc), whose luminosity cannot be attributed to the components of *normal* galaxies, such as stars, gas and dust: it can outshine the host galaxies by factors > 1000. The most efficient known way to release this amount of energy is accretion into a relativistic deep gravitational potential. Indeed, these potentials are due to SMBHs, with a mass in the range $M \approx 10^5 - 10^{10} \, \mathrm{M_\odot}$. Arguably, every galaxy hosts a central SMBH, but approximately 1-10% of them are known as active galaxies.

1.2.1 Main components of AGN

AGN are characterized by a compact central source, the *SMBH*, that provides a very intense gravitational field, whose most basic feature is the presence of an event horizon, a boundary from which matter and even light can never re-emerge. It is described by the gravitational radius, defined as

$$R_g = \frac{GM_{BH}}{c^2} \tag{1.1}$$

where G is the gravitational constant, M_{BH} the black hole mass and c the speed of light.
Around the SMBH, there is an *accretion disc*, that forms as the gas spirals inward, on scales down to a few gravitational radii. The infalling gas looses angular momentum, that is transfered outward, owing to the viscosity and turbulent processes of the disc, and spirals into the center, losing a considerable fraction of its gravitational energy. Friction heats the gas to high temperatures ($T > 10^4 \, K$), that accounts for optical through soft X-ray continuum emission.

A hot, rarefied gas ($T \sim 10^8 - 10^9 \, \mathrm{K} \; n_e \sim 10^8 \, \mathrm{cm^{-3}}$), located at $\sim 3 - 10 \, R_g$ above the disc, constitutes the so-called *hot corona*. In this region, the soft thermal photons produced by the disc are upscattered to X-ray, accounting for the energetic X-ray emission from AGN.

The deep gravitational potential at the center of the galaxy allows the presence of high density ($n_e \approx 10^9 - 10^{10} \, \mathrm{cm^{-3}}$), high velocity ($\gtrsim 2000 \, \mathrm{km \, s^{-1}}$) gas clouds with a temperature of $\approx 10^4 \, \mathrm{K}$ in proximity of the central source, composing the so-called *Broad Line Region* (BLR). The gas reprocesses the energy produced by the continuum source at ionizing ultraviolet energies, through emission lines due to recombination or de-excitation of photoionized atoms. The electron density is high enough to prevent forbidden lines from forming, being collisionally suppressed. In addition, the permitted emission lines are broad, characterized by $FWHM \approx 10^3 - 10^4 \, \mathrm{km \, s^{-1}}$.

Some clouds are located further away from the SMBH, constituting the *Narrow Line Region* (NLR), the largest spatial scale where the ionizing radiation from the central source can excite the surrounding medium. Here, the electron density is sufficiently low ($10^4 \, \mathrm{cm^{-3}}$) to allow the presence of forbidden lines, with a $FWHM \approx 10^2 \, \mathrm{km \, s^{-1}}$. The temperature is $\approx 1 - 2.5 \times 10^4 \, \mathrm{K}$.

The accretion disc is surrounded by a dusty circumnuclear material, the so-called *dusty torus*, whose typical size is around $\sim 1 - 10 \, \mathrm{pc}$. This region is located beyond the dust sublimation

radius (the dust sublimation temperature is $\approx 1000 - 1500\,\mathrm{K}$), therefore is likely to contain dust and molecular gas. More precisely, the gas at the inner radius is ionized by the central engine, whereas at larger distances dominates the neutral and molecular material. The torus emits the reprocessed radiation in the IR band, while appears to be opaque at all the other wavelength, obscuring the central source for certain lines of sight.

Finally, AGN can produce the *jets*, outflows of magnetically-bound relativistic particles, that can be extended up to $\sim 100 - 1000\,\mathrm{kpc}$. Their formation mechanism is still unknown, but is probably related to a fast rotating black hole and the presence of the magnetic field, that can collimate the outflow of charged particles. The jet structure appears to origine in the location of the optical-UV and X-ray continuum source and they mostly emit through synchrotron radiation, from the radio band to the γ-rays. The most powerful jets can overcome the host galaxy, propagating into the interstellar and intergalactic medium up to Mpc scales, while the weaker decelerate closer to the central SMBH. Their interaction with the environment leads to the formation of hot spots and large-scale radio lobes (Netzer, 2013).

The components discussed are illustrated in Fig. 1.1, while their typical sizes are summarized in Tab. 1.1.
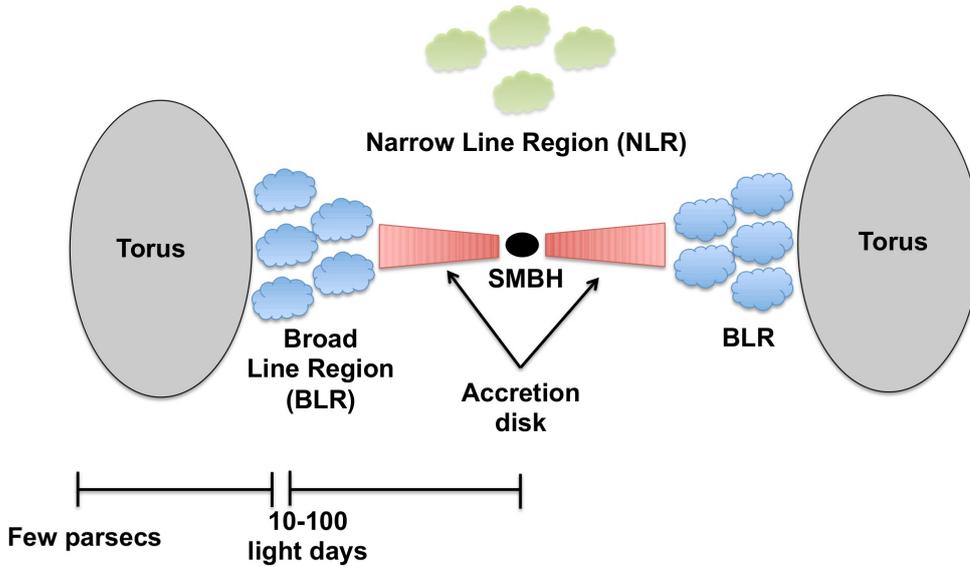
Figure 1.1: *Typical structure (not on scale) of an AGN (from http://www.isdc.unige.ch).*

AGN can be classified according to their emission properties in different spectral windows. Here, we report the main classes. On the basis of their optical spectral properties, AGN are divided in *Type-I* and *Type-II*. Type-I are objects with little or no obscuration of the central source due to the circumnuclear dust and with optical spectra characterized by strong optical/UV continuum, broad emission lines, and narrow emission lines. On the contrary, Type-II are obscured

Table 1.1: Typical size ranges of the different components of AGN.

Component	Size
SMBH	$R_S \sim 0.01 - 10\,\mathrm{AU}$
Accretion disc	$R_{in} \sim 0.01 - 60\,\mathrm{AU}$ $R_{out} \sim 1 - 1000\,\mathrm{AU}$
BLR	$R_{BLR} \sim 0.01 - 1\,\mathrm{pc}$
Dusty torus	$R_{torus} \sim 1 - 10\,\mathrm{pc}$
NLR	$R_{NLR} \sim 10^2 - 10^4\ \mathrm{pc}$
Jet	$R_{jet} \sim 100 - 1000\,\mathrm{kpc}$

AGN, whose main features are a very weak optical continuum and only narrow emission lines (NLR).

Focusing on the X-ray spectral properties, the main differences between these two categories are the progressive suppression of the primary power-law emission from Type-I to Type-II and the limited presence of nuclear emission below $2\,\mathrm{keV}$ in the most oscured objects[1]. According to hydrogen column densities of the obscuring gas, they are divided in *unobscured* ($N_H < 10^{21}\,\mathrm{cm}^{-2}$), *Compton-thin* ($10^{21} < N_H < 10^{24}\,\mathrm{cm}^{-2}$) and *Compton-thick* AGN ($N_H > 10^{24}\,\mathrm{cm}^{-2}$)[2].

In addition, concerning the radio domain, while most AGNs show some radio emission, there seems to be a clear dichotomy in this property. Therefore, the "radio loudness" parameter, R, was defined in order to separate *radio-loud* from *radio-quiet* AGNs. More precisely, an AGN is referred to as radio-loud when R, namely the ratio between the radio ($5\,\mathrm{GHz}$) and optical (B-band, 4400 Å) monochromatic luminosity, is > 10. Radio-loud objects, in turn, can be divided according to the extended radio structure and to whether they are edge brightened (*FRII sources*) or edge darkened (*FRI sources*). Among the radio-quiet AGN, there are the *Seyfert* galaxies, divided in *Seyfert 1* or *Seyfert 2* on the basis of their optical spectra (Netzer, 2013).

1.2.2 The AGN family

Historically, there are several types of AGN with a variety of names that reflect, in many cases, the period of discovery, rather than the physical properties of the objects in question. In the past, the higher-luminosity radio-loud AGN were referred to as *quasi-stellar radio objects* (QSROs), in order to distinguish them from radio-quiet luminous Type-I AGN, which were called *quasi-stellar*

---

[1]The correspondence between optical and X-ray Type I-II is $\approx 80\%$ (Lanzuisi et al., 2013).

[2]Compton thick AGN are most commonly identified in the 2-10 keV X-ray band by the measurement of a flat spectrum ($\Gamma < 1.0$) and a high Fe Kα line equivalent width (*EW*), i.e. *EW* > 1 keV (Brightman and Nandra, 2011a).

objects (QSOs). *Radio galaxies* are classified by their optical properties into broad-line radio galaxies (BLRGs) and narrow-line radio galaxies (NLRGs). The optical-UV spectrum of BLRGs is very similar to that of Type-I AGN with an additional nonthermal contribution to the optical continuum. Such objects tend to show the broadest emission lines among Type-I AGN, probably due to inclination effects. The optical emission-line spectrum of NLRGs is less well defined, covering a broad range of properties, from high-ionization Type-II AGN to low-ionization LINERs (i.e., *Low-ionization nuclear emission-line regions*). There are clear indications for obscuration in many of them. *Seyfert* galaxies, first pointed out by C. Seyfert in 1943, are characterized by the presence of strong high-ionization lines in their optical spectra, that distinguish them from normal emission spectra of H II regions. They are divided in Type-I and Type-II, on the basis of their optical spectral properties. Fig. 1.2 shows typical Seyfert galaxies spectra, illustrating the different classification of Type-I and Type-II objects, valid for the majority of AGN. Then, there is the group of *blazars*, that includes highly variable core-dominated radio-loud sources showing polarization at radio and optical wavelengths. They can be divided into BL Lacertae (BL-Lac) objects, highly variable and highly polarized objects, with virtually featureless continuous spectra, and flat-spectrum radio-loud AGN. LINERs are usually the lowest-luminosity AGN, with nuclear luminosity that can be smaller than the luminosity of high-ionization AGN by $1-5$ orders of magnitude. Perhaps many LINERs may belong to the category of real Type-II AGN, i.e. those AGN with no BLR (Netzer, 2013).
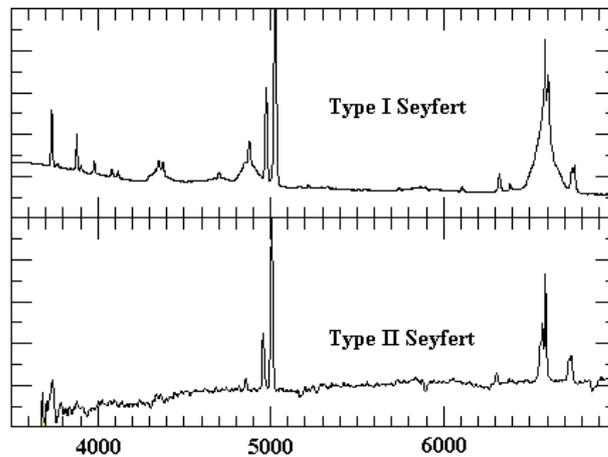
Figure 1.2: *The top panel shows the typical spectrum of a Type-I Seyfert galaxy, characterized by both broad and narrow emission lines, while the bottom panel illustrates the typical spectrum of a Type-II Seyfert galaxy, whose main features are narrow lines of highly ionized material and a partial absorption of the UV continuum (from http://www.uni.edu/morgans/astro/course/Notes/section3/new13.html).*

AGN unified model and its limits

Antonucci (1993) and Urry and Padovani (1995) introduced the AGN unified model, in order to construct a general picture, capable of shedding light on the various types of AGN. Its main driving parameter are the orientation of the AGN with respect to the line of sight and the radio loudness. The former determines the detectability of the central engine and the broad line region in the optical domain, while the latter indicates whether or not the AGN produces a significant jet. The simplest addition of a torus-like obscurer to the two central components, BH and accretion disc, can explain most of the observed differences between radio-quiet Type-I and Type-II AGN. Such a structure introduces a viewing angle parameter that determines what AGN components will be seen from a given line of sight. This can account for the different observed properties, such as the luminosity and variability of the optical–UV continuum, and the different amount of obscuration of the central X-ray source. Nevertheless, it fails to explain the properties of very low and very high luminosity AGN (e.g. some lineless AGN, the least luminous LINERs and the most luminous AGN at high redshift), where the presence of such an obscurer is questionable. In order to explain radio-loud objects, an additional component is required: a relativistic jet emanating from the vicinity of the BH (Netzer, 2013). This simple scheme is summarized in Fig. 1.3, that shows that Type-I AGN are nearly face-on objects, where both the BLR and NLR can be directly seen. On the other hand, Type-II AGN have larger viewing angles, that lead the line of sight to intercept the obscuring medium surrounding the nucleus, the dusty torus.

This simple model, produced nearly 20 years ago, is now partially updated. The smooth torus model has been recently replaced by a more sophisticated geometry (i.e., *clumpy torus model*, Hönig and Kishimoto 2010). Even more important, the variety of the AGN population (see Sec. 1.2.2) is now believed to be related to both geometrical and evolutionary effects.
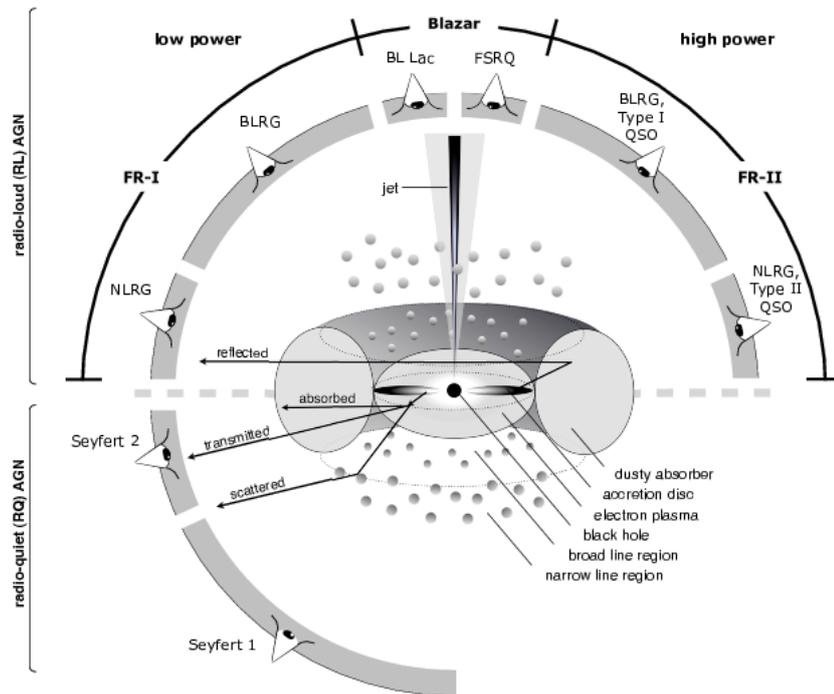
Figure 1.3: *Schematic representation of the AGN phenomenon in the unified scheme. The type of the observed object depends on the viewing angle, whether or not the AGN produces a significant jet emission, and how powerful the central engine is. Note that radio loud objects are generally thought to display symmetric jet emission (Beckmann and Shrader, 2013).*

1.3   Luminous Infrared Galaxies

Luminous Infrared Galaxies (LIRGs), firstly observed in 1983 by the *Infrared Astronomical Satellite* (IRAS), are remarkable galaxies of the local Universe exhibiting an extremely high IR luminosity, $L_{8-1000\,\mu m} > 10^{11}\,L_\odot$. These objects are hosts of an intense starburst (SB) and/or AGN activity, and are often part of a merging galaxy group (Armus et al., 1987). At the highest luminosities ($L_{8-1000\,\mu m} > 10^{12}\,L_\odot$), these extreme objects are called *Ultra-Luminous Infrared Galaxies* (ULIRGs) and appear to be mostly advanced mergers (Sanders and Mirabel, 1996).

The trigger for the intense IR emission seems to be the strong interaction/merger of molecular gas-rich spirals, and the bulk of the IR luminosity for all but the most luminous objects is due to dust heating from an intense starburst within giant molecular clouds.

Mapping of these galaxies in H I and CO has provided several important clues regarding the physical nature and origin of LIRGs. The integrated H I profiles of these galaxies are characterized by distorted *21 cm* profiles and deep absorption. High-resolution HI mapping with the VLA reveals complex structures, with much of the atomic gas spread between long tidal tails and the main body of the galaxies. Sometimes the H I shows central concentration, but often there is a central depression where the gas is predominantly molecular. The H I in the tails provides a powerful diagnostic of the orbital kinematics of the interaction or merger (Kennicutt et al., 1996).

The studies of the molecular gas, principally traced by molecules such as CO and HCN, show that the SFRs of (U)LIRGs are fueled by molecular gas masses of $10^9 - 10^{10}\,M_\odot$, with a *Star Formation Efficiency* of $SFE = L_{IR}/M(H_2) \sim 500\,L_\odot/M_\odot$. Such high SFEs are equal to the maximum reachable value, set by the radiative feedback of massive stars on the dust, mixed with the molecular gas, accreted by the star-forming sites, and are one of the many indicators of the extreme interstellar medium (ISM) conditions found in such systems (Papadopoulos et al., 2010). The large amount of cool gas is located in the central region of the galaxy, concentrated into a radius of $r \leq 0.5 - 1\,kpc$, with densities around $10^4\,cm^{-3}$ (Downes and Solomon, 1998). Such enormous gas concentrations are an ideal breeding ground for a variety of powerful phenomena, including powerful starbursts that generate superwinds, the formation of massive star clusters and, possibly, the building and/or fuelling of an AGN. Indeed, (U)LIRGs are very likely to represent an important link between starburst galaxies and the AGN phenomena. Nevertheless, it is hard to distinguish the relative roles of these power sources, owing to heavy dust obscuration.

Indeed, the fraction of galaxies hosting AGN activity is correlated to IR luminosity in the range $(8 - 1000\,\mu m)$ or SFR. On the basis of optical spectroscopy, the AGN fraction rises from $\approx 5\%$ for galaxies with $L_{IR} < 10^{11}\,L_\odot$, to $\approx 15\%$ for LIRGs and $\approx 25\%$ for ULIRGs, as shown in Fig. 1.4 (Veilleux, 1999). Concerning (U)LIRGs, the AGN fractions increase to $\approx 50-80\%$ when including MIR spectroscopy and X-ray spectra analysis (e.g., Nardini et al. 2010 and Lehmer et al. 2010). These results show that the BH grows almost continuously during periods of intense star formation.

Their large reservoirs of molecular gas mass, along with clear evidence of strong dynam-
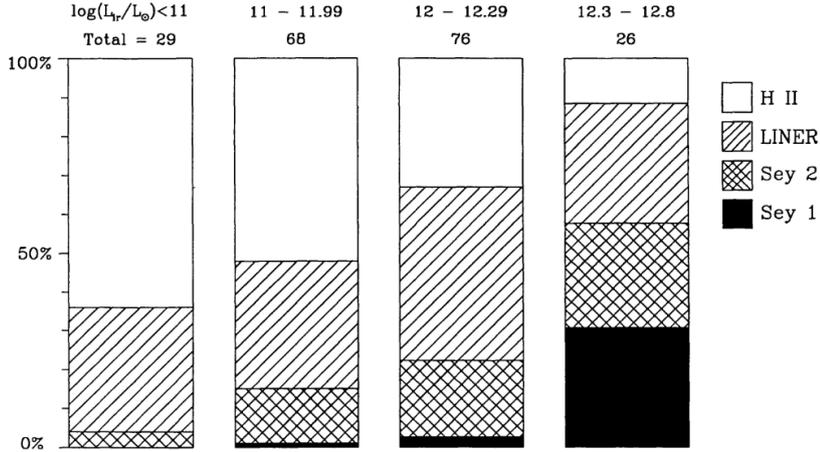
Figure 1.4: *Optical spectral classification on the function of IR luminosity, showing H II galaxies (star-forming galaxies with spectra resembling those of normal H II regions), LINERs (Low-Ionization Nuclear Emission-Line Regions), Seyfert 2s (AGN with strong low- and high-ionization lines) and Seyfert 1s (AGN with broad, quasar-like recombination lines with $FWHM \approx 2000\,km\,s^{-1}$) fractions in (U)LIRGs (Veilleux, 1999).*

ical interactions and mergers, make these systems unique local examples of dust-enshrouded galaxy formation in the distant Universe (Papadopoulos et al., 2012). Actually, (U)LIRGs are thought to represent the transitional phase in evolution from a SB galaxy to elliptical/lenticular galaxies (Sanders et al., 1988), and thus must quench their star formation during this period. Since (U)LIRGs offer a unique insight into this transitional phase from star-forming to quiescent galaxies, understanding which mechanisms are affecting the star-forming gas is crucial (Rosenberg et al., 2015).

In order to trace the high amount of injected energy, a multiwavelength approach is required, studying the emission lines that serve as a coolant along with IR emission. In particular, molecular spectral line energy distributions (SLEDs) constitute a key tool for probing the heating source of the molecular gas (SF VS AGN) and for estimating total molecular gas masses.

1.4 AGN-starburst connection

Massive galaxies in the local Universe host a central SMBH with a mass proportional to the mass and the velocity dispersion, following the relations (Magorrian et al. 1998, Ferrarese and Merritt 2000):

$$M_{BH} \propto 10^{-3} M_{bulge}$$
$$M_{BH} \propto \sigma_{bulge}^4$$

(1.2)

This tight correlation (shown in Fig. 1.5) has suggested a symbiotic connection between the formation and growth of the galaxies (directly linked to the SFR) and the BH growth (related

to AGN activity).
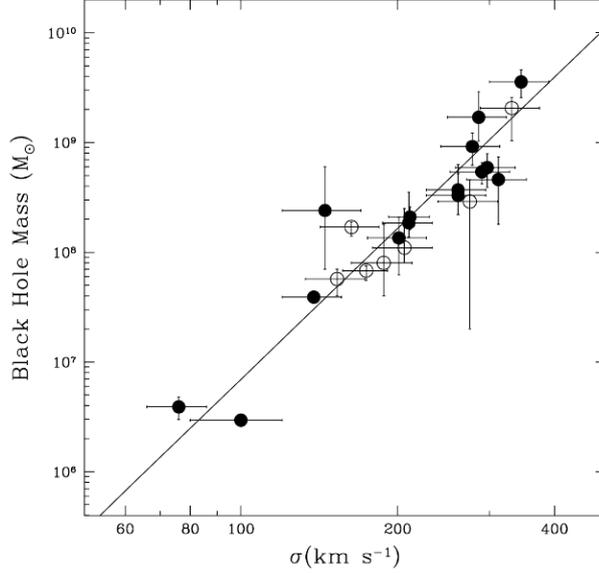
Figure 1.5: *The mass of SMBHs as a function of the velocity dispersion of the stars in the host galaxy (Ferrarese and Merritt, 2000).*

Indeed, while recent studies find no clear correlation between instantaneous BH growth and SF (i.e., Mullaney et al. 2012), probably to different time scales, the black hole accretion density and SFR history of the Universe show a similar trend with a significant growth at high redshift, a peak around $z \approx 2$ and then a decline (see Fig. 1.6) Another clue that suggests a deep connection between AGN and SF is that young stars are often found in the central regions of nearby AGN. These studies demonstrated that in 30%-50% of the cases AGN activity is associated with young stars, aged less than a few 100 Myr. This connection could stem from the fact that both these two phenomena need gas to fuel them and in some galaxies a large amount of gas has fallen towards the central region, because of an interaction or secular evolution. In addition, Davies et al. (2007), using spatially resolved spectroscopy of the central regions of nine nearby Seyfert galaxies, found that the peak of AGN activity occurs $\approx 50 - 200\,\mathrm{Myr}$ after the beginning of SF. This time delay suggests that the AGN may be fuelled by the gas located in the star-forming region through winds and supernovae (SNe) explosions.

BH growth relies on the accretion of cool gas, either from the host galaxy or the extragalactic environment, that inflows from kpc scales down to the central region. More precisely, the gas has to be driven down to $\approx 10\,\mathrm{pc}$ before coming under the influence of the BH. The most important barrier to overcome is the angular momentum, that prevents the gas from reaching the central regions: the gas has to lose $\approx 99\%$ of its angular momentum to pass from a stable orbit at $r = 10\,\mathrm{kpc}$ to $r = 10\,\mathrm{pc}$ (Alexander and Hickox, 2012). However, it can be overcome through a series of gravitational instabilities, such as large-scale gravitational torques, produced
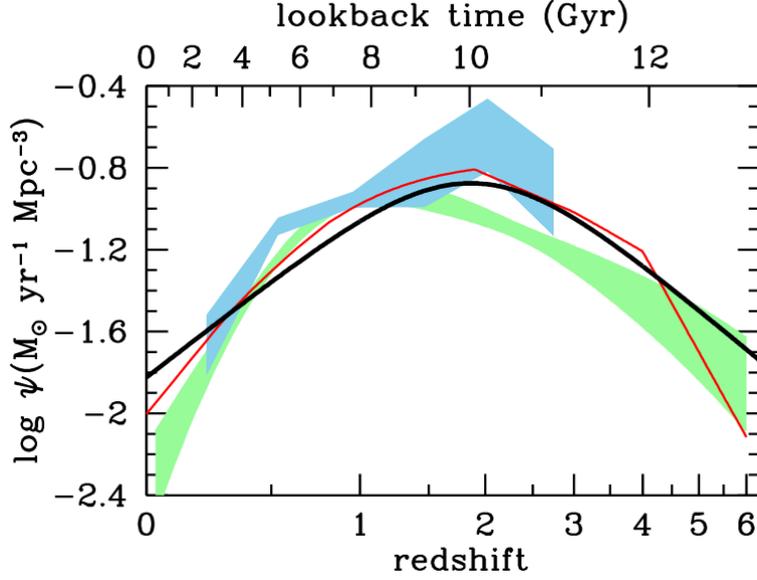
Figure 1.6: *Comparison of the best-fit star formation history (thick solid curve) with the accretion history from X-ray (red curve, Shankar et al. 2009; green curve, Aird et al. 2010) and IR (light blue shading, Delvecchio et al. 2014) data. The shading indicates the $\pm 1\sigma$ uncertainty range on the total bolometric luminosity density. The comoving rates of black hole accretion have been scaled up by a factor of 3300 to facilitate visual comparison to the star-formation history (SFH) (Madau and Dickinson, 2014).*

by galaxy bars and gas instabilities (internal mechanisms), or by galaxy interactions and galaxy major mergers (external mechanisms), summarized in Fig. 1.7. Internal processes and galaxy interactions are usually referred to as *secular evolution*. The rapid flow of cold gas, that is crucial to fuel an AGN, is extremely likely to result also in high rates of SF. In fact, mergers of gas-rich galaxies are also very efficient in producing elevated SFRs, leading to a luminous IR-active phase, making the galaxy either a LIRG or an ULIRG, according to its IR luminosity. When sufficient matter is transported to the nuclear region, an oscured quasar, whose emission becomes far brighter than the galaxy itself, forms. At higher L_{IR} the fraction of the luminosity related to the AGN component rises and the BH growth appears to be partially or totally obscured, because of the large amount of nuclear gas and dust. Then, the SFR is quenched due to AGN and SN feedback. The models based on this evolutionary scenario seem to follow the local observations. Nevertheless, powerful starbursts are rare in the local Universe and it is still unknown whether this starburst-quasar scenario (shown in Fig. 1.8) is dominant at high redshift, during the peak of AGN activity (Alexander and Hickox, 2012).
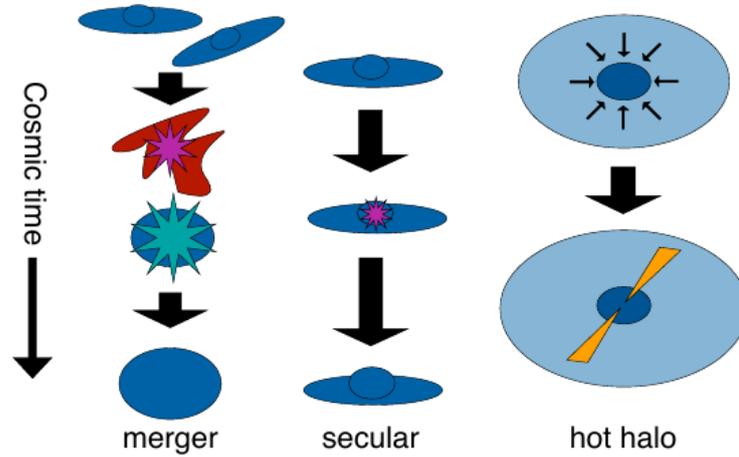
Figure 1.7: *Scheme that illustrates the large-scale processes that appear to trigger the AGN activity: major merger of gas-rich galaxies, secular evolution and hot halo accretion, that seems to dominate in low-excitation radio-loud AGN (Alexander and Hickox, 2012).*
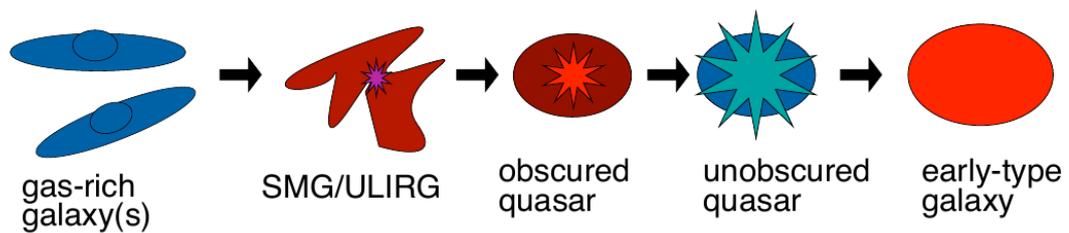

Figure 1.8: *Diagram that illustrates the principal phases of the major-merger evolutionary scenario, firstly proposed by Sanders et al. 1988 (Alexander and Hickox, 2012).*

1.5 Diagnostic diagrams

Optical line ratios have long provided a good discriminator between AGN and SB-dominated galaxies, since different line ratio values are due to different excitation mechanisms. An empirical diagnostic diagram was developed by Baldwin et al. (1981) and refined by Veilleux and Osterbrock (1987). In some cases, such as for (U)LIRGs and for some Seyfert 2 galaxies, the optical spectroscopy may fail to reveal an AGN owing to dust obscuration in the galaxy center. However, in all but the most of extreme cases is still reliable (e.g., Veilleux 1999).

Baldwin et al. (1981) proposed a suite of three diagnostic diagrams to classify the dominant energy source in emission-line galaxies. These diagrams are commonly known as *Baldwin-Phillips-Terlevich* (BPT) diagrams and are based on these four optical line ratios: [O III]/Hβ, [N II]/Hα, [S II]/Hα and [O I]/Hα. In addition, Kewley et al. (2001) (hereafter Ke01) created a theoretical *maximum starburst line* on the BPT diagrams, using a combination of stellar population synthesis models and detailed self-consistent photoionization models. Galaxies lying above this line are likely to be dominated by an AGN. Finally, Kauffmann et al. (2003) (hereafter Ka03) added an empirical line to divide pure star-forming galaxies from Seyfert-HII composite objects, whose spectra are affected by significant contribution of both AGN and SF (see Fig. 1.9). Actually, composite galaxies are likely to contain a metal-rich stellar population and an AGN.

In panel (a) of Fig. 1.9 is shown the [O III]/Hβ versus [N II]/Hα standard optical diagnostic diagram for the galaxy sample analyzed by Kewley et al. (2006). Galaxies that are located below the dashed Ka03 line are classified as HII-region-like galaxies. Star-forming galaxies form a tight sequence, the *star-forming sequence*, from low metallicities (low [N II]/Hα, high [O III]/Hβ) to high metallicities (high [N II]/Hα, low [O III]/Hβ). The AGN mixing sequence starts from the high metallicity end of the star-forming sequence and extends towards high [O III]/Hβ and [N II]/Hα values.

Panel (b) and (c) of Fig. 1.9 show the [O III]/Hβ versus [S II]/Hα and [O I]/Hα, respectively. The blue solid line represents the *Seyfert-LINER classification line* (hereafter Ke06), determined by Kewley et al. (2006), that divides Seyfert galaxies and LINERs. The former lie above the blue solid line, while the latter below it, because of their low-ionization line emission.

Zhang et al. (2008) showed that Seyfert 1 and Seyfert 2 galaxies have different distribution on the [O III]/Hβ and [N II]/Hα diagram. They contend that, as the extinction increases, the distribution on BPT diagram moves to larger [N II]/Hα value. Indeed, Seyfert 2 galaxies in their sample display a clear left boundary on the BPT diagram and only 7.3% of them lie beyond. Consequently, they added to BPT diagrams their *S12 line*, that divides Seyfert 1 from the majority of Seyfert 2 galaxies.
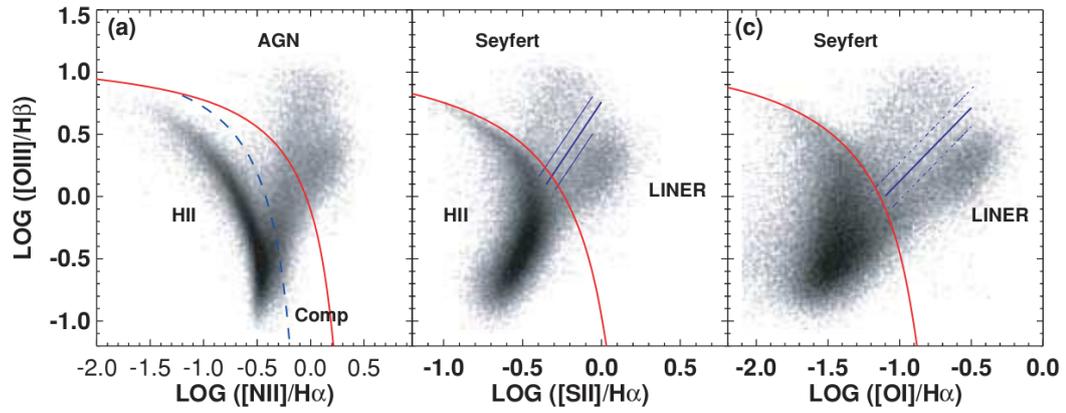
Figure 1.9: *The three BPT diagrams. (a) The [O III]/Hβ versus [N II]/Hα diagnostic diagram. The red solid line represents the ke01 classification line, the blue dashed line the ka03 classification line. (b) The [O III]/Hβ versus [S II]/Hα. (c) The [O III]/Hβ versus [O I]/Hα. The blue solid line is the ke06 classification line (Kewley et al., 2006).*
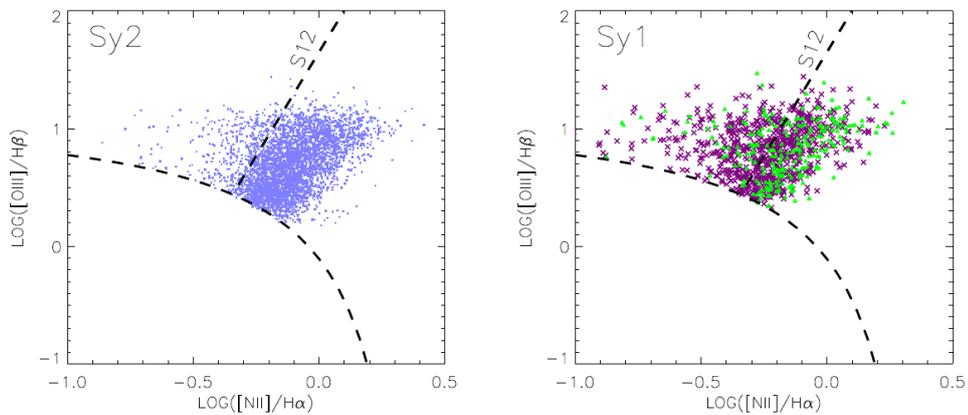
Figure 1.10: *BPT diagram for Seyfert 2 (left panel) galaxies and Seyfert 1 (right panel). The lower curve is the ke01 classification line. The straight line is the S12 line, that divides Seyfert 1 from the majority of Seyfert 2 galaxies, mainly located on the right side of the line (Zhang et al., 2008).*

1.6 MIR-X-ray correlation

The dusty circumnuclear material (see Sec. 1.2.1) around the AGN absorbs the intrinsic ultraviolet and optical radiation from the accretion disc, and typically emits, in turn, in the MIR/FIR regime. Before the Very Large Telescope (VLT), it was very difficult to disentangle the MIR emission due to the AGN from other contamination sources (i.e., clouds heated by stellar radiation). Nowadays, thanks to the VISIR[3] instrument at the VLT ($\theta \approx 0.3'' - 0.4''$), it has been possible to isolate the nuclear region for local galaxies. This has been done by Gandhi et al. (2009), who found that the MIR emission is an independent isotropic AGN indicator. The authors obtained a narrow relation from the nuclear MIR emission and the intrinsic $2 - 10$ keV luminosity, whose best-fit is given by:

$$log\left(\frac{L_{MIR}}{10^{43}}\right) = (0.19 \pm 0.05) + (1.11 \pm 0.07)log\left(\frac{L_{2-10\,\text{keV}}}{10^{43}}\right) \tag{1.3}$$

Fig. 1.11 shows the MIR-X-ray correlation. In addition, they found that both Seyfert 1 and Seyfert 2 follow the same correlation. This result was not predicted by radiative transfer models, based on a torus with a continuous smooth dust distribution, since an optically-thick line-of-sight through the torus will primarily show cooler dust and a lower MIR luminosity for the same $L_{2-10\,\text{keV}}$ than does an optically-thin one.
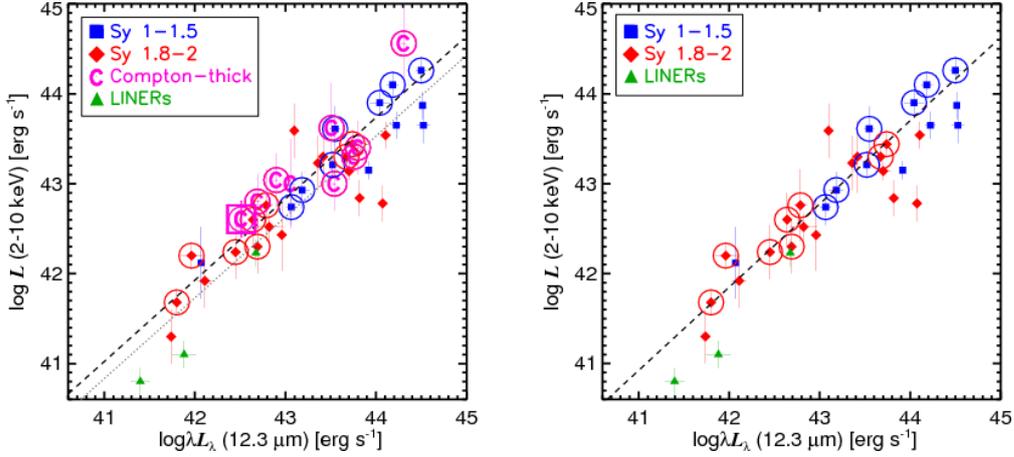
Figure 1.11: *In the left panel, the MIR-X-ray correlation for the sample analyzed by Gandhi et al. (2009) is illustrated. The observed galaxies are split into Seyfert $1 - 1.5$ (blue squares), Seyfert $1.8 - 2$ (red diamonds), LINERs (green triangles) and Compton-thick AGN (in pink). The well-resolved sources are circled and the dashed line is their fitted correlation, shown in Eq. 1.3. The dotted grey line is the correlation fit to all the sample. In the right panel, the MIR-X-ray correlation for the Compton-thin sources only is shown (Gandhi et al., 2009).*

---

[3]The VLT spectrometer and imager for the mid-infrared.

1.7 SFR indicators

There are many SFR indicators, directly or indirectly linked to the stellar emission, depending on the considered band. In the UV/optical/near-IR range ($\approx 0.1 - 5\,\mu$m), the SFR indicators probe the direct stellar light emerging from galaxies, while in the MIR/FIR ($\approx 5 - 1000\,\mu$m) trace the stellar light reprocessed by dust. As the vast majority of galaxies contain at least some dust, the first types of indicators need to be accurately corrected for the dust attenuation to be reliable. In addition, also the ionizing photons by massive stars can be used to define SFR indicators. These SFR tracers comprise hydrogen recombination lines, from the optical to radio wavelengths and forbidden metal lines. Finally, even the X-ray emission produced by high-mass X-ray binaries (HMXB), massive stars and SNe, and the radio synchrotron emission from galaxies, due to electrons accelerated by SN explosions, can be used as SFR indicators (Calzetti, 2013).

The emission contribution of a potential AGN to the luminosity (in continuum or line) used as SFR indicator can lead to a significant deviation from the correlations described in the following sections. In this case, the galaxies containing the AGN can be recognized.

1.7.1 FIR-radio correlation

In star-forming galaxies, FIR luminosity appears to be connected to radio continuum by a tight relation spanning four orders of magnitude in luminosity and up to high redshift (e.g., van der Kruit 1973, Garrett 2002):

$$log(L_{FIR}) = (0.98 \pm 0.06)log(L_{1.4\,GHz}) + 15.4 \pm 1.6 \tag{1.4}$$

with a dispersion around the best-fit relation of 0.18 (Ranalli et al., 2003). It is thought that this is due to the presence of massive, young stars ($M \gtrsim 5\,\mathrm{M_\odot}$) embedded in dust, that absorbs their UV radiation and re-emits in the IR band, while SN explosions may produce the observed synchrotron emission. Therefore, these luminosities are assumed to be indicators of the global SFR in a galaxy (Condon 1992, Kennicutt 1998)[4]:

$$SFR = \frac{L_{1.4\,\mathrm{GHz}}}{4.0 \times 10^{28}}\,\mathrm{M_\odot\,yr^{-1}}$$
$$SFR = \frac{L_{FIR}}{2.2 \times 10^{43}}\,\mathrm{M_\odot\,yr^{-1}} \tag{1.5}$$

where the FIR flux is defined after Helou et al. (1985) as

$$FIR = 1.26 \times 10^{-14}(2.58\,S_{60\mu\mathrm{m}} + S_{100\mu\mathrm{m}})\,\mathrm{W\,m^{-2}} \tag{1.6}$$

---

[4] $L_{1.4\,\mathrm{GHz}}$ is in erg s^{-1} Hz^{-1}, L_{FIR} in erg s^{-1} and IR fluxes in Jy.

In addition, Helou et al. (1985) defined the parameter

$$q \equiv log\left(\frac{FIR}{3.75 \times 10^{12}\,\mathrm{W\,m^{-2}}}\right) - log\left(\frac{S_{1.4\,GHz}}{\mathrm{W\,m^{-2}\,Hz^{-1}}}\right) \tag{1.7}$$

as a logarithmic measure of the FIR/radio flux-density ratio. The distribution of q was found to be quite narrow, $\langle q \rangle \simeq 2.3$ with a rms scatter $\simeq 0.2$, among spiral galaxies in Virgo, a large, inhomogeneous sample of spiral and irregular galaxies, Sbc galaxies, E/S0 galaxies with different level of star formation, and radio flux-limited samples of normal galaxies (Condon, 1992).

1.7.2 X-ray-FIR-radio correlation

Since star-forming galaxies are also luminous sources in the X-ray band, because of the great amount of HMXB, young supernova remnants remnants (SNR) and hot plasmas associated to star-forming regions and galactic winds, a relation that links FIR and X-ray emission is expected. In addition, since FIR and radio continuum appear to be connected, also an association between X-ray and radio continuum is foreseeable. Indeed, a relation between FIR and soft X-ray luminosities, i.e. $0.5 - 3.0\,\mathrm{keV}$, was found (e.g., Griffiths and Padovani 1990) and then extended from Ranalli et al. (2003) to the $2 - 10\,\mathrm{keV}$ band, which is essentially free from absorption. In particular, Ranalli, starting from Eq. 1.4, obtained:

$$log(L_{2-10}) = log(L_{FIR}) - 3.62\,(3.68)$$
$$log(L_{2-10}) = log(L_{1.4\,\mathrm{GHz}}) + 11.13\,(11.12) \tag{1.8}$$

with a dispersion of $\simeq 0.29$ for both fits (see Fig. 1.12). The existence of these tight linear relations suggest that the three considered bands carry the same information, which means that even X-ray luminosity can be considered as a SFR indicator (Ranalli et al., 2003). We report the so-called *Ranalli relation* linking the X-ray luminosity and the SFR:

$$SFR = 2.0 \times 10^{-40}\,L_{2-10\,\mathrm{keV}}\,\mathrm{M_\odot\,yr^{-1}} \tag{1.9}$$
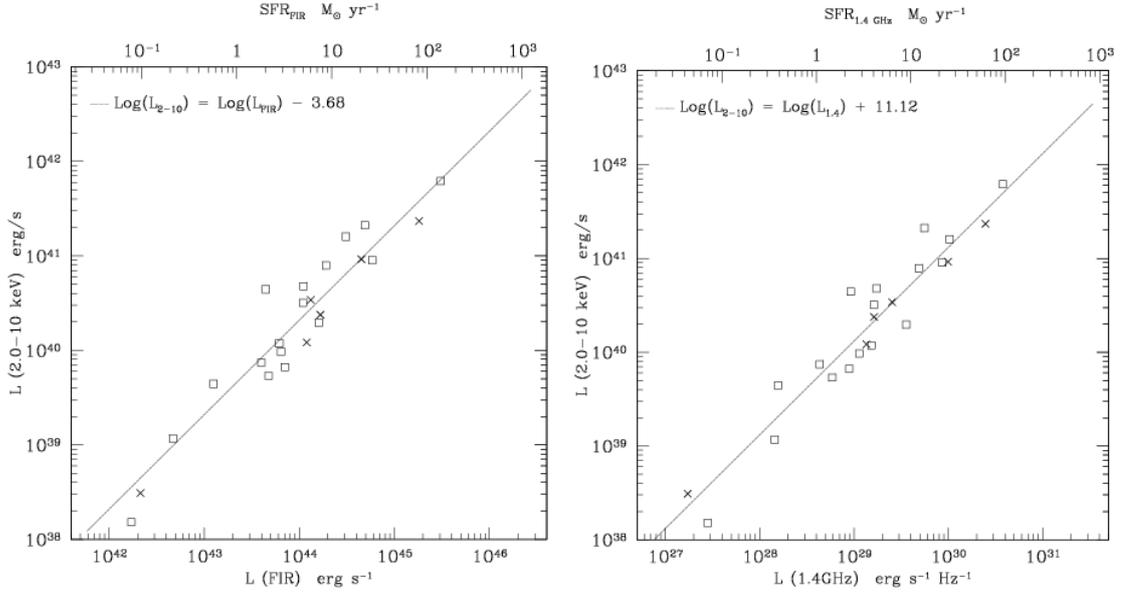
Figure 1.12: *The $2.0 - 10\,keV$ luminosity of local star-forming galaxies with respect to FIR and radio luminosities. The squares and the crosses represent the local and supplementary sample taken into account by Ranalli et al. (2003), respectively, while the dotted lines are the best fits, shown in Eq. 1.8 (Ranalli et al., 2003).*

1.8   NGC 34: a nearby "ambiguous" object

NGC 34 has been originally classified as a Seyfert 2 because of the lack of broad component in its optical spectrum (Véron-Cetty and Véron, 2006). However, others have emphasized the apparent weakness of the [O III] ($5007\,\mu$m) emission line with respect to the Balmer lines Hα and Hβ, classifying it as a narrow-emission-line galaxy (e.g., Veilleux and Osterbrock 1987) or a starburst galaxy (e.g, Mazzarella et al. 1991). Recently, the nuclear spectrum of NGC 34 has been decomposed in two components: on ($\approx 75\%$ of the total bolometric luminosity, Imanishi and Alonso-Herrero 2004) due to the SF, and the other ($\approx 25\%$ of the total) due to the AGN. Previous studies (Gonçalves et al., 1999) pointed out a $\approx 90\%$ and $\approx 10\%$ contributions, respectively.

The exact nature and origin of NGC 34 optical nuclear spectrum have long been controversial. However, it is widely accepted that this galaxy is a composite object, whose nuclear spectrum is related to both the presence of a starburst and an AGN. More precisely, because of its high luminosity in the IR band ($log(L_{IR}) \simeq 11.42$, Gruppioni et al. 2016), NGC 34 was classified as a LIRG, while its X-ray luminosity ($log(L_{2-10\,keV}) \simeq 42$, Brightman and Nandra 2011a) indicates the likely presence of an AGN.

NGC 34 is definitively gas rich, and thus, can sustain its strong central starburst and present mild AGN activity (Schweizer and Seitzer, 2007). In particular, Schweizer and Seitzer (2007) carried out a detailed analysis of NGC 34, showing that this galaxy is a late stage merger with prominent tidal tails. Their results are consistent with a merger of two gas-rich galaxies with

mass ratio of $m/M \simeq 1/2 - 1/3$, whose disks are already coalesced with a separation limit of 50 pc for any possible double nuclei configuration (Xu et al., 2014). Fig. 1.13 shows a HST image of NGC 34, with its single nucleus and tidal tails.
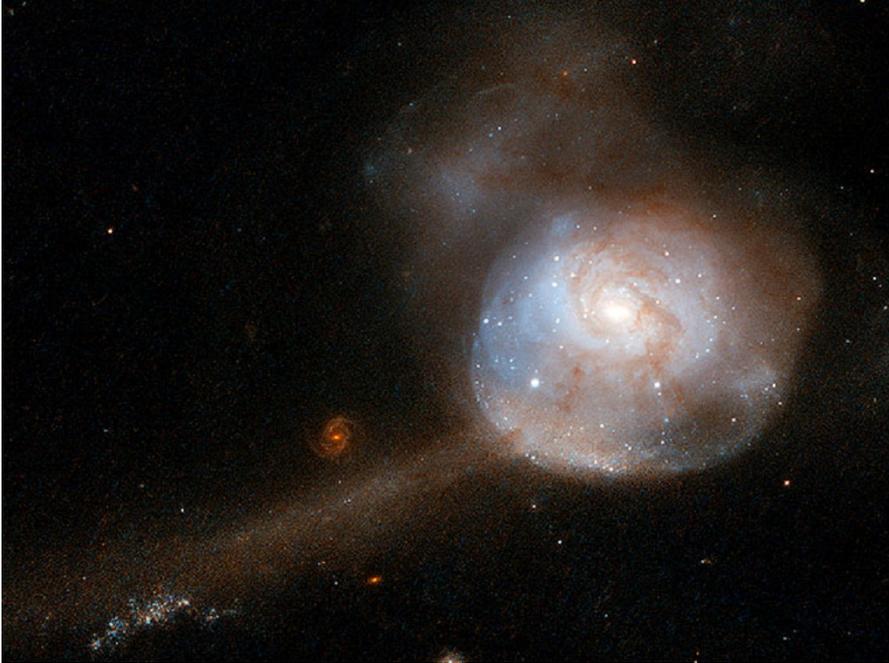
Figure 1.13: *A HST image of NGC 34. This galaxy features a single nucleus, containing a blue central disk with delicate fine structure in the outer parts and tidal tails, indicative of a merger of two former disk galaxies of unequal mass. By now, these galaxies appear to have completed their merger. Image Credit: NASA, ESA, the Hubble Heritage (STScI/AURA)-ESA/Hubble Collaboration, and A. Evans (University of Virginia, Charlottesville/NRAO/Stony Brook University).*

NGC 34 is a local galaxy at redshift $z \simeq 0.0196$, and thus it is located at a luminosity distance $D_L \simeq 85.7$ Mpc ($h = 0.696$, $\Omega_M = 0.286$ and $\Omega_\Lambda = 0.714$). Thanks to its vicinity, there are many detailed data available, from the X-rays (XMM) to the sub-mm (ALMA), for studying and characterising in detail its activity.

This galaxy is part of the local 12μm sample of Seyfert galaxies (12MGS, Rush et al. 1993), a sample of AGN unbiased against absorption, given to its MIR selection (see Sec. 1.6). In the following section, we will show the available data found in the literature and the corresponding classification.

1.8.1 NGC 34 Spectral Energy Distribution

Recently, Gruppioni et al. (2016) disentangled the AGN and SF component for the majority of the local sample 12MGS, using a detailed broad-band *spectral energy distribution* (SED) decomposition, developed by Berta et al. (2013), including three components: the emission of

stars, dust heated by stars and a possible AGN dusty torus. In order to constrain the stellar, AGN and star-formation contributions, they took advantage of data also from the X-ray. Moreover, the availability of *Spitzer-IRS* low resolution MIR spectra played a fundamental role to put constrains on the dusty torus component. Thanks to the very detailed data, available for this local sample, they could determine the crucial physical quantities that characterize the AGN and its host galaxy, such as SFR, AGN luminosity, stellar mass and AGN fraction. This has been possible because of the vicinity of these galaxies.

Fig. 1.14 shows the NGC 34 SED in the $0.1 - 1000\,\mu$m range, where all the three components (i.e., emission of stars, the dust heated by star formation and the AGN dusty torus) are shown, while Tab. 1.2 reports the main properties of NGC 34 obtained from SED-fitting decomposition. In particular, the total IR luminosity was obtained by integrating the SED in the $8 - 1000\,\mu$m rest-frame, while the SFR was obtained through the Kennicutt 1998 relation, converted to a Chabrier IMF.

Table 1.2: In this table are shown the main properties of NGC 34, derived from the SED decomposition from Gruppioni et al. 2016. In the columns are reported the logarithm of the total IR luminosity, the SFR, the logarithm of the IR luminosity due to SF, the AGN fraction and the logarithm of the bolometric AGN luminosity (in the IR and X-ray bands), respectively (Gruppioni et al., 2016).

$log(L_{IR})$	SFR	$log(L_{IR}^{SF})$	f_{AGN}	$log(L_{bol}^{AGN})_{IR}$	$log(L_{bol}^{AGN})_{X-ray}$
$log(L_\odot)$	$M_\odot\ yr^{-1}$	$log(L_\odot)$		$log(L_\odot)$	$log(L_\odot)$
11.42 ± 0.05	24.44 ± 1.79	11.39 ± 0.07	0.19 ± 0.10	11.03 ± 0.05	9.79 ± 0.17

Thanks to the SED decomposition made by Gruppioni et al. 2016, it is possible to isolate the torus contribution and calculate the corresponding MIR intrinsic luminosity, interpolating the SED at $12.3\,\mu$m and applying the correct K-correction[5]. The obtained value is $logL_{MIR} \simeq 42.13\,\mathrm{erg\,s^{-1}}$. As Fig. 1.15 shows, NGC 34 appears to follow the Gandhi relation found for Seyfert galaxies (see Sec. 1.6), reinforcing the hypothesis of a nuclear AGN.

---

[5]The K correction "corrects" for the fact that sources observed at different redshifts are, in general, compared with standards or each other at different rest-frame wavelengths.
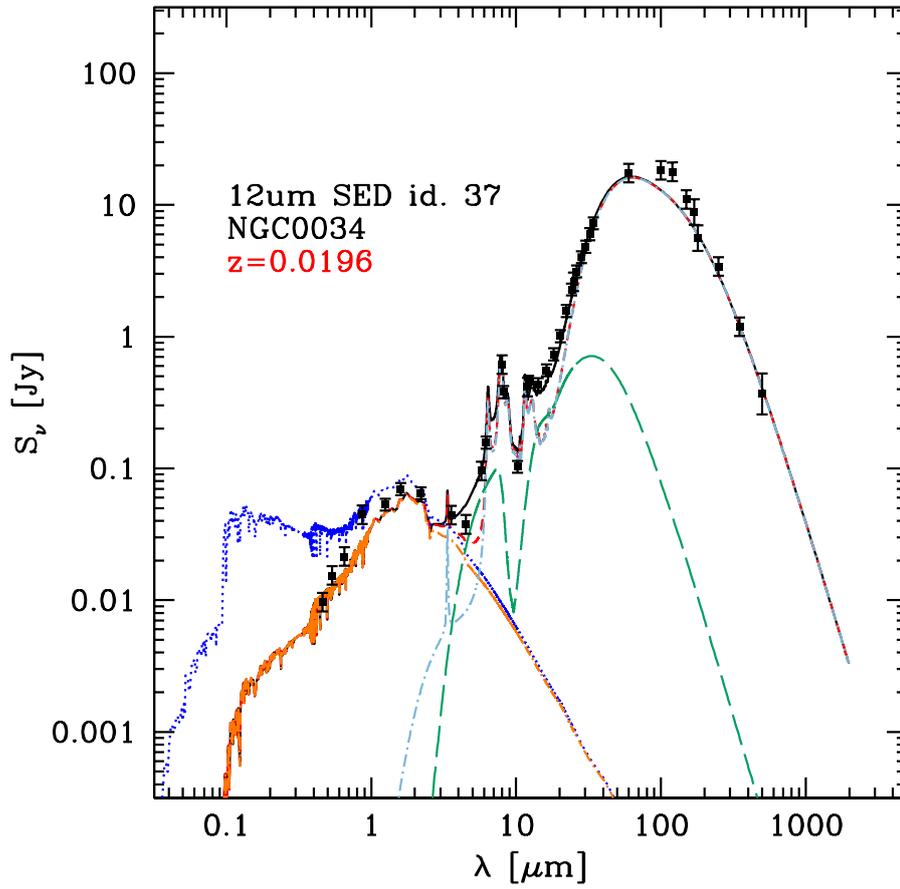
Figure 1.14: *Observed SED of NGC 34, decomposed into stellar, AGN and star-formation components. The black filled circles with error bars are the observed data of Gruppioni et al. 2016, the blue dotted line shows the unabsorbed stellar component, the red dashed line shows the combination of extinguished stars and dust IR emission, the long-dashed green line shows the dusty torus emission, whereas the pale-blue dot-dashed line shows the dust re-emission, only linked to SF. Finally, the black solid line is the sum of all components (Gruppioni et al., 2016).*
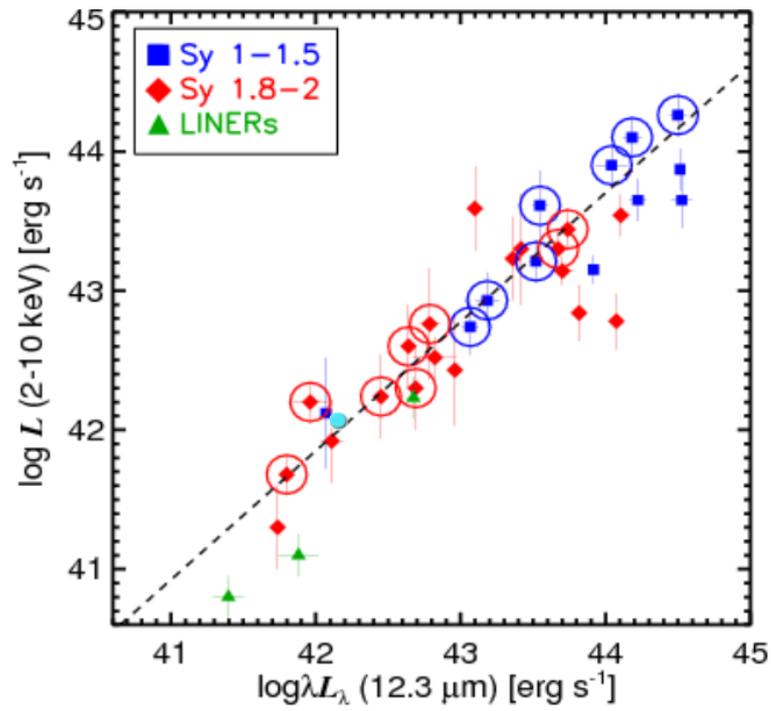
Figure 1.15: *The $2.0 - 10\,keV$ luminosity of the sample analyzed by Gandhi et al. 2009 with respect to MIR luminosity at $12.3\,\mu m$. NGC 34 is shown by the cyan circle. This figure is taken from Gandhi et al. 2009 (see the right panel of Fig. 1.11).*

1.8.2 Optical data

The classical optical method of defining AGN activity type is through BPT diagrams, discussed in Sec. 1.5, making use of the optical emission lines ratios to determine the dominant ionizing source in emission-line galaxies, that can be related to photoionization by stars, to a harder non-thermal source such as an AGN or to collisional excitation by shocks, as may be the case of LINERs. Brightman and Nandra (2011b) used the scheme introduced by Kewley et al. (2006) to classify the galaxies in 12MGS. Using the narrow-line ratios reported in Tab. 1.3 for NGC 34, our source is classified as an AGN according to the [O III]/Hβ versus [N II]/Hα diagram and as a Seyfert 2 from [O III]/Hβ versus [S II]/Hα and [O III]/Hβ versus [O I]/Hα (see Fig. 1.16).

Table 1.3: NGC 34 BPT diagnostic ratios, reported by Brightman and Nandra 2011a.

[OIII]/Hβ	[NII]/Hα	[SII]/Hα	[OI]/Hα
2.86	1.20	0.52	0.11
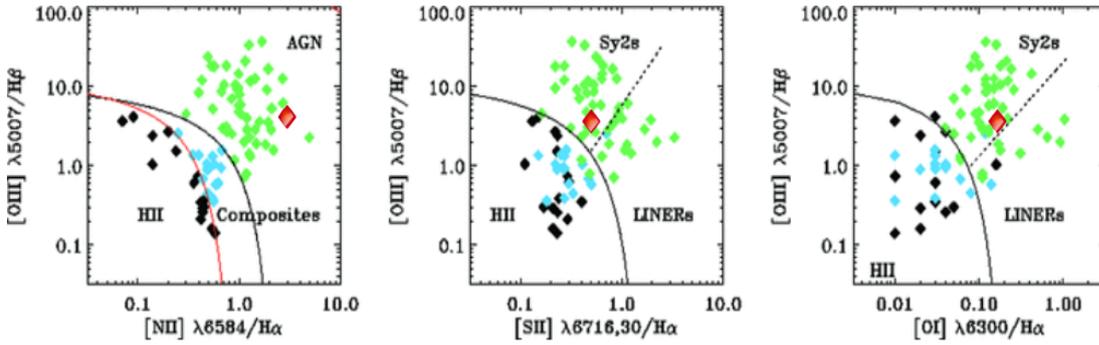
Figure 1.16: *BPT diagrams for the 12MGS: H II galaxies (in black), composite galaxies (in cyan) and Sy2s and LINERs (in green) are separated using the classification scheme of Kewley et al. 2006. NGC 34 is shown in red. The first diagram identifies pure H II galaxies (in black), H II/AGN composites (in cyan) and pure AGN (in green), but does not distinguish between Sy2s and LINERs, unlike the other two diagrams (Brightman and Nandra, 2011a).*

1.8.3 IR data

Another way for examining starburst and AGN activities is through the relative strengths of the fine-structure MIR lines in different ionization stages, that can be excited by SF, an AGN or both. The typical AGN lines are [Ne V] (14.32 and 24.32 μm) and [O IV] (25.89 μm), since they are not affected by the photoionization of stars, i.e. are weak in spectra of star-forming regions, given their high ionization potentials, 97 and 84.9 eV, respectively (Genzel et al., 1998). On the other hand, the lines and features that are mainly produced in star-forming regions are: polycyclic aromatic hydrocarbons (PAHs, 6.2 μm, 11.2 μm), [Ne II] (12.8 μm), [S III] (18.7 μm,

$33.5\,\mu$m), [Si II] ($34.5\,\mu$m), [O I] ($63\,\mu$m, $145.5\,\mu$m), [N II] ($121.9\,\mu$m) and [C II] ($157.7\,\mu$m). Other lines, such as [S IV] ($10.5\,\mu$m), [Ne III] ($15.5\,\mu$m), [O III] ($52\,\mu$m, $57\,\mu$m) and [N III] ($57\,\mu$m), are excited by both AGN and SF. These lines cover a wide range of critical densities and ionization stages, tracing different astrophysical conditions: from Photo-dissociation Regions (PDRs, see Ch. 3), to stellar/HII regions, to the AGN (Gruppioni et al., 2016). Therefore, combining their ratios has a huge importance in the definition of AGN versus SF diagnostic diagrams.

Concerning NGC 34, in the near-IR (NIR, $0.8 - 2.4\,\mu$m), relatively weak forbidden emission lines from [C I], [S III], and [Fe II] were detected, in addition to the usual permitted lines of H I, H_2, and He I, whereas in the MIR ($5 - 20\,\mu$m) the spectrum appears to be dominated by strong emission lines from PAHs and a broad, deep Silicate absorption at $10\,\mu$m (Schweizer and Seitzer, 2007). Because of the latter features, NGC 34 was declared to be the archetype of a large group of (mostly Seyfert) galaxies with very red nuclear continua, suggestive of cool dust and strong PAH emission lines (Buchanan et al., 2006). Riffel et al. (2006) stress that these absorption features are mainly of stellar origin, which suggests that NGC 34 is not a genuine AGN or that it has a buried nuclear activity at a level that is not observed at NIR wavelengths. Additional support for this conclusion comes from the lack of high-ionization lines in its spectrum, i.e. the two [Ne V] lines and the [O IV] line. As noted previously, these lines are exclusively excited by AGN and can be considered AGN spectral signatures (Tommasin et al., 2010). Consequently, Riffel et al. 2006 classified NGC 34 as a starburst galaxy.

1.8.4 X-ray data

One of the most solid evidence for the existence of an AGN in NGC 34 is found in the X-ray domain. Brightman and Nandra (2011a) developed a systematic approach to the spectral fitting of their sample, in order to determine the intrinsic X-ray continuum slope Γ, the neutral absorption column density, N_H, and the $2 - 10\,\mathrm{keV}$ intrinsic source power, $L_{2-10\,\mathrm{keV}}$ (reported in Tab. 1.4). The value of the primary power-law slope, Γ, is fundamental to shed light on the primary X-ray generation process in AGN, that is likely to be produced by the hot corona, through the Comptonization of the accretion disc photons. Moreover, this intrinsic source continuum parameter allows to compare different types of sources, such as Seyfert 1s and Seyfert 2s (Brightman and Nandra, 2011a). In addition, they defined a set of unambiguous X-ray AGN as galaxies with an observed $2 - 10$ keV luminosity greater than $\approx 10^{42}\,\mathrm{erg\,s^{-1}}$. Indeed, these sources are certainly powered by the accretion of material on to a SMBH, since no local pure star-forming galaxy has ever presented a $2 - 10$ keV luminosity above this limit. This criterium gives a contamination rate of only 3% from star-forming galaxies and appears to be in good agreement with the optical classification made through BPT diagrams, therefore is an effective discriminator for AGN activity (Brightman and Nandra, 2011b).

Given the above criteria, Brightman and Nandra (2011b) classified NGC 34 as an AGN with a luminosity $L_{2-10\,\mathrm{keV}} \approx 10^{42}\,\mathrm{erg\,s^{-1}}$, in good agreement with the optical classification made through BPT diagrams (see Sec. 1.8.2).

Table 1.4: Principal parameters of the spectral fitting method obtained by Brightman and Nandra 2011a. N_H is the neutral gas column density measured in the primary power law, due to the comptonization of accretion disc photons by the hot corona. Γ is the power-law index of the primary power law, that was fixed in the fit. $L_{2-10\,\text{keV}}$ is the intrinsic luminosity in the $2-10\,\text{keV}$ band.

N_H $[10^{22}\,\text{cm}^{-2}]$	Γ	$L_{2-10\,\text{keV}}$ $[\text{erg s}^{-1}]$
$47.0^{+30.4}_{-21.2}$	1.9	10^{42}

1.8.5 X-ray-FIR-radio correlations in NGC 34

Fig. 1.17 shows the FIR-X-ray correlation (see Eq. 1.8) and the Ranalli relation (see Eq. 1.9), where NGC 34 is indicated in red. We have obtained the FIR luminosity through the value of the FIR intrinsic quantity (see 1.6), estimated to be around $7.08 \times 10^{-10}\,\text{erg s}^{-1}\,\text{cm}^{-2}$, from the interpolation of NGC 34 SED (see Fig. 1.14). It can be noticed a difference of at least 3 σ between NGC 34 observed X-ray luminosity and the expected X-ray luminosity. Furthermore, the measured SFR of NGC 34 from the SED decomposition is $SFR \simeq 24\,\text{M}_\odot\,\text{yr}^{-1}$, while according to Eq. 1.9, should be around $100\,\text{M}_\odot\,\text{yr}^{-1}$, if the observed X-ray luminosity was only due to star formation. These differences suggest that the observed X-ray radiation cannot be explained only by the star formation, requiring the presence of an AGN. Fig. 1.18, instead, shows the FIR-X-ray correlation for a sample of galaxies that comprises star-forming galaxies, LINERs and Seyferts (LLAGN, Terashima et al. 2002), including NGC 34, that is indicated in red. As Ranalli et al. (2003) point out, the X-ray-FIR luminosity ratio for Seyfert and LINERs generally exceeds that of star-forming galaxies.

Concerning the FIR-radio relation, NGC 34 appears to have a flux of $(67.5 \pm 2.5)\,\text{mJy}$ at $1.4\,\text{GHz}$ (Condon et al., 1998), while, as reported above, the intrinsic quantity FIR (see 1.6) is around $7.08 \times 10^{-10}\,\text{erg s}^{-1}\,\text{cm}^{-2}$. Therefore, we obtained a value for the q parameter (Eq. 1.7) around 2.45, that is consistent with the one found by Clemens et al. 2008 ($q = 2.49 \pm 0.02$) and in line with the typical value for star-forming galaxies ($q = 2.3 \pm 0.02$), reported in Sec. 1.7.1.

Overall, we conclude that the the X-ray-FIR correlation suggests the presence of AGN activity, while the FIR-radio correlation and the q parameter indicate that there is no evidence of an excess of radio emission due to the AGN.
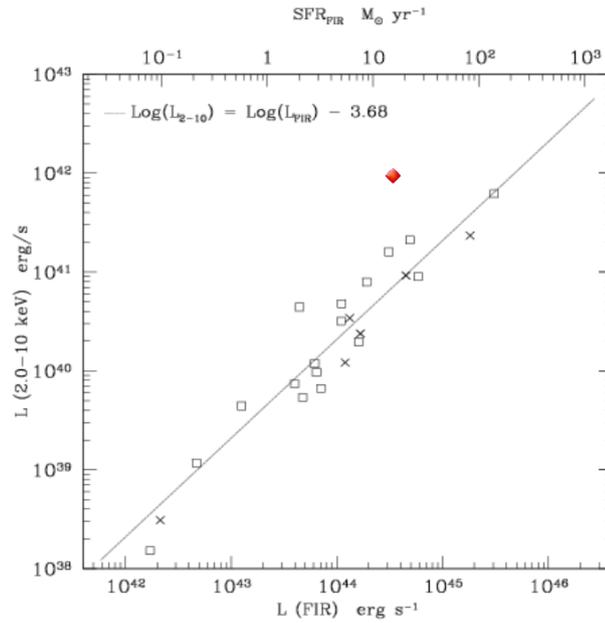
Figure 1.17: *The $2.0 - 10\,keV$ luminosity of local star-forming galaxies with respect to FIR luminosity. The squares and the crosses represent the local and supplementary sample taken into account by Ranalli et al. (2003), respectively, while the dotted lines are the best fits, shown in Eq. 1.8. NGC 34 is indicated in red (from Ranalli et al. 2003).*
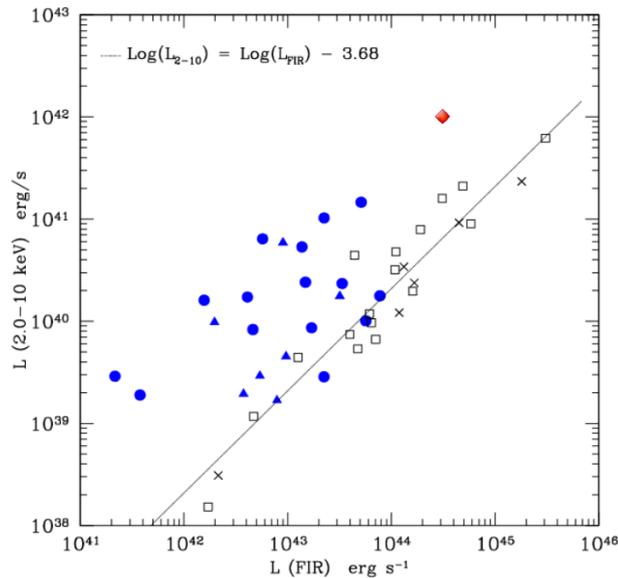
Figure 1.18: *The $2.0 - 10\,keV$ luminosity of local star-forming galaxies with respect to FIR luminosity. The squares and the crosses represent the local and supplementary sample taken into account by Ranalli et al. (2003), while the filled triangles and circles indicate LINERs and Seyfert galaxies, respectively. NGC 34 is shown in red. The dotted line is the best fit, shown in Eq. 1.8 (from Ranalli et al. 2003).*

Chapter 2

Analysis of ALMA data

2.1 An introduction to interferometry

Interferometry involves the combination of signals received from the sky by two or more physically separated antennas. The signals arrive at slightly different times, according to antenna's location in the array. As a result, an interferometer measures the interference pattern produced by the difference in the radiation path length, which is sinusoidal, by combining the signal from each antenna with that from every other, thanks to the correlator. Each data, called a visibility, consists of the brightness of the emission on the angular scale sampled, that is the amplitude of the sinusoid, and the relative position of that brightness on the sky, related to the phase of the sinusoid. All these pieces of information are contained in the u-v plane, which is the Fourier-transform plane of the angular distribution of the source on the sky. Since the complex visibility is the Fourier transform of the sky brightness distribution in the image plane, the sky brightness distribution is in turn the inverse Fourier transform of the complex visibility distribution in the visibility plane:

$$\mathcal{V}(u,v) = \int\int \mathcal{T}(x,y)\, e^{2\pi i(ux+vy)}\, dx\, dy$$
$$\mathcal{T}(x,y) = \int\int \mathcal{V}(u,v)\, e^{-2\pi i(ux+vy)}\, du\, dv$$

(2.1)

A pair of antennas instantaneously samples a single scale of the sky brightness distribution, which corresponds to two visibilities in the u-v plane, one at (u,v) and its complex conjugate at (-u,-v), since visibilities are Hermetian complex numbers. In general, an array of N antennas will have N(N-1)/2 indipendent baselines (i.e., the distance between two antennas), with each providing a single pair of points in this plane. How well the image reflects the actual sky brightness distribution depends on how completely the u-v plane has been covered. That is why a wide range of angular scales must be traced and this can be done in several ways, such as by including many pairs of antennas at different distances in an array, taking advantage of the rotation of the

Earth, that, changing the projected separations of the antenna pairs, allows more angular scales to be sampled, or arranging antennas in several configurations in order to sample different parts of the u-v plane (Asayama et al. 2016, Taylor et al. 1999).

One of the biggest advantages of interferometry is its extremely high angular resolution, defined as:

$$\theta \propto \frac{\lambda}{B_{max}} \tag{2.2}$$

In fact, θ is inversely proportional to the largest distance among antennas, that can change according to the chosen configuration. On the the other hand, one of the main drawbacks is related to the largest angular scale measured, defined as

$$LAS \propto \frac{\lambda}{B_{min}} \tag{2.3}$$

where B_{min} is the shortest baseline possible and, in an array, it occurs when two antennas are adjacent to each other. Of course, the antennas cannot be moved physically closer than their diameters, leaving a hole in the distribution of baselines at short ("short spacing" problem) and zero ("zero spacing" problem) baseline separations. As a result, spatial information from baselines shorter than the shortest baseline is not recovered. This problem has a huge impact on observations of extended objects, particularly those in which the emitted power is dominated by their large scale structures. In these cases, a possible solution is to take into account also a more compact antenna configuration (e.g., the Atacama Compact Array in ALMA), that can trace the shortest baseline, and thus the largest angular scales. Another solution is to fill in the interferometric short and zero spacings with total power maps, producing complete images.

In addition, an interferometer measures the Fourier transform of the sky brightness distribution multiplied by the antenna power response, or in other words, its relative sensitivity, which is higher on-axis. Fig. 2.1 shows an example of a one-dimensional antenna power response[1] for a 12 m diameter parabolic antenna, uniformly illuminated by emission of wavelength $\approx 0.85\,\mathrm{mm}$ (350 GHz). The central Gaussian-like feature is referred to as the *primary beam* or the *antenna beam size* and it has a Half Power Beam Width (HPBW) equal to $1.02\,\lambda/D$. The antenna power response reaches a high peak and then a low one repeatedly at ever larger angles. The constructive and destructive interference at larger angles leads to successive *sidelobes*, whose maxima go down as the angle increases, and nulls respectively. In particular, at the off-axis angle of $1.22\,\lambda/D$ radians, the path difference across the antenna diameter will equal one wavelength of the incident emission. The combination of such emission at the focus leads to destructive interference at that angle. Therefore, to counteract the angular fall-off of sensitivity due to the primary beam response, or even to observe a source more extended than the primary beam, an interferometer must observe adjacent positions, producing a mosaic (Asayama et al., 2016).

Another important feature of an interferometer is its *sensitivity* (i.e., the rms noise in the

---

[1]On the real sky, the antenna power response is two-dimensional, and is obtained by rotating the function shown in Fig.2.1 about its central axis.
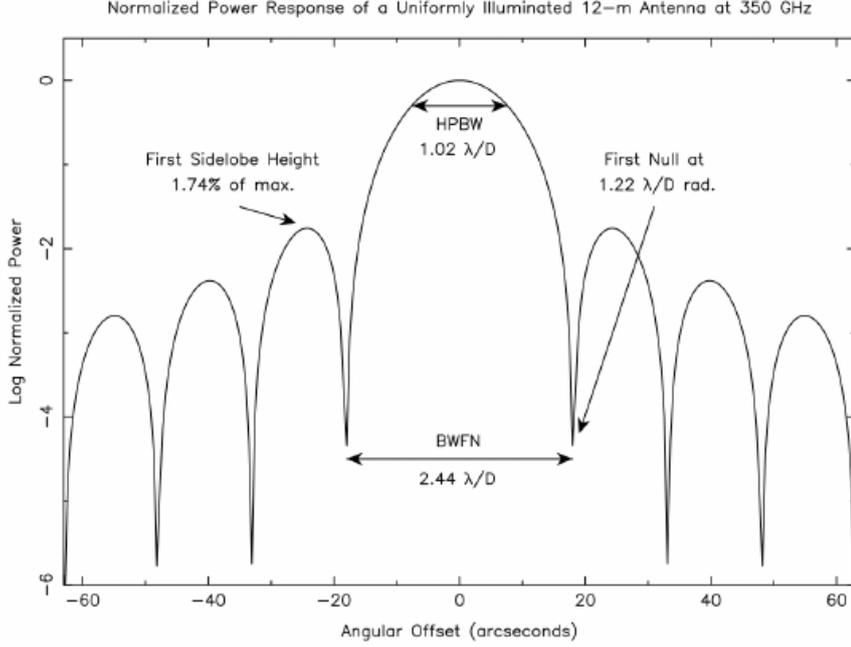
Figure 2.1: *Normalized 1-D antenna power response for a 12-m antenna uniformly illuminated at 350 GHz (Asayama et al., 2016).*

signal. The sensitivity is given by the formula[2]

$$rms = \frac{2k_B}{\eta \, A_{eff}} \frac{T_{sys}}{(N(N-1) \, \Delta\nu \, \Delta t \, n_p)^{1/2}} \tag{2.4}$$

where T_{sys} is the brightness temperature equivalent to the flux received from the antenna, that depends especially on the atmosphere, but also on the instrumental noise and the observed source. Thus, many factors can improve an interferometer sensitivity: a large number of antennas, a high spectral and time resolution and a low brightness temperature.

2.1.1 Peculiarities of waves at mm wavelengths

The sub-mm band ranges between $30 - 1000$ GHz. Radiation at these wavelengths comes from vast cold clouds in interstellar space (few tens of degrees above absolute zero), associated to dense regions where star formation takes place, and from some of the earliest and most distant galaxies in the Universe. Observing at these frequencies allows to study the chemical and physical conditions in molecular clouds, providing theorists with new constraints on the physical state of the star-forming cold gas, and gives information on the mechanisms for the formation and evolution of galaxies. These observations reveal chemical abundances and cooling mechanisms for

---

[2]k_B is the Boltzmann constant, A_{eff} the effective area, N the number of antennas and n_p the number of polarizations.

the molecules which comprise these regions, dark and obscured in visible light, but bright in this part of the spectrum, whose emission is characterized by electronic, rotational and vibrational transitions. In addition, the sub-mm emission is of particular interest in the study of star formation in high-z galaxies, because as the dust SED shifts to higher and higher redshifts, we observe closer and closer to the peak of the dust emissivity. This negative K-correction is such that it roughly compensates the inverse square law of decreasing flux density with z, due to the increased luminosity distance. Thus, a galaxy with a fixed IR luminosity will show about the same sub-mm flux density at any redshift $1 < z < 6$ (Decarli et al., 2014). Furthermore, this band is not affected by external human interference.

On the other hand, the effect of the troposphere, the lowest layer of the atmosphere (at an elevation of 7 km to 10 km), over these wavelengths cannot be overlooked. In this layer, composed mainly of N_2, O_2, water vapour, N_2O, CO_2, and particulates, such as liquid water and dust in clouds, the temperature decreases with altitude, clouds form and the effect of convection can be significant. The ability of the atmosphere to allow radiation to pass through is referred to as its transmissivity. However, it becomes increasingly opaque as the frequency increases, mostly because of the absorption by O_2 and H_2O. In particular, the atmosphere is composed by a dry component (e.g. O_2, O_3) and a wet component (e.g. H_2O vapour/clouds). Both heavily absorbe signals from space and, in turn, emit radiation. Consequently, the brightness temperature of an observed source will be given by:

$$T_{received} = T_{source}e^{\tau_{atm}/cos z} + T_{atm}(1 - e^{-\tau_{atm}/cos z}) \tag{2.5}$$

where T_{atm} is the brightness temperature of the atmosphere, z is the zenith distance and τ is atmosphere opacity.

A significant quantity that must be taken into account is the precipitable water vapour (PWV), that is defined as the depth of the water vapour if converted to the liquid phase and enhances opacity as it increases. As PWV changes, variations in the effective electrical path length take place, because of the variation of the refractive index of the atmosphere. As a result, the phase of an electromagnetic wave propagating through the troposphere changes. This phenomenon is referred to as *phase noise* and its effect is enhanced at increasing PWV values, that is to say at increasing frequencies. The relationship that links the electrical pathlegth, L_e, and the PWV is given by:

$$L_e = 1.7 \times 10^3 \frac{PWV}{T_{atm}} \approx 6.3 \, PWV$$

that, for $T_{atm} \approx 270$ K, can be also written as:

$$\phi_e \approx \frac{12.6\pi}{\lambda} \, PWV \tag{2.6}$$

where ϕ_e is the phase change experienced by an electromagnetic wave that passes through the troposphere. This relation has been verified experimentally for a number of atmospheric con-

ditions (Carilli and Holdaway, 1999). PWV variations in the line-of-sight of an antenna lead to significant delay corrections, up to 0.3 mm/s which is 30°of phase/s at 90 GHz and scales in phase linearly with frequency. Furthermore, since the refractive index of the atmosphere is similar for close antennas, the longer a baseline b is, the higher the phase noise appears, following the formula:

$$\phi_{rms} \propto \frac{b^\alpha}{\lambda} \tag{2.7}$$

where α is a parameter dependent on weather conditions.

Clearly, phase noise can be the limiting factor for the coherence time and spatial resolution of mm interferometers, that is why telescopes for this kind of astronomy must be built on high, dry sites, such as the 5000-m high plateau at Chajnantor for ALMA, one of the highest astronomical observatory sites on Earth.

Fig.2.2 illustrates the overall effect of the atmosphere, showing a series of strong absorption lines that eventually becomes an opaque "pseudo-continuum", due to the sum of the pressure broadened line wings of a lot of sub-mm and IR lines of water vapour, and the effect of PWV.
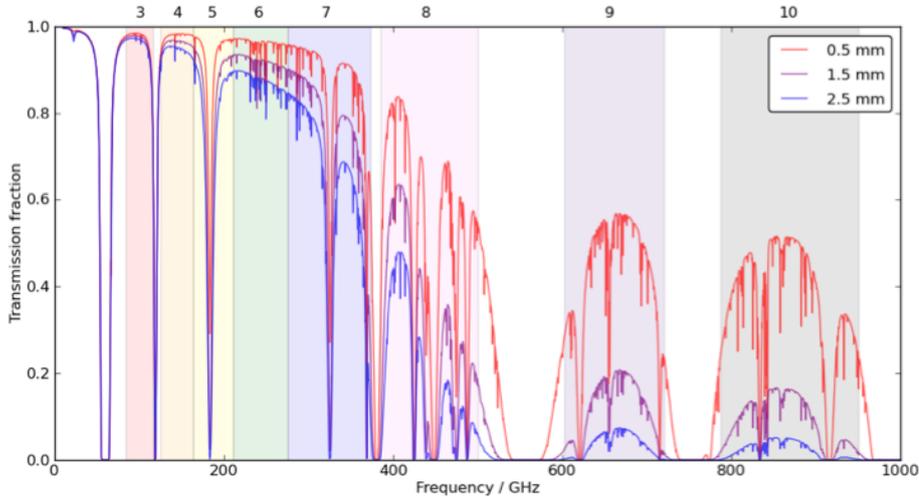
Figure 2.2: *Atmosphere transmissivity in the 0-1000 GHz range and the effect of PWV (Asayama et al., 2016).*

2.2 ALMA telescope

The Atacama Large Millimeter/sub-millimeter Array is located on the 5000-m high plateau at Chajnantor of the Chilean Andes, where the sky conditions are exceptionally dry and clear for the reasons explained in Sec. 2.1.1. When ALMA is completed, it will cover the wavelength range from 10 to 0.32 mm ($31 - 950$ GHz) and will be composed of 66 high-precision antennas

set up in (Fig. 2.3):

- the *Main Array*, a large array of fifty 12-m antennas, used for sensitive and high-resolution imaging, with a minimum baseline of 15 m and a maximum of 16 km. The 12-m Array configurations have been designed so that in the most extended the spatial angular resolution will be as small as 5 marcsec at 950 GHz.

- the *Atacama compact array* (ACA), composed of 12 closely spaced 7-m antennas and four 12-m antennas for single-dish (or total power) observations, in order to achieve high-fidelity imaging of sources with emission on angular scales larger than those corresponding to the minimum spacing of the 12-m Array. This array configuration is designed to fill missing spacings from about 0 m to ≈ 30 m, accounting for the "short" and "zero spacing" problem (Sez. 2.1).
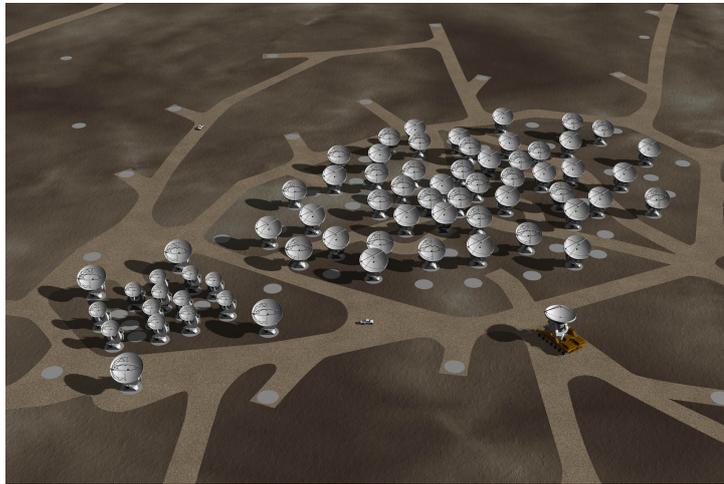
Figure 2.3:   *12-m Array on the right and Atacama compact array on the left (http://www.almaobservatory.org/en/about-alma/origins-of-the-alma-project).*

Antennas configuration can be changed, using the two special purpose ALMA antenna transporters. All the antennas have a similar arrangement: each one has one front-end, including a cryostat, that can accommodate up to 10 receiver bands, an Amplitude Calibration Device (ACD) and backend electronics. In particular, the ACD measures in each spectral channel, by consecutive autocorrelation (or total-power) integrations, the T_{rx}, that is the receiver temperature, and the T_{sys}, that is the total brightness temperature measured, related to several factors, such as the atmosphere, the electronics and the observed source. Furthermore, the antennas of the 12-m array contains a Water Vapour Radiometer (WVR), that measures the amount of PWV, in order to correct pathlength fluctuations in the troposphere, by observing the emission of the atmospheric water line within four spectral bands near 183 GHz at a rate of about 1 Hz. The online WVR correction reduces variance in visibility phases (phase noise) and allows to keep

coherence in longer-time integration of the visibilities. On the other hand, ACA do not contain a WVR, since it is so compact that PWV fluctuation does not matter (Asayama et al., 2016).

Each receiver band detects two orthogonal linear polarizations at an observed sky frequency, that need to be down converted to frequency bands between $0-2$ GHz in order to send the signals to the correlator. The frequency down conversion involves a set of Local Oscillators (LOs). It is possible to observe only one band at any time, that is chosen according to weather conditions (the lowest the PWV is, the highest frequency can be observed), up to three can be switched on simultaneously and rapid switching between those bands is possible (Asayama et al., 2016).

In particular, Band 9 covers the frequency range $602 - 720$ GHz ($0.50 - 0.42$ mm) and its atmospheric transmission is higly dependent on the PWV. Phase stability also limits when observations can be made. Therefore, most observations in Band 9 will be done at night during austral winter. As well as having a higher atmospheric opacity and a less stable atmosphere, Band 9 provides several challenges for observing: finding sufficiently bright calibrators (most QSOs are relatively faint at this frequency), requiring accurate pointing for the relatively small primary beam and the need for the highest level of stability in the rest of the system. Overall, this band (and also Band 10) is referred to as "out of the ordinary" (Asayama et al., 2016). Fig. 2.4 and Fig. 2.5 show the trasmissivity of the atmosphere and the brightness temperature measured by the receiver due to the atmosphere contribution only, respectively.
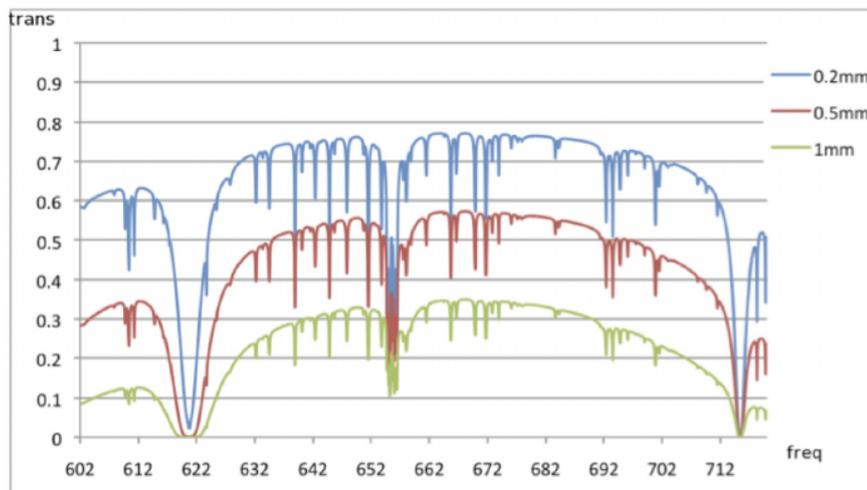

Figure 2.4: *Band 9 zenith transmission as a function of the frequency (in GHz) for PWV = 0.2, 0.5, 1 mm (Asayama et al., 2016).*
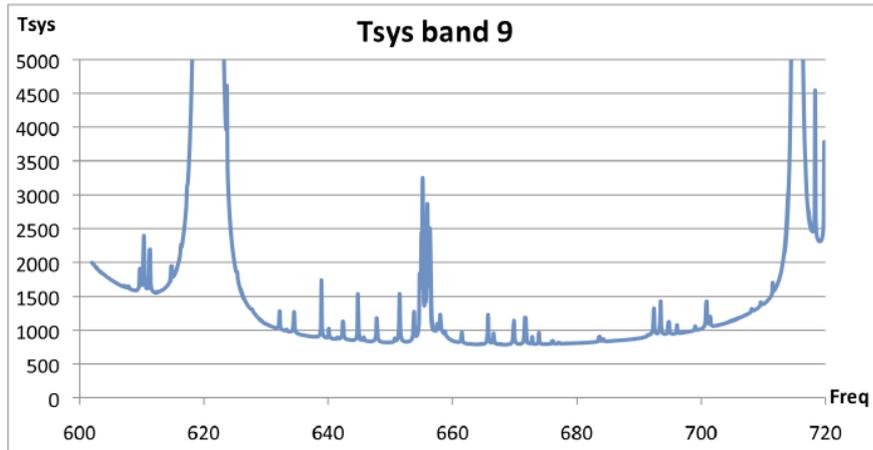
Figure 2.5: *Temperature of the receiver (i.e., T_{sys}, in K) as a function of the frequency (in GHz) at zenith for Band 9 with PWV = 0.472 mm (Asayama et al., 2016).*

2.3   The ALMA archive

ALMA observations are organized in Cycles (up to now, from Cycle 0 to Cycle 4). An observing proposal submitted to the ALMA archive will have an associated structure, the so-called *Observing project*, set up and divided into several hierarchical steps. Generally, observations are divided into *Science Goals* (SG), namely the minimum proposed observational unit, including targets in the same sky regions that roughly share the same calibration, aimed at reaching a requested sensitivity in a given angular resolution, largest angular scale and spectral setup. Each SG is converted into *scheduling blocks* (SBs), that are the minimum observational units, including targets in the same sky region and their calibrators, observed with the same instrumental setup. Generally, each SB lasts $\approx 30\,min$, in order to allow flexibility of scheduling. Each repetition of the observation of a SB is defined as an *Execution Block* (EB), that is the minimum observative and data reduction unit (including all the calibrators for an observative session). Typically, an observation is composed by several EBs, separated by observations that check atmospherical conditions. Finally, ALMA data are set up in several tables, called measurement sets (MS), that contain all the pieces of information about visibilities, that can be reduced and/or displayed with *CASA* (Common Astronomy Software Application) software.

The ALMA Archive is at the center of the operations of the telescope array and is designed to manage the 200 TB of data that are taken each year. It stores the observed raw data and metadata, as well as the reduced data products and their metadata resulting of the second Quality Assurance (QA2) processing[3]. So, from the archive it is possible to download raw data, calibration scripts and tables, that allow to generate the calibrated data, using the proper

---

[3]The ALMA QA2 data reduction team performs for each ALMA science data set a detailed analysis to confirm that the observations have achieved the science goals requested by the PI, and thus the frequency setup, spatial setup, and continuum and line detection sensitivity are verified.

version of CASA, and also reliable science-ready final data product. Ultimately, the large amount of easily accessible science-grade data are a fundamental resource, since there is strong demand for new ALMA data.

Nevertheless, early science Cycles might differ in product formats, pipeline availability or CASA version to run calibration scripts. During Cycle 0 (September 30, 2011 - January 1, 2013), the whole array was on Science Verification phase: only a limited number of antennas, frequencies, array configurations, observing modes were available and there was no pipeline (Vilaro and Nyman, 2011). Furthermore, data were calibrated with CASA 3.2-3.4, but there have been several updates since then. Ultimately, the rule of thumb is to download ALMA Cycle 0 data and reduce them again, before making any scientific consideration.

The data analyzed in this thesis project were carried out during ALMA Early Science Cycle 0 program. Our aim is to obtain good final products, therefore we reduced ALMA archival data, using the last CASA version (4.5.2), checking for the reliability of the calibration.

2.4 NGC 34: ALMA data reduction and analysis

In this thesis project, archival band 9[4] ALMA data of NGC 34 have been reduced and analyzed. These data are part of the ALMA Cycle 0 Early Science program. In addition to what said in Sec. 2.3, the main reason why Cycle 0 data re-processing is strongly recommended, is that a more reliable flux calibration can be obtained, owing to the new flux model libraries available. Therefore, making use of the CASA software, version 4.5.2, we have generated new reduction scripts and compared them with those of the archive[5], analysing step by step the archival calibration and processing raw data, for the purpose of possibly providing an improvement. Overall, this section deals with the calibration and analysis of ALMA Cycle 0 observation of the CO(6-5) line emission and of the dust continuum emission in the nuclear region of NGC 34 (project 2011.0.00182.S). In particular, we present data properties and the steps followed for the reduction process, focusing on some peculiarities of the analyzed dataset.

2.4.1 NGC 34 Band 9 observation

NGC 34 observation is divided in six EBs, whose main features are summarized in Tab. 2.1. Xba3, Xd36, Xec9, X334 and X4c7 are characterized by an extended antennas configuration (see Fig. 2.6), while the last EB, X43b, has both a compact and an extended configuration and a larger number of antennas (see Fig. 2.7). In order to make Band 9 observations, PVW must have quite small values: looking at Tab. 2.1, it is evident that these data are affected by minimal atmospheric absorption, with the average PWV ranging from 0.29 to 0.59 mm. The four spectral windows are centered at the sky frequencies of 679.8, 678.0, 676.3 and 674.3 GHz, respectively, each with a bandwidth of ≈ 2 GHz and are divided in 128 channels (time division mode). The

---

[4]See Sec. 2.2.

[5]The archival data were published by Xu et al. 2014.

Table 2.1: Main properties of the ALMA Cycle 0 observations of NGC 34. Columm (1) - observation date; (2) - identificative archival name of the EBs; (3) - observation time; (4) - antennas configuration; (5) - mean amount of PWV; (6) - number of antennas; (7) - the system temperature mean value.

| Date	EBs	Time [UTC]	Configuration	Avg PWV [mm]	# Ant	T_{sys} [K]
2012-05-20	Xba3	09:17:15-10:35:34	E	0.39	16	850
2012-05-20	Xd36	10:48:14-12:06:33	E	0.35	16	653
2012-05-20	Xec9	12:22:31-13:07:05	E	0.34	16	654
2012-05-21	X334	09:47:04-11:06:00	E	0.31	16	634
2012-05-21	X4c7	11:20:00-10:41:09	E	0.29	16	528
2012-08-25	X43b	03:30:38-05:01:41	E+C	0.59	28	1058
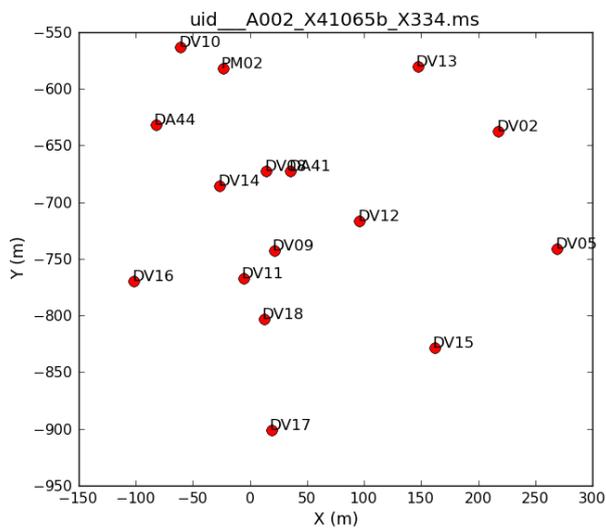
Figure 2.6: *Extended antenna configuration (EB X334).*
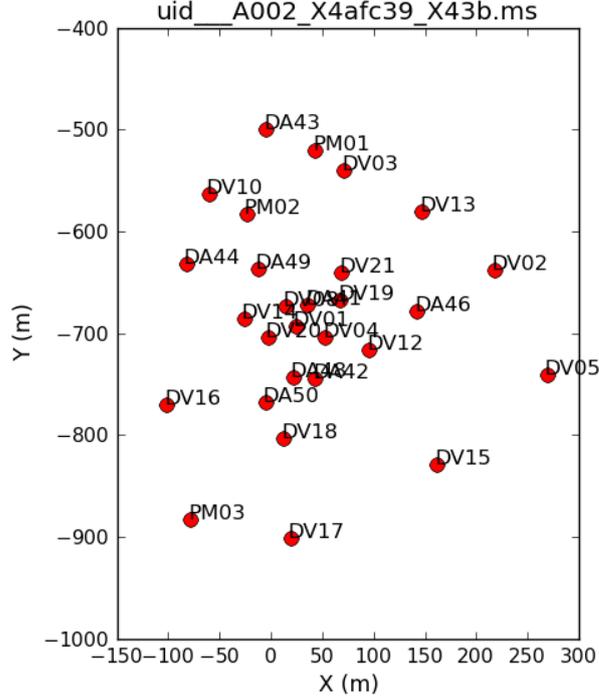
Figure 2.7: *Extended and compact antenna configuration (EB X43b).*

total on-target integration time was 2.25 hr. The calibrators observed are the QSOs 2348-165 and 3C 454.3, and the asteroid Pallas[6], and are the same for all the EBs.

2.4.2 An overview on calibration

A two-element correlation interferometer measures the spatial coherence function of the radiation field at a location given by the antenna separation, or baseline, measured in wavelength. All these measurements can be considered to lie upon a plane. This spatial coherence is referred to as *true visibility function* (V_{true}^{ij}). An interferometer samples the measured visibility function (V_{obs}^{ij}), obtained by recording data collected from each antenna pair, that differs from the true visibility for a multitude of reasons, such as antenna tracking inaccuracies, the effect of atmosphere and problems related to electronics. The calibration consists in finding out the corrections (i.e., gains) to apply to the observed visibility, in order to recover the true visibility (Taylor et al., 1999).

The basic calibration formula can be written as:

$$V_{obs}^{ij}(\nu, t) = G^{ij}(\nu, t)V_{true}^{ij}(\nu, t) + \epsilon_{ij}(\nu, t) + \eta_{ij}(\nu, t) \tag{2.8}$$

where G^{ij} are the baseline-based complex gain, ϵ_{ij} is a baseline-based complex offset and η_{ij} is

---

[6]Pallas, minor-planet designation 2 Pallas, is the second asteroid to have been discovered (after Ceres), and it is one of the largest asteroids in the Solar System, located in the asteroid belt.

a stochastic complex noise. Two hypotheses have to be considered:

- nearly all of the corrections are antenna-based: all the effects that occur in the signal path are associated with one particular antenna, from the troposphere above the antenna, through all of the electronic processing along the antenna path, up to the correlator;

- frequency corrections are time-independent, while time corrections are frequency-independent.

The baseline-based complex gain G^{ij} can be approximated by the product of the two associated antenna-based complex gains g_i and g_j, that are often described by their amplitude and phase components, since virtually all of the calibrations operate on amplitude and phase, rather than real and imaginary parts of the visibility function:

$$G^{ij}(\nu, t) = g_i(\nu, t) g_j^*(\nu, t) = a_i(\nu, t) a_j(\nu, t) e^{i(\phi_i(\nu, t) - \phi_j \nu, (t))} \tag{2.9}$$

where $a_i(\nu, t)$ is an antenna-based amplitude correction and $\phi_i(\nu, t)$ is the antenna-based phase correction. Interferometric ALMA observations rely upon accurate and trustworthy calibration of the electronics and atmospheric phase and amplitude variations in order to produce high quality scientific data. Short observations (scans, that is to say the fundamental observational piece) of radio sources as calibrators are included in observing programs in order to determine these variations with time and frequency. Therefore, G^{ij} for each of the N(N-1)/2 baselines can be determined by comparing well known calibrator sources to models taken into account, that are the Fourier transform of the expected calibrator image:

$$G^{ij} = V_{obs} / V_{model} \tag{2.10}$$

Quasars are among the best radio source candidates because their emission is bright, lack spectral features and are point-like, with a size smaller than 0.01 *arcsec*.

2.4.3   A typical observation

Fig. 2.8 illustrates the observing schedule of the EB X334, showing that a typical observation starts with a bandpass calibration, in order to measure the spectral response of the system. Therefore, the bandpass calibrator should be a bright source with simple spectral properties, such as a bright quasar, that is a point-like source with no emission or absorption lines and a reasonably flat spectrum. The flux (or amplitude) calibration is taken, by observing the flux of a well-known source, that will be compared with its own established model flux, in order to obtain the scaling factor (from Kelvin to Jansky) to apply to all the other sources in the SB. Ideally, these sources should be small with respect to the synthesized beam, so as not to resolve the source structure. At mm-wavelengths, quasars have a very variable flux density, thus solar system objects, such as planets and moons, are usually preferred as flux calibrators. Finally, the phase calibrator is observed with the purpose of calibrating the phase variation of the target

during an observation, caused by the unpredictable variations of the atmosphere. The phase is expected to change much more rapidly in time than the amplitude. Therefore, this calibrator is observed several times, before and after the observation of the science target, and the phase corrections to apply to the target are computed by a linear interpolation in time. Furthermore, since the phase varies on small scales on the sky, this calibrator must be as close as possible to the target, so their signals will have similar paths through the atmosphere (van Kempen et al., 2014). In addition, the receiver temperature and the sky emission are measured by comparing the signals on the sky, ambient and instrumentation. This is known as atmospheric calibration, required to correct for differences in the atmospheric transmission between the science and the celestial amplitude calibrators, and is normally done during observations, both near the science target and the flux calibrator (Asayama et al., 2016).


Figure 2.8: *Observing schedule for X334: the bandpass calibration is indicated in red, the flux calibration in green and the phase calibration in cyan, while the target calibration is shown in blue. The observations made to check the pointing precision are indicated in orange, whereas the atmospheric calibration in yellow.*

2.4.4 Data calibration

After having imported the data stored in the archive, the reduction of the six EBs is done thanks to the reduction scripts generated by CASA 4.5.2 and can be divided in these main steps:

1. Editing;

2. T_{sys} and WVR corrections;

3. Antenna positions check;

4. Frequency-depend calibration (i.e., bandpass calibration);

5. Time-dependent calibration (i.e., phase calibration);

6. Modeling the flux calibrator and amplitude calibration;

7. Application of the calibration tables obtained.

After the application of the calibration tables, the EBs will be concatenated to obtain only one measurement set, where *cleaning algorithm* is applied (see Sec. 2.5). In the following, the several steps involved will be explained in details.

Editing

Data editing, also known as flagging, consists in removing data affected by spurious fluctuations related to instrumental problems (e.g., an antenna with a high T_{sys}), that cannot be solved by the calibration. In addition, there is a group of initial flags, which can be done "a priori" (i.e., without inspecting data), comprising:

- *Pointing* and *Atmosphere*: scans performed to check the poiting precision and for the atmosphere calibration, which are automatically saved in a subtable of the main table that gathers all the data);

- *Autocorrelations*: the combination of the signal of each antenna with itself, flagged owing to its high noise;

- *Shadowing*: the removal of data by antennas that were partially or totally shadowed during the observations, according to the declination of the sources;

- *Edge channels*: the edge channels of each spectral window, that appear to be more affected by noise than the central channels.

T$_{sys}$ and WVR corrections

At millimeter and submillimeter wavelengths, the atmosphere both attenuates signals and acts as a black body emitter, adding additional noise to any measurements. This effect depends on frequency, elevation, the column of wet and dry constituents of the atmosphere, and the temperature of the atmosphere.

The ACD (see Sec. 2.2) samples the receiver temperature T_{rx} and the total brightness temperature T_{sys} every 5-15 minutes, depending on the observed frequency, since the opacity of the atmosphere becomes higher and higher, as the frequency increases (see Sec. 2.1.1). A higher level of opacity, related to the presence of an emission line, means that the signal is more absorbed and this leads to a higher value of T_{sys}. For instance, Fig. 2.9 shows all the antenna

responses for each spectral window of the EB X334, as a function of frequency at a given time. It can be noticed that all the antenna responses are characterized by the same features, that represent the typical atmosphere emission lines. This can be verified by looking at the black line, that represents the trasmissivity of the atmosphere (see Sec. 2.1.1), because it declines exactly in corrispondence of the emission lines. In particular, this curve is drawn such that 0% is at the bottom and 100% is at the top of the y-axis, regardless of what plotrange is set for the amplitude and is produced by taking into account a median value of PWV. The trasmissivity in the four spectral windows is equal to 54%, 52%, 56% and 57%, respectively.


Figure 2.9: T_{sys} of the EB X43b, colorized per antenna, as a function of frequency, at a given time, in the four spectral windows. The solid and the dashed lines represent the two polarizations, XX and YY. The black line on the top indicates the trasmissivity, that in the four spectral windows is equal to 54%, 52%, 56% and 57%, respectively.

Ultimately, the T_{sys} calibration corrects for the effects of the atmosphere opacity, that causes signal attenuation and fake absorption lines in the spectra. Once the T_{sys} gains have been obtained, it is useful to inspect them, in order to check for the presence of atmospheric emission features and unusual antenna behaviours. For example, in the EB X43b the antenna $DV03$ measured a much higher T_{sys} than all the others. This was likely due to a malfunction, and thus

we decided to flag it (Fig.2.10).
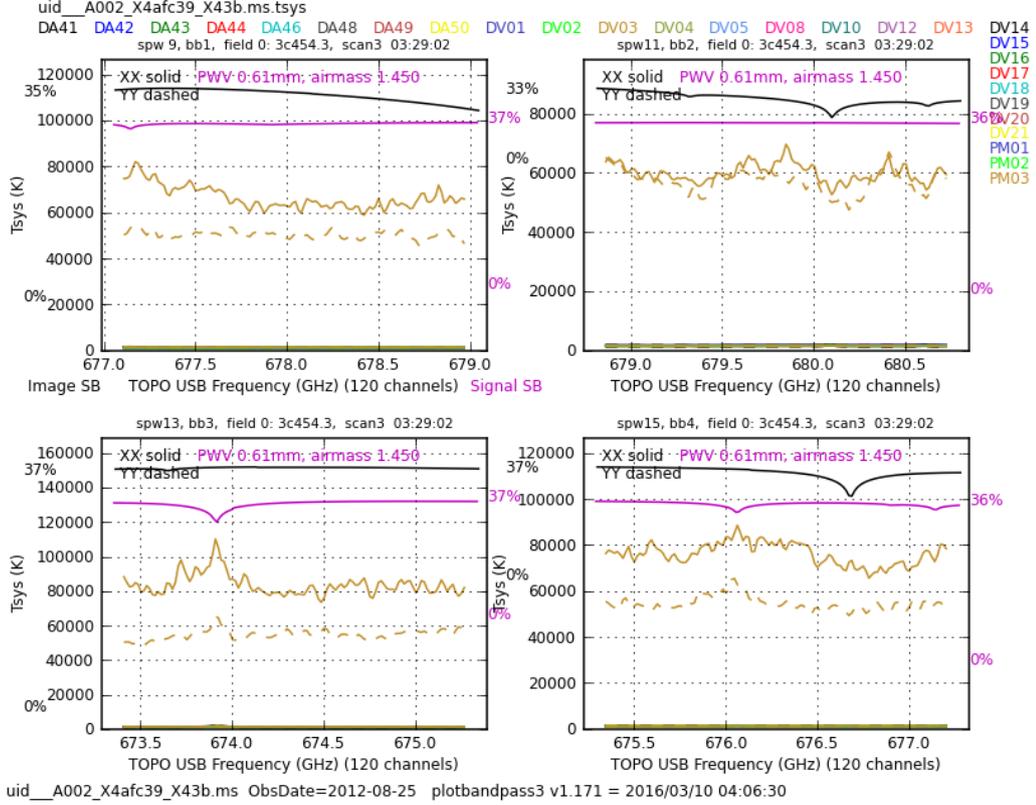
Figure 2.10: T_{sys} of the EB X43b, colorized per antenna, as a function of frequency, at a given time, in the four spectral windows. The solid and the dashed lines represent the two polarizations, XX and YY. It is evident that the antenna DV03 (in orange) measures a T_{sys} far higher than all the others.

The WVR (see Sec. 2.2), instead, corrects the observed visibilities for the phase variations on short timescales, the phase noise (see Sec. 2.1.1), depending on the amount of PWV. Atmospheric models are used to convert the emission measured into delay changes, that is given by Eq.2.6. This estimated delay difference between any two antennas is removed from the visibility phase, that will appear slightly less affected by dispersion. Fig. 2.11 shows the phases before and after the WVR corrections, in blue and in green respectively, for each antenna in the EB X334. In general, it can be noticed that the phase fluctuation is more enhanced before the application of the corrections. Nevertheless, there is only a slight improvement between the blue and the green curves. Indeed, both the phase delay and the correction applied are inversely proportional to the observed wavelength, thus in Band 9 observations the effect of PWV is more significant and it is difficult to see the difference between corrected and not corrected visibilities, especially for the longest baselines.
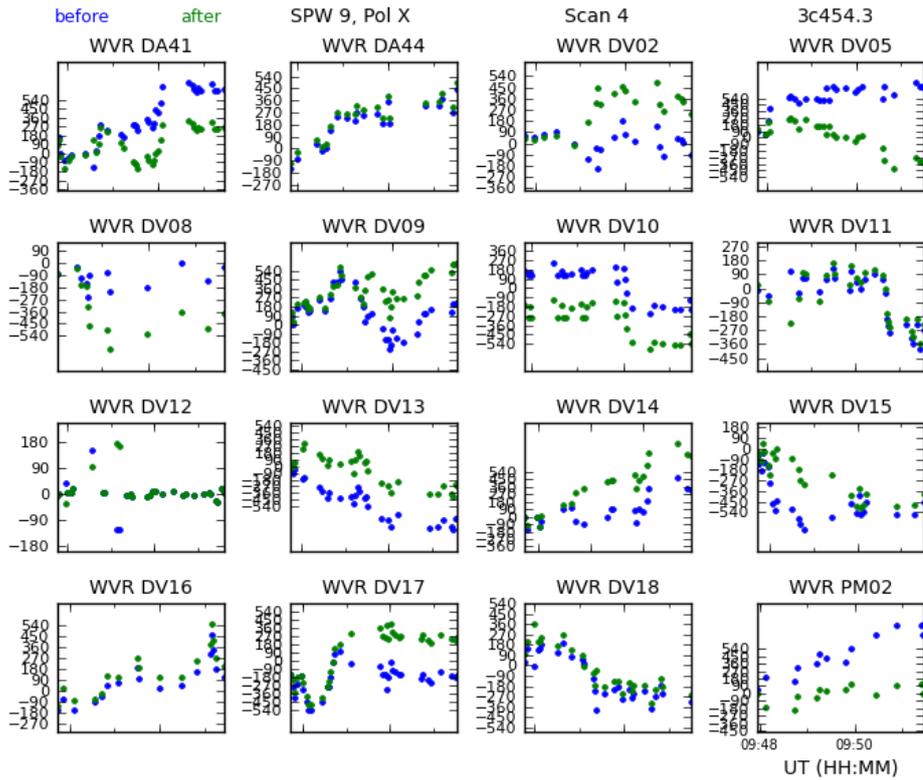
Figure 2.11: *Phase as a function of time before and after the WVR corrections, in blue and in green respectively, for each antenna in the EB X334. The phase fluctuation of the blue curve is slightly enhanced with respect to the greeen curve.*

Antenna positions check

The relative location of each antenna (i.e., the relative positions of their focal points) must be known to within a fraction of the observing wavelength, about 50 microns. The baseline runs (as they are called) are executed by the ALMA staff at least once per week, but also whenever one or more antennas change pad locations. The observations cover a wide range of elevation and azimuth to determine the three spatial offsets of the antenna position. Because of weather conditions and other array operation constraints, the position of a recently moved antenna may not be updated for several days. Consequently, the correlator delay model will be incorrect and the visibility phase for data associated with this antenna can have significant phase variations (Asayama et al., 2016). For example, after having completed all the calibration steps, the antenna $DA41$ appeared to have the same phase offset in all the data collected during May, 2013. Furthermore, the images obtained concatenating all the EBs were characterized by parallel band features, that were evidently related to an error in phase calibration. That is why, we came up with the solution that $DA41$ position had to be corrected. After having applied this correction, the phase offset and the parallel features are less visible (Fig.2.12-2.13 and Fig.2.14-2.15).
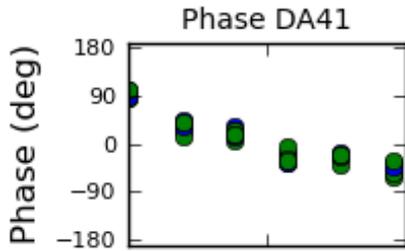

Figure 2.12: *Phase as a function of time before correcting DA41.*
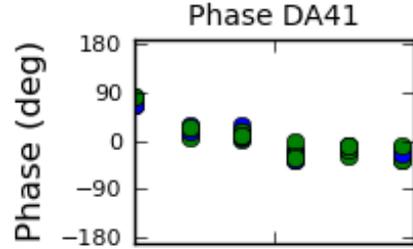
Figure 2.13: *Phase as a function of time after correcting DA41.*

Frequency-dependent calibration

In order to correct the variation of phase and amplitude as a function of frequency due to the electronics, the bandpass calibration is applied, using the CASA task *bandpass*. As introduced in Sec. 2.4.3, the bandpass calibrator must be a bright QSOs, observed at the beginning of the observation, that allows to obtain a high signal-to-noise ratio (SNR) in a short observation time-scale. In our data, the bandpass calibrator is the QSO 3C 454.3.

The frequency gains are found by comparing the bandpass calibrator to its model, a point-like source, characterized by a unitary amplitude and a phase equal to 0, and then applied to all sources, including the science target. Since we assume frequency variations as time-indipendent (see Sec. 2.4.2), these gains can be worked out averaging over all integration time, maximizing the SNR. Actually, in order to avoid signal decorrelation, before solving for bandpass, the phase
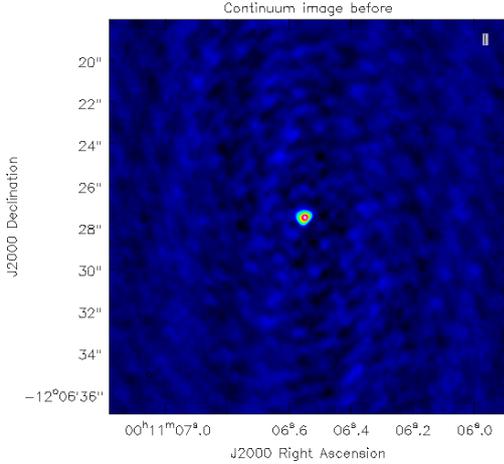
Figure 2.14: *Continuum image before correcting DA41 (see Sec. 2.5).*
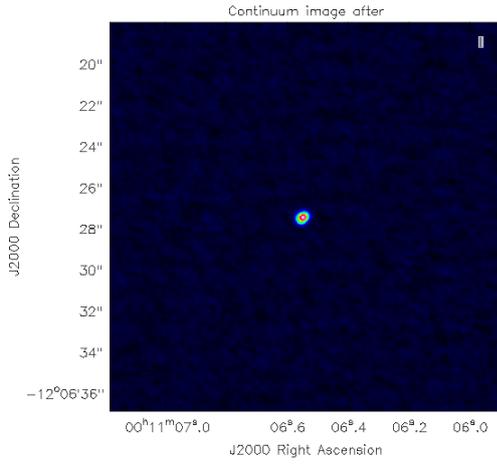
Figure 2.15: *Continuum image after correcting DA41 (see Sec. 2.5).*

corrections as a function of time, on very short timescale, must be calculated, using the *gaincal* task, in order to apply them "on the fly" when calculating bandpass ones. Since our data are Band 9 observations, the bandpass calibrator 3C 454.3 appears to be very weak and the signal-to-noise ratio of the solutions found very low. Consequently, we found phase gains every 60 s (using the *solint=60s* parameter), instead of for any integration (*solint=int*), in order to maximize the SNR, and we put the signal-to-noise threshold equal to 1.5, instead of 3, the recommended value, to find as many solutions as possible. Finally, in order to maximize the bandpass gain SNR, we computed one bandpass solution every 30 channels (*solint='inf,30ch'*), instead of for any channel.

The observed visibilities will be corrected by interpolating the bandpass gains with a broken line. This can be considered a big approximation, because the randomatic effect of noise can be overlooked. Another possibility is to carry out a polynomial fit for every channel[7] (using *bandtype=BPOLY* parameter, instead of *bandtype=B*). We compared the two different approaches, that are shown in Fig.2.16 for the antenna DV08 of the EB X4c7, where the broken lines represent the B solution for the two polarizations (XX in blue and YY in green), while the curves represent the BPOLY solution for the two polarizations (XX in black and YY in cyan). It can be noticed that at certain frequencies, the BPOLY interpolation appears to oscillate too much with respect to the B one, probably because of the lower SNR of the solutions. That is why, finally we decided to apply the B solution type.

Nevertheless, since 3C 454.3 is very weak, at the end of the calibration process, after the concatenation of the six EBs, we found again bandpass solutions, using the phase calibrator. This procedure out of the ordinary is added at the end, because when the visibilities are already

---

[7]Here it was not possible to average channels, because otherwise the polynomial fit did not work. However, this means that the solutions SNR is lower.
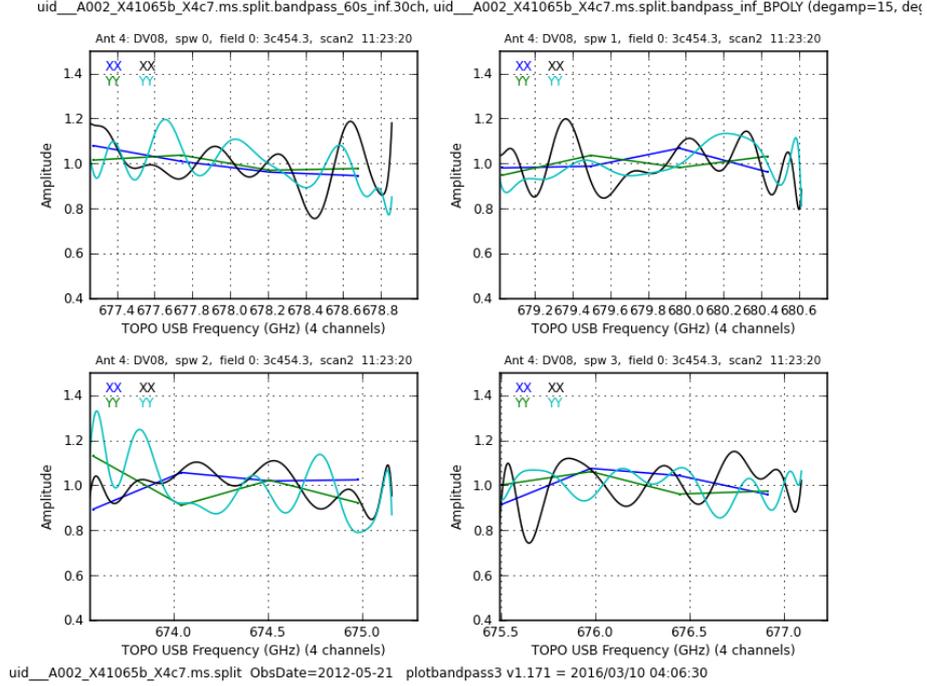
Figure 2.16: *Comparison between the two bandpass solution for the antenna DV08 in the EB X4c7. The broken lines represent the B solution for the two polarizations (XX in blue and YY in green), while the curves represent the BPOLY solution for the two polarizations (XX in black and YY in cyan)*

calibrated, it could be easier to track the systematic offset due to the electronics.

Time-dependent calibration

Once the corrections in frequency have been found, it is necessary to work out the time-dependent gains, due to the atmospheric turbolence, using the CASA task *gaincal*. Time-dependent gains are obtained by comparing the phase calibrator with its point-like source model, applying on the fly the bandpass solutions calculated before, in order to avoid signal decorrelation, when averaging in frequency. As said in Sec. 2.4.3, the phase calibrator is typically a QSOs with known characteristics, such as position, spectrum and flux-density, that has to be as close as possible to the observed target. In our data, the phase calibrator is the QSO 2348-165. Since these gains are assumed to be frequency-independent (see Sec. 2.4.2), it is possible to average over all frequencies to obtain a higher SNR. In addition, the phase gains are found by computing one solution every 60 s (one for each polarization and spectral window) to obtain a more statistically significant solution. Finally, the amplitude solutions are calculated, computing one solution for both polarizations. The possible signal loss due to decorrelation is avoided thanks to the previous phase correction. Once the phase calibrator has been corrected, it has flat amplitudes and phases

at zero.

Modeling the flux calibrator and amplitude calibration

This step consists in modeling the flux calibrator by comparing it with its own model flux, using the CASA task *setjy*, with the purpose of obtaining the scaling factor (from Kelvin to Jansky) to apply to the other calibrators (i.e., bandpass and phase calibrators), and thus carrying out the amplitude calibration.

The model applied to the flux calibrator fills the Model column of the MS with the corresponding information of the source. For well-known flux calibrators, the task automatically computes the flux density as a function of time, frequency and baseline length. The flux calibrator models are stored in *Butler-JPL-Horizons* standards, where these objects are currently modeled as uniform temperature disks (this may oversimplify objects, in particular asteroids), on the basis of their ephemerides at the time of the observation (Butler, 2012). We have applied the "Butler-JPL-Horizons 2012" model to Pallas, the asteroid used as flux calibrator. Fig. 2.17 compares this calibration Pallas model amplitude as a function of the UV distance (i.e. the increasing baseline length for each antenna pair), represented by the upper curve, with the archival model ("Butler-JPL-Horizons 2010"), the lower curve. It is evident that there is a difference of about 20% between the two cases. Indeed, Butler 2012 contend that many of the models used to calculate the flux density calculation of solar system bodies in the 2010 version were incorrect with respect to the new ones of 2012 (i.e., Butler-JPL-Horizons 2012), that use new brightness temperature models and a new flux calculation code that replaces the "Butler-JPL-Horizons 2010" standard used before. Concerning Pallas, its new constant brightness temperature value is 189 K, obtained from a combination of Chamberlain et al. 2009 and Altenhoff et al. 1994, while previously its value was 164 K (unknown provenance). This means that the flux densities calculated with "Butler-JPL-Horizons 2012" are expected to give higher and more precise values of the calibrators flux density, that is to say more precise values of the object flux densities.

Finally, using the CASA *fluxscale* task, the scaling factor from Kelvin to Jansky, obtained thanks to the flux calibrator, is applied to the bandpass and phase calibrators, since the raw correlation amplitudes are in Kelvin units, but the flux density is measured in Jansky. In Tab. 2.2 the bandpass and phase calibrators fluxdensities obtained by this work calibration are compared with the ones reported in the archive. Overall, our fluxdensity values are 20% higher than those from archive. The error in the flux calibration is estimated to be $\approx 15\%$ for Band 9 data (Asayama et al., 2016).

Ideally, the flux calibrators should be small with respect to the synthesized beam, so as not to resolve the source structure. However, solar system objects structures may be moderately resolved. For example, during the observation of the last EB, X43b, the flux calibrator, Pallas, was by far nearer to Earth ($d \approx 2.154\,\mathrm{UA}$, while, for instance, in the EB X334 $d \approx 3.566\,\mathrm{UA}$), and, as a result, it appears more resolved (Fig. 2.18-2.19). As said before, the Solar System objects are modeled as uniform temperature disks, and thus their Fourier transform in the visibility
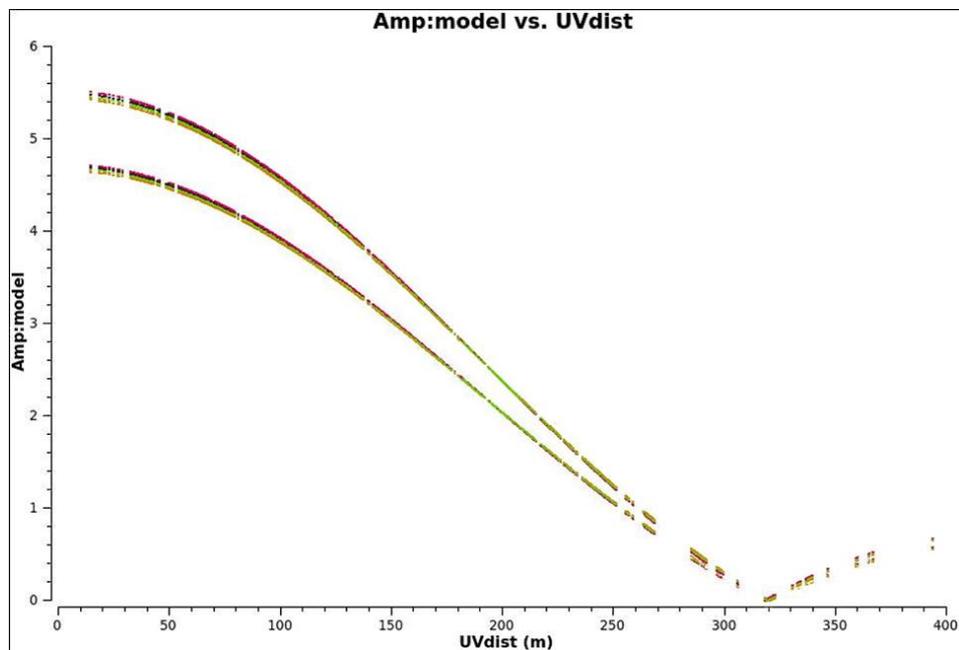
Figure 2.17: *Comparison between the model amplitude as a function of UV distance for our data reduction (upper curve) and the archival one (lower curve). The two curves are colorized per spectral window. It is evident that there is a difference of about 20% between the two cases.*

Table 2.2: This table compares the flux density values obtained by this work calibration with the one reported in the archive. 3C 454.3 is the bandpass calibrator, while 2348-165 is the phase calibrator. All the values are reported in Jy. The curves are colorized per spectral windows.

EBs	This work 3C 454.3	Archive 3C 454.3	This work 2348-165	Archive 2348-165
Xba3	0.57	0.45	0.56	0.41
Xd36	0.52	0.41	0.53	0.40
Xec9	0.52	0.43	0.47	0.37
X334	0.73	0.63	0.86	0.72
X4c7	0.55	0.44	0.43	0.35
X43b	0.96	0.82	0.97	0.73

plane is a Bessel function. According to the Bessel function theoretical shape, the flux density drops down to zero and then rises again, as is shown in Fig. 2.18, while the phases have a jump at ±180°. In 2.19 the drop is not visible because Pallas is less resolved. Null flux density value cannot be used for computing the K/Jy scaling factor. In this case, the time-dependent gains of the flux calibrator have to be computed on a subset of antennas, excluding the outermost ones (i.e. the antennas corresponding to the largest baselines).
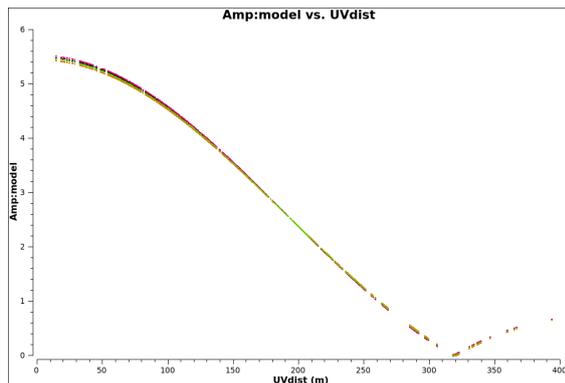

Figure 2.18: *Flux calibrator model in X43b.*
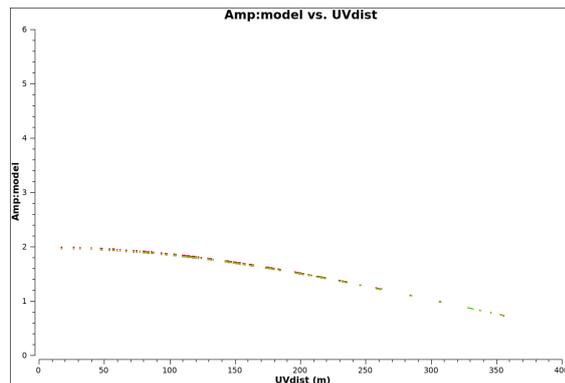
Figure 2.19: *Flux calibrator model in X334.*

Application of the calibration tables obtained

Once all the correction factors have been computed computed, we applied the bandpass, flux calibrated amplitude and phase solutions to the observed visibilities. The corrected data were then inspected, in order to check the reliability of the calibration procedure, by making plots of the corrected phase and amplitude as a function of time, colorized per field (Fig. 2.20 and Fig. 2.21). As expected, the bandpass (in black) and phase (in green) calibrators have flat phases, centered at zero and a constant amplitude, since they are modeled as point-like sources.

In order to check the frequency-dependent calibration, the amplitude of the phase calibrator as a function of frequency is shown in Fig. 2.22, 2.23, 2.24 and 2.25 for spectral windows 0, 1, 2 and 3, respectively. As expected, the amplitudes appear generally constant all over the bandpass.

Before concatenating the six EBs and starting with the imaging process, we further investigated the quality of this work calibration, by producing the QA2 (see Sec. 2.3) diagnostic plots. For instance, Fig. 2.26 and 2.27 show two significant diagnostic plots, representing the amplitude and phase gains, respectively, as a function of time for each antenna. Generally, when low amplitude gains are found, the corresponding antenna is flagged. Concerning phases, when the gains show a meaningful phase scatter, it is recommended to check their effect on corrected data. Fig. 2.26 and 2.27 show that overall the computed gains are stable for all the antennas.
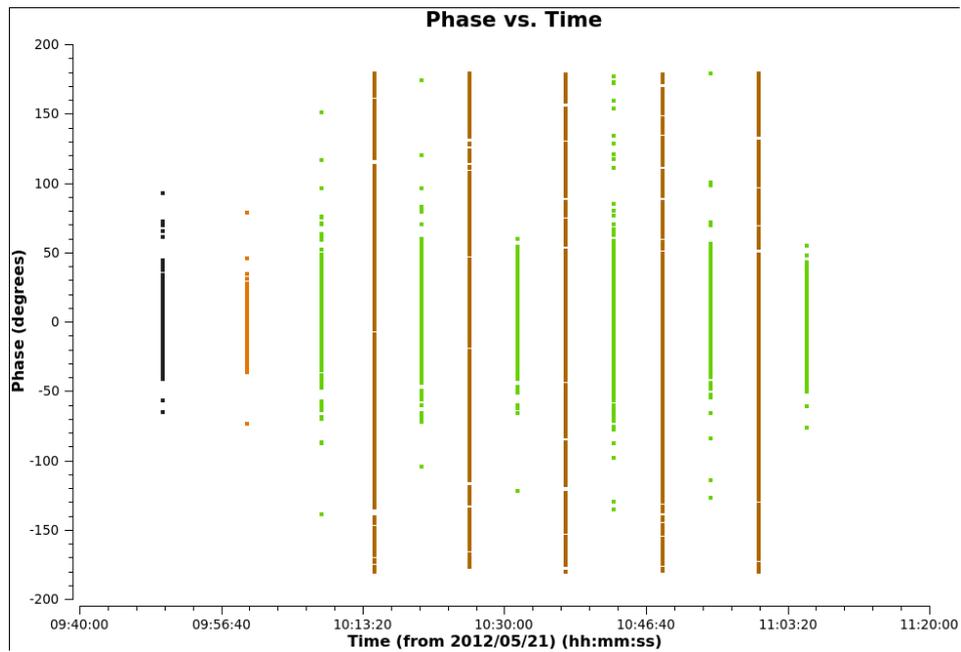
Figure 2.20: *Phase of the corrected visibilities as a function of time for the EB X334, colorized per field: the bandpass calibrator is indicated in black, the flux calibrator in orange, the phase calibrator in green and the target in brown.*
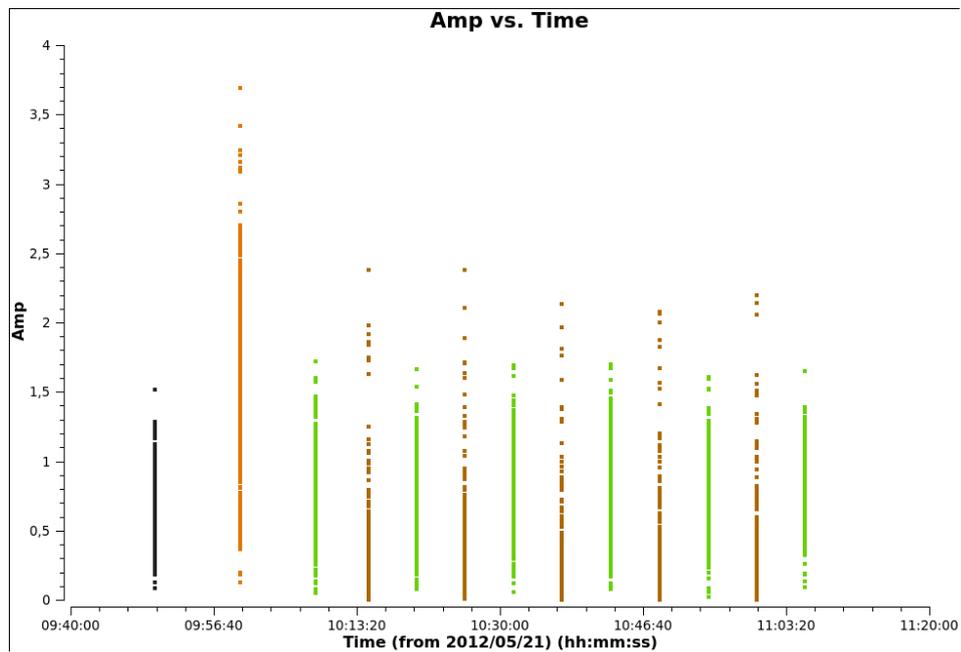

Figure 2.21: *Amplitude of the corrected visibilities as a function of time, colorized per field: the bandpass calibrator is indicated in black, the flux calibrator in orange, the phase calibrator in green and the target in brown.*
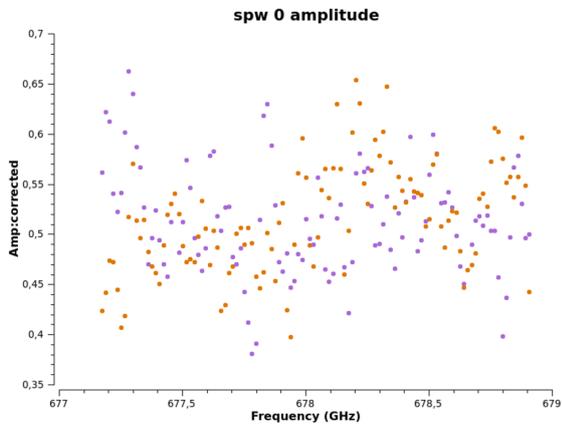
Figure 2.22: *Phase calibrator amplitude as a function of frequency in spw 0, colorized per polarization.*
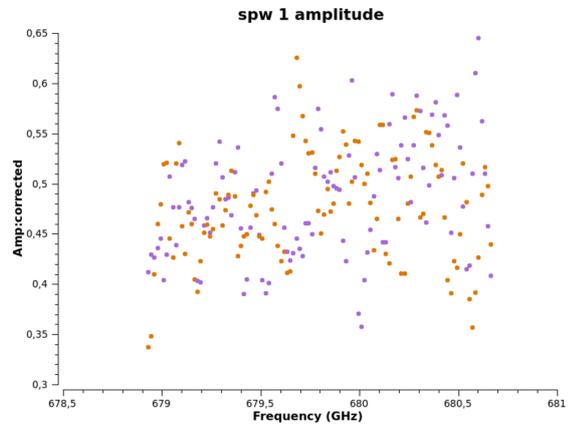
Figure 2.23: *Phase calibrator amplitude as a function of frequency in spw 1, colorized per polarization.*
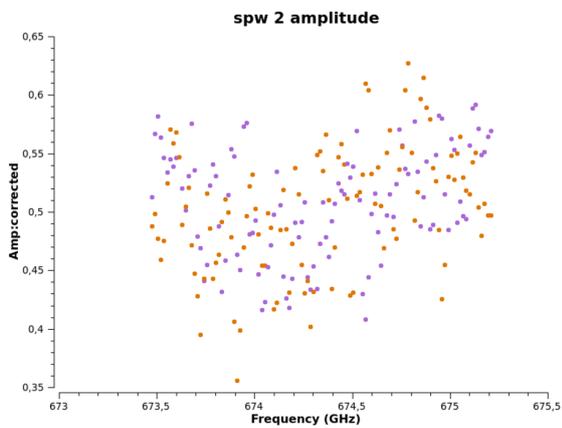
Figure 2.24: *Phase calibrator amplitude as a function of frequency in spw 2, colorized per polarization.*
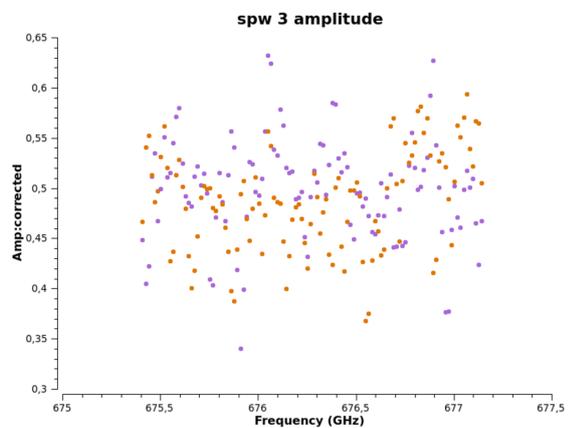
Figure 2.25: *Phase calibrator amplitude as a function of frequency in spw 3, colorized per polarization.*
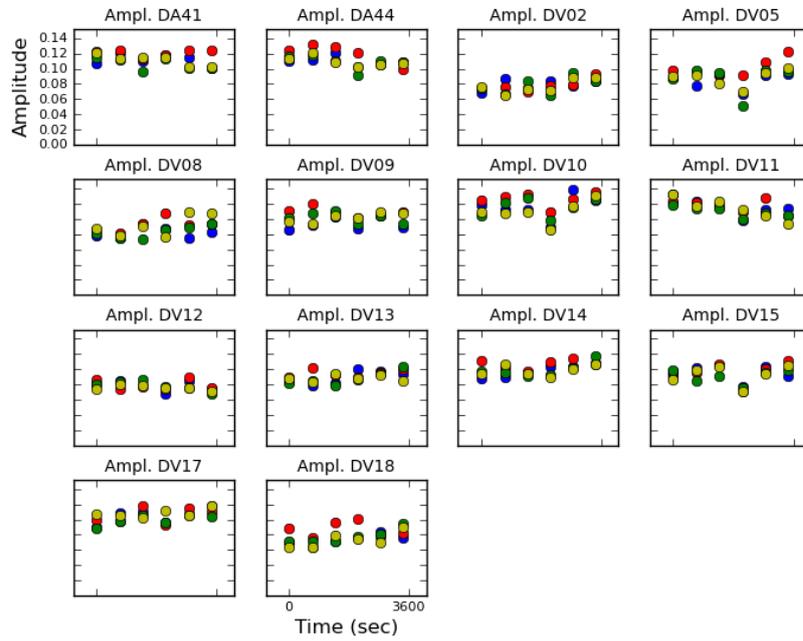
Figure 2.26: *Amplitude solutions as a function of time for each antenna, colorized by polarization.*
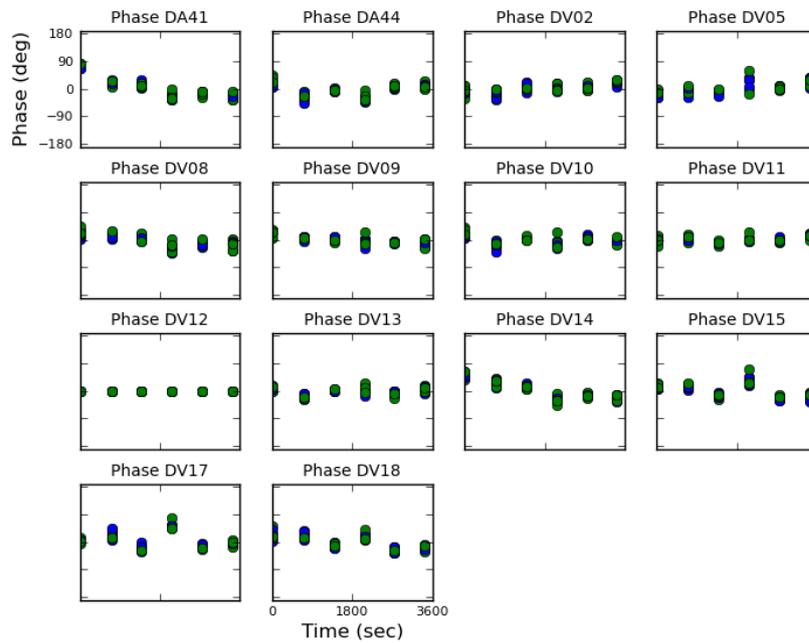
Figure 2.27: *Phase solutions as a function of time for each antenna, colorized by polarization.*

Lastly, we concatenated the six EBs, obtaining one final measurement set. Fig. 2.28 shows the part of the spectrum of NGC 34 with the CO(6-5) emission line, clearly visible at the observed frequency $\nu_{obs} = 678.181$ GHz, while Fig. 2.29-2.30-2.31 show the continuum emission. The emission line has a broadened double horn profile, which suggests that the gas emitting region is rotating.
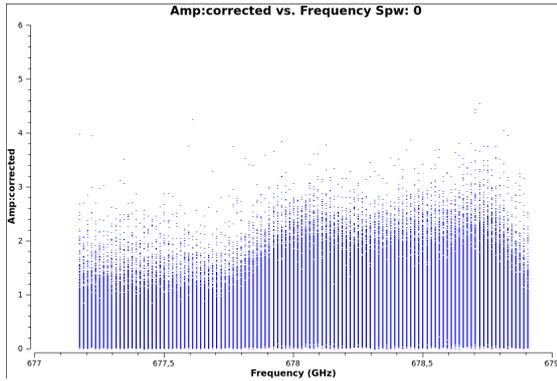
Figure 2.28: *Spectrum of NGC34 in spw 0: CO(6-5) emission line.*
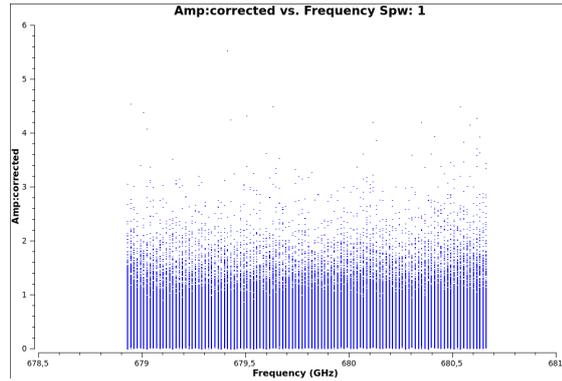
Figure 2.29: *Spectrum of NGC34 in spw 1: continuum emission.*
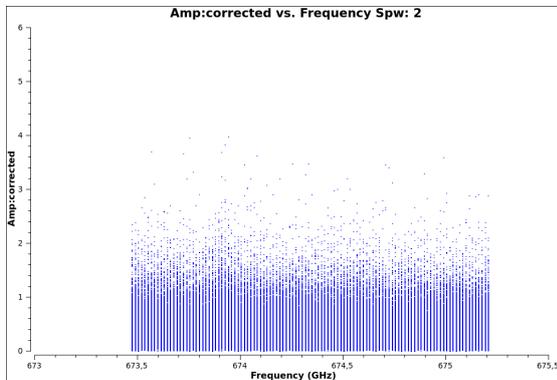
Figure 2.30: *Spectrum of NGC34 in spw 3: continuum emission.*
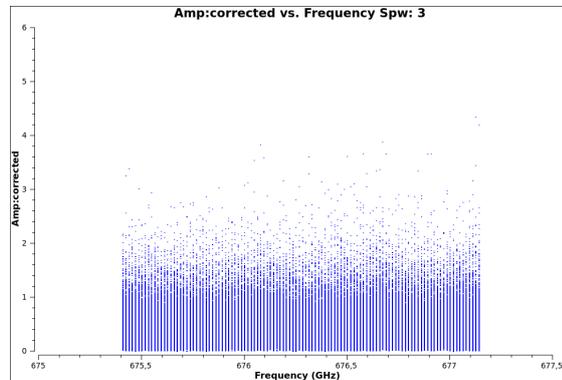
Figure 2.31: *Spectrum of NGC34 in spw 3: continuum emission.*

2.5   Imaging

As the interferometer observes a point on the celestial sphere, the rotation of the Earth causes the u and v components of the baseline to trace out an elliptical locus. For an array of antennas the ensemble of elliptical loci is referred to as *the transfer function* or *sampling function*, $s(u, v)$, which is a function of the declination of the observation as well as the antenna configuration. The transfer function indicates the values of u and v at which the visibility function is sampled, in particular it traces the response of the array as a spatial frequency filter. The visibility function for a point source at the (l,m) origin is a constant in u and v, that is why the Fourier transform of the transfer function indicated the response to a point source, i.e., *the synthesized beam* (Taylor et al., 1999). This means that the interferometer elements are sensible to the direction of arrival of the radiation, that is referred to as *primary beam effect*. Eq. 2.1 then becomes:

$$\mathcal{V}(u, v) = \int \int \mathcal{A}(x, y)\mathcal{T}(x, y)\, e^{2\pi i(ux+vy)}\, dx\, dy \tag{2.11}$$

where $A(x, y)$ is the primary beam pattern. Consequently, the response of the antennas in the array must be corrected for during imaging to get accurate intensities for source outside the core of the beam and this procedure is called *cleaning*.

2.5.1   Cleaning

The Fourier domain is sampled at discrete points, so the measured and (now) calibrated visibilities are given by the convolution between the true visibilities and the sampling function, that is equal to 1 at points where visibilities are measured and equal to 0 where they are not:

$$V_{meas}(u, v) = s(u, v)V_{true}(u, v) \tag{2.12}$$

The incomplete sampling of the u-v plane causes *alias* in the dirty image, which are copies of the source, apparently unnoticeable from the real one. The Fourier transform of the sampled visibilities, that is named *dirty image*, gives the true sky brightness convolved with the Fourier transform of the sampling function, called *dirty beam*, that is the instrument point spread function (PSF). Therefore, the cleaning procedure consist in doing the deconvolution for the dirty beam, using CASA *clean* task, with the *a priori* hypothesis that the observed source is composed by N point-like sources, following several steps:

- the residual map is initialized to the dirty image;

- the pixel that corresponds to the maximum emission is located in the residual map and seen as a point-like source, then a Dirac delta function is saved among the clean components;

- each clean component is convolved with a fraction of the dirty beam (10-15%) and subtracted from the residual map;

- these steps are repeated, considering other peaks, until a flux threshold or a number of iterations have been reached;

- finally, the saved clean components are convolved with the *clean beam*, obtained by fitting the dirty beam with a gaussian curve, and restored to the residual map.

This procedure is partially interactive because, thanks to the *viewer* task, it is possible to draw a region, that is referred to as a *mask*, on the initial image, where the peaks are likely to be found.

The interferometer resolution is given by the Fourier transform of the sampling function. According to Nyquist theorem, to result in a faithful sampling of the instrument resolution, the pixel size (called *cellsize*) must be $\approx 1/5$ of the synthesized beam. We have chosen a cellsize equal to 0.03 *arcsec*.

Each visibility has its own weight, that depends on the inverse of its noise variance, related to the T_{sys} measured. Furthermore, some u-v ranges are sampled more than others. The *clean* task allows to choose which weight to associate to each baseline, thanks to the *weighting* parameter. For *weighting='natural'*, visibilities are weighted only by the data weights. Even though this generally produces images with the poorest angular resolution, since short baselines are sampled more than the long ones, we have chosen this option because it produces images with the lowest noise. Other two possibilities are *weighting='uniform'* and *weighting='briggs'*. For the former, the dependence of spatial-scale sensitivity on the density of visibilities in uv-plane is removed (i.e., even though short baselines are sampled more than the long ones, they are associated to the same weight); this sharpens the resolution and reduces the sidelobe level in the field-of-view, but increases the rms imagine noise. The latter is a middle way between the other two options, introduced to bridge the extremes (Asayama et al., 2016).

2.5.2 The phase calibrator image

Before starting with the cleaning procedure, we have checked the image of the phase calibrator, shown in Fig. 2.32, in order to verify the quality of the calibration. As said in Sec. 2.4.3, at (sub)millimeter wavelengths, generally the phase calibrator is a bright quasar, that, once calibrated, should appear as a point-like source in the image plane, as Fig. 2.32 confirms. Since it is a point-like source, the flux density must be given by the peak value: the peak value of our image is $\approx 0.60\,Jy$, in line with the calibration results. The rms can be estimated by the signal-free portion of the image and it will be always bigger than the theoretical value given by Eq. 2.4, owing to the calibration errors. In this image, the rms is $\approx 2.0\,mJy$. In general, the flux uncertainties are given by the formula

$$\sigma = \sqrt{(0.15\,F)^2 + rms^2} \tag{2.13}$$

where F is the flux, and they are dominated by the flux calibration error. Tab. 2.3 compares our peak value and its corresponding rms with the archival results. It can be noticed that, as already said in Sec. 2.4.4, 2348-165 flux density is at least a 20% higher than the one reported in the archive[8]. Furthermore, despite the higher value obtained for the phase calibrator flux, the rms values are consistent: this implies that our image is improved with respect to the archival one.
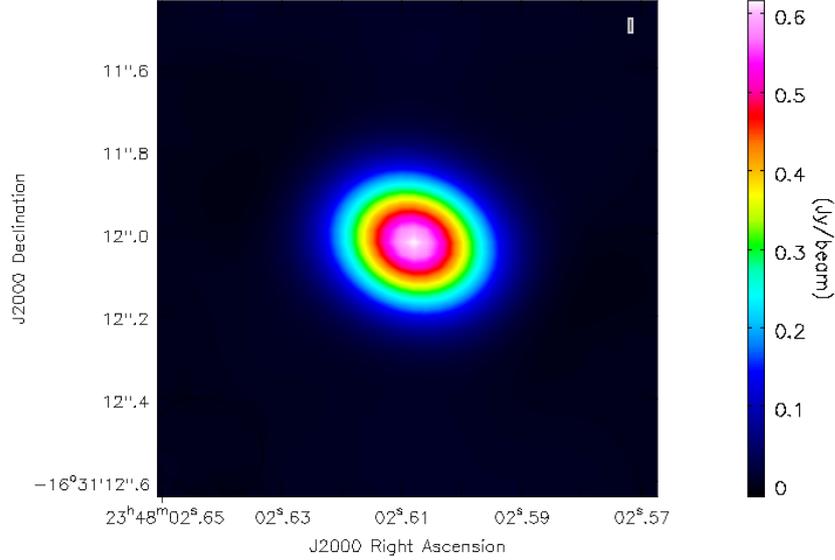
Figure 2.32: *Image of the phase calibrator 2348-165. The peak flux is* 0.60 ± 0.09 *Jy, while the rms is* $\approx 2.0 \, mJy$.

Table 2.3: This table compares the phase calibrators peak value and its corresponding rms obtained by this work calibration with those reported in the archive.

2348-165	Peak flux [Jy]	rms [mJy]
This work calibration	0.60 ± 0.09	2.0
Archival calibration	0.38 ± 0.06	1.0

---

[8]Actually, here the difference is $\approx 40\%$. Indeed, in the archival calibration, the flux density of the phase calibrator was fixed to the value of 0.38 Jy, on the basis of 2348-165 spectral index and flux measurements, estimated by SMA (Submillimeter Array) observations, made in may 2013.

2.5.3 Self-calibration

Calibration is the most important factor in determining the quality of the final deconvolved image, because small quasi-random errors in the amplitude and phase calibration of the visibility data produce an increased level of noise in the weaker regions of the image, and other systematic errors can cause defects in the final image. The ordinary calibration procedure described in Sec. 2.4.2 is based on observations of well-known radio sources in order to determine gains that will be applied to observed data. The gain for any array element has two contributing components: a slowly varying instrumental part and a more rapidly varying part due to atmosphere, that nearly always dominate the overall variation of the element gains. The solutions obtained for the phase calibrator are transferred to a different (even though near) position in the sky where the target is located, at a different time and the linear interpolation is an assumption (Asayama et al., 2016).

Hence, self-calibration is another method like the cleaning, that is used to interpret the visibility data. This procedure is based on the idea that objects with enough signal-to-noise ratio can be used to calibrate themselves. In order to do this, a model of the sky intensity distribution of the source is needed and can be obtained by carrying out an initial imaging of the source. The procedure can be iterated as model improves and usually starts by calibrating only the phase and finally, if it is needed at all, the amplitude. A typical procedure in which the model is iteratively refined is the following:

- an initial image of the source is made following the cleaning procedure and the deconvolution builds a model;

- data are calibrated to match to the model, finding solutions averaged in time (*gaincal* task);

- the new calibration is applied (*applycal* task);

- a new image of the better calibrated data is made;

- if the image is improved (higher signal-to-noise ratio), the procedure can be iterated.

Even if the source is bright enough, some degree of averaging is usually needed. In general, the time interval chosen to average data must be longer than a scan.

We have made the image of the emission in spectral window 0 by selecting only the channels were the emission line was brighter, built a model and found phase solutions averaged on 600 s (i.e., approximately two scans). Then, we iterated again and found phase and amplitude solutions, averaging 1200 s and combining scans. Fig. 2.33, 2.34 and 2.35 illustrates the steps of the self-calibration applied: the first panel shows the initial image, the second shows what changed after the application of the phase correction and the last the final image, after having applied the phase and amplitude corrections. The contours [-1, 1, 2, 3, 4, 6, 8, 10, 12, 16, 20, 24, 30, 40] are set in units of the rms noise level of the image.
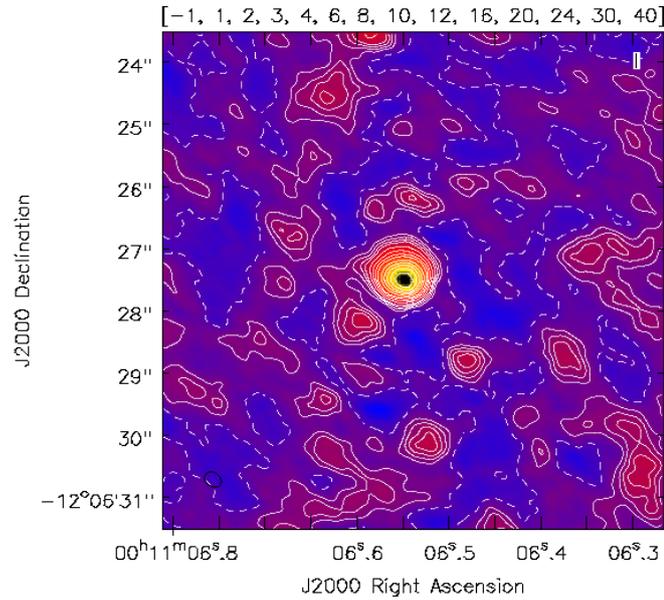
Figure 2.33: *Image of the emission in spw 0, obtained by selecting only the channels were the emission line was brighter, before applying the self-calibration. The contours [-1, 1, 2, 3, 4, 6, 8, 10, 12, 16, 20, 24, 30, 40] are set in units of the rms noise level of the image.*
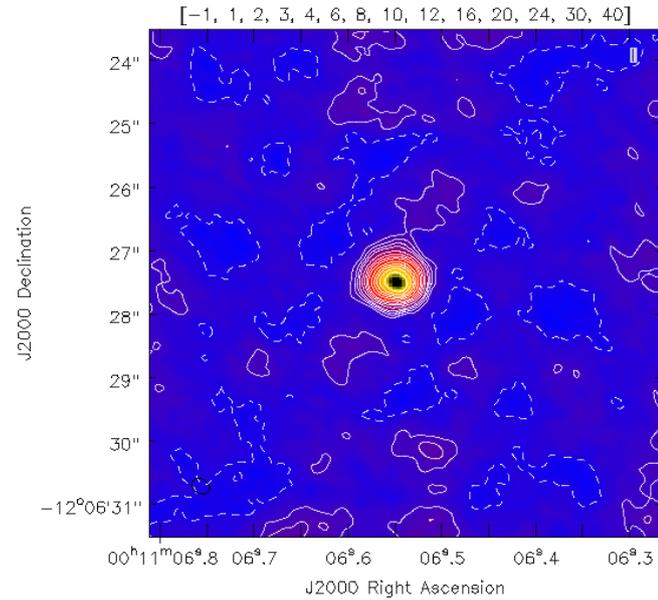
Figure 2.34: *Image of the emission in spw 0, obtained by selecting only the channels were the emission line was brighter, after the self-calibration of the phase. The contours [-1, 1, 2, 3, 4, 6, 8, 10, 12, 16, 20, 24, 30, 40] are set in units of the rms noise level of the image. It can be noticed that there is an improvement with respect to Fig. 2.33.*
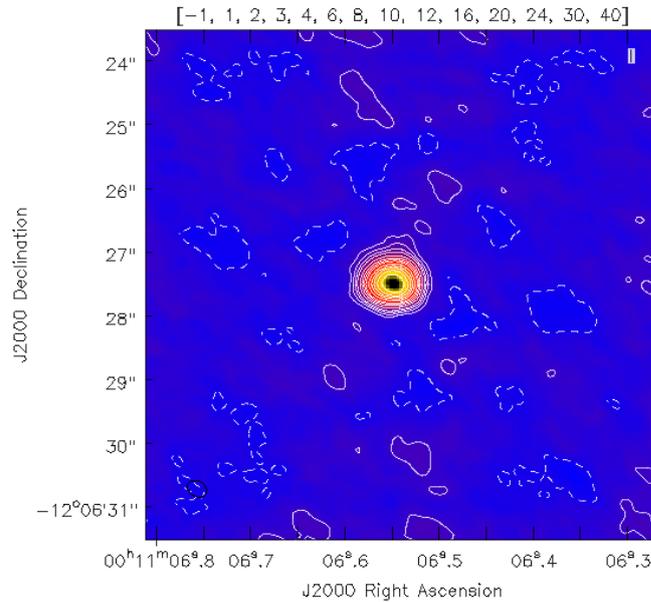
Figure 2.35: *Image of the emission in spw 0, obtained by selecting only the channels were the emission line was brighter, after the self-calibration of the amplitude. The contours [-1, 1, 2, 3, 4, 6, 8, 10, 12, 16, 20, 24, 30, 40] are set in units of the rms noise level of the image.*

2.5.4   Analysis of fluxes, maps and moments obtained

Each spectral window has 128 channels and a 2 GHz width, therefore the channel resolution is ≈ 30 MHz. Frequency/channels and velocity are linked by the relation:

$$\frac{\Delta v}{c} = \frac{\Delta \nu_{chan}}{\nu} \tag{2.14}$$

Therefore, the velocity resolution is ≈ 14 km/s. We created a data cube, a three-dimensional array of images, where the x, y and z axis are RA and DEC coordinates and channel/frequency/velocity, respectively, binning into channels with a width of $\approx 34z$ km/s, in order to increase the signal-to-noise ratio. After having subtracted the continuum emission, thanks to the *uvcontsub* task, we obtained the channel map of the CO(6-5) emission line, showed in Fig. 2.36, where contours in units of the rms noise level of the image are set. The rms of this image is ≈ 6.7 mJy.

Fig. 2.37 shows the asymmetrical double horn line profile.

The CASA Viewer can collapse a data cube into an image, in particular there are two mathematical formula particularly important:

- Moment 0, that allows to obtain the integrated emission of the line:

$$\int S_v \, dv \qquad [\mathrm{Jy \, km \, s^{-1}}] \tag{2.15}$$
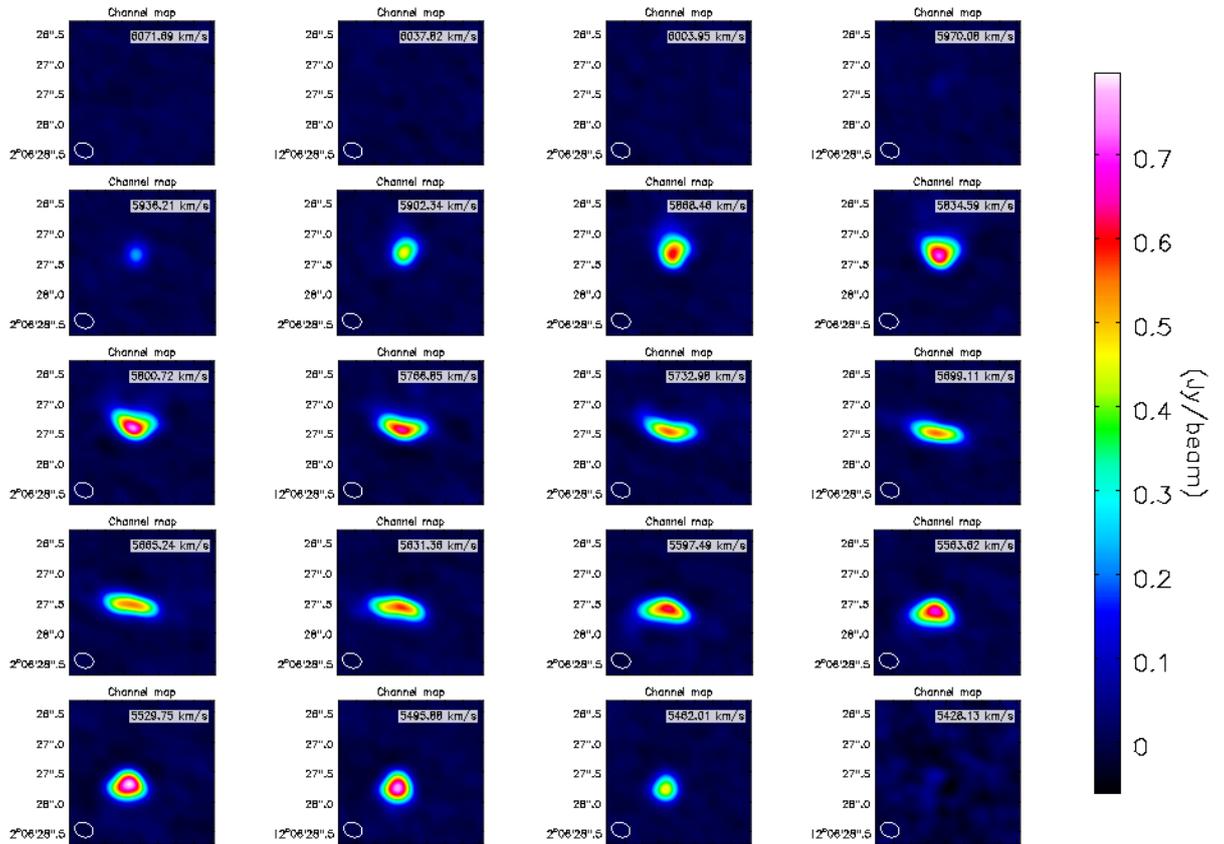
Figure 2.36: *Channel map of the CO(6-5) line. The wedge on the right shows the color-scale of the map in Jy beam^{-1}. The rms of this image is ≈ 6.7 mJy.*
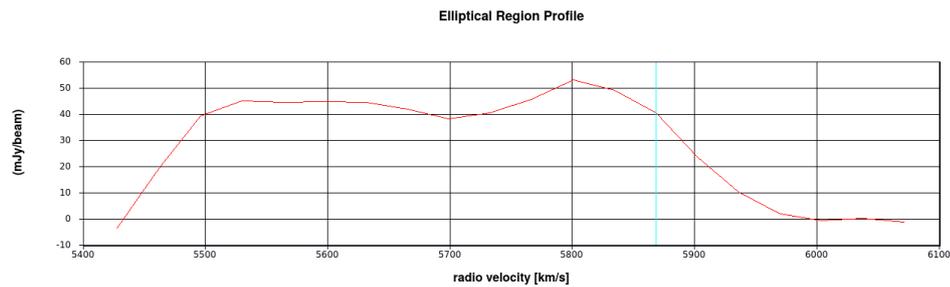
Figure 2.37: *Asymmetrical double horn profile of the CO(6-5) emission line. The x-axis indicates the velocity in km s^{-1} in the BARY (Solar System Barycenter) reference frame, while the y-axis the corrisponding flux.*

- Moment 1, that indicates the velocity value in the various regions of the source:

$$\int \frac{S_v\, v\, dv}{S_v\, dv} \qquad [\mathrm{km\, s^{-1}}] \tag{2.16}$$

In order to avoid to sum the rms during the integration of Moment 1, we put a flux threshold equal to $\approx 3 - 5\, rms$ (in our case, we chose a threshold of 30 mJy).

Fig. 2.38 shows the Moment 0 of the line emission, where contours in units of the rms noise level of the image are set. The rms of the image is 1.3 Jy.
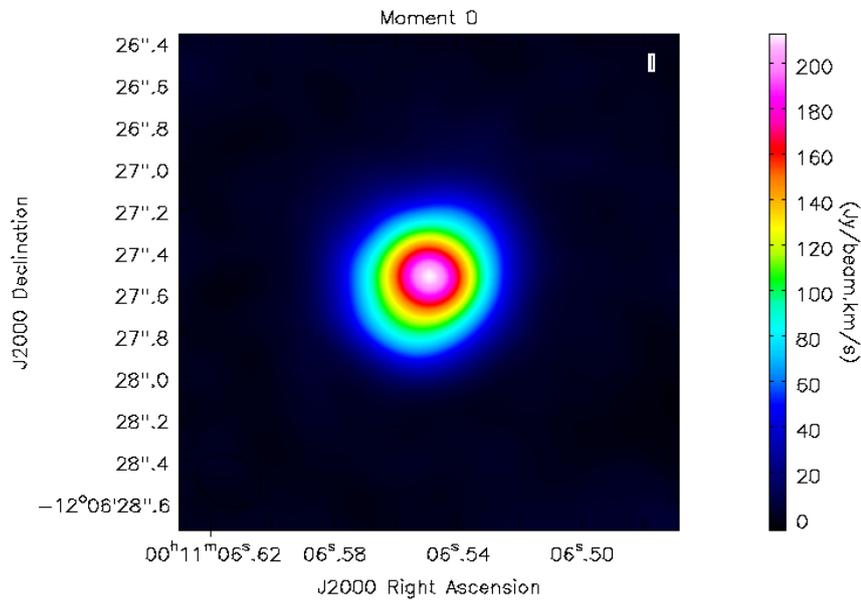
Figure 2.38: *Integrated emission of the CO(6-5) line. The wedge on the right shows the colorscale of the map in $Jy\, beam^{-1}\, km\, s^{-1}$. The rms noise level is $\approx 1.3\, Jy\, km\, s^{-1}$. The integrated flux density results $(731 \pm 110)\, Jy\, km\, s^{-1}$.*

We choose not to fit the emission with a 2D gaussian, because the emission line has a double asymmetrical horn, so we drew several circular regions around the emission, at different radii and then we produced a graph, that shows the flux density as a function of the area considered (obtained multiplying the number of pixels comprised in each region by the pixel size in *pc*). As Fig. 2.39 shows, the broader is the area considered, the higher the flux density is, until it reaches a plateau.
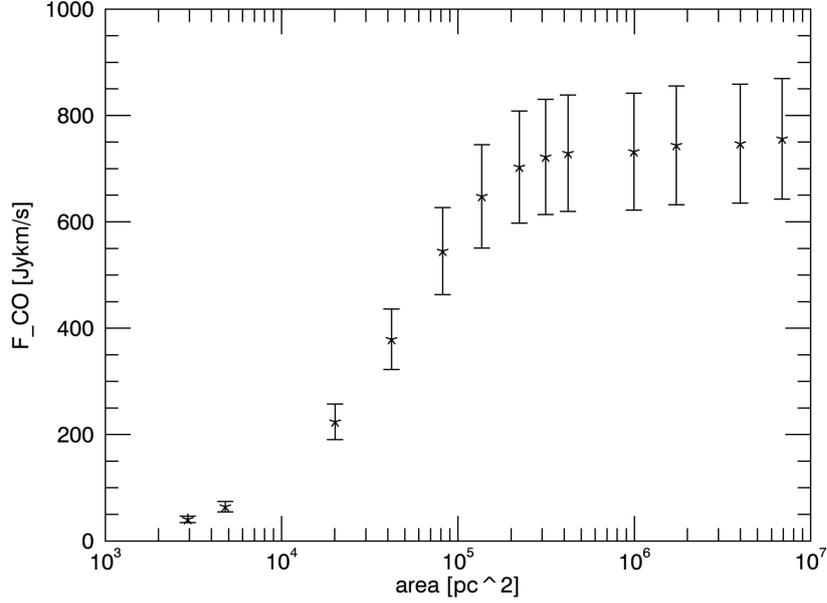
Figure 2.39: *Flux density of the integrated line emission as a function of the area of the region considered.*

Considering a radius of $\approx 0.8''$, the Moment 0 is $(731 \pm 109.7)\, Jy\, km/s$ with a peak of $(213 \pm 40.0)\, \mathrm{Jy\, km/s}$ and the emission comes from a region, whose size is $\approx 200 \times 200\, \mathrm{pc}^2$. In Tab. 2.4, this work calibration and archival data for the channel maps rms and Moment 0 characteristics are reported. It can be noticed that we obtained a Moment 0 value that is $\approx 25\%$ lower than the archival one, while the peak flux and rms values are totally consistent. In order to understand the cause of this discrepancy, we tried to reproduce archival images, following archival scripts, but we have not been able to reproduce such results.

Table 2.4: This table compares the line image characteristics obtained by this work calibration with the archival results. In the second column is reported the rms of the channel maps, shown in Fig. 2.37. In the last three columns are reported the Flux of the integrated line, the corresponding rms and the peak flux, respectively.

NGC 34 channel maps:	rms [mJy]	Moment 0:	Flux [Jy km s^{-1}]	rms [Jy km s^{-1}]	Peak flux [Jy km s^{-1}]
This work calibration	6.7		731 ± 110	1.3	213 ± 40
Archival calibration	5.5		1004 ± 41	1.2	196 ± 29

As Fig. 2.40 shows, the emitting region has diffent velocities, ranging from 5550 to 5850 km/s (in the topocentric coordinate system), and is clearly rotating, since the blue region is blue-shifted, while the red one is red-shifted.
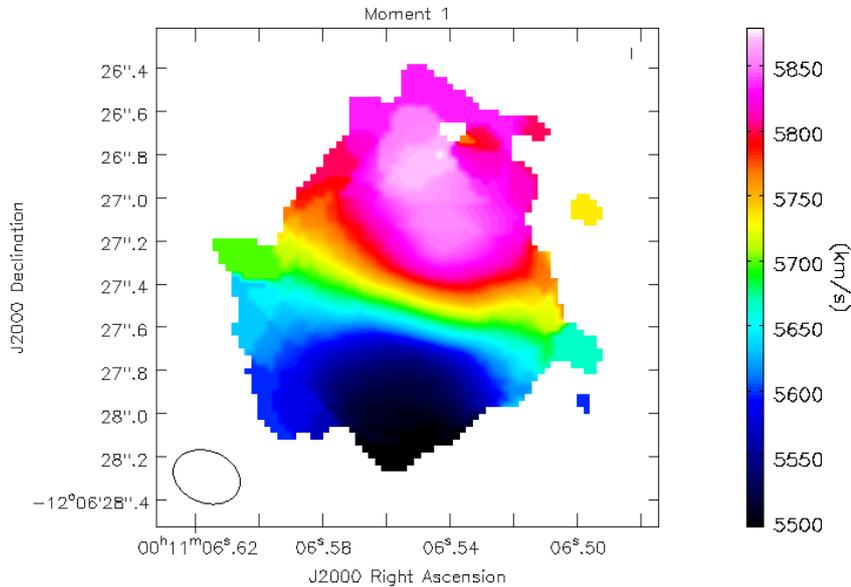
Figure 2.40: *Moment 1. The emission is restricted to regions where the rms in the CO data cube is larger than 3. The color bar on the right shows the color scale in* $km\,s^{-1}$.

Fig. 2.41 shows NGC 34 nuclear region continuum emission (spws 1, 2 and 3), associated to dust continuum emission. We obtained a flux density equal to (277.8 ± 41.7) mJy, with a peak of (98.6 ± 14.8) mJy. The rms of the image is ≈ 1.0 mJy. The size of the emitting region (deconvolved) is 452.4×282.5 marcsec^2, that corresponds to $\approx 187.8 \times 117.4$ pc^2, considering a luminosity distance of 85.7 Mpc. Furthermore, Fig. 2.41 shows also contours set in units of the rms noise level of the image.

Tab 2.5 compares the continuum flux, rms and peak obtained from this work calibration with the archival results. It can be noticed that, the flux values are consistent, while our rms appears slightly lower and the peak flux higher.

Fig. 2.42 illustrates the integrated emission of the CO(6-5) line with continuum contours and this suggests that both the emissions come from the same region of the galaxy. More precisely, the continuum appears to be only in the inner part of the CO(6-5) disk. Xu et al. 2014 contend that both the size and the orientation of the continuum emission region agree well with those of the "nuclear bulge" found in the HST-V-band image by Schweizer and Seitzer 2007. In addition, they said that there is a hint that the CO(6-5) line emission may have a central component
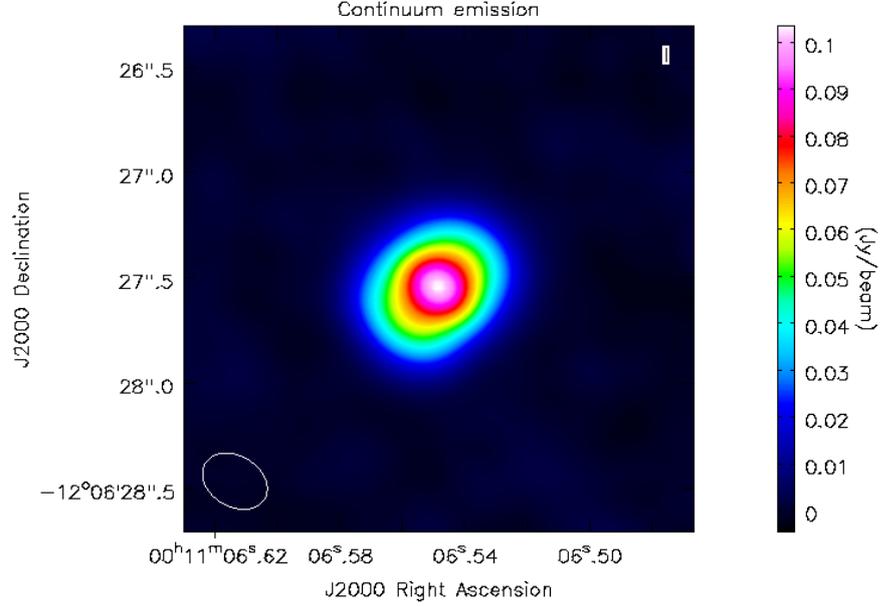
Figure 2.41: *Continuum emission. The flux obtained is equal to* $(277.8 \pm 41.7)\, mJy$, *with a peak of* $(98.6 \pm 14.8) mJy$. *The rms of the image is* $\approx 1.0\, mJy$

Table 2.5: This table compares the continuum image characteristics with those reported in the archive: the continuum flux, its corresponding rms and the peak flux.

NGC 34 continuum image	Flux [mJy]	rms [mJy]	Peak flux [mJy]
This work calibration	278 ± 42	1.0	98.6 ± 14.8
Archival calibration	275 ± 41	1.9	76.2 ± 11.4

corresponding to the same nuclear bulge and a more extended component, undetected in the continuum, that corresponds to the V-band nuclear disk.
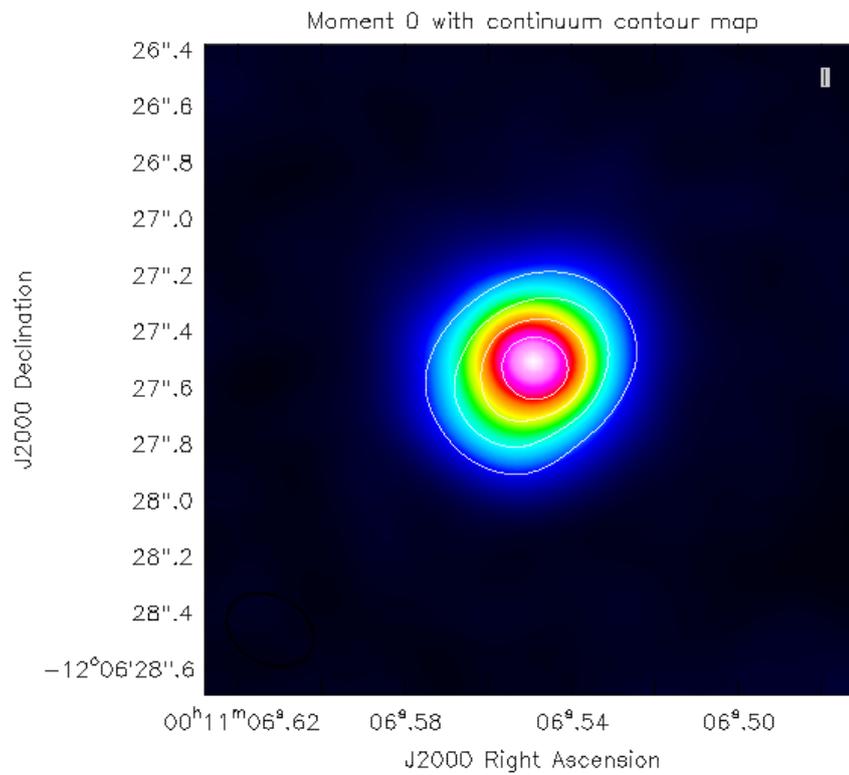
Figure 2.42: *Integrated emission of the CO(6-5) line with continuum contours [0.2, 0.4, 0.6, 0.8].*

Chapter 3

The Physics of Interstellar Medium

The gaseous component of galaxies is generally referred to as *interstellar medium* (ISM), the *diffuse matter*. It can be seen as the primary galactic "repository", where star formation takes place and deposits energy, momentum and enriched material. Consequently, the ISM plays a crucial role in the galactic matter cycle, both in the formation and evolution of galaxies. Its physical properties are governed by the radiation emitted by stars, the far-ultraviolet (FUV) radiation ($6\,\text{eV} < h\nu < 13.6\,\text{eV}$), that has an influence on the chemistry of the neutral atomic gas and much of the molecular gas in galaxies (Hollenbach and Tielens, 1999). In addition, it can be exposed also to X-ray radiation, that can have profound effects on the chemical and thermal structure of molecular clouds (MCs) (Maloney et al., 1999). Overall, the ISM properties and dynamics on large scales are influenced by the microphysics behind the heating and cooling processes. Moreover, there is a great number of competing feedback loops, such as winds, ultraviolet fluxes and supernova explosions of stars, capable of triggering or quenching star formation and generating *turbulence*[1] (Klessen and Glover, 2014).

3.1 The ISM composition and gas phases

The ISM is mainly composed by hydrogen (H, $\approx 70\%$) and helium (He, $\approx 28\%$), and a little amount of metals (Z, $\approx 2\%$), that, even though negligible in terms of mass, is essential for cooling processes. The thermal and chemical state of the ISM are conventionally described in terms of a number of distinct phases, defined by the chemical state of hydrogen, that can be ionized, neutral or molecular. More precisely, the ISM is composed by a neutral phase, an ionized phase and by dense molecular gas, constituting the Giant Molecular Clouds (GMCs), in which stars

---

[1]Turbulence plays a dual role: it creates overdensities that lead to gravitational contraction or collapse and counters gravity in these overdense regions.

form. Their main properties are summarized in Tab. 3.1 and discussed in more detail in what follows.

Table 3.1: ISM gas phases.

Component	Temperature [K]	Density [cm^{-3}]	Fractional ionization
Molecular gas	10-20	$> 10^2$	$< 10^{-6}$
Cold Neutral Medium (CNM)	50-100	20-50	$\sim 10^{-4}$
Warm Neutral Medium (WNM)	6000-8000	0.2-0.5	~ 0.1
Warm Ionized Medium (WIM)	$\sim 10^4$	0.2-0.5	1.0
Hot Ionized Medium (HIM)	$\sim 10^6$	$\sim 10^{-3}$	1.0

3.1.1   Atomic neutral gas

The neutral gas is characterized by two different termally stable phases: one of cold, dense gas that is traditionally considered to be distributed in compact clouds with temperatures around 70 K, called *cold neutral medium* (CNM), and a second related to warm and diffuse gas with temperatures around 6000-8000 K, defined as *warm neutral medium* (WNM). Field et al. (1969) demonstrated that the CNM and the WNM could coexist in pressure equilibrium, so that the neutral atomic gas could be considered to be a two-phase medium.

The properties of atomic hydrogen (H I) are best studied by looking at the 21cm hyperfine transition. More precisely, the transition happens between the coupled and decoupled spins of electron and proton in the hydrogen atom at its lowest energy state, as Fig. 3.1 shows. Within the ISM, collisions are frequent and what usually happens, such as in this case, is that the excited state is collisionally induced. This is a forbidden transition because the Einstein coefficient of spontaneous emission is $A_{21} = 2.8 \times 10^{-15}\,\mathrm{s}^{-1}$, that corresponds to a spontaneous emission timescale of $\tau_{21cm} \simeq 10^7\,\mathrm{yr}$. Despite this drawback, this transition is observed thanks to the great abundance of hydrogen atoms and represents the best way to study the distribution of gas in local galaxies, since from the line width it is possible to measure the typical random velocities of the gas. The observed lines are approximately gaussian with a dispersion that ranges from 7 to 20 km s^{-1}, that is far larger than the value they would have taking into account only the thermal broadening. This leads to the conclusion that the ISM is turbolent.

3.1.2   Ionized gas

McKee and Ostriker (1977) extended the two-phase model proposed by Field et al. (1969), adding a third, hot phase, the *hot ionized medium*[2] (HIM). What happens is that blast waves, generated by supernova explosions, create large, collisionally ionized bubble, filled with hot ($T \approx 10^6\,\mathrm{K}$)

---

[2]The supernova-shocked inter-cloud medium.
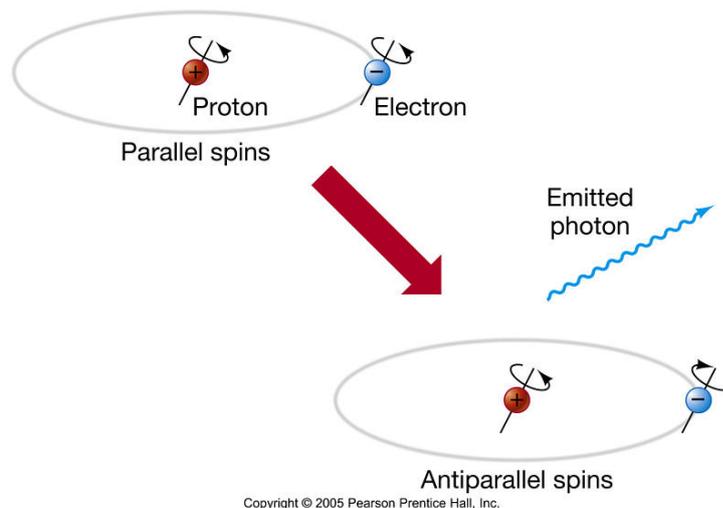
Figure 3.1: *Hydrogen hyperfine transition (from https://safe.nrao.edu/wiki/bin/view/Main/ ExgalHIProject).*

and diffuse gas ($n \approx 3 \times 10^{-3}\,\text{cm}^{-3}$) in pressure equilibrium with the neutral diffuse gas. In order to ionize the gas collisionally, a very high temperature is required, according to the condition

$$k\,T_{ion} > 13.6\,\text{eV} \tag{3.1}$$

which leads to a temperature of $T_{ion} \gtrsim 1.6 \times 10^5\,\text{K}$. However, given that the distribution of particle velocities is Maxwellian, even for temperatures far below this value ($\approx 2 \times 10^4\,\text{K}$), there are some particles with a very high velocity, due to shock waves, capable of ionizing most of the gas. Collisionally ionized gas accounts for the majority of the radiation at soft X-ray wavelengths, emitted mainly for thermal bremsstrahlung, radiation caused by the collisions between electrons and ions. This gas would eventually cool, but in a very long time, as the relation of the cooling time of thermal bremsstrahlung suggests:

$$\tau_{cool} \propto 10^3\,\frac{T^{1/2}}{n}\,\text{yr} \tag{3.2}$$

There is also another ionized phase in the ISM, related to radiatively ionized hydrogen with density $n \approx 1\,\text{cm}^{-3}$ and $T \approx 10^4\,\text{K}$, the *warm ionized medium* (WIM). Photo-ionized regions are called HII regions and are located in the surroundings of massive O and B stars, characterized by a surface temperature around $T \approx 2 - 5 \times 10^5\,\text{K}$. O and B stars irradiate photons with energy $h\nu > 13.6\,\text{eV}$, capable of ionizing neutral hydrogen in a sphere all around (the so called *Strömgren sphere*). In an homogeneous medium, HII regions would appear to be spheres filled with almost fully ionized medium and sharp edges, that divide them from almost fully neutral medium. The size of the *Strömgren sphere* is obtained by solving the equilibrium equation between recombina-

tion and ionization. When recombination occurs, the electron does not necessarily fall directly to the ground state, producing a number of lower energy photons, that are not capable of ionizing anymore. HII regions are traced through the hydrogen recombination lines (e.g., Balmer lines) or forbidden lines of extremely low density elements, such as [O III] or [N II]. In addition, photo-ionized gas emits, like any plasma with free electrons, for bremsstrahlung, that, at typical temperature of HII regions ($T \simeq 10^4$ K), shines at radio wavelengths[3].

3.1.3   Molecular gas

The transition between atomic and molecular gas occurs at very low temperatures (below 40 K) in GMCs, which are sufficiently dense and well-shielded against the dissociating effects of ultraviolet radiation to allow H atoms to bind together. These regions are composed mainly of H_2, that is highly simmetric, since it contains two identical hydrogen atoms. Due to this simmetry, the molecule has no dipole moment (i.e., is an homonuclear molecule) and exists in two indipendent states, namely ortho-H_2 (spins of H nuclei parallel) and para-H_2 (spins antiparallel). As a result, ro-vibrational dipole transitions ($J + 1 \rightarrow J$, where J is the rotational quantum number) are forbidden (i.e., their Einstein coefficient are very low, indicating that these transitions are quite unlikely), so within the electronic ground state H_2 weakly radiates only through quadrupolar transitions ($J + 2 \rightarrow J$). The first allowed electronic dipole transitions occur in the presence of FUV radiation. In these cases, the molecule is radiatively pumped into its electronically excited states and, as it decays back into the electronic ground state, it populates the high vibrational levels, producing IR emission. Therefore, direct detections of H_2 are not trivial. Electronic transitions occur in the ultraviolet, to which Earth's atmosphere is opaque, so observations can only be made from space, while ro-vibrational transitions appear to be very weak. Concerning IR emission, it is generally related to gas strongly heated by shocks or radiation ($T > 100$ K), tracing only a small fraction of the overall amount of molecular hydrogen. This is the reason why the H_2 cooling is efficient at relatively high temperatures ($T > 100$ K) (Habart et al., 2004)).

Hence, carbon mono-oxide (CO), the second most abundant molecule in the universe (even though about 10^{-5} times less abundant than H_2) is the most widely used tracer of molecular gas. In fact, CO is far easier to detect, emitting radio and sub-millimeter emission through rotational transitions. The easier CO isotopologue to observe is $^{12}C^{16}O$ (namely, ^{12}C or just CO) thanks to its large quantity, but often it is so abundant that its emission appear to be optically thick. This means that it can be used to trace conditions only in the surface layers. Other important isotopologues are $^{13}C^{16}O$ (usually called just ^{13}C) and $^{12}C^{18}O$ (usually just $C^{18}O$), whose optically thin emission allows to trace the full volume of the cloud. CO cooling dominates once the gas density reach $n \simeq 1000$ cm^{-3} at temperatures $T < 100$ K, typical values of the MCs.

---

[3]The bremsstrahlung spectrum is rather constant until a cut-off frequency, that depends only on the temperature of the gas and is given by the relation: $v_{cut-off} \simeq 10^{10} \times$T Hz.

3.2 Interstellar Dust

The reddening of starlight in the ISM and its tight correlation with the hydrogen column density point out that there is an additional component of the ISM, capable of absorbing light over a wide range of frequencies. Furthermore, measurement of elemental abundances in the local ISM reveals that a number of elements, notably silicon and iron, are considerably less abundant in the gas-phase than in the Sun. Finally, mid-infrared and far-infrared observations show that there is a widespread continuum emission, with a spectrum close to that of a black body and an intensity that correlates well with the hydrogen column density. All these pieces of information lead to the conclusion that there must be a particulate component, which is associated to CNM and GMCs, and accounts for around 1% of the total mass of the ISM, commonly referred to as *dust* (Klessen and Glover, 2014).

Dust has a crucial role in several physical processes, such as the formation of molecular hydrogen and the absorpion of UV and optical radiation. In addition, since it absorbs UV radiation that can dissociate molecules and, in turn, emits radiation at FIR wavelengths, it facilitates ISM chemistry and helps in cooling the gas, accelerating the process of star formation. This phenomenon of absorbing and scattering part of the electromagnetic radiation emitted by an astronomical object is called *extinction*. As Fig. 3.2 shows, the intensity of radiation that passes through a cloud of dust and gas appears to be attenuated by a factor that depends on its wavelength, the depth l, the density n of the cloud and the cross section of the material σ:

$$I_\lambda = I_{0\lambda} e^{-\tau_\lambda} \tag{3.3}$$

where τ is the *optical depth*, given by the relation $\tau = \int \sigma n dl$, in which $N = nl \, [\text{cm}^{-2}]$ is the column density of the gas. An object that suffers from extinction appears to be "reddened" since the redder wavelengths have arrived to the observer, while the bluer ones have not. Therefore, this phenomenon is referred to as *interstellar reddening*.
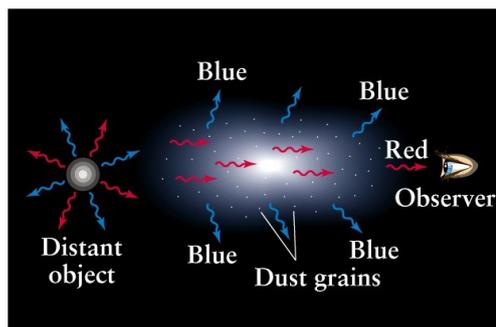

Figure 3.2: *Radiation emitted by an astronomical object that passes through a cloud of dust grains and gas is partly extincted in function of its frequency: the higher frequencies (UV, optical) appears to be scattered and absorbed, while the redder ones (IR) can pass through unchanged (from http://english.cas.cn/newsroom/research_news/201504/t20150416_146426.shtml).*

The amount of extinction measured in magnitudes at a certain wavelength is given by

$$A_\lambda = -2.5 log \left(\frac{I_\lambda}{I_{0\lambda}} \right) \tag{3.4}$$

and is related to the optical depth by the formula:

$$A_\lambda = 1.086 \, \tau_\lambda \tag{3.5}$$

Assuming a gas-to-dust ratio, it is possible to obtain a relation between the extinction and the column density of the gas. In any photometric system interstellar reddening can be described by color excess, defined as the difference between an object's observed color index and its intrinsic color index, $E(B-V) = (B-V)_{obs} - (B-V)_0$.

Approximately, individual dust grains absorb only those photons with wavelengths smaller than the physical size of the grain ($a \gtrsim \lambda/(2\pi)$). Therefore, the fact that we see a large amount of absorption and scattering in the ultraviolet ($\lambda \simeq 0.1 \, \mu$m), somewhat less in the optical and even less at infrared wavelengths ($\approx 1 \, \mu$m) provides immediately that the majority of dust grains are small ($\approx 0.016 \, \mu$m), rather than large ($\approx 0.1 \, \mu$m) (Cardelli et al., 2004). Dust particles usually range in size from the molecular domain to sizes around $0.3 \, \mu$m and are composed largely of amorphus carbon or graphite, aromatic hydrocarbons, silicates, ices, silicon carbide, and, possibly, iron particles, metallic oxides and sulfides. At the small end of the size regime lie polycyclic aromatic hydrocarbons (PAHs), which are large, planar molecules. The extinction curve gives information on which kind of grain can lead to a particular feature, such as the 2175 Å bump, associated to graphite, or the infrared bands at $9.7 \, \mu$m and $18 \, \mu$m, related to amorphous silicates (Klessen and Glover, 2014). In the wavelength range of $0.125 \, \mu$m $\leq \lambda \leq 3.5 \, \mu$m, the Galactic extinction curves (Fig. 3.3) can be approximated by an analytical formula, depending only on the parameter $R_V = A_V/E(B-V)$, the total-to-selective extinction ratio, with $R_V \approx 3.1$ for the Galactic average (Cardelli et al., 2004). The optical/UV extinction curves and R_V show considerable variations, that depend on the environment. Lower-density regions have a smaller R_V, a stronger 2175 Å bump and a steeper far-UV rise ($\lambda^{-1} > 4 \, \mu$m^{-1}), implying smaller dust grains in these regions. On the other hand, denser regions have a larger R_V, a weaker 2175 Å bump and a flatter far-UV rise, which means that dust grains are larger.
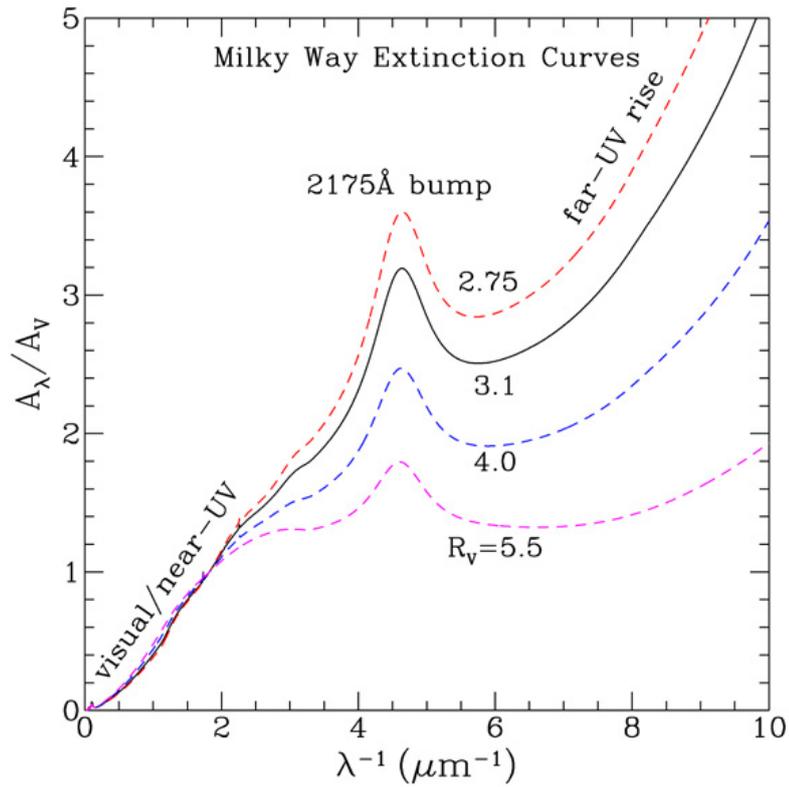
Figure 3.3: *Interstellar extinction curve of the Milky Way ($R_V = 2.75, 3.1, 4.0, 5.5$). There are significant variations in the Galactic optical/UV extinction curves, indicating that dust grain size distribution changes, according to the line-of-sight (from https://ned.ipac.caltech.edu).*

3.3   Molecular clouds

The molecular gas out of which stars form is located in GMCs, which play a negligible role in filling the gas volume, but comprise a significant fraction of the mass. These regions have masses in excess of $10^3 \, \mathrm{M_\odot}$ and up to $10^6 - 10^7 \, \mathrm{M_\odot}$, and a hierarchical structure, that extends from the scale of the cloud[4] ($r \approx 10 - 30 \, \mathrm{pc}$) down to overdense and less massive regions ($r \approx 10^{-2} \, \mathrm{pc}$, $M \approx 1 \, \mathrm{M_\odot}$), termed *clumps* and *cores*[5]. Typical temperatures within MCs, inferred from the CO luminosity and theoretically reproduced through numerical simulations, ranges from $T \approx 10$ K to $T \simeq 50 - 60 \, \mathrm{K}$ (see 3.1).

Even though stars continuously form, MCs tend to be very close to an equilibrium condition, which means that their self-gravity attraction is balanced by internal forces. Their formation and evolution are intrinsically connected with the physical properties of the surrounding ISM and stem from the complex interplay between the turbulence, the action of the magnetic field and the effect of gravitation. Molecular cloud formation is a very complex and still not quite yet understood process. One of the simplest models is the *coagulation model*, firstly proposed by Oort (1954) and then improved by other authors (e.g, Tasker and Tan 2009). According to this model, in the ISM the cold atomic and molecular gas are set up in clouds with a range of different masses. The smaller clouds dissipate energy through collisions and tend to coagulate, forming larger and larger clouds. Eventually, they become big enough to shield themselves from the incident radiation, becoming dominated by molecular gas. However, this model suffers from a major problem, related to the fact that the largest MCs ($10^6 - 10^7 \, \mathrm{M_\odot}$) would be built in $\approx 100 \, \mathrm{Myr}$, that is an order of magnitude larger than the estimate GMCs lifetime[6] (Klessen and Glover, 2014). Overall, MCs are likely to be the highest density regions within a far more extended turbulent flow of gas, rather than discrete objects (*converging or colliding flow model*, Clark et al. 2012).

Generally, MCs are surrounded by a layer of atomic gas that shields the molecules from the interstellar UV radiation field, preventing them from being photodissociated. In the solar vicinity, this layer is observed to have a column density of $N_H \simeq 2 \times 10^{20} \, \mathrm{cm^{-2}}$, corresponding to a visual extinction $A_V \simeq 0.1 \, \mathrm{mag}$ (Bohlin et al., 1978)[7]. The typical hydrogen column density of a GMC is around $10^{22} \, \mathrm{cm^{-2}}$, i.e., $A_V \approx 10$, but variations are observed in the range $10^{21} - 10^{23} \, \mathrm{cm^{-2}}$, i.e., $A_V \approx 1 - 100$ (McKee and Ostriker, 2007). Therefore, in regions with low column densities ($N_H < 10^{20} \mathrm{cm^{-3}}$), photodissociation of H_2 and CO is very efficient and the amount of molecular gas is small. On the other hand, in regions with high column densities, molecular self-shielding and dust shielding dramatically reduce the photodissociation rates of H_2 and CO, allowing the equilibrium molecular fraction to become large. In particular, dust plays a crucial role in the

---

[4]In the solar neighborhood, the mean diameter of a GMC is around 45 pc (Blitz, 1993).

[5]Cores are the densest parts of GMCs where SF occurs.

[6]Estimated by the stars inside them.

[7](Bohlin et al., 1978) found out a relation that links total neutral hydrogen $N(\mathrm{H \ I + H_2})$ to color excess E(B-V): $\langle N(\mathrm{H \ I + H_2})/E(B-V) \rangle = 5.8 \times 10^{21} \, \mathrm{atoms \, cm^{-2} \, mag^{-1}}$. This relation was obtained by analysing Copernicus data, that surveyed the specral region near Lyα in order to trace the column density of interstellar H I toward 100 stars.

formation of H_2. In fact, the simplest way to form H_2 in the ISM would be through the radiative association of two hydrogen atoms:

$$H + H \rightarrow H_2 + \gamma \tag{3.6}$$

Nevertheless, this reaction is quite unlikely since the rate coefficient for this reaction is very small. Another way, that accounts only for a H_2 fractional abundance larger than around $f_{H_2} \approx 10^{-2}$, can be via the ion-neutral reaction pathways:

$$H + e^- \rightarrow H^- + \gamma$$
$$H^- + H \rightarrow H_2 + e^- \tag{3.7}$$

and

$$H + h^+ \rightarrow H^+{}_2 + \gamma$$
$$H_2^+ + H \rightarrow H_2 + H^+ \tag{3.8}$$
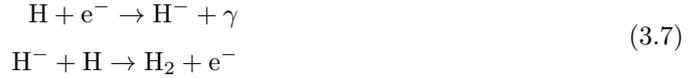
Overall, even though we observe large quantities of H_2 in MCs, the gas-phase formation of H_2 in typical ISM conditions appears to be very inefficient (Klessen and Glover, 2014). What happens is that most of the H_2 in the ISM does not form in the gas-phase, but on the surface of dust grains (Gould and Salpeter, 1963), as Fig. 3.4 shows. Association reactions between adsorbed hydrogen atoms occur readily on grain surfaces in two possible ways:

- diffusive mechanism (Langmuir-Hinshelwood): an H atom is adsorbed by a dust grain and, thanks to its mobility, it scans the surface until it finds another atoms to combine with; the energy released in the reaction that produces H_2 in the ground state is $\Delta E = 4.5 \, \text{eV}$, large enough to overcome the H_2-grain bonds, so the molecule is ejected from the grain surface.

- direct mechanism (Eley-Rideal): an H atom collides with the grain, it combines with another atom and the newly formed H_2 leaves the grain with a certain velocity; this process becomes significant at higher temperatures than diffusive mechanism.

3.3.1 Molecular gas mass

As reported in Sec. 3.1.3, although H_2 is the most abundant molecule, CO molecule is used as tracer of the molecular content. CO formation takes place around $N_H \simeq 10^{21} \, \text{cm}^{-2}$ and from the luminosity of the CO(1-0) transition at $115 \, \text{GHz}$ is possible to derive the H_2 molecular mass. The CO(1-0) rotational transition is chosen because it has a low critical density, around $2.1 \times 10^3 \, \text{cm}^{-3}$, so it traces extended and diffuse regions, which constitutes the majority of the mass (overdense regions have a crucial role in the formation of stars, but account for a little fraction of the mass). Furthermore, the intensity of higher J transitions is more related to the heating source, rather than to the gas mass. The relation between the hydrogen column density
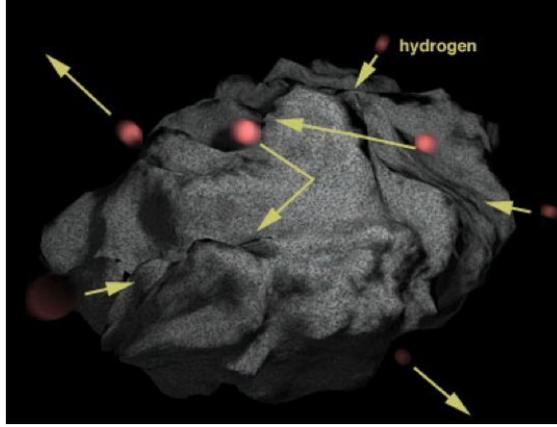
Figure 3.4: *Formation of H_2 on a dust grain (from http://phys.org/news/2014-04-group-interstellar-molecules.html).*

N_{H_2} and the CO(1-0) intensity $I_{\text{CO}(1-0)}$ is:

$$\frac{N(\text{H}_2)}{I_{\text{CO}(1-0)}} = X \tag{3.9}$$

where $X \approx 2 \times 10^{20}\,\text{cm}^{-2}\,\text{K}^{-1}\,\text{km}^{-1}\,\text{s}$ for the Milky Way (MW). Various methods have been used to infer the value of X in the Galaxy, such as:

- subtracting the neutral atomic hydrogen contribution to the total amount of interstellar matter, estimated from observations of γ-rays emitted by cosmic rays interacting with the ISM ($X \simeq 1.9 \times 10^{20}\,\text{cm}^{-2}\,\text{K}^{-1}\,\text{km}^{-1}\,s$, Strong and Mattox 1996);

- comparing the predicted molecular column density map, obtained from complete and unbiased FIR and 21 cm surveys of MW, with the observed CO intensity map ($X \simeq 1.8 \times 10^{20}\,\text{cm}^{-2}\,K^{-1}\,\text{km}^{-1}\,\text{s}$, Dame et al. 2001).

A corollary of Eq. 3.9 arises from integrating over the emitting area and correcting by the mass contribution of heavier elements:

$$M_{mol} = \alpha_{\text{CO}} L_{\text{CO}(1-0)} \tag{3.10}$$

where M_{mol} has units of $M_\odot$ and L_{CO} is usually expressed in units of K km s^{-1} pc^2. $L_{\text{CO}(1-0)}$ is related to the observed integrated flux density in galaxies through the equation:

$$L_{\text{CO}(1-0)} = 3.25 \times 10^7 S d\nu\,\nu_{obs}{}^{-2} D_L{}^2 (1+z)^{-3} \tag{3.11}$$

where $Sd\nu$ is the integrated CO flux in Jy km s^{-1}, ν_{obs} is the observed frequency in GHz and D_L is the luminosity distance in Mpc (Solomon et al., 1997). Thus, α_{CO} is a mass-to-light

ratio, estimated to be $\approx 4.3\,\mathrm{M_\odot}/(\mathrm{K\,km\,s^{-1}\,pc^2})$ for star-forming galaxies similar to the MW and $\approx 0.8\,\mathrm{M_\odot}/(\mathrm{K\,km\,s^{-1}\,pc^2})$ for starburst systems.

The observed mass distribution of GMCs is a power law with a relatively sharp cutoff (McKee and Ostriker, 2007):

$$\frac{dN}{dM} \sim M^{-\alpha} \tag{3.12}$$

with $\alpha \approx 1.5$ (Rathborne et al., 2009). Defining $dN_c(M)$ as the number of GMCs with masses in the range M to $M + dM$, observations of GMCs inside the solar circle are consistent with the mass distribution obtained by (Williams and McKee, 1997):

$$\frac{dN_c(M)}{dlnM} = dN_{cu}\left(\frac{M_u}{M}\right)^{\beta} \tag{3.13}$$

with $\beta = \alpha - 1$ and no GMCs exceeding M_u. The quantity N_{cu} is approximately the number of clouds in the mass range from $M_u/2$ to M_u. Using this notation, the total mass in GMCs is related to the upper and lower mass cutoff ($M_l < M < M_u$, with $M_u \simeq 6 \times 10^6\,M_\odot$ and $M_l \simeq 10^3\,M_\odot$ for the MW) and the power law index by the relation:

$$M_{tot} = \int_{M_l}^{M_u} M \frac{dN_c}{dlnM} dlnM \tag{3.14}$$

which can be also written as

$$M_{tot} = \frac{N_u M_u}{1 - \beta}\left[1 - \left(\frac{M_l}{M_u}\right)^{1-\beta}\right] \tag{3.15}$$

The main implications are that most of the mass in GMCs is in large clouds: a significant fraction is in clouds with mass above $10^6\,\mathrm{M_\odot}$ and more than 80% is in clouds with mass above $10^5\,\mathrm{M_\odot}$. The upper mass limit M_u may be set by the processes that form GMCs out of diffuse gas (McKee and Ostriker 2007, Murray 2011).

3.3.2 Clumps and cores

GMCs are highly clumped: a typical molecule is in a region with a density significantly greater than the average. Furthermore, star-forming clumps are themselves clumpy and contain the cores that will evolve into stars. The typical density of molecular gas in the Galactic plane is $n_H \simeq 3 \times 10^3\,\mathrm{cm^{-3}}$ (Liszt, 1993), but the mean density is considerably less. Given that $M \propto n_H R^3$ and $\bar{N}_H \propto n_H R$, the mean density is:

$$\bar{n}_H = \frac{84}{M_6^{1/2}}\left(\frac{\bar{N}_H}{1.5 \times 10^{22}\,\mathrm{cm^{-2}}}\right)^{3/2}\,\mathrm{cm^{-3}} \tag{3.16}$$

where the column density is normalized to the typical value of Solomon et al. (1987) sample. Consequently, the effective filling factor of the molecular gas is:

$$\phi \equiv \frac{\bar{n}_H}{n_H} = \frac{0.028}{M_6^{1/2}} \left(\frac{3000\,\mathrm{cm}^{-3}}{n_H}\right) \left(\frac{\bar{N}_H}{1.5 \times 10^{22}\,\mathrm{cm}^{-2}}\right)^{3/2} \tag{3.17}$$

Clouds with $M \lesssim 10^3\,\mathrm{M}_\odot$ and typical density of $n_H \sim 3000\,\mathrm{cm}^{-3}$ must have column densities smaller than the Solomon et al. (1987) value, since $\phi \leq 1$. Generally, turbolent clouds are expected to have small filling factor (McKee and Ostriker, 2007).

3.4 Photo-Dissociation Regions

The gas in the diffuse phases of the ISM is almost entirely atomic, whereas MCs are, by definition, dominated by molecular gas. Photo-Dissociation Regions (PDRs, Hollenbach and Tielens 1999) form at the surfaces of MCs, where FUV radiation ($6\,\mathrm{eV} < h\nu < 13.6\,\mathrm{eV}$) due to stellar sources, dominated by the emission of O and B stars, encounters and dissociates the molecular gas. They are the transition zone between the dense, cold molecular gas and the tenuous, warm ionized gas. PDRs are defined as regions whose thermal and chemical structure completely stems from the FUV flux, that has a dramatic effect on the structure and line emission as deep as $A_v \approx 10$ into MCs. As explained in Sec. 3.3, MCs have column densities in the range $10^{22} - 10^{23}\,\mathrm{cm}^{-2}$, and thus PDRs include a significant volume and mass of the dense, opaque clouds (Tielens and Hollenbach, 1985). Studying these environments allows to understand the energy balance of interstellar gas (heating VS cooling) and how processes in ISM work.

3.4.1 Key parameters and physical processes

The key parameters that influence mostly the global characteristics of PDRs are:

- the strength of the FUV incident radiation field, G_0[8], that is related to the total available radiative flux;

- the total hydrogen density, $n = n(\mathrm{H}) + 2n(\mathrm{H}_2)$, that, together with the temperature, plays an important role in the pace of the chemical reactions and the excitation rates of the coolants;

- the metallicity Z, in units of the solar value $\mathrm{Z}_\odot$, that has an influence on the total abundances possible for carbon and oxigen species, affecting the chemical and thermal structure[9];

---

[8]G_0 is expressed in units of an average interstellar flux between $6\,\mathrm{eV} < h\nu < 13.6\,\mathrm{eV}$ of $1.6 \times 10^{-3}\,\mathrm{erg\,cm}^{-2}\,\mathrm{s}^{-1}$ and is referred to as *Habing flux*.

[9]A low metallicity galaxy will have a low dust content, which means that UV photons can penetrate deeper into the cloud, resulting in smaller MCs.

- the spectral shape of the incident radiation field, in function of the colour temperature T_{eff} for black bodies or the frequency slope for power laws, that fixes the distribution of photon flux over energy.

Heating processes

The penetrating FUV photons drive the chemistry and the composition of PDRs through photoionization and photodissociation reactions. They can have an influence on the large number of physical processes that play a role in determining the global properties of PDRs. Broadly speaking, the gas heating always happens through the transfer of kinetic energy to atoms, molecules and ions. The main heating processes in PDRs are (Meijerink and Spaans, 2005):

- photo-electric emission;

- gas-grain collisional heating;

- gas-grain viscous heating[10];

- H_2 photo-dissociation (FUV pumping), followed by collisional de-excitation;

- carbon ionization.

The dominant source of heating to a column density of $10^{22}\,\mathrm{cm^{-2}}$ is photo-electric emission from grains (i.e., Coulomb heating with thermal electrons). What happens is that dust grains and polycyclic aromatic hydrocarbons (PAHs) absorb FUV radiation, that causes the photoelectric ejection of electrons, which eventually heat the gas collisionally (Fig. 3.5). The resulting free electron has an energy $E_e = h\nu - W$, where W is the work done to extract the electron from the grain and $h\nu$ the energy of the incident photon. For instance, $W \simeq 5\,\mathrm{eV}$ for carbonaceous grains, which means that an energy around $E_e \geq 1\,\mathrm{eV}$ is released in the gas in the form of heat.

Furthermore, gas and grain temperature or velocity can be different. In the first case, they can transfer heat through collisions, while in the latter, grains are accelerated relative to the gas because of the radiation pressure, so the resulting drag contributes viscous heating to the gas (Meijerink and Spaans, 2005).

FUV pumping of H_2 consists in absorbing a UV photon ($E > 11.2\,\mathrm{eV}$), pumping the molecule to a bound excited electronic state and then releasing radiation. If this transition occurs into a bound ro-vibrational level in the ground state, the molecule survives. If it occurs into the vibrational continuum, instead, H_2 dissociates and the probability that it happens is around 15%. The UV absorption lines produced by this process are referred to as the *Lyman and Werner bands*. At low densities, the excited (bound) vibrational states can cascade down to the ground vibrational state through the emission of IR photons, while at high densities ($n \gtrsim 10^{4-5}\,\mathrm{cm^{-3}}$),

---

[10]Viscous heating represents the effect of an irreversible process by means of which the work done by a fluid on adjacent layers due to the action of shear forces is transformed into heat.
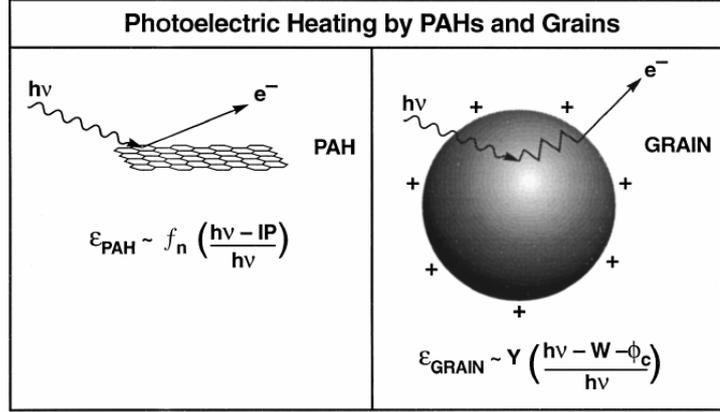
Figure 3.5: *A schematic view of the photoelectric heating mechanism. A FUV photon absorbed by a dust grain leads to the ejection of a photoelectron which diffuses through the grain until it loses all its excess energy due to collisions. For PAHs, the diffusion is not significant. A simple expression for the heating efficiency ε is reported (from Hollenbach and Tielens 1999).*

collisions with atomic H can be an important deexcitation mechanism, resulting in heating the gas and thermalizing the rotovibrational states (Hollenbach and Tielens 1999, Klessen and Glover 2014).

Finally, at the edge of the cloud, there is a large amount of singly ionized carbon, whose photo-electron energy released in an ionization is $\Delta E = 1.06\,\text{eV}$. This heating process can play an important role when the density is higher.

Overall, according to the various characteristics of the gas, some processes can have a higher influence than others. Meijerink and Spaans (2005) carried out a series of models of PDRs, taking into account different values of the density of the gas and radiation field:

- Model 1: $n \approx 10^3\,\text{cm}^{-3}$, $F_{FUV} = 1.6\,\text{erg}\,\text{cm}^{-2}\,\text{s}^{-1}$, $G_0 = 10^3$;

- Model 2: $n \approx 10^3\,\text{cm}^{-3}$, $F_{FUV} = 160\,\text{erg}\,\text{cm}^{-2}\,\text{s}^{-1}$, $G_0 = 10^5$;

- Model 3: $n \approx 10^{5.5}\,\text{cm}^{-3}$, $F_{FUV} = 1.6\,\text{erg}\,\text{cm}^{-2}\,\text{s}^{-1}$, $G_0 = 10^3$;

- Model 4: $n \approx 10^{5.5}\,\text{cm}^{-3}$, $F_{FUV} = 160\,\text{erg}\,\text{cm}^{-2}\,\text{s}^{-1}$, $G_0 = 10^5$.

Although photo-electric emission from grains is generally the dominant source of heating, in case of moderately low density and radiation field (Model 1), viscous heating is about equally important and, if the radiation field increases (Model 2), it contributes more. If the radiation field is lower, but the density value increases (Model 3), carbon ionization appears to be the second most significant process. When both the density and the radiation field are high (Model 4), H_2 pumping becomes the second most important. Furthermore, at high column densities (e.g., $N_H > 10^{22.5}$ cm^{-2}), [O I] 63 μm absorption and gas-grain heating play an important role. In particular, [O I] 63 μm becomes dominant when the density decreases (Models 1 and 2),
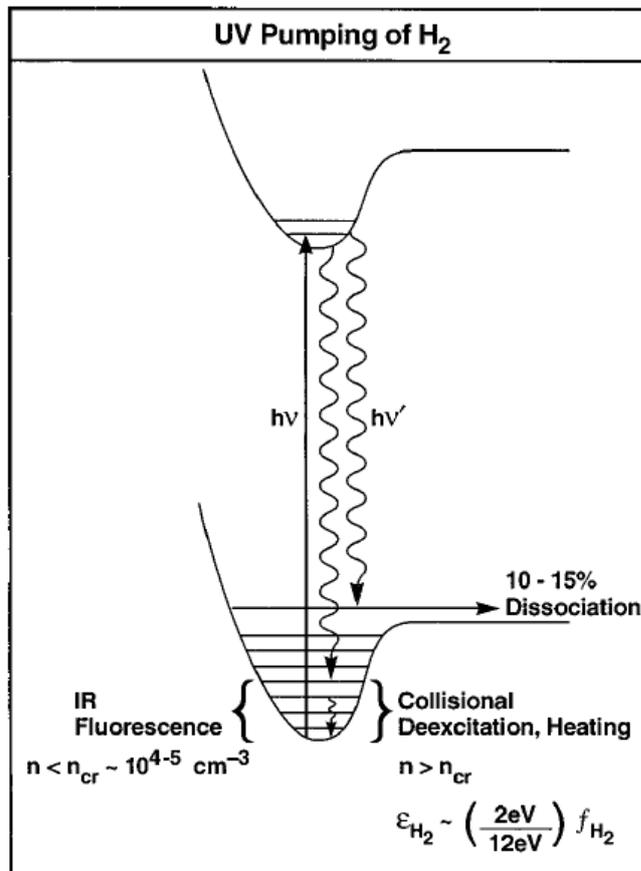
Figure 3.6: *A schematic view of H_2 FUV pumping, dissociation and heating mechanism. ε_{H_2} indicates a simple expression for the heating efficiencies, where f_{H_2} is the fraction of the FUV photon flux pumping H_2. A simple expression for the heating efficiency ε is reported (from Hollenbach and Tielens 1999).*

while gas-grain heating gains in importance at higher density values (Models 3 and 4). Other heating processes have a little impact, contributing less than 10%, but they may play a role in determining the thermal balance.

Cooling processes

Cooling processes fundamentally involve the conversion of kinetic energy into radiation that escapes from the gas. In the ISM, the gas is generally cooled by (Tielens and Hollenbach, 1985):

- radiative cooling, due to infrared fine-structure lines from atoms (e.g., [C I] 609, [C II] 158, [O I] 146 and 63 μm);

- molecular line cooling by warm molecular gas (e.g., CO, H_2, H_2O, OH and CH);

- electronic recombination on dust grains.

Looking at Meijerink and Spaans (2005) models, discussed above, [O I] 63 μm cooling dominates at column densities around $N_H = 10^{21.5}\,\mathrm{cm}^{-2}$. When the density is low (Models 1 and 2), [C II] 158 μm contribution is higher than 10% of the total cooling rate, while at higher densitie values (Models 3 and 4), gas-grain cooling becomes the second most important contribute and gains importance (till 40%) with increasing radiation field (Model 4). At higher column densities, going deep into the cloud, [C I] 609 μm and CO line cooling play an important role, while H_2 contribution never overcomes the 10% of the total cooling rate.

3.4.2   The penetration of FUV radiation

The penetration of FUV radiation is linked to dust absorption and scattering, as well as to the geometry and the global structure of interstellar clouds. In particular, the mean intensity of the FUV continuum flux deep inside semi-infinite slabs is given by the relation:

$$I_\lambda \propto e^{-k\xi_\lambda A_V} \qquad\qquad (3.18)$$

where k is a quantity that depends on the scattering properties[11], ξ_λ is the ratio of the extinction at λ to that at visual wavelength and A_V is the visual extinction measured in magnitudes from the surface. A factor that should be taken into account and that makes the situation far more complex, since it can have a profound influence on the penetration of FUV flux, is that interstellar clouds appear to have a clumpy nature, being inhomogeneous on all scales. Fig. 3.7 shows a clumpy PDR: FUV photons scatter and penetrate through the interclump medium, reaching far deeper points in the region than if the material had an uniform density.

---

[11] At the first order, k is given by the diffusion approximation, $k = \sqrt{3(1-\omega)(1-\omega g)}$, where ω is the albedo and g the mean cosine of the scattering angle.
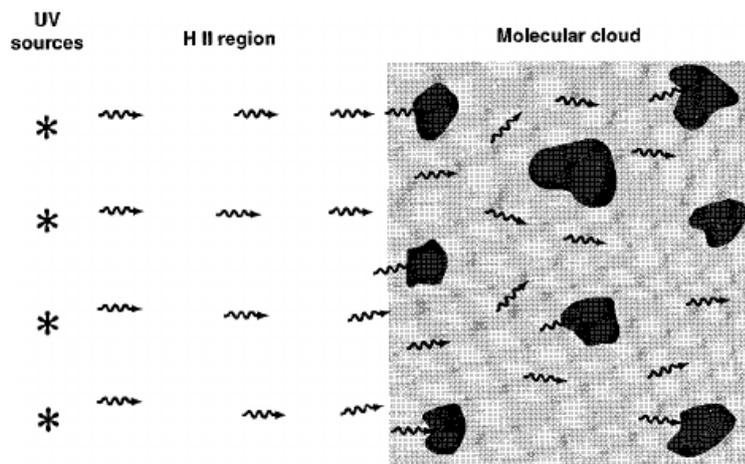
Figure 3.7: *Illustration of a clumpy PDR. FUV photons scatter and penetrate through the inter-clump material and, thanks to its clumpiness, can reach considerable depths.*

3.4.3 Chemical and thermal structure

The intense FUV flux generally is not energetic enough to ionize hydrogen and create HII regions, but can dissociate the molecules and photoionize those heavy elements with ionization potentials smaller than the Lyman limit. It originates the majority of the non-stellar infrared, associated with interstellar dust, and the millimeter and submillimeter CO emission, having an influence even on the chemistry of oxygen, carbon and the ionization fraction.

A scheme of a typical PDR is shown in Fig. 3.8. The ultraviolet flux from nearby hot stars or the interstellar radiation field (ISRF) reaches a neutral cloud of density n. PDRs are often surrounded by HII gas and a thin HII/HI interface, where the Lyman continuum photons are absorbed. As one moves into a PDR, the extinction along the line of sight increases and the incident radiation field is attenuated. The first fundamental change that takes place is the transition of H to H_2. In fact, in the outer part there is a layer filled with H, whose extention depends on the ratio G_0/n and typically is around hydrogen nucleus column densities of $N = 2 - 4 \times 10^{21} \, \mathrm{cm}^{-2}$, followed by an H/H_2 interface, that corresponds to a peak in the far-ultraviolet emission from H_2. Deeper into the PDR, there are a layer of C^+ and one of atomic oxygen. Eventually, as the FUV flux decreases due to dust absorption and H_2 self-shielding, even the transition from C^+ to the neutral state and then to CO occurs. PDRs key parameters, described above, can play a role even in determining the location of the transitions from H to H_2 and from C^+ to CO, which generally appear to be quite sharp. In fact, if a cloud is exposed to a stronger radiation field, the transitions occur deeper, since the photo-dissociation rates are larger. At higher densities, the transitions occur closer to the surface of the cloud, since the recombination rates scale as n^2. Furthermore, the H^+ and O^+ fractional abundances are far higher in the low density models (Meijerink and Spaans, 2005).
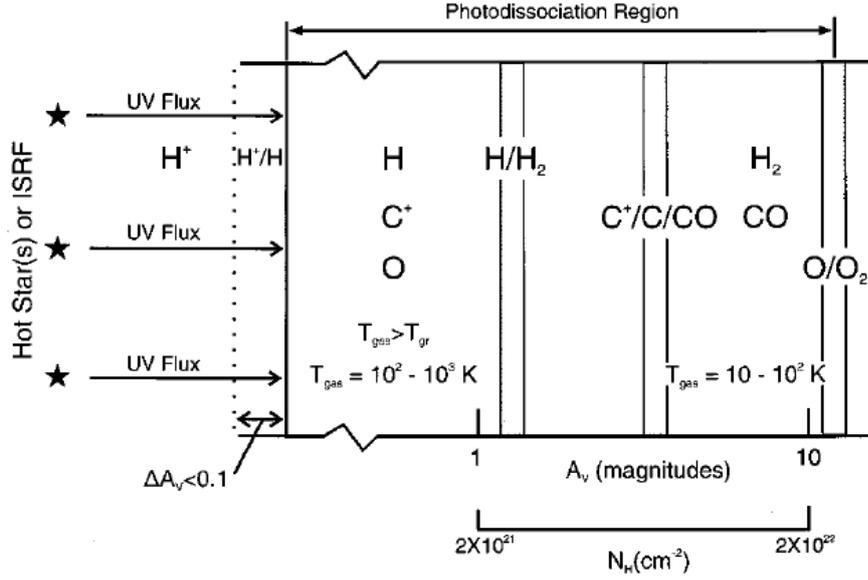
Figure 3.8: *A schematic diagram of a PDR, illuminated from the left and extended from the predominantly atomic surface region ($N_H \approx 2 \times 10^{21}$ cm^{-2}, i.e., $A_V \approx 1$) to the point where O_2 is not appreciably photodissociated ($N_H \approx 2 \times 10^{22}$ cm^{-2}, i.e., $A_V \approx 10$). From Hollenbach and Tielens (1999).*

Ultimately, PDRs consist of gas that is predominantly neutral, characterized by large column of warm O, C, C^+, CO and vibrationally excited H_2, including all the atomic and at least 90% of the molecular gas of the galaxy. An example of PDR is showed in Fig. 3.9, that illustrates a schematic diagram of the derived morphology of M17SW, a star-forming region, where dense clumps are embedded in an interclump medium in the core, surrounded by a more diffuse halo (Hollenbach and Tielens, 1999).

Transition from H to H$_2$

If H_2 is not formed on grain surfaces (see Sec. 3.3), then the important mechanism for H_2 formation is by radiative association reaction

$$H + e^- \rightarrow H^- + h\nu \tag{3.19}$$

followed by the associative detachment reaction

$$H^- + H \rightarrow H_2 + e^- \tag{3.20}$$
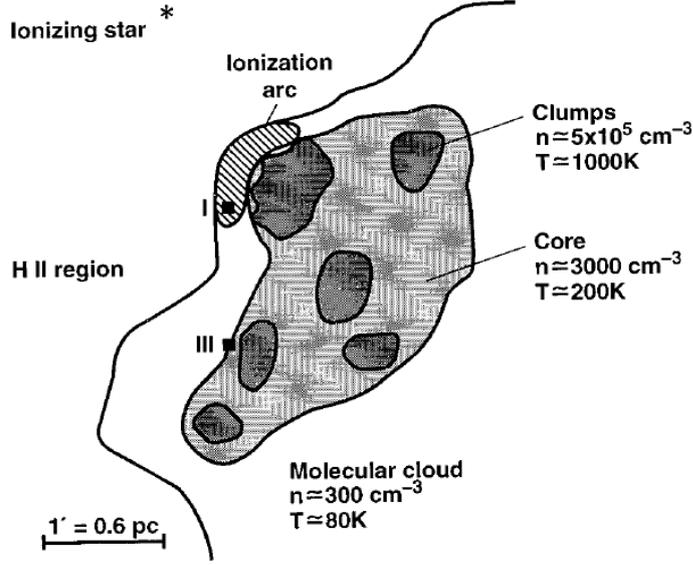
Figure 3.9: *A schematic view of the M17SW PDR region, showing a three component clumpy core and halo model, whose approximate densities and temperatures are reported. The* [O I], [Si II] *and high-level* CO *originate in the high-density clumps, embedded in the interclump medium in the core, whereas the* [C II], [C I] *and low-level* CO *in lower-density interclump gas (Hollenbach and Tielens, 1999).*

Then, in a warm and dense gas, such as in molecular outflows, molecular hydrogen can be collisionally dissociated by

$$H_2 + H \rightarrow H + H + H$$
$$H_2 + H_2 \rightarrow H + H + H_2 0$$

$$(3.21)$$

However, the dominant process capable of destroying H_2 in the local ISM is photodissociation. An important property of molecular hydrogen is *self-shielding*, that stems from the fact that H_2 photodissociation is line-based. What happens is that, in a region with a high H_2 column density, the Lyman-Werner photons are mostly absorbed by H_2 in the outer layers of the region and cannot pass through. This process is efficient as soon as the column density exceeds $N_{H_2} \approx 10^{14} \, cm^{-2}$. In case of an unshielded gas, the total column density of molecular hydrogen depends on the strength of the ISRF (given by G_0 in Habing units) and the density of the gas. In order to reduce the H_2 photodissociation rate by a factor of ten, the visual extinction required is around $A_V \approx 0.65$, which corresponds to a total hydrogen column density $N \approx 10^{21} \, cm^{-2}$. This means that, if G_0/N is small, such as in CNM clouds far away from the regions of massive star formation, the effect of dust shielding becomes important later than self-shielding, while, if G_0/N is large, like in photodissociation regions close to massive stars, dust extinction becomes far more significant (Klessen and Glover, 2014). The location of the H I/H_2 is related to the effect of self-shielding, that dominates on dissociation; therefore the transition zone appears to be very sharp.

Transition from C^+ to CO

Atomic carbon forms via the radiative recombination of C^+

$$C^+ + e^- \rightarrow C + \gamma \tag{3.22}$$

and is destroyed by photoionization

$$C + \gamma \rightarrow C^+ + e^- \tag{3.23}$$

However, the situation is far more complex, since there are various pathways responsible for CO formation. Most of CO located in clouds stems from chemical intermediates, such as hydroxyl (OH), its positive ion (OH$^+$) and their products, or the hydrocarbons CH and CH$_2$ and their positive ions. Then, it can form thanks to the neutral-neutral reaction, whose effectiveness lasts even at low temperatures, since it has no activation energy:

$$C + OH \rightarrow CO + H \tag{3.24}$$

Furthermore, if there is a large amount of C^+, another forming mechanism can be:

$$C^+ + OH \rightarrow CO^+ + H$$
$$CO^+ + H \rightarrow CO + H^+ \tag{3.25}$$

or

$$CO^+ + H_2 \rightarrow HCO^+ + H$$
$$HCO^+ + e^- \rightarrow CO + H \tag{3.26}$$

The rate-limiting step of these reactions is the formation of the initial OH$^+$ ion, that involves directly or indirectly the presence of H$_2$. This means that CO formation via the OH pathway is very sensitive to the amount of H$_2$. As we said before, CO can be formed even thanks to the hydrocarbons CH and CH$_2$, whose pathway shares some common features with the OH pathway, confirming that substantial quantities of CO will form only in regions that are already filled with H$_2$, even though timescales involved in its formation are in general shorter.

The destruction of CO is dominated by photodissociation

$$CO + \gamma \rightarrow C + O \tag{3.27}$$

that occurs when a UV photon with $E > 11.09\,\mathrm{eV}$ causes an electronic state to be excited. Dissociation is typically more likely than decay back to the ground state, therefore the lifetimes of the excited electronic states are very short and, because of Heinsenberg's uncertainty principle, the absorption lines associated with this process are much broader than those of H$_2$, resulting in a far less effective self-shielding (Klessen and Glover, 2014).

3.5 X-ray Dominated Regions

Molecular gas can be exposed to X-rays in several astrophysical environments. AGNs, SNR, fast shocks and X-ray binaries some of the main sources of X-ray photons. Clouds exposed directly to X-ray have a highly ionized surface, resulting in an HII region, followed by a PDR only if the ratio of X-ray flux to gas density is low. The deeper region of the cloud ($N_H \approx 1-2 \times 10^{22} \, \mathrm{cm}^{-2}$) is dominated by the X-ray flux, that has an influence on its heating and chemical composition, creating the so-called *X-ray Dominated Regions* (XDRs, Maloney et al. 1999)). On the other hand, if the cloud is shielded from the direct light of the source, the HII region and the PDR will not be present.

3.5.1 Key parameters and physical processes

In general, the physical and chemical state of clouds illuminated by an X-ray source is not affected by the shape of the X-ray spectrum, but depends mostly on the ratio between the local X-ray energy deposition rate per particle[12], H_X, and the total hydrogen density of the gas, n. This characteristic stems from the chemical and thermal balance, since the molecular destruction and heating rates related to X-ray induced ionization are proportional to $n \, H_X$, while the molecular formation and cooling rates are generally proportional to n^2 times a rate coefficient. As a result, the X-ray deposition rates, and therefore the physical conditions, change slowly with depth.

Another important feature of XDRs is that 2-10 keV photons can penetrate deep in MCs, up to a hydrogen column density of about $10^{24} \, \mathrm{cm}^{-2}$, because of X-ray absorption cross sections scale roughly as E^{-3}, where E is the photon energy (Spaans et al., 2008). These characteristics make XDRs noticeably different from PDRs, where the column density is limited to $N \simeq 10^{21} - 10^{22} \, \mathrm{cm}^{-2}$ by dust absorption and the physical conditions change rapidly with depth because of the dramatic decline of incident UV photons (Maloney et al., 1999). In addition, since X-ray penetrate much deeper into the cloud, high temperatures are maintained to much greater depths.

Heating processes

The heating processes that play a role in the physics and chemistry of XDRs are the following (Meijerink and Spaans, 2005):

- photo-ionisation heating (namely, Coulomb heating with thermal electrons);

- ion-molecule reactions driven by the ionisation degree;

- the ionisation balance of atomic gas due to photo-ionisation reactions driven by X-ray photon and charge transfer.

---

[12]Adopting the X-ray photoelectric cross section per hydrogen nucleus σ of cold neutral matter (Morrison and McCammon, 1983), the local X-ray energy deposition rate per particle is defined as $H_X = \int \sigma(E) F(E) dE$, where $F(E)$ is the local photon energy flux per unit energy interval (Maloney et al., 1999).

The flow chart in Fig. 3.10 provides detailed information about the several mechanisms that make the electrons lose energy. Unlike PDRs, XDRs are mainly heated by direct photoionization of the gas, resulting in the production of fast electrons that lose energy through collisions with other electrons, as well as H and H_2. An important thing to underline is that the ionization rate of hydrogen related to X-ray irradiation of neutral gas is dominated by the *secondary* ionizations, generated by the primary photoelectrons, owing to their large energies around $\approx$ keV.
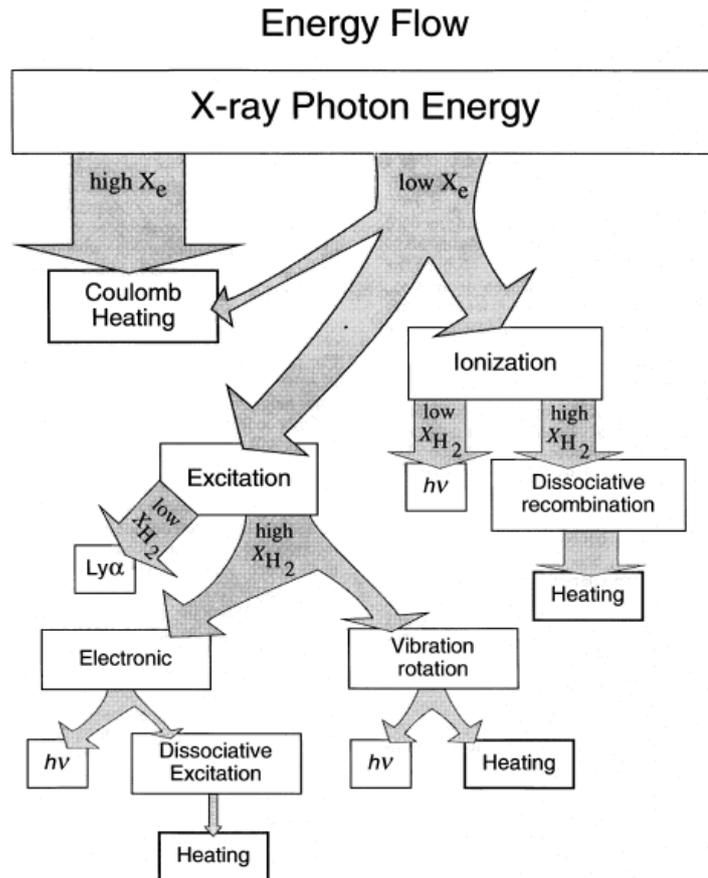
Figure 3.10: *Loss routes for energetic electrons in dense atomic and molecular gas. Note that the widths of the arrows indicate the approximate fractions of the primary photoelectron energy that are deposited in the indicated process, whereas the branching depends on the value of the electron fraction x_e and the molecular hydrogen fraction x_{H2} (Maloney et al., 1999).*

In general, only a fraction of the energy locally deposited by the X-rays will heat the gas, whereas the remainder will excite the atoms and molecules, which then release radiation. Eventually, this radiation is absorbed by dust. The energy deposition and the loss routes for energetic electrons are related to the ionization fraction: if the gas is largely ionized ($x_e \approx 1$), all the primary photoelectron kinetic energy deposited in the gas will result in heating, via Coulomb interactions with the thermal electrons of the cloud; as the ionization fraction declines, heating

via Coulomb losses plummets, and other mechanisms, such as ionization and excitation, gain in importance (e.g., low-ionization limit: $\approx 40\%$ in ionization, $\approx 50\%$ in excitation and the remainder in heating).

Assuming a pure atomic hydrogen gas, only electrons with energy greater than $10.2\,\text{eV}$ (threshold for excitation of Lyα) would excite or ionize the gas, while all of the secondary less energetic ones would heat the gas. This would be the only possible heating process, that becomes negligible at low ionization fraction. Nevertheless, MCs are composed of several molecular species. In this case, the heating efficiency is much larger, because an ion can release its energy into kinetic energy, either dissociatively recombining with an electron or reacting with other species, resulting in heating the gas. For example, the reaction

$$\text{H}_2^+ + \text{H}_2 \rightarrow \text{H}_3^+ + \text{H} \tag{3.28}$$

is exothermic, with a yield of 11 eV (Maloney et al., 1999).

Taking into account Meijerink and Spaans models discussed in Sec. 3.4.1, it is possible to show the characteristics of XDRs and the differences among PDRs and XDRs. The parameters used to describe XDRs are the same of PDRs:

- Model 1: $n \approx 10^3\,\text{cm}^{-3}$, $F_X = 1.6\,\text{erg}\,\text{cm}^{-2}\,\text{s}^{-1}$;

- Model 2: $n \approx 10^3\,\text{cm}^{-3}$, $F_X = 160\,\text{erg}\,\text{cm}^{-2}\,\text{s}^{-1}$;

- Model 3: $n \approx 10^{5.5}\,\text{cm}^{-3}$, $F_X = 1.6\,\text{erg}\,\text{cm}^{-2}\,\text{s}^{-1}$;

- Model 4: $n \approx 10^{5.5}\,\text{cm}^{-3}$, $F_X = 160\,\text{erg}\,\text{cm}^{-2}\,\text{s}^{-1}$.

Fig. 3.11 shows the different heating source as a function of the total hydrogen column density. In general, the heating is all due to X-rays, depending on the ionization fractions. In the case of Models 1, 2 and 4 (H_X/n high to $N_H > 10^{23}\,\text{cm}^{-2}$), where the gas in highly ionized (i.e., $x_e \approx 0.1$), $\approx 70\%$ of the kinetic energy of the non-thermal electrons goes into Coulomb heating. If the ionization fraction is smaller ($x_e \approx 10^{-4}$), ionizing heating contribution becomes significant or even dominant. In Model 3, ionization heating and Coulomb heating are equally important at $N_H < 10^{21.8}\,\text{cm}^{-2}$. Note that in all models, ionization heating dominates especially at high column densities (Meijerink and Spaans, 2005).

There are differences that allows to discriminate between PDRs and XDRs. In fact, as we said in Sec. 3.4.1, PDRs are generally dominated by dust grain photoelectric heating mechanism, while XDRs are heated by the X-ray-induced photoelectrons from the gas. Consequently, in XDRs gas heating is far higher than dust heating, resulting in a larger value of the ratio between cooling lines and IR continuum. In addition, FUV photons in XDRs are capable to ionize other atoms, such as carbon and sulfur, whereas those in PDRs are not energetic enough.
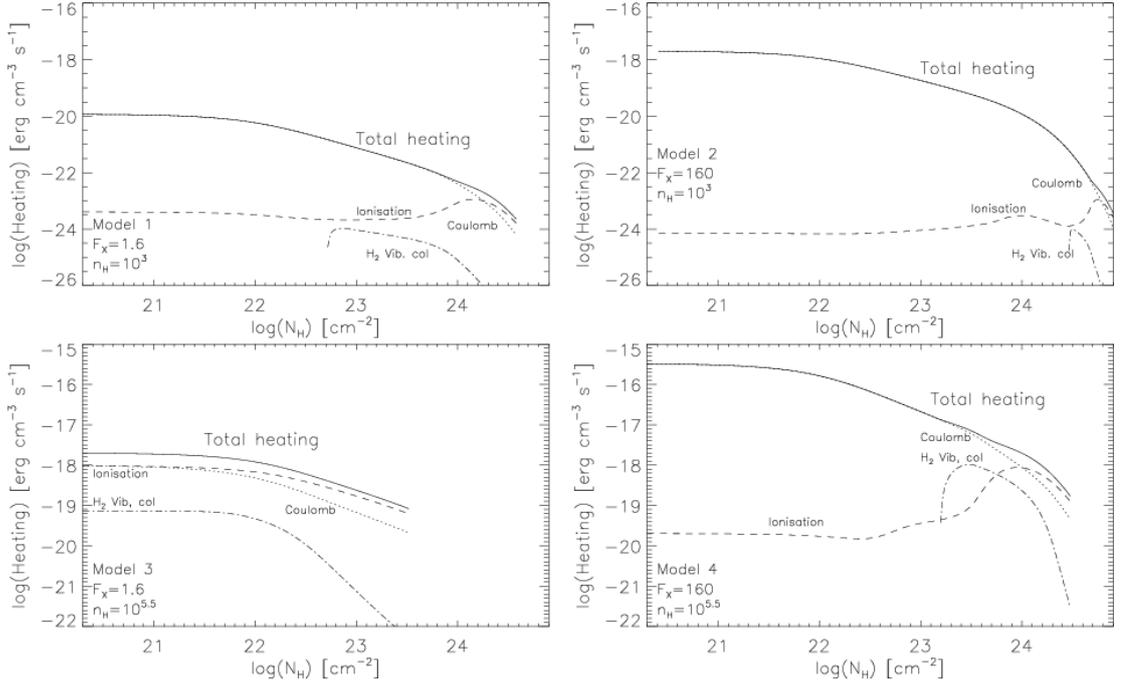
Figure 3.11: *Heating processes for Model 1 (top left), 2 (top right), 3 (bottom left) and 4 (bottom right). From Meijerink and Spaans (2005).*

Cooling processes

As said before in Sec. 3.4.1, cooling processes convert the kinetic energy into radiation, that escapes from the gas. In XDRs, the main cooling processes are (Meijerink and Spaans, 2005), shown in Fig. 3.12:

- emission from meta-stable lines of [C I] 9823, 9850 Åand [O I] 6300 $\mathring{A}$, fine-structure line cooling of [C II] 158 and [O I] 63 and 146 μm and Lyα emission;

- molecular line cooling, such as CO, H_2, H_2O and OH, as well as gas-grain cooling.

At the highest temperatures the dominant process is the collisional excitation of Lyα and forbidden and semiforbidden transitions, such as [O I], [C I], [Fe II] and [Si II], while as the temperature decreases ($T \approx 5000\,\mathrm{K}$) fine-structure transitions of neutral and singly ionized atomic species, such as [O I], [Si II], [C II] and [C I], start to dominate. Other cooling mechanisms are related to the rotational and vibrational transitions of H_2, H_2O, CO and OH.
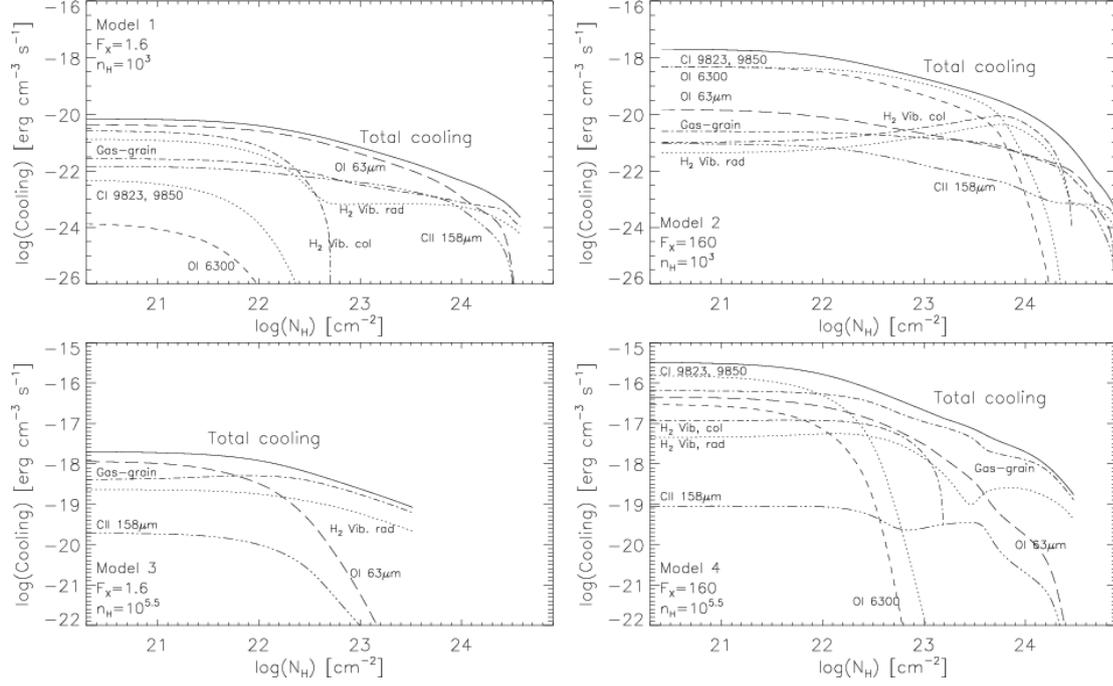
Figure 3.12: *Cooling processes for Model 1 (top left), 2 (top right), 3 (bottom left) and 4 (bottom right). From Meijerink and Spaans (2005).*

3.5.2   Thermal and chemical structure

Fig. 3.13 shows the typical structure of an XDR. The structure of this environment is characterized by a warm ($T \approx 10^4 \, \mathrm{K}$), largely atomic ($\chi_{H_2} \lesssim 10^{-4}$), but partially ionized ($\chi_e \simeq 0.1$) gas located in the outer layers, where the ratio H_X/n is high, and by a cool ($T \approx 10 \, \mathrm{K}$), molecular ($\chi_{H_2} \approx 0.5$) and largely neutral ($\chi_e \simeq 10^{-6}$) gas in the inner ones, with a low H_X/n value (Maloney et al., 1999). Looking at the thermal and chemical structure of an XDR, it can be noticed that the most striking difference with PDRs is the absence of a well-defined transition layer from C^+ to CO, resulting in C and C^+ particles throughout most of the cloud, whereas the transition from atomic to molecular hydrogen happens more gradually (Meijerink and Spaans 2005, Maloney et al. 1999).

Figure 3.13: *A schematic structure of an X-ray dominated region.*

Chapter 4

Interpreting the CO spectral line distribution of NGC 34

Molecular gas plays a significant role in the physics of Luminous Infrared Galaxies, such as NGC 34, providing material for star formation and fueling a possible AGN. Therefore, shedding light on the mechanisms driving the emission from molecular clouds (MCs) in crucial to understand the physical processes ongoing in the central region of these galaxies, where MCs are mainly located. In order to do this, we model the interaction between the radiation and the MCs, using the state-of-the-art photoionization code CLOUDY (Ferland, 2013). The CLOUDY models allow to determine the thermal and chemical balance of molecular gas exposed to X-rays (i.e., XDRs, see Ch. 3) and FUV (i.e., PDRs, see Ch.3) radiation, as a function of depth. Ultimately, we compared the observed data of CO rotational transitions with a grid of PDR and XDR models that span ranges in density, distance from the source and column density, in order to understand which is the dominant radiation field and the physical properties (e.g., density, temperature, radius, mass) of the MCs.

4.1 Observed data

NGC 34 is characterized by a relatively high SFR, equal to $SFR \approx 24.44$ (Gruppioni et al., 2016), and is optically classified as a Seyfert 2 from BPT diagrams (Baldwin et al. 1981, see Ch. 1), with an intrinsic X-ray luminosity in the range 2-10 keV $\approx 10^{42} \, \mathrm{erg \, s^{-1}}$ (Brightman and Nandra, 2011a). Theoretical models show that the spectral energy distribution of the radiation due to star formation and AGN activity has a different influence on the thermal and chemical balance of the ISM, creating PDRs and XDRs (see Ch. 3). The best way to probe deeply into the large column densities of gas and dust is through atomic, nuclear and dust emission in the FIR and (sub-)mm range (Meijerink et al., 2007). Consequently, we take into account CO rotational transitions up to J=13 emitted by the molecular gas, investigating the physical origin of the CO

emission as a function of the rotational transition level J (i.e, the CO spectral line distribution, *CO SLED*). The CO(6-5) transition was observed with ALMA and its analysis and characteristics are described in Ch. 2^1. We have then considered Herschel/SPIRE FTS data (from J=4-3 to J=13-12) and ground-based observations for the lower-J transitions from the literature. The NGC 34 CO SLED, obtained from the final data set, is shown in Fig. 4.1.
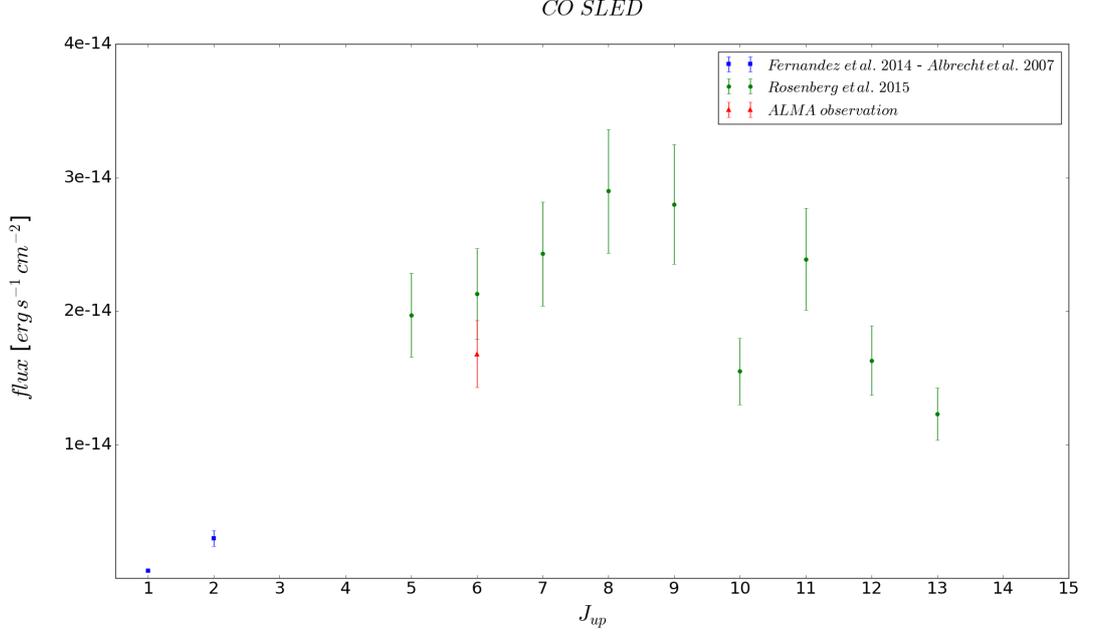

Figure 4.1: *Observed CO SLED of NGC 34. The blue squares represent the low-J transitions CO(1-0) and CO(2-1), the red triangle the CO(6-5) transition observed with ALMA and the green circles the Herschel/SPIRE FTS data from $J_{up} = 4$ to $J_{up} = 13$.*

Having a two different data set for the J=6-5 transition allows a consistency check. CO(6-5) integrated flux obtained with ALMA, though slightly smaller than Herschel/SPIRE measurement, is in good agreement within $1\,\sigma$.

In Tab. 4.1, Herschel/SPIRE FTS data are reported, while Fig. 4.2 shows NGC 34 spectrum, observed by Herschel. The SPIRE/FTS beam size varies between $17''$-$42''$, which correspond to $\approx 7 - 20$ kpc at the distance of NGC 34 ($D_L \simeq 85.7$) Mpc, appearing as a point-like source at this resolution.

Since the flux value of the CO(10-9) transition is far lower than the others, we decided to reject it in the CO SLED-fitting procedure described in the following sections. On the other hand, Tab. 4.2 shows the ground-based observations for the lower-J transitions. The transi-

---

[1]The integrated flux of CO(6-5) is (731 ± 110) Jy km s^{-1}. Taking into account the relationship that links frequency and velocity, given by $\Delta v = \Delta \nu\, c/\nu$, and that $1\,Jy = 10^{-26}$ W m^{-2} Hz^{-1}, where 1 W$= 10^7$ erg s^{-1}, it is possible to obtain the integrated flux in units of erg s^{-1} cm^{-2}. Finally, CO(6-5) integrated flux is $(1.68 \pm 0.25) \times 10^{-14}$ erg s^{-1} cm^{-2} and the emission region is $\approx 200 \times 200$ pc^2.

tion CO(1-0) was observed by the Combined Array for Reasearch in Millimeter-wave Astronomy (CARMA) in 2011, that detected a regularly rotating disk of molecular gas with a diameter of 2.1 kpc. This molecular disk is located in the central region of NGC 34 and appears to be much smaller than the optical disk, as Fig. 4.3 shows (Fernández et al., 2014).

Table 4.1: Herschel/SPIRE FTS data, that cover the $210 - 670 \,\mu$m ($450 - 1440\,$GHz) spectral range. Herschel beam size varies from $17''$-$42''$. The integrated fluxes are in units of $10^{-14}\,$erg s^{-1} cm^{-2} and have a calibration error around the 16% (from Rosenberg et al. 2015).

| Transition	Integrated flux	Transition	Integrated flux
CO(4-3)	-	CO(9-8)	2.80
CO(5-4)	1.97	CO(10-9)	1.55
CO(6-5)	2.13	CO(11-10)	2.39
CO(7-6)	2.43	CO(12-11)	1.63
CO(8-7)	2.90	CO(13-12)	1.23
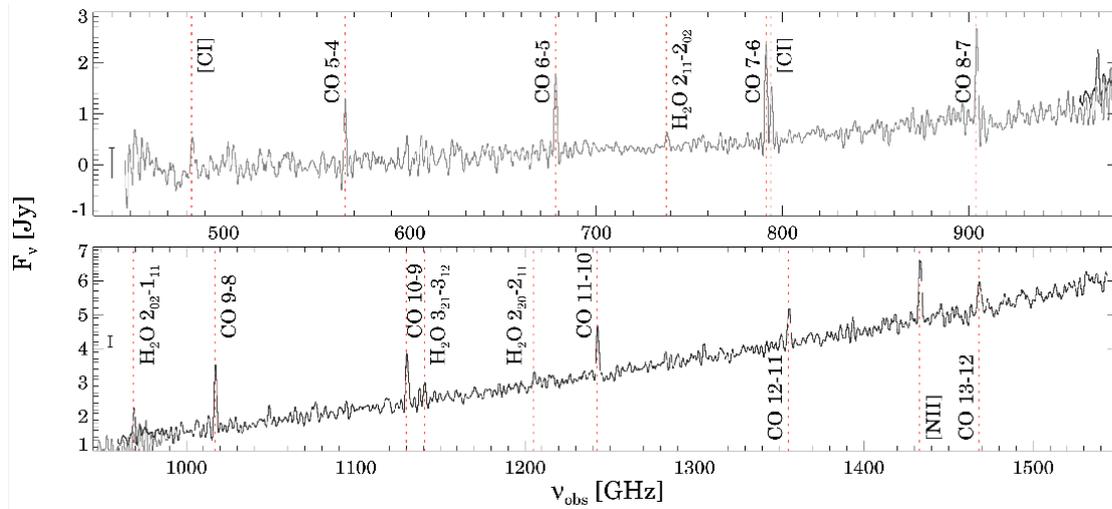
Figure 4.2: *Observed SPIRE/FTS spectra of NGC 34 (from Pereira-Santaella et al. 2014).*

Table 4.2: Ground-based CO data. The CO(1-0) is reported by Fernández et al. 2014, while the CO(2-1) by Albrecht et al. 2007. The integrated flux is in units of $10^{-16}\,\mathrm{erg\,s^{-1}\,cm^{-2}}$.

| Transition	Integrated flux
CO(1-0)	5.72 ± 0.43
CO(2-1)	29.7 ± 5.92
CO(3-2)	-
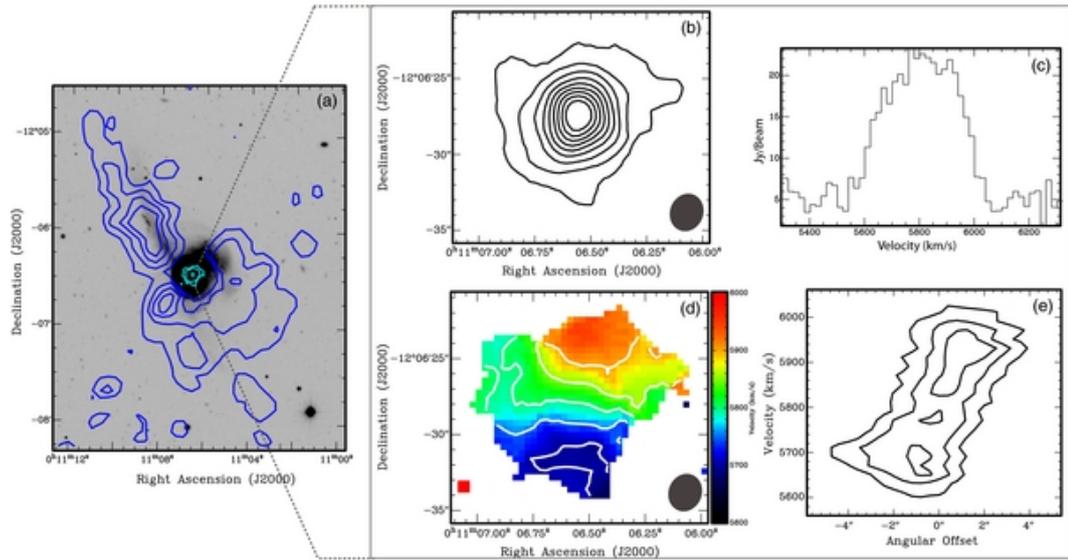
Figure 4.3: *This figure shows the maps of the distribution and kinematics of the CO(1-0) disk at the center of NGC 34. (a) CO(1-0) emission is compared to the optical and HI emission; the cyan contours indicate the CO(1-0) emission, while the blue contours show the HI emission in levels of $(8, 28, 48, 68, 108) \times 10^{19}\,cm^{-2}$, overlaid on an optical image. (b) CO(1-0) integrated flux (Moment 0) contours drawn starting at 5% of the peak, in intervals of 10%. (c) The spectrum of the CO(1-0) emission was obtained by setting a box around the emission, showing how much CO there is in a given velocity bin. (d) Velocity map (Moment 1) overlaid with isovelocity contours drawn in intervals of $50\,km\,s^{-1}$. (e) Position-velocity diagram along the major axis of the optical disk. These figures are taken from Fernández et al. 2014.*

4.1.1   Rotational lines as diagnostics

Molecular rotational lines are characteristic of the physical condition of the ISM and may be used to constrain the gas emission densities and the incident radiation fields. As we have already discussed in Sec. 3.1.3, CO is one of the most abundant molecules in ISM. Therefore, it is considered a good tracer of the molecular gas and a fundamental tool in the study of the star formation energetics and the effects of AGNs (Mashian et al., 2015). In Tab. 4.3, the main properties of CO transitions are reported.

Table 4.3: In this table the fundamental parameters are summarized for CO rotational transitions up to $J_{up} = 13$. E.P. is the excitation potential of the upper level above ground. A is the Einstein coefficient related to spontaneous decay from an upper to a lower level. The critical density is the density at which the rate of the collisional depopulation of a quantum level equals the spontaneous radiative decay rate (Carilli and Walter, 2013).

Transition	E.P. $[K]$	λ $[\mu m]$	ν $[GHz]$	A $[s^{-1}]$	n_{crit} $[cm^{-3}]$
J=1-0	5.5	2601.0	115.3	7.2×10^{-8}	2.1×10^3
J=2-1	16.6	1300.0	230.5	6.9×10^{-7}	1.1×10^4
J=3-2	33.2	867.0	345.8	2.5×10^{-6}	3.6×10^4
J=4-3	55.3	650.3	461.0	6.1×10^{-6}	8.7×10^4
J=5-4	83.0	520.2	576.3	1.2×10^{-5}	1.7×10^5
J=6-5	116.2	433.6	691.5	2.1×10^{-5}	2.9×10^5
J=7-6	154.9	371.7	806.7	3.4×10^{-5}	4.5×10^5
J=8-7	199.1	325.2	921.8	5.1×10^{-5}	6.4×10^5
J=9-8	248.9	289.1	1036.9	7.3×10^{-5}	8.7×10^5
J=10-9	304.2	260.2	1152.0	1.1×10^{-4}	1.1×10^6
J=11-10	364.0	237.0	1267.0	1.4×10^{-4}	$> 10^6$
J=12-11	431.3	217.0	1382.0	1.9×10^{-4}	$> 10^6$
J=13-12	503.0	200.4	1496.9	2.4×10^{-4}	$> 10^6$

The effective critical densities for excitation rise from 2.1×10^3 for CO(1–0) to $\approx 10^6\,\mathrm{cm}^{-3}$ for $J_{up} \simeq 13$. This makes CO(1-0) the most sensitive to the total gas reservoir (see Sec. 3.3 for a complete discussion), including more diffuse components, whereas $J_{up} > 1$ transitions are increasingly sensitive to the denser star-forming gas (Daddi et al., 2015). Furthermore, the lowest three rotational transitions of CO have low excitation potentials, so they trace the cooler gas component ($T \simeq 10 - 20\,K$), and can be relatively easily observed with ground-based radio and submillimeter telescopes in many local galaxies.

On the other hand, FIR CO rotational lines, with $J_{up} \geq 13$, arise from states $500 - 7000\,K$ above ground. These transitions trace the warmer and denser molecular gas in the center of galaxies and are difficult to excite solely with star formation. Therefore, they represent the best

way to test models that distinguish between AGN and starburst systems (Mashian et al., 2015).

4.2 Model description

The grid of PDR and XDR models adopted in these thesis have been taken from L. Vallini et al. (in Preparation) an they are obtained with CLOUDY (Ferland, 2013), a photoionization code designed to simulate conditions in ISM under a broad range of conditions. CLOUDY makes prediction of intensities of a very large number of spectral lines. The input to the CLOUDY code are:

- the shape and intensity of the external radiation field striking a cloud;

- the chemical composition and grain content of the gas;

- the geometry of the gas, including its radial extent and the gas density dependence on radius.

The incident photons represent the external radiation field emitted by the central object (i.e., the collective light of stars in PDRs and an X-ray point-like source in XDRs) that impinges the illuminated face of the cloud and is assumed as the only source of heat and ionization (see Fig. 4.4).
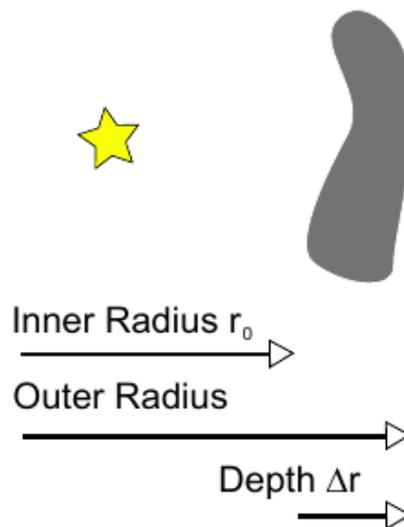

Figure 4.4: *The star represents the source of ionizing radiation, while the shaded area represents the cloud (from Ferland 2013).*

In our PDR models, the SED of the stellar component is calculated using the stellar population synthesis code Starburst99, assuming a Salpeter Initial Mass Function in the range 1-100

$M_\odot$, a solar metallicity and the SFR of NGC 34, as found by Gruppioni et al. 2016. In our XDR models, the external radiation field is indicated as an intensity, namely the energy incident upon a unit area of a cloud, obtained from the X-ray luminosity in the range 2-100 keV. In general, the grain content of the gas is modelled, assuming the MW dust-to-gas ratio ($\approx$ 160, e.g., Zubko et al. 2004), whereas the region between the heating source and the clouds is assumed to be dust-free.

The grid of models were constructed at three different typical distances from the source: 125, 250 and 500 pc. Consequently, in PDR models, the radiation fields at the cloud surface are:

- $G_0 = 1.76 \times 10^4$ at $r = 125\,\mathrm{pc}$;

- $G_0 = 4.39 \times 10^3$ at $r = 250\,\mathrm{pc}$;

- $G_0 = 1.10 \times 10^3$ at $r = 500\,\mathrm{pc}$;

where $G_0 = 1$ corresponds to a flux equal to $1.6\,\mathrm{erg\,cm^{-2}\,s^{-1}}$. In XDR models, instead, the values of the radiation field at the cloud surface are:

- $r = 125\,pc$, $F_X = 3.91\,\mathrm{erg\,s^{-1}\,cm^{-2}}$;

- $r = 250\,pc$, $F_X = 0.97\,\mathrm{erg\,s^{-1}\,cm^{-2}}$;

- $r = 500\,pc$, $F_X = 0.24\,\mathrm{erg\,s^{-1}\,cm^{-2}}$.

Concerning PDRs, we have created models with four different atomic H densities ($10^{2.5}$, $10^{3.5}$, $10^{4.5}$, 10^5 cm^{-3}), while we consider only three atomic H densities for XDRs ($10^{3.5}$, $10^{4.5}$, $10^{5.5}$ cm^{-3}).

The code computes the radiative transfer through the slab up to a hydrogen column density $N = 10^{23}\,\mathrm{cm^{-2}}$, defined as:

$$N = \int \left\{ n(\mathrm{HI}) + n(\mathrm{H^+}) + 2n(\mathrm{H_2}) + \Sigma n(\mathrm{H_{other}}) \right\} f(r)dr \ \ [\mathrm{cm^{-2}}] \tag{4.1}$$

where $f(r)$ is the filling factor. This stopping criterium is chosen for two main reasons (Vallini et al., 2016):

- to cover the whole range of column densities of the clouds responsible for the observed CO emission;

- to fully sample the molecular part of the illuminated slab, typically located at $N_H \gtrsim 2 \times 10^{22}\,\mathrm{cm^{-2}}$.

Increasing values of N correspond to larger and larger depths within the molecular gas.

Ultimately, each model represents an individual cloud, assumed to have a radius equal to the depth reached, with a constant density and a fixed distance from the source.

4.2.1 PDR models

In this section, we discuss how PDR models change as a function of the radiation field and the density.

If a cloud is exposed to a stronger radiation field[2], CO transitions (originating from molecular gas phase) occur at higher depths, since the FUV photon dissociation molecules penetrate deeper into the cloud. At higher density values (e.g., $n \simeq 10^{3.5}\,\mathrm{cm^{-3}}$) the transitions occur closer to the surface of the cloud, since the recombination scales as n^2. In Fig. 4.5, we show three PDR models that reproduce CO transitions in a gas with a density of $n = 10^{3.5}\,\mathrm{cm^{-3}}$, located at $r = 125\,\mathrm{pc}$, $r = 250\,\mathrm{pc}$, $r = 500\,\mathrm{pc}$ from the source, respectively. In the x-axis there is the number of the transition considered (J_{up}), while in the y-axis the integrated flux of the modelled CO transitions. As the distance from the source increases, the radiation field decreases and the CO SLED peaks at lower and lower J_{up}.
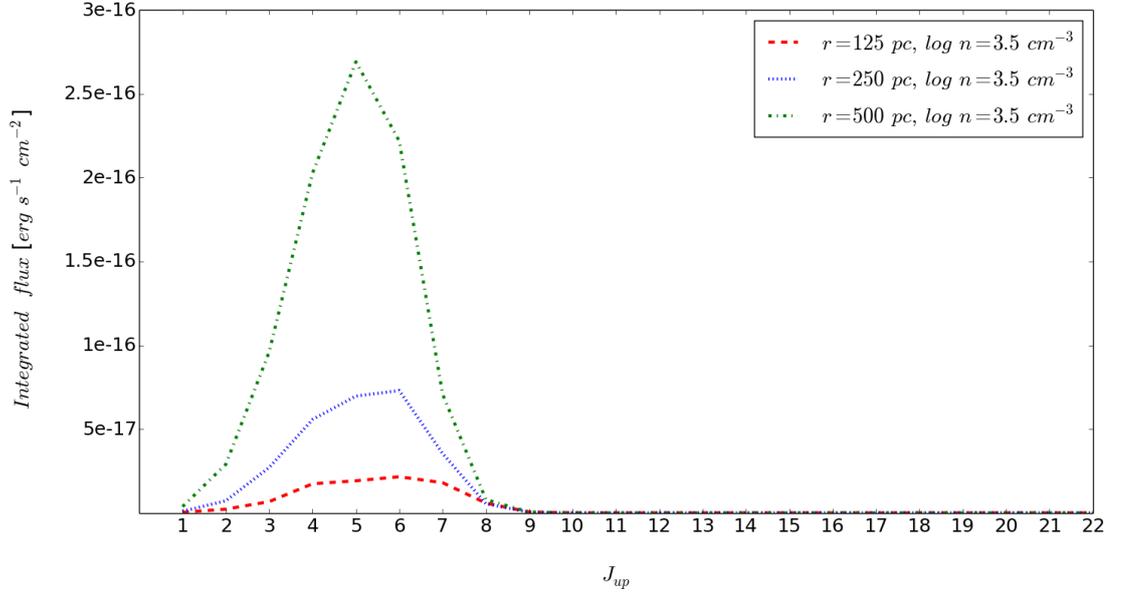

Figure 4.5: *PDR models as a function of the radiation field. The three models describe a gas with a density of $n = 10^{3.5}\,cm^{-3}$, at three different distance from the source: $r = 125\,pc$ (in red), $r = 250\,pc$ (in blue), $r = 500\,pc$ (in green).*

Fig. 4.6, instead, shows four PDR models that reproduce CO transitions in a gas located at $500\,\mathrm{pc}$ from the source, with a density of $10^{2.5}, 10^{3.5}, 10^{4.5}, 10^{5}\,\mathrm{cm^{-3}}$, respectively. As the density increases, the CO SLED peaks at higher J_{up} (see Tab. 4.3).

---

[2]$G_0 \simeq 10^4$ at $r = 125\,\mathrm{pc}$ with respect to $G_0 \simeq 10^3$ at $r = 500\,\mathrm{pc}$.
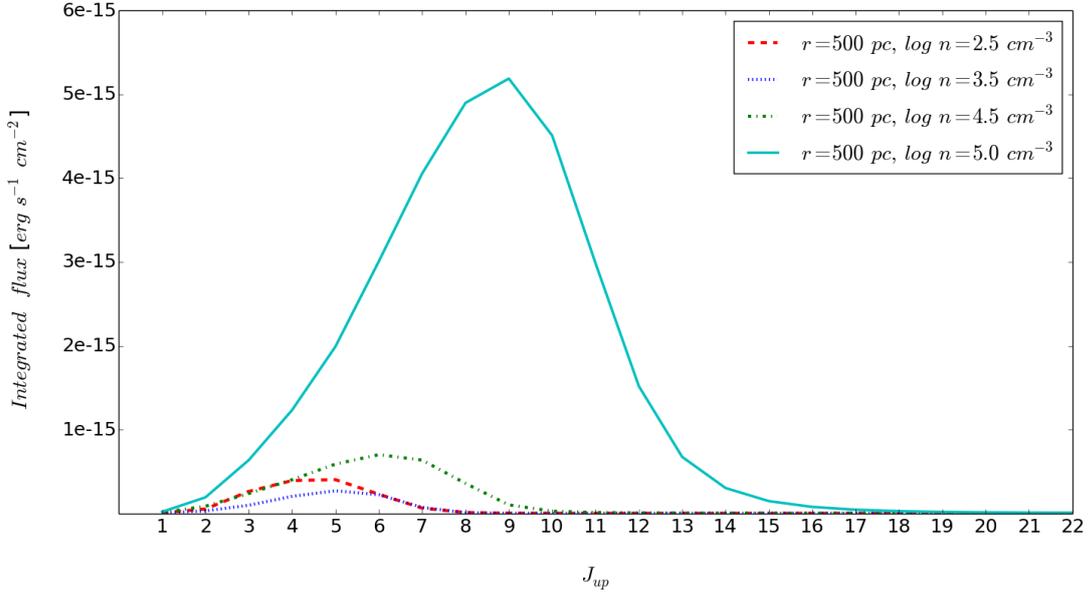
Figure 4.6: *PDR models as a function of the density. The four models describe a gas located at 500 pc from the source, with a density of $10^{2.5}\ cm^{-3}$ (in red), $10^{3.5}\ cm^{-3}$ (in blue), $10^{4.5}\ cm^{-3}$ (in green), $10^{5}\ cm^{-3}$ (in cyan), respectively.*

Fig. 4.7 and Fig. 4.8 show how the temperature changes as a function of the distance from the source and the density, respectively. In the x-axis there is the depth of the cloud in cm, while in the y-axis the temperature in K. As Fig. 4.7 shows, the temperature decreases moving deeper into the cloud. More precisely, Fig. 4.7 illustrates three PDR models that reproduce CO transitions in a gas with a constant density of $n = 10^{2.5}\ \mathrm{cm}^{-3}$, located at $r = 125\,\mathrm{pc}$, $r = 250\,pc$, $r = 500\,\mathrm{pc}$ from the source, respectively. As the distance from the source increases, the FUV flux at the cloud surface decreases ($\propto r^{-2}$) and the temperature drops at lower column densities into the MCs. Indeed, a lower radiation field (i.e., a lower number of incident photons) can heat the gas, through photoelectric effect in dust grains. On the other hand, keeping constant the distance (see Fig. 4.8), the higher the density, the smaller the depth into the MCs at which the temperature drops. This is because the higher is n, the higher id the FUV optical depth, hence the photoelectric heating caused by FUV photons affects the MC at shorter depths.
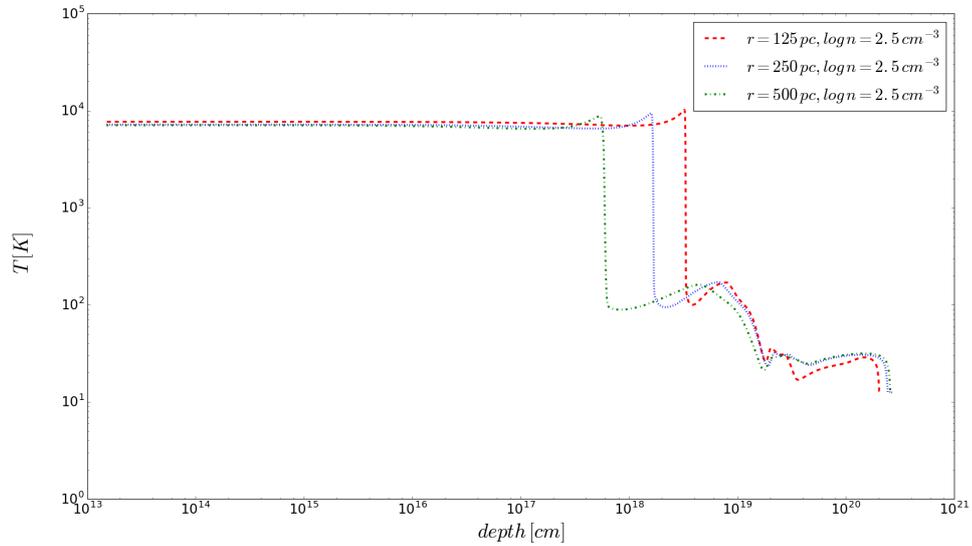
Figure 4.7: *PDR temperature as a function of the radiation field. The three models describe a gas with a density of $n = 10^{2.5}\ cm^{-3}$, at three different distance from the source: $r = 125\,pc$ (in red), $r = 250\,pc$ (in blue), $r = 500\,pc$ (in green).*
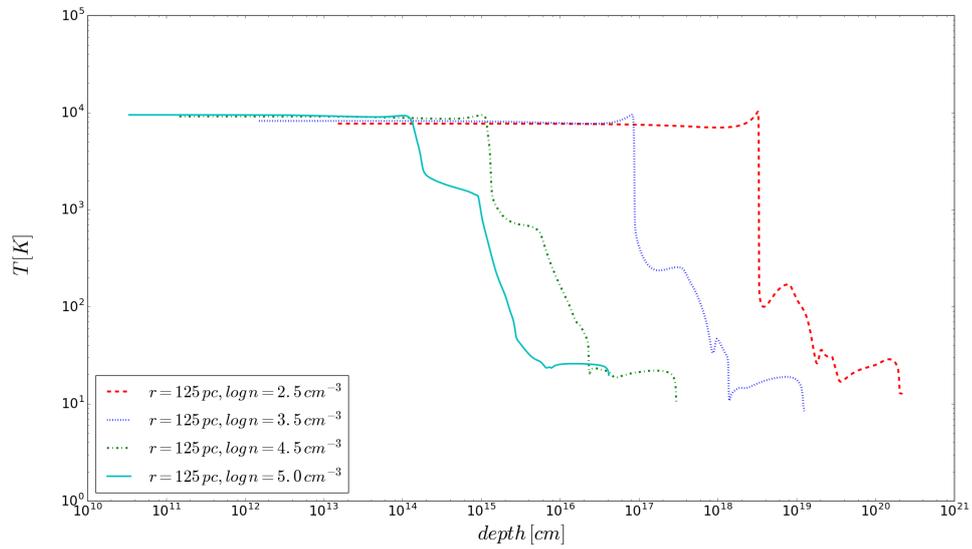

Figure 4.8: *PDR temperature as a function of the density. The four models describe a gas located at 125 pc from the source, with a density of $10^{2.5}\ cm^{-3}$ (in red), $10^{3.5}\ cm^{-3}$ (in blue), $10^{4.5}\ cm^{-3}$ (in green) and $10^{5}\ cm^{-3}$ (in cyan), respectively.*

4.2.2 XDR models

In this section, we discuss how XDR models change as a function of radiation field and density.

As said in Sec. 4.2.1 for PDRs, keeping fixed the distance, as the density increases, the CO SLED peaks at higher J_{up} (Fig. 4.10). A noticeable feature is that, at fixed n, XDR CO SLEDs peak at higher J_{up} with respect to PDR CO SLEDs (see Fig. 4.6).
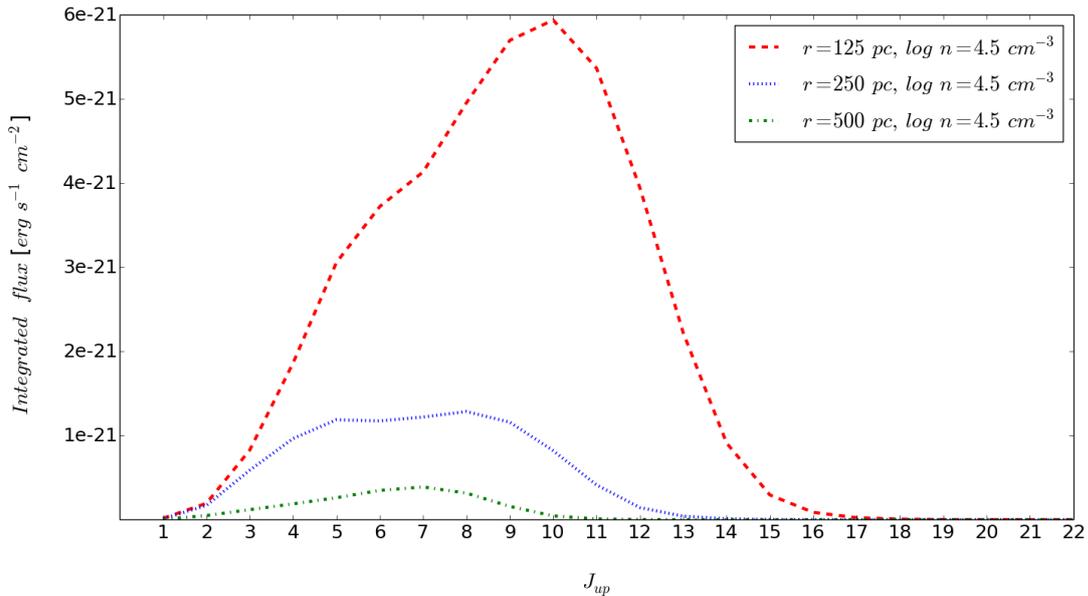

Figure 4.9: *XDR models as a function of the radiation field. The three models describe a gas with a density of $n = 10^{4.5}\ cm^{-3}$, at three different distance from the source: $r = 125\ pc$ (in red), $r = 250\ pc$ (in blue), $r = 500\ pc$ (in green).*

Fig. 4.11 and Fig. 4.12 show how the temperature changes as a function of the distance from the source and the density, respectively. A closer look at these figures reveals that what said before in Sec. 4.2.1 for PDRs is analogous for XDRs. Note that the cross section (σ) of X-rays is smaller than that of FUV, being $\sigma \propto E^{-3}$. This is the reason why X-ray photons penetrate deeper into the cloud, keeping the temperature higher at larger column densities into the MCs, as the comparison between Fig. 4.7 and Fig. 4.9 shows. Moreover, X-ray heating efficiency (i.e., the fraction of initial energy that goes into gas heating) can be $> 70\%$, unlike PDRs, where about 0.5-3 % of the photon energy goes into gas heating.
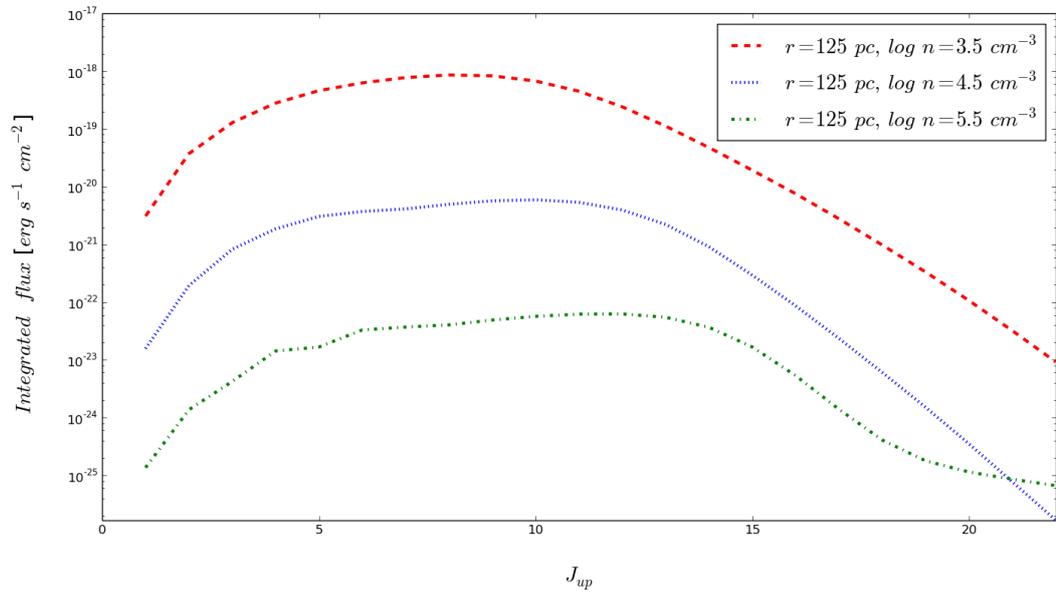
Figure 4.10: *XDR models as a function of the density. The three models describe a gas located at 125 pc from the source, with a density of $10^{3.5} \, cm^{-3}$ (in red), $10^{4.5} \, cm^{-3}$ (in blue), $10^{5.5} \, cm^{-3}$ (in green), respectively.*
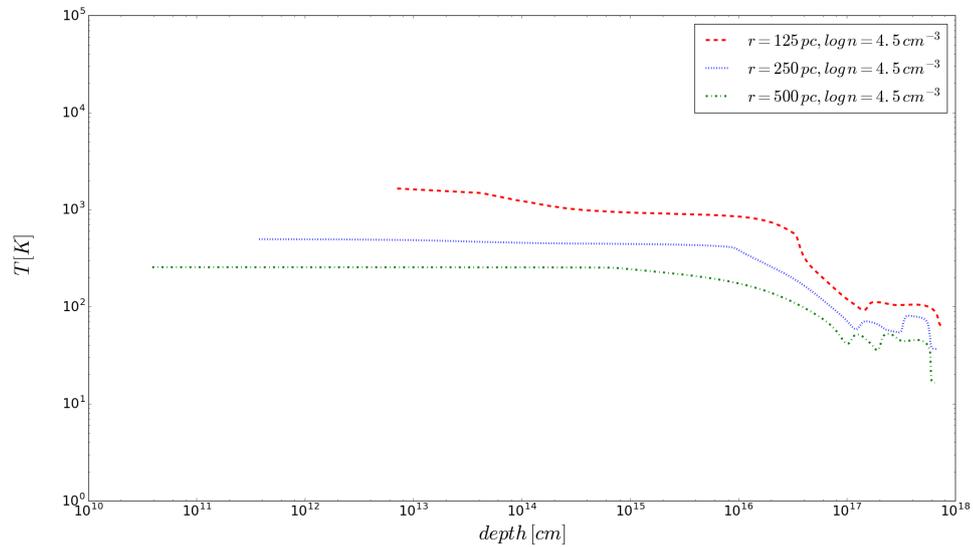
Figure 4.11: *XDR temperature as a function of the radiation field. The three models describe a gas with a density of $n = 10^{4.5} \, cm^{-3}$, at three different distance from the source: $r = 125 \, pc$ (in red), $r = 250 \, pc$ (in blue), $r = 500 \, pc$ (in green).*
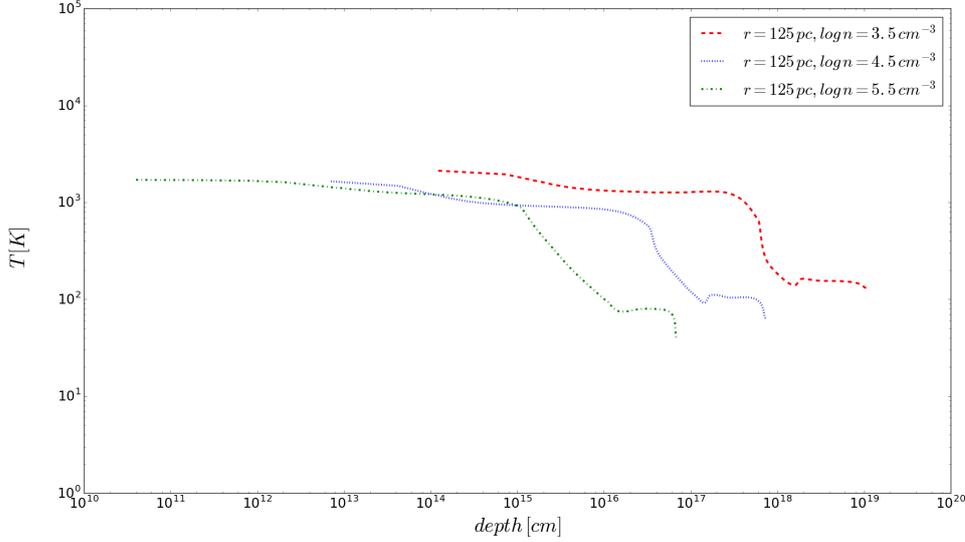
Figure 4.12: *XDR temperature as a function of the density. The three models describe a gas located at 125 pc from the source, with a density of $10^{3.5}$ cm^{-3} (in red), $10^{4.5}$ cm^{-3} (in blue), $10^{5.5}$ cm^{-3} (in green), respectively.*

4.3   CO SLED fitting

In order to model the observed CO emission in NGC 34, we consider the molecular gas in the galaxy as a collection of clouds with different densities, radii and distances from the radiation source (either SF and AGN). The output of a single MC model is the multiplied by a factor that represents the number of that particular type of clouds. A constrain to the number of clouds is the filling factor ϕ (Eq. 3.17): the volume occupied by the clouds must be smaller than the region considered.

It is currently impossible to resolve individual clouds in extragalactic sources. Telescopes, such as Herschel (whose beam size varies from $17''$-$42''$ for NGC 34 observed CO transitions, i.e. $\approx 7 - 20$ Kpc, taking into account a $D_L \simeq 85.7$ Mpc), measure the combined emission from a large ensemble of MCs. ALMA resolution is far higher instead ($0.22''$ for CO(6-5), i.e. ≈ 100 pc), and allows to constrain the region of the emission of the observed transition, but cannot resolve individual clouds anyway. As a consequence, it is impossible to use a single model cloud solution to describe the observed molecular lines, which means that more complicated solutions involving two or more model clouds, with different densities and incident radiation fields, are needed (Meijerink et al., 2007).

4.3.1 Low-J transitions

As discussed in Sec. 4.1.1, low-J CO transitions are generally produced in the coldest and more diffuse molecular gas. The observation of the transition CO(1-0) in NGC 34, reported by Fernández et al. 2014, reveals an extended disk of molecular gas in the central region of the galaxy with a diameter of 2.1 kpc (see Sec. 4.1). Moreover, in diffuse clouds ($n \simeq 10^2 - 10^3$ cm^{-3}), even at the point furthest from the cloud edge, the low density causes a small decline in temperature (see Fig. 4.8). Consequently, in case of a high incident radiation (e.g., $r = 125$ pc), the gas reaches very high temperatures and a highly ionized state throughout. Under these conditions warm CO gas is present, but only in small amounts, resulting in very weak line emission (Meijerink et al., 2007). This is the reason why we focused our attention on PDR models reproducing MCs at $r = 500$ pc (low radiation field) from the radiation source and with low densities $n = 10^{2.5}$ cm^{-3}. We chose a distance of $r = 500$ pc also because, as we have shown in Sec. 4.2.1, as the distance increases, the CO SLED peak moves to lower J.

At constant n, the column density N increases with the depth. The depth of the gas slab is essentially the radius of the cloud responsible for the emission. Fig. 4.13 shows four models of PDR, that represent clouds located at $500\,pc$ from the source, with density $n = 10^{2.5}$ cm^{-3}, at four different values of depth ($l \simeq 4.5 - 6.6 - 10.4 - 16.4 \times 10^{19}$ cm, i.e. $l \simeq 14.7 - 21.4 - 33.7 - 53.1$ pc) and column density $N \simeq 1.7 - 2.5 - 3.9 - 6.2 \times 10^{22}$ cm^{-2}). In the solar neighborhood, the mean radius of a GMC is ≈ 23 pc (Blitz, 1993). This means that column densities with values $N \gtrsim 3 \times 10^{22}$ cm^{-2} are unlikely.
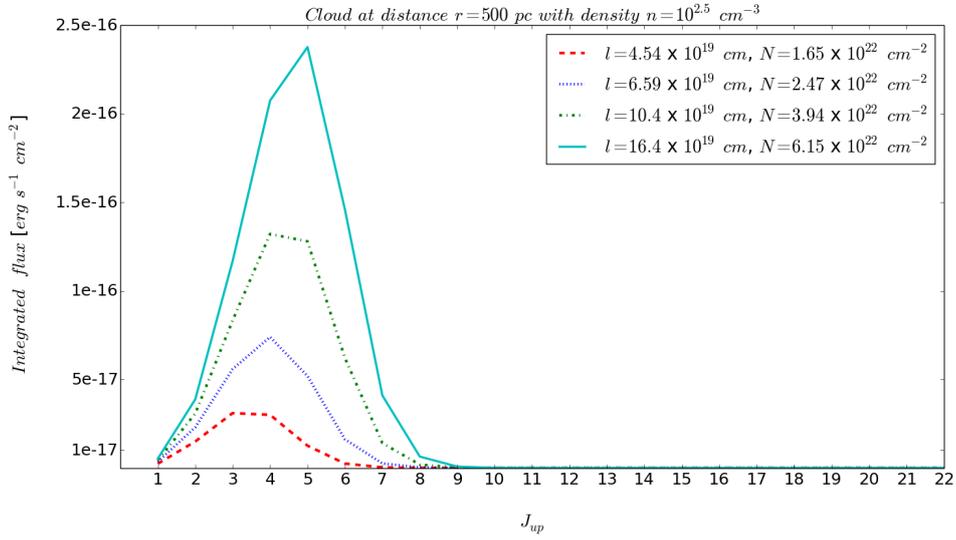

Figure 4.13: *PDR models as a function of the depth and column density. The four models describe a gas located at 500 pc from the source, with a density of $10^{2.5}$ cm^{-3}, at four different values of depth ($l \simeq 4.5 - 16.4 \times 10^{19}$ cm) and column density ($N \simeq 1.7 - 6.2 \times 10^{22}$ cm^{-2}), showed in red, blue, green and cyan, respectively.*

4.3.2 Mid- and high-J transitions

Mid- and high-J transitions, instead, are associated to a warmer and denser gas. A challenge is presented by the highest CO lines, at $J_{up} = 13$ and $J_{up} = 12$, arising from levels 503 and 461 K above the ground state (see Sec. 4.1.1). Generally, PDR models fails at reproducing these transitions, since the resulting gas temperatures are too low enough for significant population of the $J > 10$ levels. (van der Werf et al., 2010). Consequently, these lines require the presence of another excitation component, which can be either a high excitation PDR (with high density, e.g., $n = 10^5 \, \mathrm{cm}^{-3}$) or an XDR. Therefore, we tried two different approaches:

- we take into account only the starburst component, using a high density PDR model (hereafter *Model 1*);

- we consider also the X-ray radiation generated by the AGN, using a high density XDR model (hereafter *Model 2*).

Model 1

Unlike Herschel, whose beam is too large to resolve the emission region, ALMA allows to constrain it: CO(6-5) line emission comes from a central region of $200 \times 200 \, \mathrm{pc}^2$ (see Ch. 2). Therefore, among the available PDR models, we chose the one that represents clouds located at 125 pc from the source[3]. As explained in Sec. 4.1.1, CO SLED peak moves to higher J values, as the density increases. In order to reproduce the observed data, a high density PDR with $n = 10^5 \, \mathrm{cm}^{-3}$ is needed (Fig. 4.14), since the observed CO SLED peaks at $J_{up} = 8$ (Fig. 4.1). To verify that this model agrees to the observed data, we compared the observed line ratios CO(8-7)/CO(7-6)= 1.19 and CO(12-11)/CO(9-8)= 0.58 with the corresponding ratios of PDR models with $r = 125 \, \mathrm{pc}$, making the contours as a function of the density n and the column density N, showed in Fig. 4.15 and 4.16, respectively. A closer look at these figures reveals that a model with density $n \simeq 10^5 \, \mathrm{cm}^{-3}$ and a column density $N \simeq 10^{23} \, \mathrm{cm}^{-2}$ reproduce both the observed ratios.

Model 2

Fig. 4.17, 4.18 and 4.19 show the available XDR models. As explained before in Sec. 4.2, the values of the radiation field considered in out models are:

- $r = 125 \, \mathrm{pc}$, $F_X \simeq 3.91 \, \mathrm{erg} \, s^{-1} \, \mathrm{cm}^{-2}$;

- $r = 250 \, \mathrm{pc}$, $F_X \simeq 0.97 \, \mathrm{erg} \, s^{-1} \, \mathrm{cm}^{-2}$;

- $r = 500 \, \mathrm{pc}$, $F_X \simeq 0.24 \, \mathrm{erg} \, s^{-1} \, \mathrm{cm}^{-2}$.

---

[3]Among the three available distance values, only $125 \, pc$ is consistent with the information given by ALMA observation.
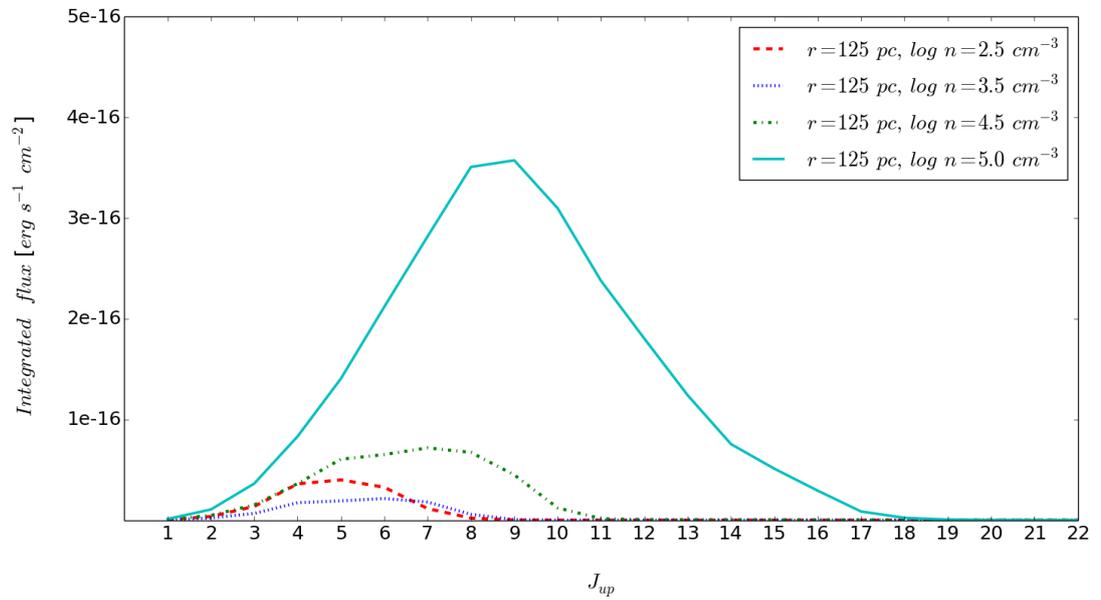
Figure 4.14: *PDR models as a function of the density. The four models describe a gas located at 125 pc from the source, with a density of $10^{2.5}$ cm^{-3} (in red), $10^{3.5}$ cm^{-3} (in blue), $10^{4.5}$ cm^{-3} (in green), 10^5 cm^{-3} (in cyan), respectively. The curve with density up to $n = 10^{4.5}$ cm^{-3} peak at $J_{up} < 8$, while the cyan curve peak is around $J_{up} \simeq 8$.*
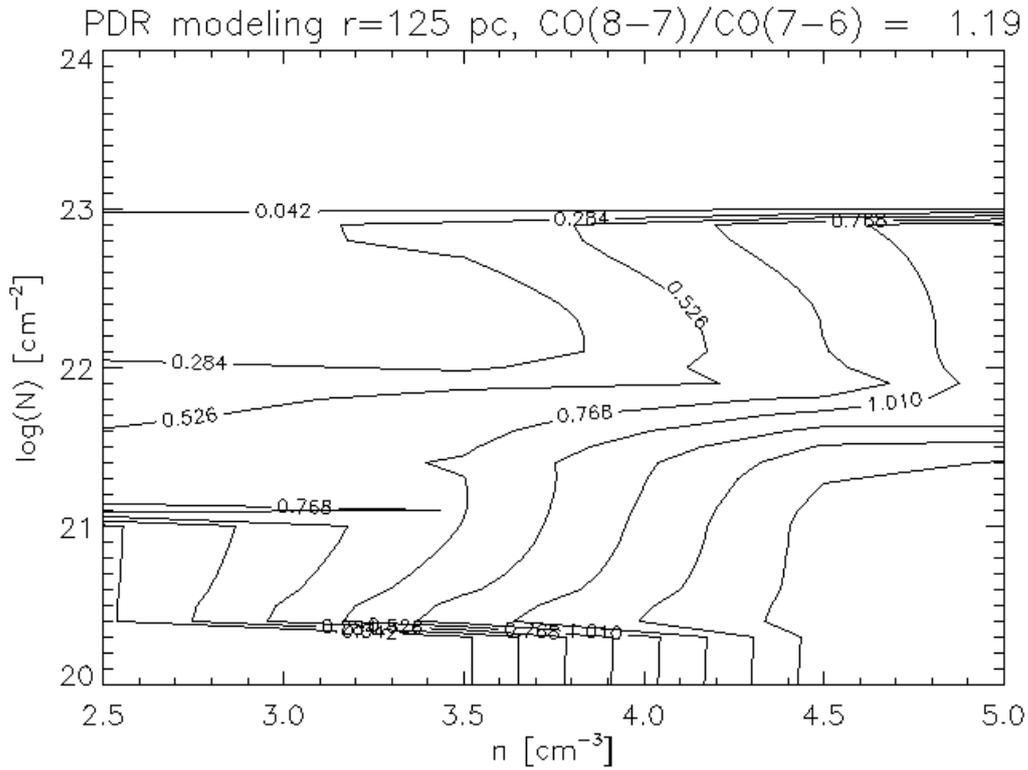
Figure 4.15: *This figure shows the contours of the ratio CO(8-7)/CO(7-6) as a function of the density n and the column density N for PDR models with $r = 125\,pc$. We take into account column densities up to the stopping criterium at $N = 10^{23}\ cm^{-2}$.*
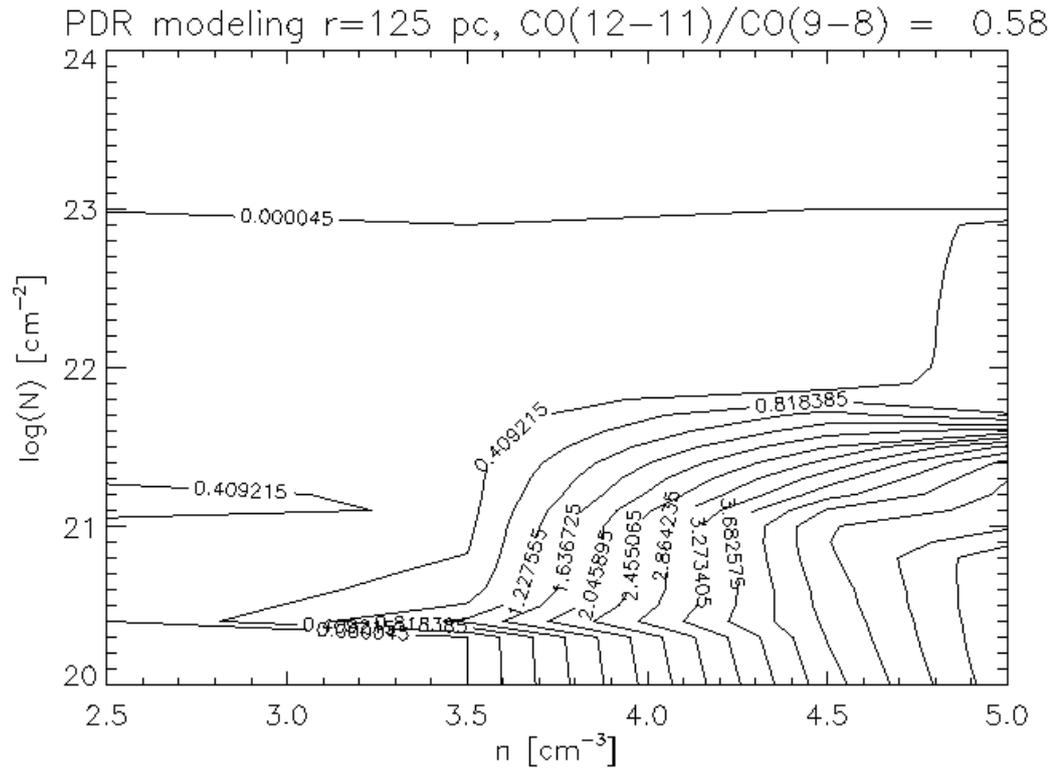
Figure 4.16: *This figure shows the contours of the ratio CO(12-11)/CO(9-8) as a function of the density n and the column density N for PDR models with r = 125 pc. We take into account column densities up to the stopping criterium at $N = 10^{23}$ cm^{-2}.*

Comparing our F_X values with those analyzed by Meijerink and Spaans $(2005)^4$, when modeling XDR in low radiation regimes ($F_X^{low} = 1.6 \, \mathrm{erg \, s^{-1} \, cm^{-2}}$), we note that for $r \geq 250 \, \mathrm{pc}$, $F_X < F_X^{low}$. Hence, we consider only models with $r = 125 \, \mathrm{pc}$.
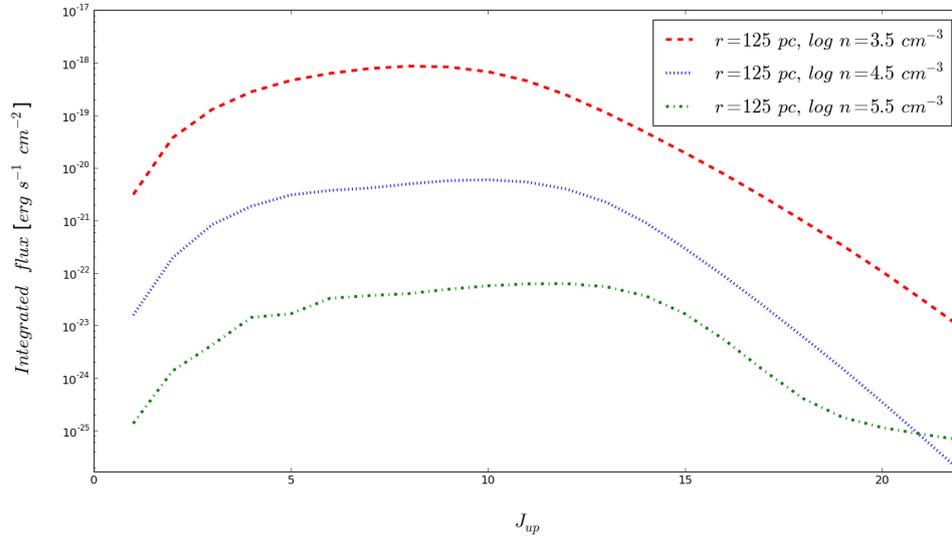

Figure 4.17: *XDR models as a function of the density. The three models describe a gas located at 125 pc from the source, with a density of $10^{3.5} \, cm^{-3}$ (in red), $10^{4.5} \, cm^{-3}$ (in blue), $10^{5.5} \, cm^{-3}$ (in green), respectively and a column density of $10^{23} \, cm^{-2}$.*

---

[4]The standard benchmark for PDR and XDR models.
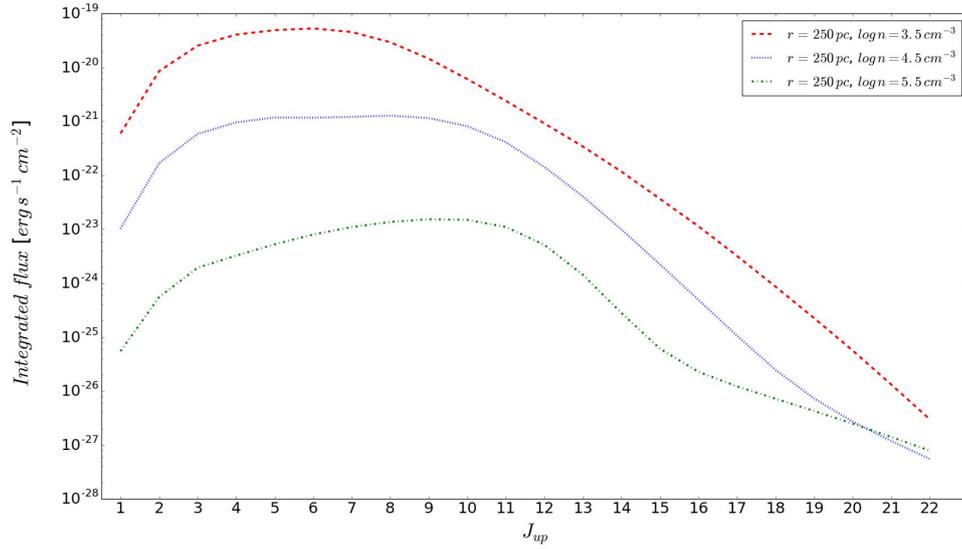
Figure 4.18: *XDR models as a function of the density. The three models describe a gas located at 250 pc from the source, with a density of $10^{3.5}$ cm^{-3} (in red), $10^{4.5}$ cm^{-3} (in blue), $10^{5.5}$ cm^{-3} (in green), respectively and a column density of 10^{23} cm^{-2}.*
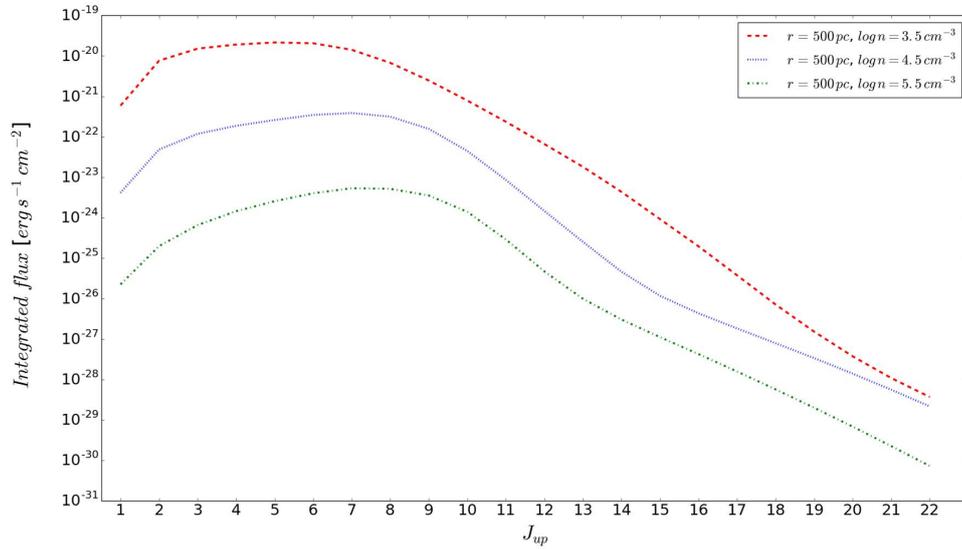

Figure 4.19: *XDR models as a function of the density. The three models describe a gas located at 500 pc from the source, with a density of $10^{3.5}$ cm^{-3} (in red), $10^{4.5}$ cm^{-3} (in blue), $10^{5.5}$ cm^{-3} (in green), respectively and a column density of 10^{23} cm^{-2}.*

In Fig. 4.17 we show that the CO fluxes from XDR models are between $10^{-18} - 10^{-23} \, \mathrm{erg \, s^{-1} \, cm^{-2}}$, while the observed flux values are around $10^{-14} \, \mathrm{erg \, s^{-1} \, cm^{-2}}$. This means that we need a normalization factor in the range $\approx 10^4 - 10^9$ to reproduce the observed CO SLED. Fig. 4.20 shows XDR models that describe clouds at $r = 125 \, pc$ from the source with density of $n = 10^{3.5} \, \mathrm{cm^{-3}}$, $n = 10^{4.5} \, \mathrm{cm^{-3}}$ and $n = 10^{5.5} \, \mathrm{cm^{-3}}$ multiplied by a normalization factor of $\approx 3.7 \times 10^4$, $\approx 4.5 \times 10^6$, and $\approx 2.5 \times 10^8$, respectively[5]. Although the red curve can fit well CO SLED peak, it cannot reproduce the higher-J values, that correspond to the more energetic transitions. The green curve is the one that best reproduce higher-J transitions[6].
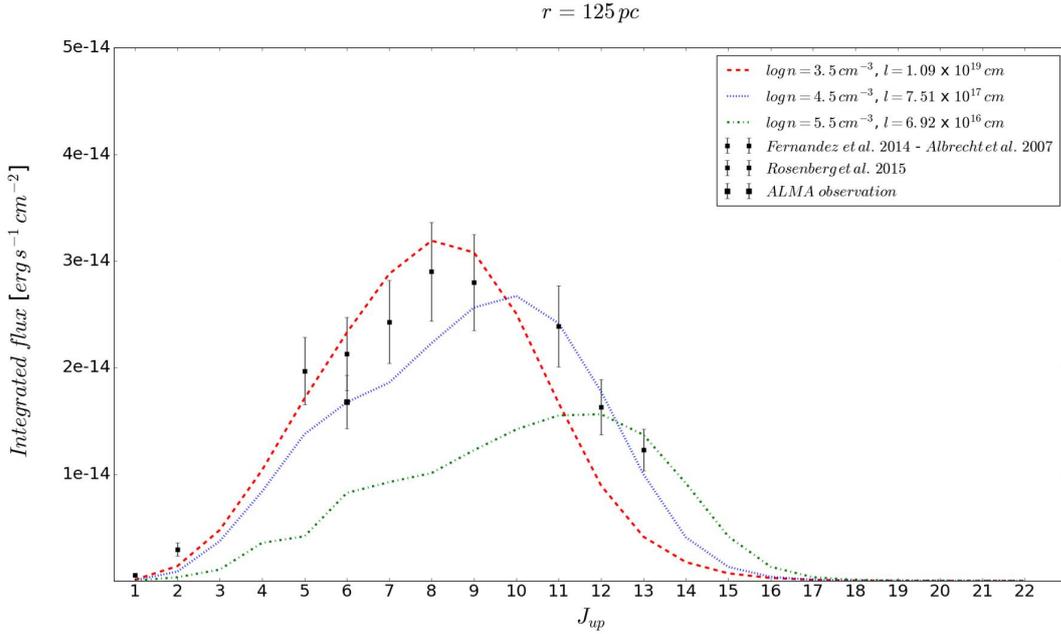
Figure 4.20: *XDR models that describe clouds at* $r = 125 \, pc$ *from the source with density of* $n = 10^{3.5} \, cm^{-3}$ *(in red),* $n = 10^{4.5} \, cm^{-3}$ *(in green) and* $n = 10^{5.5} \, cm^{-3}$ *(in blue) multiplied for a normalization factor of* $\approx 3.7 \times 10^4$, $\approx 4.5 \times 10^6$, *and* $\approx 2.5 \times 10^8$, *respectively.*

In addition, we note that neither the green, nor the blue curve can fit the mid-J transitions. That is why, a mid-density PDR model must be added to reproduce them. There are two available models to reproduce these mid-J:

(a) $r = 125 \, \mathrm{pc}$ and $n = 10^{3.5} \, \mathrm{cm^{-3}}$;

(b) $r = 125 \, \mathrm{pc}$ and $n = 10^{4.5} \, \mathrm{cm^{-3}}$.

In Tab. 4.4, we summarize the models discussed in this section.

---

[5]These normalization factors are chosen in order to reproduce the observed data.

[6]Here, we always take into account a column density of $10^{23} \, \mathrm{cm^{-2}}$.

Table 4.4: Selected models that reproduce the observed CO SLED: *Model 1* is characterized by a low and a high density PDR, while *Model 2* by a low and a mid (two possible values) density PDR, and a XDR. The low density component has a column density $N \approx 10^{22}\,\mathrm{cm}^{-2}$ and is located at 500 pc from the central source, while the higher density components have both a column density $N \approx 10^{23}\,\mathrm{cm}^{-2}$ and are located at 125 pc from the central source.

Models	Low-J PDR	Mid/High-J PDR	High-J XDR
Model 1	$n = 10^{2.5}\,\mathrm{cm}^{-3}$	$n = 10^{5}\,\mathrm{cm}^{-3}$	-
Model 2a	$n = 10^{2.5}\,\mathrm{cm}^{-3}$	$n = 10^{3.5}\,\mathrm{cm}^{-3}$	$n = 10^{4.5}\,\mathrm{cm}^{-3}$
Model 2b	$n = 10^{2.5}\,\mathrm{cm}^{-3}$	$n = 10^{4.5}\,\mathrm{cm}^{-3}$	$n = 10^{4.5}\,\mathrm{cm}^{-3}$

4.3.3 Best-fit

The models so far discussed have been selected on the basis of physical considerations and analysis of key CO line ratios. Here, we present a statistical analysis aimed at finding the accurate normalization factors and the best-fit to the observed data (*Model 1* VS *Model 2*, see Tab. 4.4). We have carried out a χ^2 analysis, looking for the two or three normalization factors (for *Model 1* and *Model 2* introduced in Sec. 4.3.2, respectively) that minimize the χ^2 value.

The general formula of the χ^2 distribution is given by:

$$\chi^2 = \sum_{i=1}^{n} \left(\frac{x_{obs_i} - x_{model_i}}{\sigma_i} \right)^2 \tag{4.2}$$

where n is the number of observed values, x_{obs_i} are the observed values, x_{model_i} the expected ones and σ_i their associated errors. χ^2 is a statistic that characterizes the dispersion of the observations from the expected values. If the observed values were to agree exactly with the predictions, then we should find $\chi^2 = 0$. However, this is not a very likely outcome for an experiment. The numerator of Eq. 4.2 is a measure of the spread of the observations, while the denominator a measure of the expected spread. In case of good agreement, the average spread of the data would correspond to the expected spread, thus we should get a contribution of about one from each values, or $\chi^2 = n$ for the entire distribution. Actually, the true expectation value for χ^2 is not the number of observations, but

$$\langle \chi^2 \rangle = \nu = n - n_c \tag{4.3}$$

where ν is the number of degrees of freedom and is equal to the number of observed values minus the number n_c of contraints, that in our case are the normalization factors (Bevington and Robinson, 2003).

In our case, having rejected the CO(10-9) transition because its flux was lower than the others, $n = 10$, so the number of degrees of freedom is $\nu_1 = 10 - 2 = 8$ for *Model 1* and $\nu_2 = 10 - 3 = 7$ for *Model 2*.

In order to compare *Model 1* and *Model 2*, it is convenient to define the *reduced χ-square* as

$$\tilde{\chi}^2 \equiv \frac{\chi^2}{\nu} \tag{4.4}$$

with expectation value $\langle \tilde{\chi}^2 = 1 \rangle$.

Along with the best-fit model, all the acceptable solutions within $1\,\sigma$ confidence level have been considered, by taking into account all the solutions with $\chi^2 - \chi^2_{min} = \Delta\chi \lesssim 2.3\,(3.5)$ for *Model 1* and *Model 2*, respectively (see Lampton et al. 1976 and Pozzi et al. 2010). In Tab. 4.5, the minimum values χ^2_{min} and $\tilde{\chi}^2_{min}$, and the normalization factors found for *Model 1* and *Model 2*, with their corresponding uncertainties at $1\,\sigma$, are reported.

Table 4.5: χ^2 analysis results for *Model 1* and *Model 2*. The errors associated to the normalization factors are reported at $1\,\sigma$. The asterisk indicates the best-fit value found for $norm_2$ in *Model 2a*.

Models	χ^2_{min}	$\tilde{\chi}^2_{min}$	$norm_1$	$norm_2$	$norm_3$
Model 1	8.8	1.10	$(1.3^{+0.1}_{-0.1}) \times 10^5$	84^{+9}_{-5}	-
Model 2a	6.2	0.9	$(1.2^{+0.3}_{-0.5}) \times 10^5$	$< 146\,(104)^*$	$(4.8^{+0.6}_{-0.7}) \times 10^6$
Model 2b	5.2	0.7	$(1.3^{+0.1}_{-0.2}) \times 10^5$	44^{+46}_{-39}	$(4.61 \pm 0.5) \times 10^6$

Fig. 4.21 shows *Model 1*:

- a PDR that represents clouds with $n = 10^{2.5}\,\mathrm{cm}^{-3}$ and at $r = 500\,\mathrm{pc}$ from the source, multiplied by the best-fit normalization factor, for the low-J transitions (blue curve);

- a PDR that represents clouds with $n = 10^5\,\mathrm{cm}^{-3}$ and at $r = 125\,\mathrm{pc}$ from the source, multiplied by the best-fit normalization factor, for the mid- and high-J transitions (red curve).

The black line represents the sum of the models used. Fig. 4.22 shows the contours of χ^2 as a function of the two normalization factors, *norm1* and *norm2*, at $0.25\,\sigma$, $1\,\sigma$, $1.6\,\sigma$ and $2.6\,\sigma$ confidence levels.
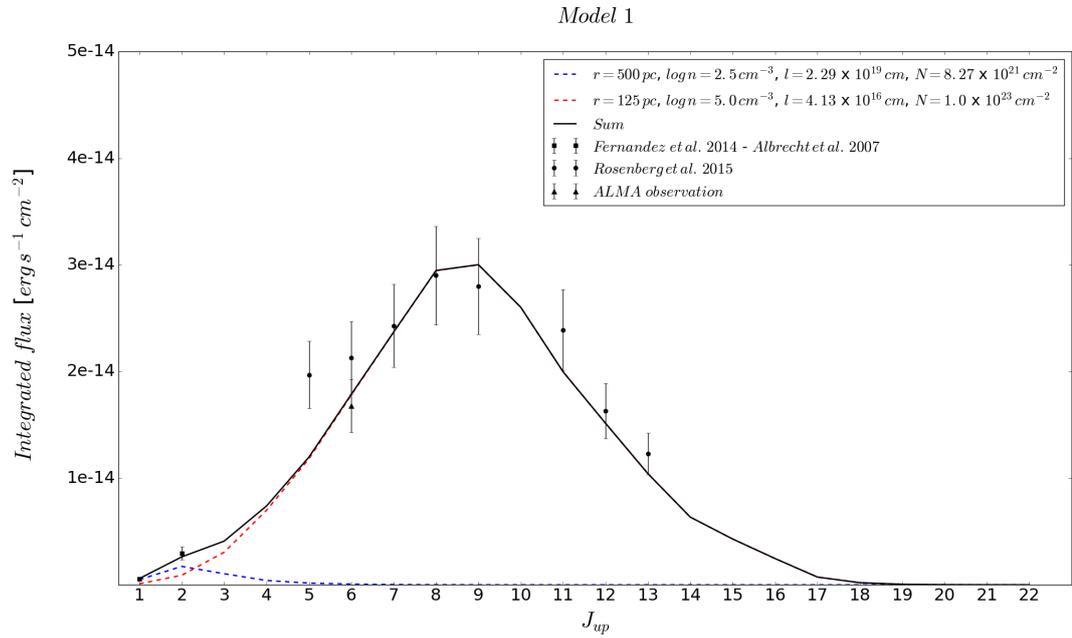
Figure 4.21: *Best-fit for Model 1. The blue curve represents the low density PDR and the red curve the mid/high density PDR.*
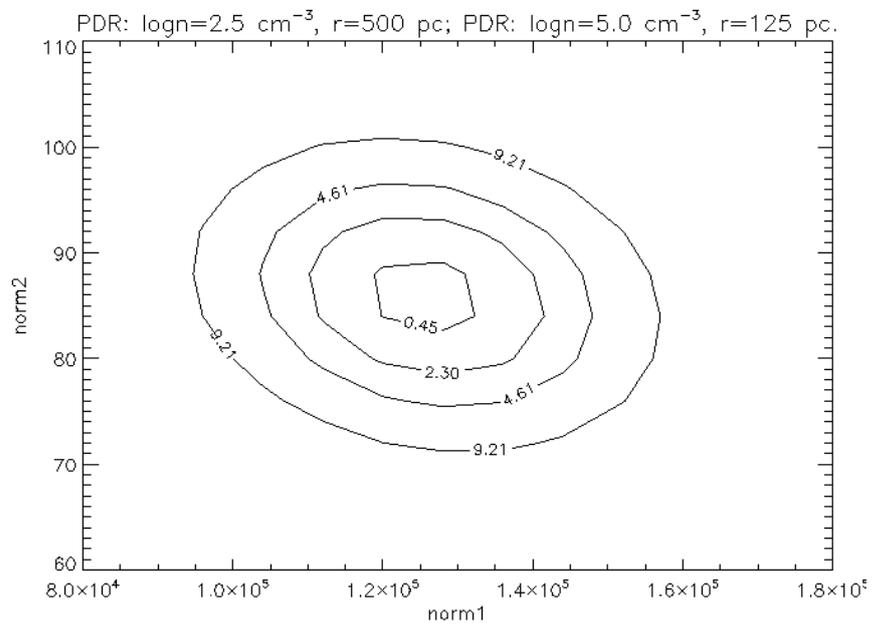

Figure 4.22: *Model 1: Contours of χ^2 with confidence levels corresponding to $0.25\,\sigma$, $1\,\sigma$, $1.6\,\sigma$ and $2.6\,\sigma$.*

Fig. 4.23 and 4.24, instead, show the best-fit for *Model 2a* and *Model 2b*, respectively:

- a PDR that represents clouds with $n = 10^{2.5}\,\mathrm{cm}^{-3}$ and at $r = 500\,\mathrm{pc}$ from the source, multiplied by the best-fit normalization factor, for the low-J transitions (blue curve);

- a PDR that represents clouds with $n = 10^{3.5}\,\mathrm{cm}^{-3}$ or $n = 10^{4.5}\,\mathrm{cm}^{-3}$ and at $r = 125\,\mathrm{pc}$ from the source, multiplied by the best-fit normalization factor, for the mid-J transitions (red curve);

- a XDR that represents clouds with $n = 10^{4.5}\,\mathrm{cm}^{-3}$ and at $r = 125\,\mathrm{pc}$ from the source, multiplied by the best-fit normalization factor, for the high-J transitions (green curve).

In both figures, the black line represents the sum of the models used. Fig. 4.25 and 4.27 show
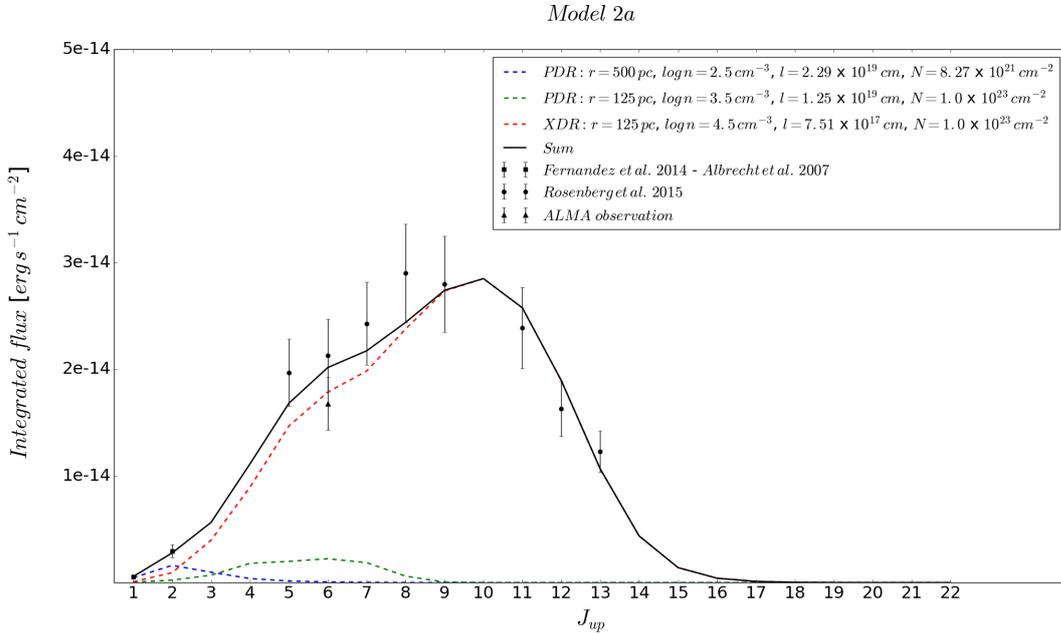
Figure 4.23: *Best-fit for Model 2a. The blue curve represents the low density PDR, the red curve the mid density PDR and the green curve the XDR.*

the contours of χ^2 as a function of $norm_1$ and $norm_3$, holding $norm_2$ fixed at its best-fit value, for *Model 2a* and *Model 2b*, respectively. Fig. 4.26 and 4.28 illustrate the contours of χ^2 as a function of $norm_1$ and $norm_2$, holding $norm_3$ fixed at its best-fit value, for *Model 2a* and *Model 2b*, respectively. All the contours are shown at $0.25\,\sigma$, $1\,\sigma$, $1.6\,\sigma$ and $2.6\,\sigma$ confidence levels.

Finally, Fig. 4.29, 4.30 and 4.31 show all the acceptable solutions within $1\,\sigma$ confidence level for *Model 1*, *Model 2a* and *Model 2b*, respectively.
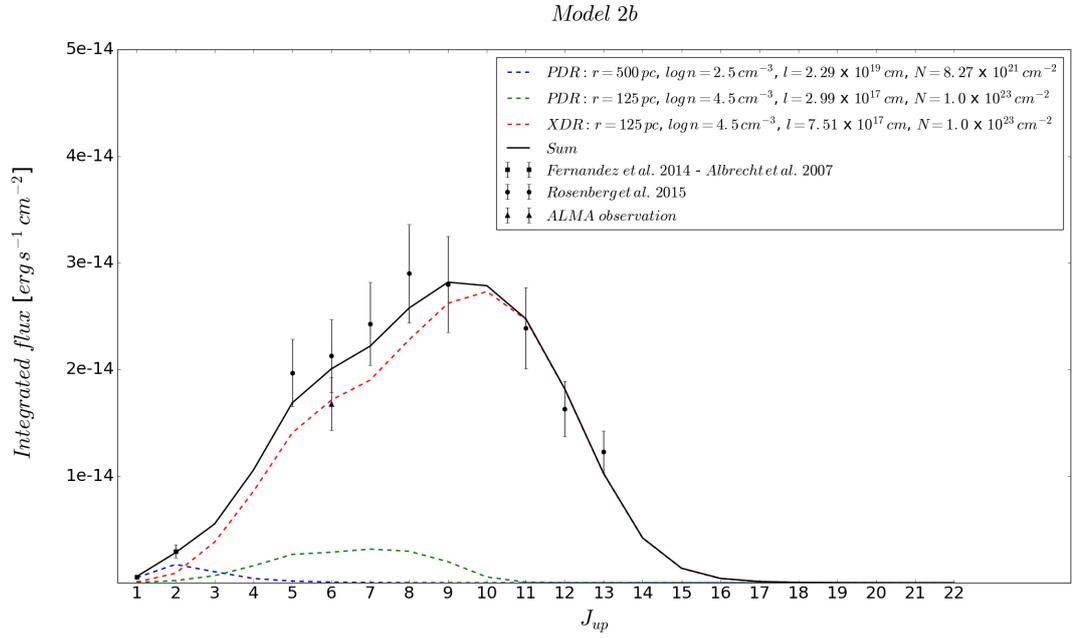
Figure 4.24: *Best-fit for Model 2b. The blue curve represents the low density PDR, the red curve the mid density PDR and the green curve the XDR.*
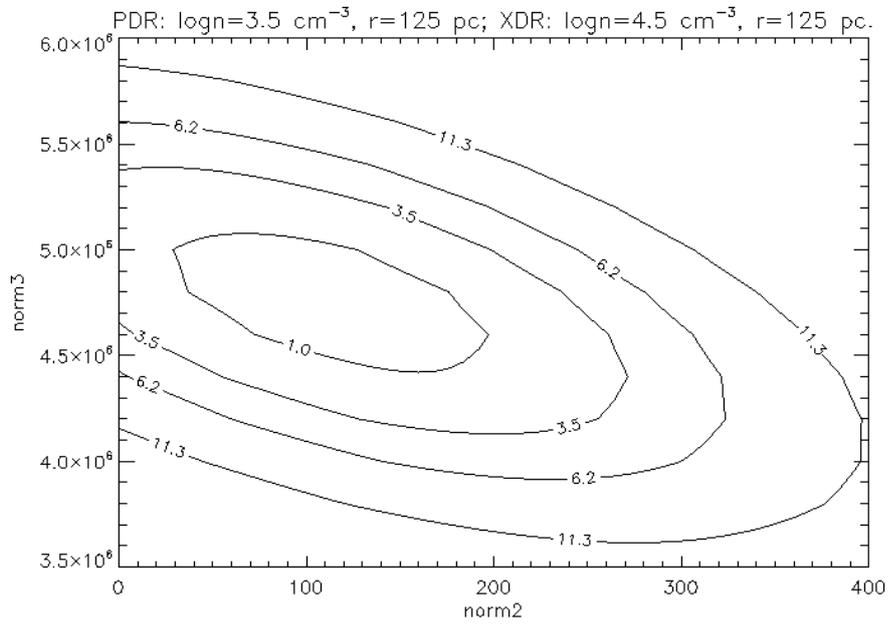
Figure 4.25: *Model 2a: Contours of χ^2 with confidence levels corresponding to $0.25\,\sigma$, $1\,\sigma$, $1.6\,\sigma$ and $2.6\,\sigma$.*
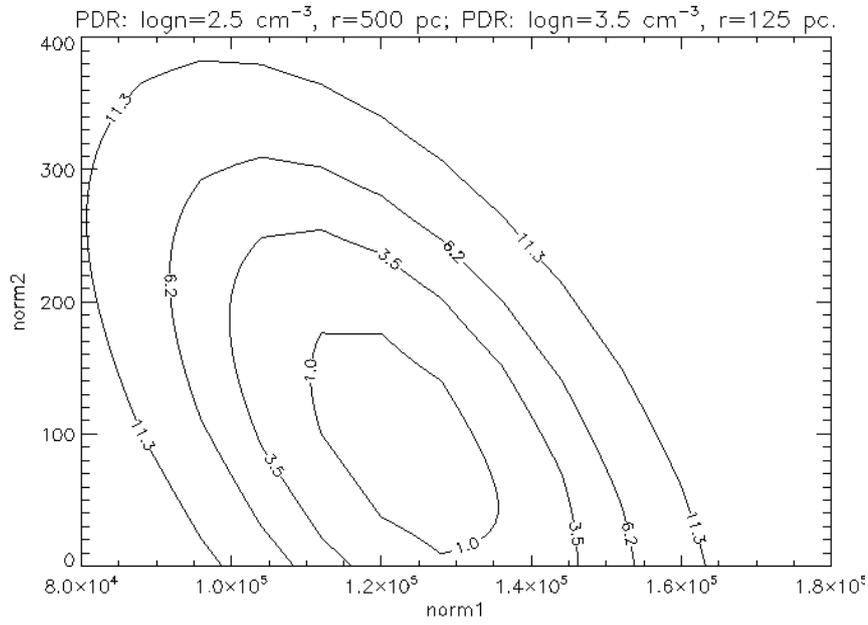
Figure 4.26: *Model 2a: Contours of χ^2 with confidence levels corresponding to $0.25\,\sigma$, $1\,\sigma$, $1.6\,\sigma$ and $2.6\,\sigma$.*
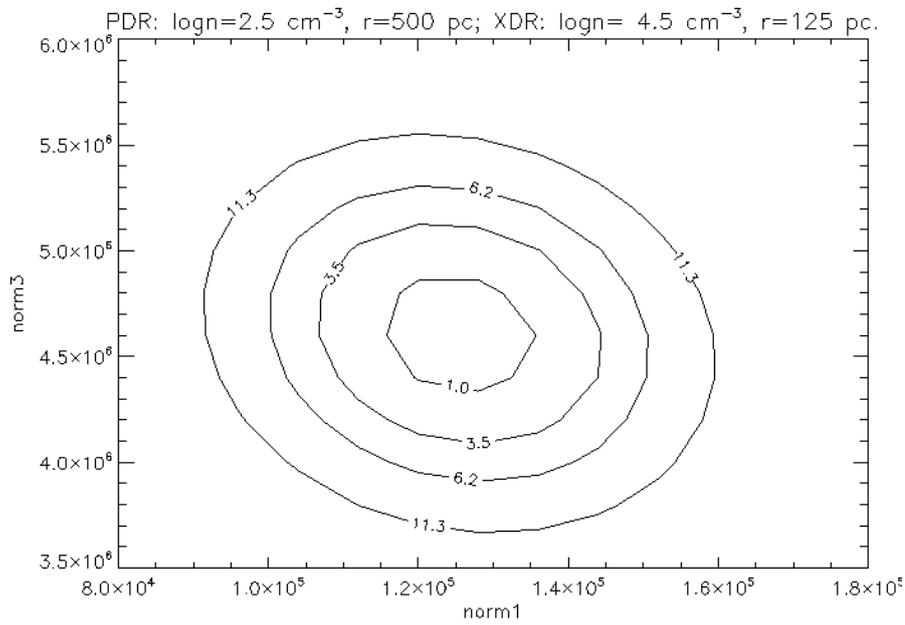
Figure 4.27: *Model 2b: Contours of χ^2 with confidence levels corresponding to $0.25\,\sigma$, $1\,\sigma$, $1.6\,\sigma$ and $2.6\,\sigma$.*
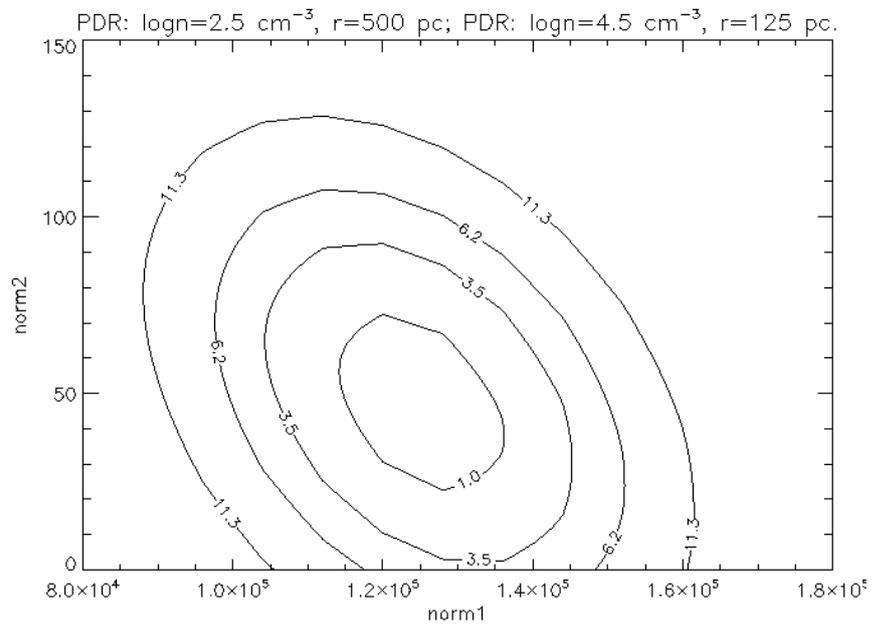
Figure 4.28: *Model 2b: Contours of* χ^2 *with confidence levels corresponding to* $0.25\,\sigma$, $1\,\sigma$, $1.6\,\sigma$ *and* $2.6\,\sigma$.
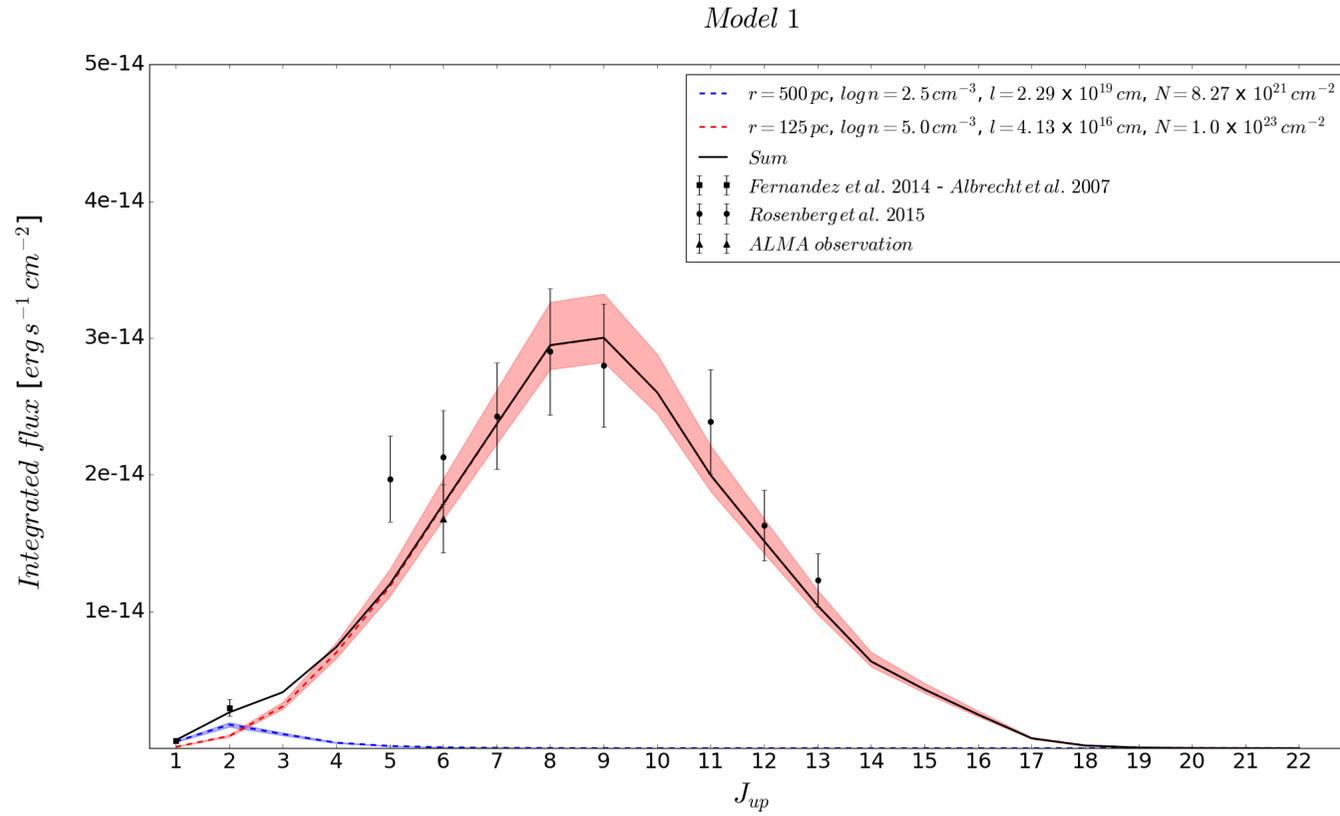
Figure 4.29: *Best-fit for Model 1: the blue and green shading indicates the $\pm 1\sigma$ uncertainty range of the low (high) density PDR normalizations, respectively. The black line indicates the sum of the two model best-fit.*
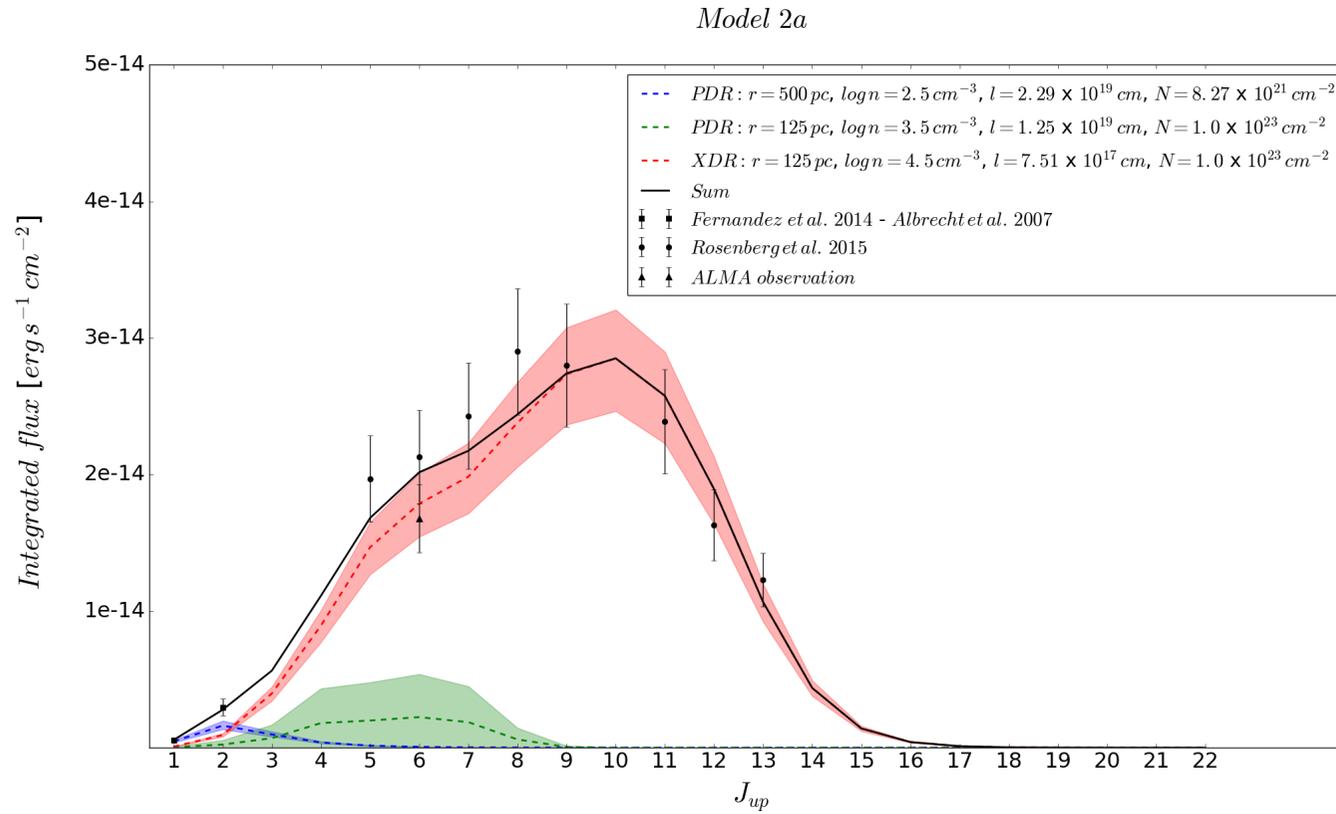
Figure 4.30: *Best-fit for Model 2a: the blue and green shading indicates the ±1σ uncertainty range of the low (middle) density PDR normalizations, respectively, whereas the red shading indicates the ±1σ uncertainty range of the the XDR normalization. The black line indicates the sum of the three model best-fit.*
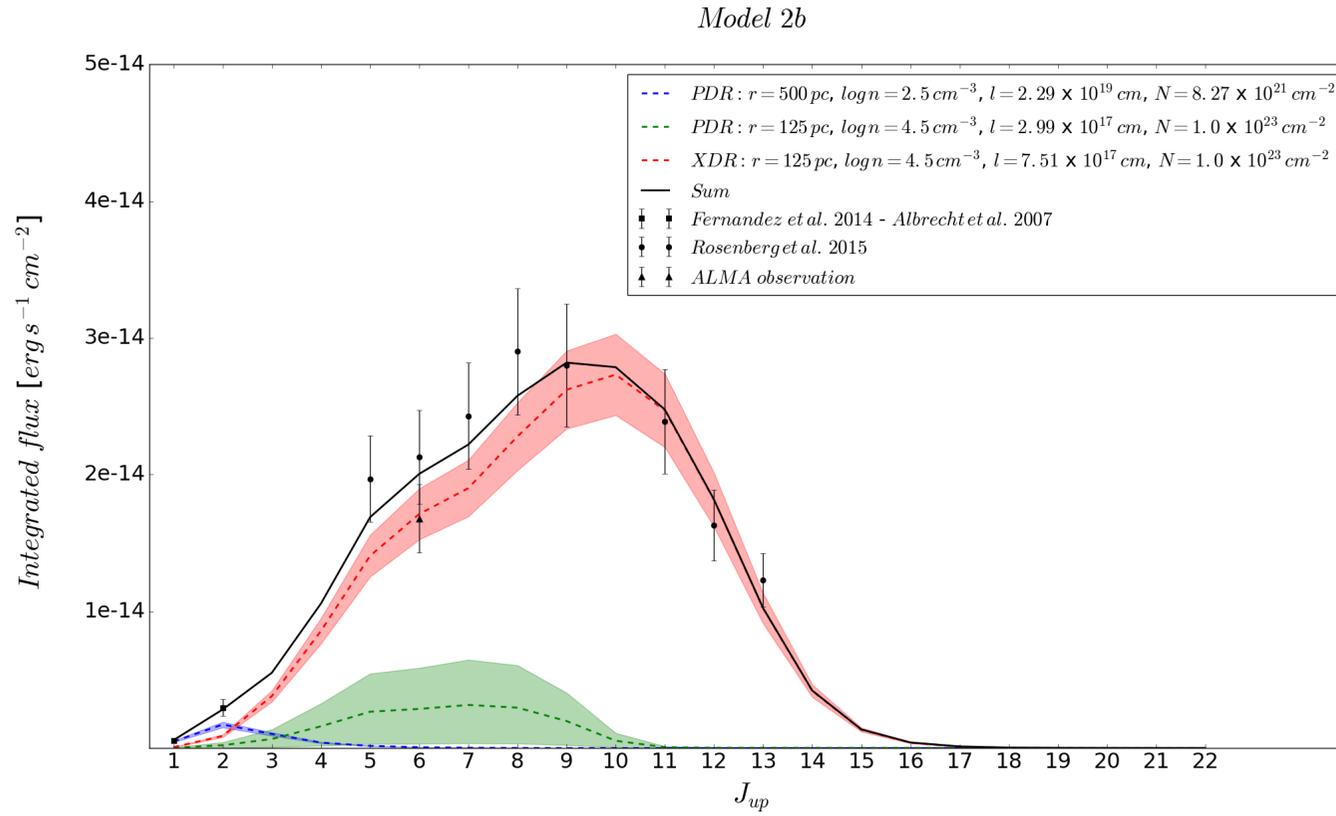
Figure 4.31: *Best-fit for Model 2b: the blue and green shading indicates the $\pm 1\sigma$ uncertainty range of the low (middle) density PDR normalizations, respectively, whereas the red shading indicates the $\pm 1\sigma$ uncertainty range of the XDR normalization. The black line indicates the sum of the three model best-fit.*

4.3.4 The F-test

The *F-test* is often used to compare models, characterized by different numbers of parameters, as *Model 1* (2 parameters) and *Model 2* (3 parameters). The *F-test* is based on the additive nature of functions that obey the χ^2: the difference of two functions that are distributed as χ^2, is still distributed as χ^2. In particular, if we fit a set of data with a function having m terms, the resulting χ^2 has $N - m$ degrees of freedom. If we add another term to the fitting function, the new χ^2 will have $N - m - 1$ degrees of freedom. Therefore, the difference between these two cases must follow a χ^2 distribution with 1 degree of freedom (Bevington and Robinson, 2003). The ratio of the difference $\chi^2(m) - \chi^2(m+1)$ and the new value $\chi^2(m+1)/(N - m - 1)$ (i.e., $\tilde{\chi}^2(m+1)$) provides a statistic F_χ that follows the *F distribution* with $\nu_1 = 1$ (degree of freedom of the numerator) and $\nu_2 = N - m - 1$ (degrees of freedom of the denominator):

$$F_\chi = \frac{\chi^2(m) - \chi^2(m+1)}{\chi^2(m+1)/(N - m - 1)} = \Delta\chi^2/\tilde{\chi}^2_\nu \tag{4.5}$$

This ratio measures how much the additional term has improved the value of the $\tilde{\chi}^2$: small values mean that the additional term is not significant, while large values suggest that the added component improves the fit. If F_χ exceeds the test value for F, we can be fairly confident that the new component should be included (Bevington and Robinson, 2003).

More precisely, in our case:

- $N = 10$;

- in *Model 1*, $m = 2$;

- in *Model 2*, $m = 3$.

Therefore, the F distribution is defined by the parameters $\nu_1 = 1$ and $\nu_2 = 7$. The first column of Tab. 4.6 shows the values obtained from the *F-test*, calculated thanks to Eq. 1.5. Looking at the *F distribution* tables (see Bevington and Robinson 2003) where the test values of F are reported, it can be seen that F_χ values lie between the probability $P_F(F, \nu_1, \nu_2) = 0.25$ of exceeding F (test value $F = 1.57$) and $P_F(F, \nu_1, \nu_2) = 0.10$ (test value $F = 3.59$). Consequently, our confidence range lies between 75% and 90%. In particular, we calculated the cumulative probabilities that a F statistic will be less than or equal to F_χ obtained (see the second column of Tab. 4.6), thanks to the *F Distribution Calculator* (`http://stattrek.com/online-calculator`). Overall, we are $\approx 90\%$ confident that *Model 2*, characterized by an additional component, is significantly improved with respect to *Model 1*.

Table 4.6: The first column reports the F_χ values found by comparing *Model 1* with *Model 2a* (*Model 2b*). The second column reports the cumulative probability $P(F \leq F_\chi)$, calculated thanks to the *F Distribution Calculator* (`http://stattrek.com/online-calculator`).

Models	F_χ	$P(F \leq F_\chi)$
Model 1-Model 2a	2.97	87 %
Model 1-Model 2b	3.53	90 %

4.4 Molecular mass

The low-J transitions are produced by an extended low excitation PDR component that accounts for the majority of the mass. This component is made up by $\approx 3.1 \times 10^5$ clouds with a radius of ≈ 7.2 pc (normalization factor and depth from the best-fit model), a density of $n = 10^{2.5}$ cm^{-3}, and located at 500 pc from the source. Assuming that these clouds are approximately spherical, their molecular mass can be calculated as:

$$M_{cloud} = 2m_p \frac{4\pi}{3} n l^3 \ \text{[g]} \tag{4.6}$$

where $m_p \simeq 1.7 \times 10^{-24}$ g is the proton mass and l the radius of the cloud in cm. Considering $l = 2.3 \times 10^{19}$ cm and $n = 10^{2.5}$ cm^{-3}, $M_{cloud} \simeq 2.7 \times 10^4$ M$_\odot$. Then, M_{cloud} is multiplied by the normalization factor $\approx 3.1 \times 10^5$, resulting in a total mass of $M_{tot} \simeq 3.4 \times 10^9$ M$_\odot$. This value is obtained by modelling the molecular gas responsible for the CO emission, but is consistent with the total molecular mass found by Fernández et al. 2014, who estimated $M_{tot} = (2.1 \pm 0.2) \times 10^9$ M$_\odot$, by multiplying the CO(1-0) luminosity (obtained thanks to Eq. 3.11) by the standard conversion factor for starbursting systems $\alpha_{CO} = 0.8$ M$_\odot$/(K km s^{-1} pc^2) (see Sec. 3.3.1).

According to *Model 1*, a very dense, high illumination PDR can account for the highest CO lines. The small surface area (given by the depth squared, where the depth is 1.3×10^{-2} pc) indicates a number of small high density clumps in a very strong UV field. Considering $l = 4.1 \times 10^{16}$ cm and $n = 10^5$ cm^{-3}, $M_{cloud} \simeq 4.9 \times 10^{-2}$ M$_\odot$. Since the best-fit normalization factor is 84, these small and dense clouds account for a total mass of $M_{tot} \simeq 4$ M$_\odot$. Therefore, their contribution is negligible with respect to the diffuse component.

On the other hand, *Model 2* predicts a less extended and denser central XDR region, composed by clouds with radius $\approx 2.4 \times 10^{-1}$ pc and a low number of dense small clouds close to massive stars (dense PDR component), with a radius of ≈ 4.1 pc and $\approx 9.7 \times 10^{-2}$ pc, for case *a* and *b*, respectively. Even in this case, their mass contribution is negligible with respect to the diffuse component.

More precisely, for the XDR component we found: $M_{cloud} \simeq 93.2$ M$_\odot$ and $M_{tot} \simeq 4.3 \times 10^8$ M$_\odot$ or $M_{tot} \simeq 4.5 \times 10^8$ M$_\odot$, considering a normalization factor of 4.6×10^6 or 4.8×10^6, in case *a* and *b*, respectively.

For the dense PDR with n=$10^{3.5}$ cm^{-3} (*Model 2a*): $M_{cloud} \simeq 4.3 \times 10^4$ M$_\odot$ and $M_{tot} \simeq 4.5 \times$

10^6 M$_\odot$, considering a normalization factor of 104. While, for the dense PDR with n=$10^{4.5}$ cm^{-3} (*Model 2b*): $M_{cloud} \simeq 5.9\,M_\odot$ and $M_{tot} \simeq 2.6 \times 10^2$ M$_\odot$, considering a normalization factor of 44.

These two components are probably embedded in a more diffuse component, that cannot be the one used to explain the low-J radiation, because produced by more distant clouds (500 pc). The addition of an extra diffuse component at $r = 125$ pc (with a normation factor of $\approx$ 1500) gives a negligible contribution in terms of the total mass, but can supply the diffuse high mass MCs within which the small and dense clumps reside.

In Tab. 4.7, the total molecular masses with their associated errors, found for each component by considering the normalization uncertainties at $1\,\sigma$, are reported. In addition, also the typical temperature values of the three components are reported, estimated by looking at Fig. 4.7, 4.8, 4.12, respectively.

Table 4.7: Total molecular masses (in M$_\odot$) calculated and typical temperature (K) for *Model 1*, *Model 2a* and *Model 2b*. The temperature values have been obtained by looking at Fig. 4.7, 4.8, 4.12, respectively.

Models	Low-J PDR	Mid/High-J PDR	High-J XDR
Model 1	$(3.4^{+0.3}_{-0.4}) \times 10^9$	$4.0^{+0.4}_{-0.3}$	-
Model 2a	$(3.4^{+0.7}_{-1.2}) \times 10^9$	$< 6.3 \times 10^6$	$\simeq (4.3^{+0.6}_{-0.6}) \times 10^8$
Model 2b	$(3.4^{+0.4}_{-0.4}) \times 10^9$	$2.6^{+2.7}_{-2.3} \times 10^2$	$\simeq (4.5 \pm 0.5) \times 10^8$

Chapter 5

Summary and conclusions

In this chapter, we summarize the results obtained, giving an insight into possible future perspectives.

In the last decades, many pieces of evidence in support of the AGN-starburst connection were found (e.g., Magorrian et al. 1998, Ferrarese and Merritt 2000, Davies et al. 2007, Alexander and Hickox 2012, Madau and Dickinson 2014), making it a key topic of the modern astrophysics. As explained in Ch. 1, studying galaxies where the two phenomena co-exist, such as the galaxy studied in detail in this work (NGC 34), is crucial to understand the tight AGN-starburst connection. NGC 34 is a local galaxy ($z \approx 0.0196$) classified as a Seyfert 2 from optical BPT diagrams and X-ray data (Brightman and Nandra 2011b, Ranalli et al. 2003), and as a LIRG, owing to its large IR luminosity (Gruppioni et al., 2016).

The aim of this thesis is the study of the molecular component of NGC 34, since the molecular gas plays a key role, providing material for star formation and fuelling a possible AGN. In particular, we have investigated the molecular carbon monoxide (CO) as a function of the rotational level (CO SLED), in order to probe the physical properties of the gas, such as density, temperature and the main source that causes the emission (SF or AGN). Thanks to NGC 34 vicinity, many detailed multiwavelength data are available. In particular, we have reduced and analyzed archival band 9 ALMA data (see Ch. 2), obtaining improved continuum and CO(6-5) line images, thanks to the more reliable flux calibration (see Butler 2012). Then, taking into account Herschel/SPIRE FTS data (from J=4-3 to J=13-12) and ground-based observations for the lower-J transitions from the literature, we have modelled the CO SLED, using a grid of PDR (Photo-dissociation Region) and XDR (X-ray Dominated Region) models that span ranges in density, distance from the source and column density (see Ch. 4), obtained with the photoionization code CLOUDY (Ferland, 2013).

5.1   Main results

Our main results can be summarized as follows.

- We have started the ALMA data analysis from the raw data available in the archive, calibrating them step by step, correcting for antenna positions, atmosphere effects and electronics. We have applied a more reliable flux calibration, making use of the latest model library releases, eventually obtaining an integrated flux (Moment 0) of the CO(6-5) transition equal to (731 ± 110) $\mathrm{Jy\,km\,s^{-1}}$, with a peak flux of (213 ± 40) $\mathrm{Jy\,km\,s^{-1}}$, and a continuum flux equal to (278 ± 42) mJy, with a peak flux of (98.6 ± 14.8) mJy. Comparing these results with the data published by Xu et al. (2014), we noted that this work calibration provides a Moment $0 \approx 25\%$ lower, while the rms, the peak flux and the continuum flux values are consistent within $1\ \sigma$. We report in Fig. 5.1 the CO(6-5) integrated flux obtained.
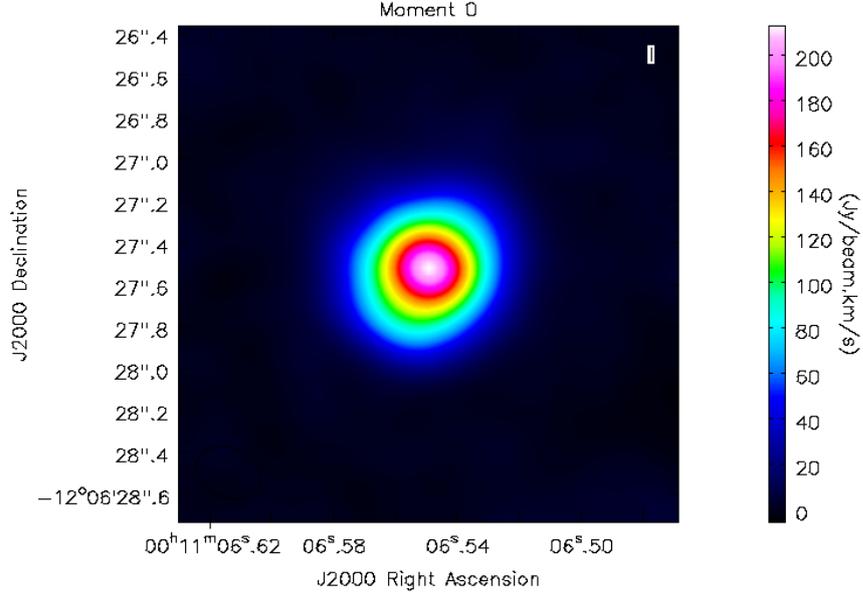
Figure 5.1: *Integrated emission of the CO(6-5) line. The wedge on the right shows the color-scale of the map in $Jy\,beam^{-1}\,km\,s^{-1}$. The rms noise level is $\approx 1.3\,Jy\,km\,s^{-1}$. The integrated flux density results $(731 \pm 110)\,Jy\,km\,s^{-1}$.*

- In the CO SLED analysis, we compared PDR and XDR models to the observed data. We select PDR and XDR models that best reproduce the observation, on the basis of physical considerations and analysis of observed CO line ratios (CO(8-7)/CO(2-1), CO(8-7)/CO(7-6), CO(12-11)/CO(9-8)). We find that the low-J lines are reproduced by a low density

PDR ($n = 10^{2.5}\,\mathrm{cm}^{-3}$) with gas located 500 pc from the source. On the other hand, the mid/high-J transitions can be explained by two different approaches (see Sec. 4.3), that we called *Model 1*, that takes into account only the starburst component, and *Model 2* (*a* and *b*), that considers also the X-ray radiation generated by the AGN. *Model 1* is characterized by a very dense, high illumination PDR ($n = 10^5\,\mathrm{cm}^{-3}$, $r = 125$ pc), while *Model 2* predicts a concentrated and dense central XDR region ($n = 10^{4.5}\,\mathrm{cm}^{-3}$, $r = 125$ pc) to reproduce the higher-J transitions and mid-density PDR ($n = 10^{3.5}\,\mathrm{cm}^{-3}$ in *Model 2a* and $n = 10^{4.5}\,\mathrm{cm}^{-3}$ in *Model 2b*, $r = 125pc$), to account for the mid-J lines.

- For both *Model 1* and *Model 2*, we presented a χ^2 analysis aimed at finding the best-fit normalization factors for each component (that represent the number of that particular type of clouds). Along with the best-fit model, we have accepted all the solutions within $1\,\sigma$ confidence level, taking into account all the solutions with $\chi^2 - \chi^2_{min} = \Delta\chi \lesssim 2.3\,(3.5)$ for *Model 1* and *Model 2*, respectively (see Lampton et al. 1976 and Pozzi et al. 2010).

- In order to compare *Model 1* and *Model 2*, we have calculated the $\tilde{\chi}^2$ and done the *F-test* analysis. From the F-test analysis we conclude that we are $\approx 90\%$ confident that *Model 2*, that includes also the XDR, is significantly improved with respect to *Model 1*. We report in Fig. 5.2 the observed CO SLED with the best-fit model (*Model 2*) obtained.
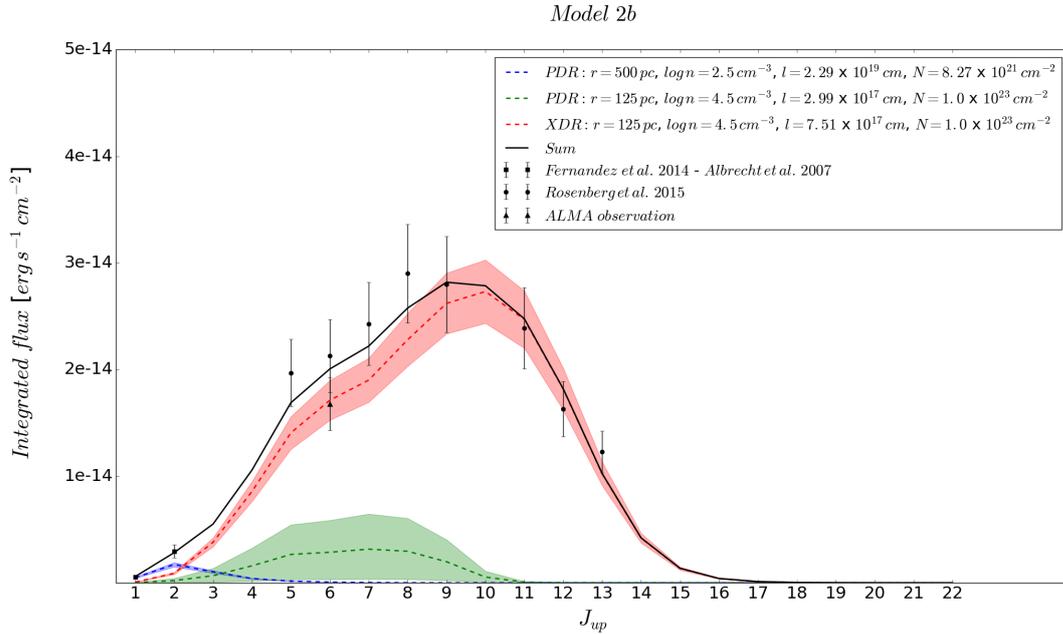

Figure 5.2: *Model 2b: the blue and green shading indicates the $\pm 1\sigma$ uncertainty range of the low (middle) density PDR normalizations, respectively, whereas the red shading indicates the $\pm 1\sigma$ uncertainty range of the XDR normalization. The black line indicates the sum of the three model best-fit.*

- Finally, we have calculated the molecular mass associated to the analyzed components, assuming that clouds are approximately spherical. We noted that the contribution of the PDRs/XDRs used to account for the mid/high-J lines is negligible with respect to the diffuse component, necessary to explain the low-J transitions. In particular, we found a total mass of $M_{tot} = (3.4^{+0.3}_{-0.4}) \times 10^9 \, M_\odot$ associated to the diffuse component. This result is consistent with the total molecular mass found by Fernández et al. (2014), who estimated $M_{tot} = (2.1 \pm 0.2) \times 10^9 \, M_\odot$, by multiplying the CO(1-0) luminosity by the standard conversion factor for starbursting systems $\alpha_{CO} = 0.8 \, M_\odot/(K \, km \, s^{-1} \, pc^2)$ (see Sec. 3.3.1).

5.2   Further considerations and future perspectives

In this thesis project, analysing the CO SLED, we have concluded that a model with a XDR component (due to the AGN) better reproduce the data than a model with only PDRs (due to SF), even though it is significant only at a 90% level.

In order to distinguish unanbiguosly between AGN-induced XDRs and SF-induced PDRs, very high-J CO SLEDs ($J \geq 8-10$) are needed (Sec. 4.1.1). Furthermore, unlike PDR/starburst, XDR/AGN contribution is significant only on small angular scales (Meijerink et al., 2007), therefore high resolution observations of NGC 34 nuclear region are needed to determine the real contribution of the AGN activity. A very useful tool is the intensity ratio of high rotational transitions, such as the CO(16-15)/CO(1-0), CO(16-15)/CO(10-9), CO(10-9)/CO(7-6) and the CO(7-6)/CO(3-2), which have much higher values in XDRs than in PDRs (Meijerink et al. 2007, see App. A). Unfortunately, CO(16-15) and CO(3-2) transitions are not observed, while we have rejected the CO(10-9) owing to its low flux. Therefore, other constraints are needed to distinguish between PDRs and XDRs (i.e., between *Model 1* and *Model 2*). Papadopoulos et al. (2012) proposed that, in addition to CO rotational lines, a combination of low- to mid-J rotational lines of heavy rotor molecules with high critical densities, such as HCO^+, HCN, HNC and CN, is necessary to probe the large range of physical properties within GMCs ($T_{kin} \sim 15-100 \, K$, $n(H_2) \sim 10^2 - 10^6 \, cm^{-3}$). For instance, HCO^+ lines appears to be stronger in XDRs than in PDRs by a factor of at least three, while CN/HCN ratio is far higher in PDRs than in XDRs, where it is expected to be $\sim 5-10$ (see App. B). In light of these considerations, high resolution observations of high critical density molecules with ALMA, characterized by a very high spatial and spectral resolution, could provide new insights on physical properties of NGC 34, allowing to separate the PDR and XDR contributions. Therefore, a proposal for the next ALMA cycle (Cycle 5) to investigate HCN emission could be done.

In addition, in order to shed light on NGC 34 AGN activity, it would be interesting the re-analysis of the X-ray spectra, including data from the Nuclear Spectroscopic Telescope Array (NUSTAR), that focus light in the high energy X-ray range (3 - 79 keV), less affected from obscuration.

Finally, we performed our analysis only on one galaxy, but we aim at enlarging our sample in

the near future. We could search potential candidates of galaxies, where AGN and SF activities co-exist, in the 12MGS sample, looking for their counterpart in the (sub)millimeter wavelengths in the ALMA archive.

Appendix A

High CO rotational transitions

CO(16-15)/CO(1-0), CO(16-15)/CO(10-9), CO(10-9)/CO(7-6) and the CO(7-6)/CO(3-2) have much higher values in XDRs than in PDRs (Meijerink et al., 2007), as Fig. A.1 and A.2 show.
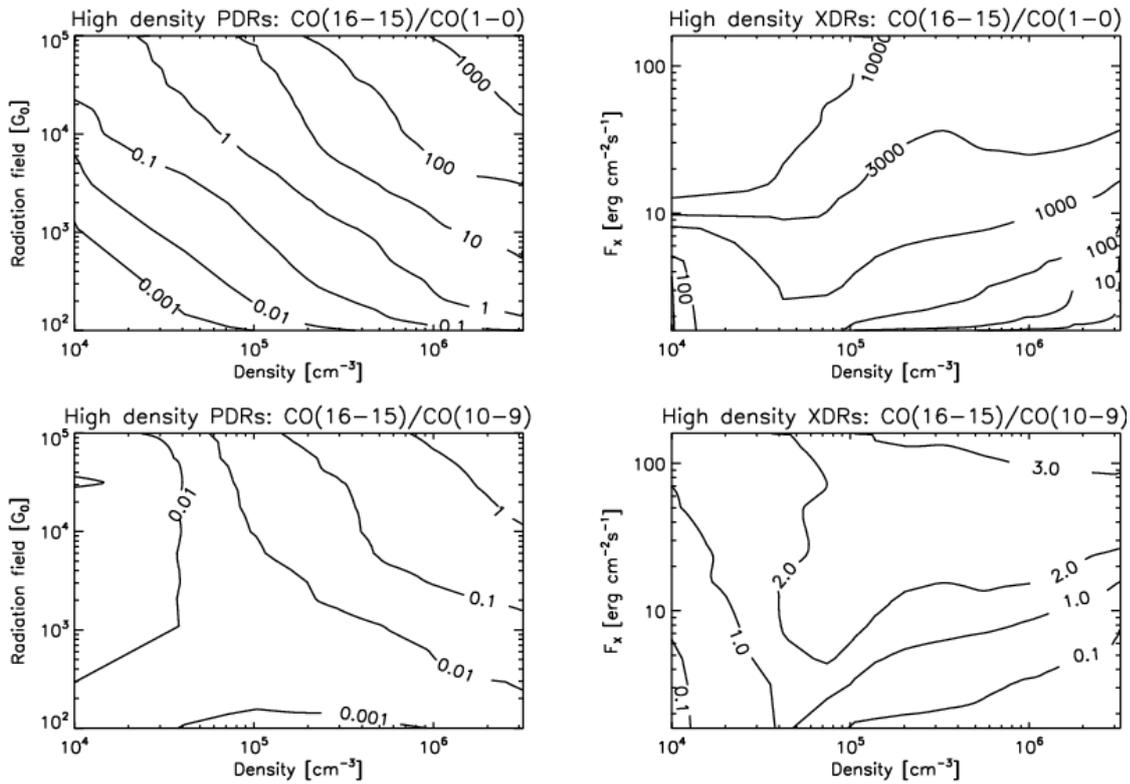
Figure A.1: *CO(16-15)/CO(1-0) and CO(16-15)/CO(10-9) line intensity ratios for PDR (left) and XDR (right) models at densities ranging from $n = 10^4 - 10^6$ cm^{-3} and incident fluxes between $G_0 = 10^3 - 10^5$ ($F_X = 1.6 - 160$ $erg\,s^{-1}\,cm^{-2}$) (Meijerink et al., 2007).*
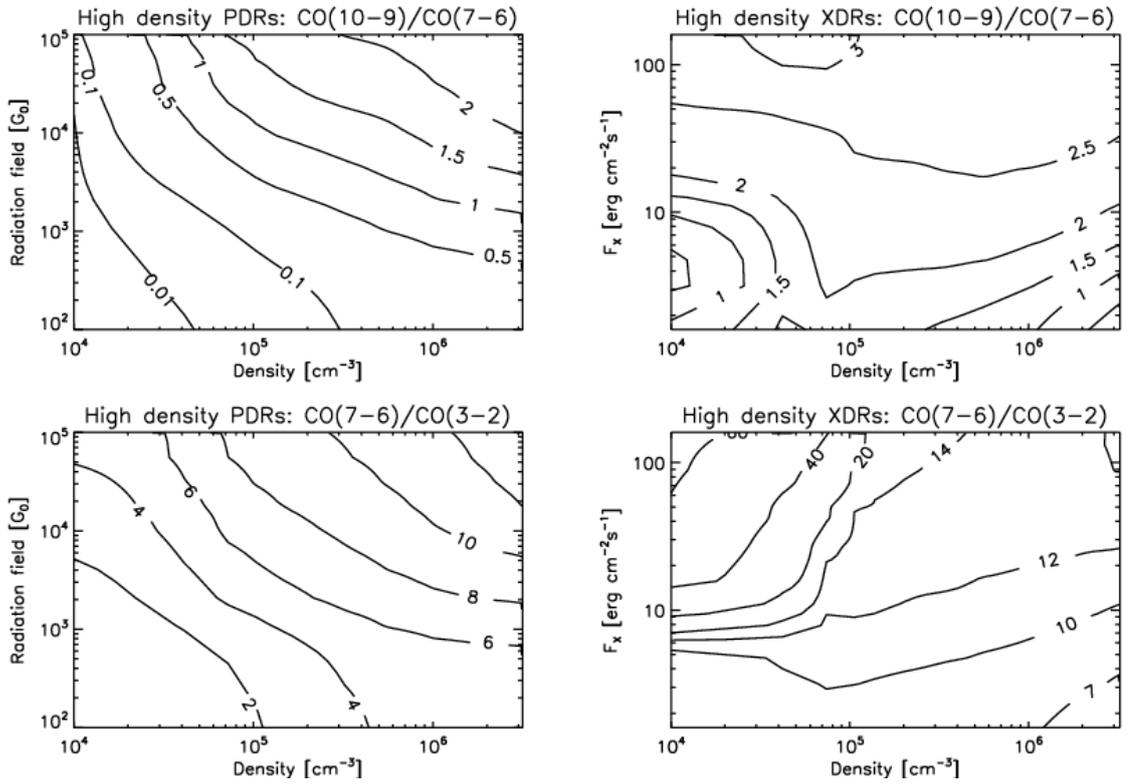
Figure A.2: *CO(10-9)/CO(7-6) and CO(7-6)/CO(3-2) line intensity ratios for PDR (left) and XDR (right) models at densities ranging from $n = 10^4 - 10^6\ cm^{-3}$ and incident fluxes between $G_0 = 10^3 - 10^5$ $(F_X = 1.6 - 160\ erg\,s^{-1}\ cm^{-2})$ (Meijerink et al., 2007).*

Appendix B

High critical density molecules as diagnostics

HCN ($n_{crit} \sim 4-10 \times 10^6$ cm^{-3} for J=1-0 and 3-2) and HCO$^+$ ($n_{crit} \sim 1.5-30 \times 10^5$ cm^{-3} for J=1-0 and J=3-2) molecules are the most abundant H$_2$ mass tracers after CO and their much higher dipole moments make their transitions excellent tracers of dense molecular gas in galaxies. The HCN and HCO$^+$ abundances partly determine the fraction of the dense gas that can be traced by their luminous and optically thick J=1-0 line emissions within a given GMC. Generally, the ratio HCN/HCO$^+$ is expected to be $\gtrsim 1$ for the dense gas because the abundance of the neutral HCN can remain unchanged, while the amount of the ion HCO$^+$ declines through recombination with free electrons. Therefore, HCO$^+$ is very sensitive to the ambient free electron abundance, and even small increases of the latter can lead to its severe depletion (Papadopoulos, 2007). As a result of the higher ionization degree in XDRs, typically, the HCO$^+$ lines are stronger in XDRs than in PDRs by a factor of at least three. Fig. B.1 shows that the HCN/HCO$^+$ ratio can discriminate between PDRs and in XDRs in the density range between $n = 10^5$ and $10^{6.5}$ cm^{-3} (Meijerink et al., 2007).

HNC molecule is the isomer of (and chemically linked to) HCN and has almost the same critical density, so the only difference in line ratio should be related to the abundances. At high temperatures HNC can be transferred into HCN (HNC + H $\rightarrow$ HCN + H) and thus, the HCN/HNC ratio is predicted to increase with increasing temperature and gas density (Aalto et al., 2002). For instance, Meijerink et al. 2007 studied HNC(1-0)/HCN(1-0). In PDRs, HCN is more abundant at high depths, where the abundance ratio approaches unity. Consequently, the HNC(1-0)/HCN(1-0) line intensity ratio is around one for the PDRs if the column density is larger than 10^{22} cm^{-2}, while is less than unity for $N < 10^{22}$ cm^{-2} (see Fig. B.2). In XDRs, HCN is more abundant in the highly ionized part of the cloud. Nevertheless, HNC is equally or even more abundant than HCN deep into the cloud. XDR models show low ratios for the low densities (e.g., 10^4 cm^{-3}) and strong radiation fields (e.g., > 10 erg s^{-1} cm^{-2}). The ratios
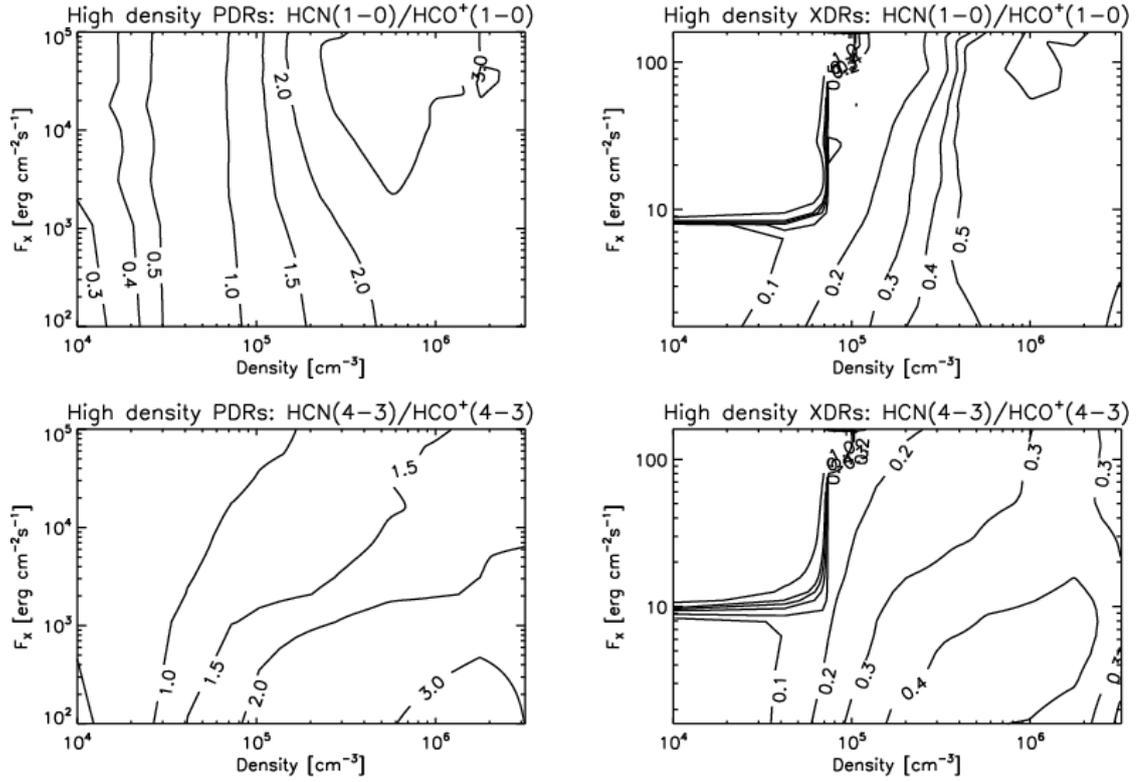
Figure B.1: *Line intensity ratio for PDR (left) and XDR (right) models at densities ranging from $n = 10^4 - 10^6 \, cm^{-3}$ and incident fluxes between $G_0 = 10^3 - 10^5$ ($F_X = 1.6 - 160 \, erg \, s^{-1} \, cm^{-2}$) (Meijerink et al., 2007).*

increase for lower incident radiation fields, and at highest densities (e.g., $n = 10^{6.5}\,\mathrm{cm^{-3}}$) the line ratios are always larger than one, whatever radiation field values (see Fig. B.2).
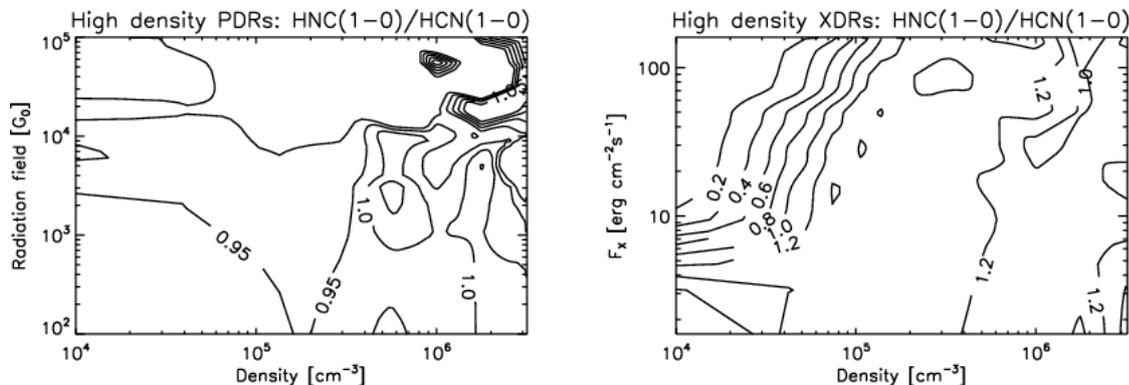

Figure B.2: *Line intensity ratio for PDR (left) and XDR (right) models at densities ranging from $n = 10^4 - 10^6\ cm^{-3}$ and incident fluxes between $G_0 = 10^3 - 10^5$ ($F_X = 1.6 - 160\ erg\,s^{-1}\,cm^{-2}$) (Meijerink et al., 2007)*

Rotational transitions of CN are also important dense gas mass tracers, even though its critical density is by a factor of 5 lower than HCN. This molecule is an excellent tracer of regions affected by UV radiation, therefore it is one of the most effective diagnostics of PDRs (Rodriguez-Franco et al., 1998). Consequently, models of PDRs yield mostly very large CN/HCN ratios (CN/HCN$\gg 1$), while in XDRs, CN/HCN is expected to be $\sim 5 - 10$. Nevertheless, this ratio appears to be lower in LIRGs, suggesting a negligible contribution of XDRs to the bulk of the large molecular gas reservoirs found in these galaxies. For instance, the well-studied case of the molecular gas in the starburst/AGN Seyfert 2 galaxy NGC 1068 reveals that the influence of XDRs is limited just to the small fraction of the total molecular gas located very close to the AGN, where HCN intensity appears to be enhanced, while HCO$^+$ intesity declines (Papadopoulos, 2007). This is in line with what declared by Meijerink et al. 2007, who stressed that the XDR/AGN contribution will typically be of a much smaller angular scale than that of a PDR/starburst.

Bibliography

S. Aalto, A. G. Polatidis, S. Hüttemeister, and S. J. Curran. CN and HNC line emission in IR luminous galaxies. *Astronomy and Astrophysics*, 381:783–794, January 2002.

J. Aird, K. Nandra, E. S. Laird, A. Georgakakis, M. L. N. Ashby, P. Barmby, A. L. Coil, J.-S. Huang, A. M. Koekemoer, C. C. Steidel, and C. N. A. Willmer. The evolution of the hard X-ray luminosity function of AGN. *Monthly Notices of the RAS*, 401:2531–2551, February 2010.

M. Albrecht, E. Krügel, and R. Chini. Dust and CO emission towards the centers of normal galaxies, starburst galaxies and active galactic nuclei. I. New data and updated catalogue. *Astronomy and Astrophysics*, 462:575–579, February 2007.

D. M. Alexander and R. C. Hickox. What drives the growth of black holes? *New Astronomy Review*, 56:93–121, June 2012.

W. J. Altenhoff, K. J. Johnston, P. Stumpff, and W. J. Webster. Millimeter-wavelength observations of minor planets. *Astronomy and Astrophysics*, 287:641–646, July 1994.

R. Antonucci. Unified models for active galactic nuclei and quasars. *Annual Review of Astron and Astrophys*, 31:473–521, 1993.

L. Armus, T. Heckman, and G. Miley. Multicolor optical imaging of powerful far-infrared galaxies - More evidence for a link between galaxy mergers and far-infrared emission. *Astronomical Journal*, 94:831–846, October 1987.

S. Asayama, A. Biggs, and I. de Gregorio. *ALMA Cycle 4 Technical Handbook*. ALMA Partnership, 2016.

J. A. Baldwin, M. M. Phillips, and R. Terlevich. Classification parameters for the emission-line spectra of extragalactic objects. *Publications of the ASP*, 93:5–19, February 1981.

V. Beckmann and C. R. Shrader. The AGN phenomenon: open issues. 2013.

S. Berta, D. Lutz, P. Santini, S. Wuyts, D. Rosario, D. Brisbin, A. Cooray, A. Franceschini, C. Gruppioni, E. Hatziminaoglou, H. S. Hwang, E. Le Floc'h, B. Magnelli, R. Nordon, S. Oliver,

M. J. Page, P. Popesso, L. Pozzetti, F. Pozzi, L. Riguccini, G. Rodighiero, I. Roseboom, D. Scott, M. Symeonidis, I. Valtchanov, M. Viero, and L. Wang. Panchromatic spectral energy distributions of Herschel sources. *Astronomy and Astrophysics*, 551:A100, March 2013.

P. R. Bevington and D. K. Robinson. McGraw-Hill Higher Education, third edition, 2003.

L. Blitz. *Giant molecular clouds*. 1993.

R. C. Bohlin, B. D. Savage, and J. F. Drake. A survey of interstellar hi from lalfa absorption measurements. *Astrophysical Journal*, 224:132-142, August 1978.

M. Brightman and K. Nandra. An XMM-Newton spectral survey of 12 μm selected galaxies - I. X-ray data. *Monthly Notices of the RAS*, 413:1206–1235, May 2011a.

M. Brightman and K. Nandra. An XMM-Newton spectral survey of 12 μm selected galaxies - II. Implications for AGN selection and unification. *Monthly Notices of the RAS*, 414:3084–3104, July 2011b.

C. L. Buchanan, J. F. Gallimore, C. P. O'Dea, S. A. Baum, D. J. Axon, A. Robinson, M. Elitzur, and M. Elvis. Spitzer IRS Spectra of a Large Sample of Seyfert Galaxies: A Variety of Infrared Spectral Energy Distributions in the Local Active Galactic Nucleus Population. *Astronomical Journal*, 132:401–419, July 2006.

B. Butler. *ALMA memo 594: Flux Density Models for Solar System Bodies in CASA*. 2012.

D. Calzetti. *Star Formation Rate Indicators*, page 419. October 2013.

J. A. Cardelli, G. C. Clayton, and J. S. Mathis. The relationship between infrared, optical and ultraviolet exctinction. *Astrophysical Journal*, 345:245-256, October 2004.

C. L. Carilli and M. A. Holdaway. Mma memo 262: Tropospheric phase calibration in millimeter interferometry. *Radio Science*, 1999.

C. L. Carilli and F. Walter. Cool Gas in High-Redshift Galaxies. *Annual Review of Astron and Astrophys*, 51:105–161, August 2013.

M. A. Chamberlain, A. J. Lovell, and M. V. Sykes. Submillimeter photometry and lightcurves of Ceres and other large asteroids. *Icarus*, 202:487–501, August 2009.

P. C. Clark, S. C. O. Glover, R. S. Klessen, and I. A. Bonnell. Star formation in disk galaxies. i. formation and evolution of giant molecular clouds via gravitational instability and cloud collisions. *Monthly Notices of the RAS*, 424:2599-2613, August 2012.

M. S. Clemens, O. Vega, A. Bressan, G. L. Granato, L. Silva, and P. Panuzzo. Modeling the spectral energy distribution of ULIRGs. I. The radio spectra. *Astronomy and Astrophysics*, 477:95–104, January 2008.

J. J. Condon. Radio emission from normal galaxies. *Annual Review of Astron and Astrophys*, 30:575–611, 1992.

J. J. Condon, W. D. Cotton, E. W. Greisen, Q. F. Yin, R. A. Perley, G. B. Taylor, and J. J. Broderick. The NRAO VLA Sky Survey. *Astronomical Journal*, 115:1693–1716, May 1998.

E. A. Corbett, L. Kewley, P. N. Appleton, V. Charmandaris, M. A. Dopita, C. A. Heisler, R. P. Norris, A. Zezas, and A. Marston. COLA. II. Radio and Spectroscopic Diagnostics of Nuclear Activity in Galaxies. *Astrophysical Journal*, 583:670–688, February 2003.

E. Daddi, H. Dannerbauer, D. Liu, M. Aravena, F. Bournaud, F. Walter, D. Riechers, G. Magdis, M. Sargent, M. Béthermin, C. Carilli, A. Cibinel, M. Dickinson, D. Elbaz, Y. Gao, R. Gobat, J. Hodge, and M. Krips. CO excitation of normal star-forming galaxies out to z = 1.5 as regulated by the properties of their interstellar medium. *Astronomy and Astrophysics*, 577: A46, May 2015.

T. M. Dame, D. Hartmann, and P. Thaddeus. The milky way in molecular clouds: A new complete co survey. *Astrophysical Journal*, 547, February 2001.

R. I. Davies, F. Müller Sánchez, R. Genzel, L. J. Tacconi, E. K. S. Hicks, S. Friedrich, and A. Sternberg. A Close Look at Star Formation around Active Galactic Nuclei. *Astrophysical Journal*, 671:1388–1412, December 2007.

R. Decarli, I. Smail, F. Walter, A. M. Swinbank, S. Chapman, K. E. K. Coppin, P. Cox, H. Dannerbauer, T. R. Greve, J.A. Hodge, R. Ivison, A. Karim, K. K. Knudsen, L. Lindroos, H. W. Rix, E. Schinnerer, J. M. Simpson, P. van der Werf, and A. Weiss. An alma survey of sub-millimeter galaxies in the extended chandra deep field south: Sub-millimeter properties of color-selected galaxies. *The Astrophysical Journal*, 780(2):115, 2014.

I. Delvecchio, C. Gruppioni, F. Pozzi, S. Berta, G. Zamorani, A. Cimatti, D. Lutz, D. Scott, C. Vignali, G. Cresci, A. Feltre, A. Cooray, M. Vaccari, J. Fritz, E. Le Floc'h, B. Magnelli, P. Popesso, S. Oliver, J. Bock, M. Carollo, T. Contini, O. Le Févre, S. Lilly, V. Mainieri, A. Renzini, and M. Scodeggio. Tracing the cosmic growth of supermassive black holes to z ∼ 3 with Herschel. *Monthly Notices of the RAS*, 439:2736–2754, April 2014.

D. Downes and P. M. Solomon. Rotating Nuclear Rings and Extreme Starbursts in Ultraluminous Galaxies. *Astrophysical Journal*, 507:615–654, November 1998. doi: 10.1086/306339.

G. J. Ferland. *Hazy: a brief introduction to CLOUDY C13.1 1. Introduction and command.* 2013.

X. Fernández, A. O. Petric, F. Schweizer, and J. H. van Gorkom. Discovery of a Small Central Disk of CO and H I in the Merger Remnant NGC 34. *Astronomical Journal*, 147:74, April 2014.

L. Ferrarese and D. Merritt. A Fundamental Relation between Supermassive Black Holes and Their Host Galaxies. *Astrophysical Journal, Letters*, 539, August 2000.

G. B. Field, D. W. Goldsmith, and H. J. Habing. Cosmic-ray heating of the interstellar gas. *Astrophysical Journal*, 155, March 1969.

P. Gandhi, H. Horst, A. Smette, S. Hönig, A. Comastri, R. Gilli, C. Vignali, and W. Duschl. Resolving the mid-infrared cores of local Seyferts. *Astronomy and Astrophysics*, 502:457–472, August 2009.

M. A. Garrett. The FIR/Radio correlation of high redshift galaxies in the region of the HDF-N. *Astronomy and Astrophysics*, 384:L19–L22, March 2002.

R. Genzel, D. Lutz, E. Sturm, E. Egami, D. Kunze, A. F. M. Moorwood, D. Rigopoulou, H. W. W. Spoon, A. Sternberg, L. E. Tacconi-Garman, L. Tacconi, and N. Thatte. What Powers Ultraluminous IRAS Galaxies? *Astrophysical Journal*, 498:579–605, May 1998.

A. C. Gonçalves, M.-P. Véron-Cetty, and P. Véron. AGNs with composite spectra. II. Additional data. *Astronomy and Astrophysics, Supplement*, 135:437–466, March 1999.

R. J. Gould and E. Salpeter. The interstellar abudance of the hydrogen molecule. i basic processes. *Astrophysical Journal*, February 1963.

R. E. Griffiths and P. Padovani. Star-forming galaxies and the X-ray background. *Astrophysical Journal*, 360:483–489, September 1990.

C. Gruppioni, S. Berta, L. Spinoglio, M. Pereira-Santaella, F. Pozzi, P. Andreani, M. Bonato, G. De Zotti, M. Malkan, M. Negrello, L. Vallini, and C. Vignali. Tracing black hole accretion with SED decomposition and IR lines: from local galaxies to the high-z Universe. *Monthly Notices of the RAS*, 458:4297–4320, June 2016.

E. Habart, C. M. Walmsley, L. Verstraete, S. Cazaux, R. Maiolino, P. Cox, F. Boulanger, and G. P. des Forêts. Molecular hydrogen. 2004.

G. Helou, B. T. Soifer, and M. Rowan-Robinson. Thermal infrared and nonthermal radio - Remarkable correlation in disks of galaxies. *Astrophysical Journal, Letters*, 298:L7–L11, November 1985.

D. W. Hogg, I. K. Baldry, M. R. Blanton, and D. J. Eisenstein. The K correction. *ArXiv Astrophysics e-prints*, October 2002.

D. J. Hollenbach and A. G. G. M. Tielens. Photodissociation regions in the interstellar medium of galaxies. *Reviews of Modern Physics*, 71(1), January 1999.

S. F. Hönig and M. Kishimoto. The dusty heart of nearby active galaxies. II. From clumpy torus models to physical properties of dust around AGN. *Astronomy and Astrophysics*, 523, November 2010.

M. Imanishi and A. Alonso-Herrero. Near-infrared K-Band Spectroscopic Investigation of Seyfert 2 Nuclei in the CfA and 12 Micron Samples. *Astrophysical Journal*, 614:122–134, October 2004.

G. Kauffmann, T. M. Heckman, C. Tremonti, J. Brinchmann, S. Charlot, S. D. M. White, S. E. Ridgway, J. Brinkmann, M. Fukugita, P. B. Hall, Ž. Ivezić, G. T. Richards, and D. P. Schneider. The host galaxies of active galactic nuclei. *Monthly Notices of the RAS*, 346: 1055–1077, December 2003.

R. C. Kennicutt, Jr. F. Schweizer, and J. E. Barnes. *Galaxies: Interactions and Induced Star Formation*. 1996.

R. C. Kennicutt, Jr. The Global Schmidt Law in Star-forming Galaxies. *Astrophysical Journal*, 498:541–552, May 1998.

L. J. Kewley, M. A. Dopita, R. S. Sutherland, C. A. Heisler, and J. Trevena. Theoretical Modeling of Starburst Galaxies. *Astrophysical Journal*, 556:121–140, July 2001.

L. J. Kewley, B. Groves, G. Kauffmann, and T. Heckman. The host galaxies and classification of active galactic nuclei. *Monthly Notices of the RAS*, 372:961–976, November 2006.

R. S. Klessen and S. C. O. Glover. Physical processes in the interstellar medium. July 2014.

M. Lampton, B. Margon, and S. Bowyer. Parameter estimation in X-ray astronomy. *Astrophysical Journal*, 208:177–190, August 1976.

G. Lanzuisi, F. Civano, M. Elvis, M. Salvato, G. Hasinger, C. Vignali, G. Zamorani, T. Aldcroft, M. Brusa, A. Comastri, F. Fiore, A. Fruscione, R. Gilli, L. C. Ho, V. Mainieri, A. Merloni, and A. Siemiginowska. The Chandra-COSMOS survey - IV. X-ray spectra of the bright sample. *Monthly Notices of the RAS*, 431:978–996, May 2013.

B. D. Lehmer, D. M. Alexander, F. E. Bauer, W. N. Brandt, A. D. Goulding, L. P. Jenkins, A. Ptak, and T. P. Roberts. A Chandra Perspective on Galaxy-wide X-ray Binary Emission and its Correlation with Star Formation Rate and Stellar Mass: New Results from Luminous Infrared Galaxies. *Astrophysical Journal*, 724:559–571, November 2010.

H. S. Liszt. Hunt for variations in molecular gas and cloud properties across the inner, northern Galactic disk. *Astrophysical Journal*, 411:720–728, July 1993.

P. Madau and M. Dickinson. Cosmic Star-Formation History. *Annual Review of Astron and Astrophys*, 52:415–486, August 2014.

J. Magorrian, S. Tremaine, D. Richstone, R. Bender, G. Bower, A. Dressler, S. M. Faber, K. Gebhardt, R. Green, C. Grillmair, J. Kormendy, and T. Lauer. The Demography of Massive Dark Objects in Galaxy Centers. *Astronomical Journal*, 115:2285–2305, June 1998.

P. R. Maloney, D. J. Hollenbach, and A. G. G. M. Tielens. X-ray-irradiated molecular gas. i physical processes and general results. *Astrophysical Journal*, July 1999.

N. Mashian, E. Sturm, A. Sternberg, A. Janssen, S. Hailey-Dunsheath, J. Fischer, A. Contursi, E. González-Alfonso, J. Graciá-Carpio, A. Poglitsch, S. Veilleux, R. Davies, R. Genzel, D. Lutz, L. Tacconi, A. Verma, A. Weiß, E. Polisensky, and T. Nikola. High-J CO Sleds in Nearby Infrared Bright Galaxies Observed By Herschel/PACS. *Astrophysical Journal*, 802:81, April 2015.

J. M. Mazzarella, G. D. Bothun, and T. A. Boroson. Far-infrared properties of Markarian galaxies with multiple nuclei - Warm dust emission in mergers. *Astronomical Journal*, 101:2034–2055, June 1991. doi: 10.1086/115828.

C. F. McKee and E. C. Ostriker. A theory of the interstellar medium: three components regulated by supernova explosions in an inhomogeneous substrate. *Astrophysical Journal*, 218:148-169, November 1977.

C. F. McKee and E. C. Ostriker. Theory of star formation. *Annual Review of Astronomy and Astrophysics*, 45, July 2007.

R. Meijerink and M. S. Spaans. Diagnostics of irradiated gas in galaxy nuclei. i a far-ultraviolet and x-ray dominated region code. *Astronomy and Astrophysics*, February 2005.

R. Meijerink, M. Spaans, and F. P. Israel. Diagnostics of irradiated dense gas in galaxy nuclei. ii a grid of xdr and pdr models. *Astronomy and Astrophysics*, 461,793-811, 2007.

R. Morrison and D. McCammon. Interstellar photoelectric absorption cross sections, 0.03-10 keV. *Astrophysical Journal*, 270:119–122, July 1983.

J. R. Mullaney, M. Pannella, E. Daddi, D. M. Alexander, D. Elbaz, R. C. Hickox, F. Bournaud, B. Altieri, H. Aussel, D. Coia, H. Dannerbauer, K. Dasyra, M. Dickinson, H. S. Hwang, J. Kartaltepe, R. Leiton, G. Magdis, B. Magnelli, P. Popesso, I. Valtchanov, F. E. Bauer, W. N. Brandt, A. Del Moro, D. J. Hanish, R. J. Ivison, S. Juneau, B. Luo, D. Lutz, M. T. Sargent, D. Scott, and Y. Q. Xue. GOODS-Herschel: the far-infrared view of star formation in active galactic nucleus host galaxies since z $\sim$ 3. *Monthly Notices of the RAS*, 419:95–115, January 2012.

N. Murray. Star formation efficienties and lifetimes of giant molecular clouds in the milky way. *Astrophysical Journal*, March 2011.

D. Narayanan and M. R. Krumholz. A theory for the excitation of co in star forming galaxies. *Monthly Notices of the Royal Astronomical Society*, 2014.

E. Nardini, G. Risaliti, Y. Watabe, M. Salvati, and E. Sani. The role of nuclear activity as the power source of ultraluminous infrared galaxies. *Monthly Notices of the RAS*, 405:2505–2520, July 2010.

H. Netzer. *Physics and evoltion of Active Galactic Nuclei*. 2013.

J. H. Oort. Outline of a theory on the origin and acceleration of interstellar clouds and o associations. *Bulletin of the Astronomical Institutes of the Netherlands*, 12, September 1954.

J. Ott and J Kern. *CASA Synthesis & Single Dish Reduction, Reference Manual & Cookbook*. 2016.

P. P. Papadopoulos. HCN versus HCO$^+$ as Dense Molecular Gas Mass Tracers in Luminous Infrared Galaxies. *Astrophysical Journal*, 656:792–797, February 2007.

P. P. Papadopoulos, P. van der Werf, K. Isaak, and E. M. Xilouris. CO Spectral Line Energy Distributions of Infrared-Luminous Galaxies and Active Galactic Nuclei. *Astrophysical Journal*, 715:775–792, June 2010.

P. P. Papadopoulos, P. P. van der Werf, E. M. Xilouris, K. G. Isaak, Y. Gao, and S. Mühle. The molecular gas in luminous infrared galaxies - I. CO lines, extreme physical conditions and their drivers. *Monthly Notices of the RAS*, 426:2601–2629, November 2012.

M. Pereira-Santaella, A. M. Diamond-Stanic, A. Alonso-Herrero, and G. H. Rieke. The Mid-infrared High-ionization Lines from Active Galactic Nuclei and Star-forming Galaxies. *Astrophysical Journal*, 725:2270–2280, December 2010.

M. Pereira-Santaella, L. Spinoglio, P. P. van der Werf, and J. Piqueras López. Warm molecular gas temperature distribution in six local infrared bright Seyfert galaxies. *Astronomy and Astrophysics*, 566:A49, June 2014.

F. Pozzi, C. Vignali, A. Comastri, E. Bellocchi, J. Fritz, C. Gruppioni, M. Mignoli, R. Maiolino, L. Pozzetti, M. Brusa, F. Fiore, and G. Zamorani. The HELLAS2XMM survey. XIII. Multi-component analysis of the spectral energy distribution of obscured AGN. *Astronomy and Astrophysics*, 517, July 2010.

P. Ranalli, A. Comastri, and G. Setti. The 2-10 keV luminosity as a Star Formation Rate indicator. *Astronomy and Astrophysics*, 399:39–50, February 2003.

J. M. Rathborne, A. M. Johnson, J. M. Jackson, R. Y. Shah, and R. Simon. Molecular clouds and clumps in the boston university-five college radio astronomy observatory galactic ring survey. *Astrophysical Journal, Supplement*, 182:131-142, May 2009.

R. Riffel, A. Rodríguez-Ardila, and M. G. Pastoriza. A 0.8-2.4 μm spectral atlas of active galactic nuclei. *Astronomy and Astrophysics*, 457:61–70, October 2006.

A. Rodriguez-Franco, J. Martin-Pintado, and A. Fuente. CN emission in Orion. The high density interface between the H II region and the molecular cloud. *Astronomy and Astrophysics*, 329: 1097–1110, January 1998.

M. J. F. Rosenberg, P. P. van der Werf, S. Aalto, L. Armus, V. Charmandaris, T. Díaz-Santos, A. S. Evans, J. Fischer, Y. Gao, E. González-Alfonso, T. R. Greve, A. I. Harris, C. Henkel, F. P. Israel, K. G. Isaak, C. Kramer, R. Meijerink, D. A. Naylor, D. B. Sanders, H. A. Smith, M. Spaans, L. Spinoglio, G. J. Stacey, I. Veenendaal, S. Veilleux, F. Walter, A. Weiß, M. C. Wiedner, M. H. D. van der Wiel, and E. M. Xilouris. The Herschel Comprehensive (U)LIRG Emission Survey (HERCULES): CO Ladders, Fine Structure Lines, and Neutral Gas Cooling. *Astrophysical Journal*, 801:72, March 2015.

B. Rush, M. A. Malkan, and L. Spinoglio. The extended 12 micron galaxy sample. *Astrophysical Journal, Supplement*, 89:1–33, November 1993.

D. B. Sanders and I. F. Mirabel. Luminous Infrared Galaxies. *Annual Review of Astron and Astrophys*, 34:749, 1996.

D. B. Sanders, B. T. Soifer, J. H. Elias, B. F. Madore, K. Matthews, G. Neugebauer, and N. Z. Scoville. Ultraluminous infrared galaxies and the origin of quasars. *Astrophysical Journal*, 325: 74–91, February 1988.

D. B. Sanders, E. S. Phinney, G. Neugebauer, B. T. Soifer, and K. Matthews. Continuum energy distribution of quasars - Shapes and origins. *Astrophysical Journal*, 347:29–51, December 1989.

F. Schweizer and P. Seitzer. Remnant of a "Wet" Merger: NGC 34 and Its Young Massive Clusters, Young Stellar Disk, and Strong Gaseous Outflow. *Astronomical Journal*, 133, May 2007.

F. Shankar, D. H. Weinberg, and J. Miralda-Escudé. Self-Consistent Models of the AGN and Black Hole Populations: Duty Cycles, Accretion Rates, and the Mean Radiative Efficiency. *Astrophysical Journal*, 690:20–41, January 2009.

P. M. Solomon, A. R. Rivolo, J. Barrett, and A. Yahil. Mass, luminosity, and line width relations of Galactic molecular clouds. *Astrophysical Journal*, 319:730–741, August 1987.

P. M. Solomon, D. Downes, S. J. E. Radford, and J. W. Barrett. The molecular interstellar medium in ultraluminous infrared galaxies. *Astrophysical Journal*, March 1997.

M. Spaans and R. Meijerink. On the Detection of High-Redshift Black Holes with ALMA through CO and H_2 Emission. *Astrophysical Journal, Letters*, 678:L5, May 2008.

M. Spaans, R. Meijerink, F. P. Israel, A. F. Loenen, and W. A. Baan. The irradiated ism of ulirgs. *International Astronomical Union*, 2008.

A. W. Strong and J. R. Mattox. Gradient model analysis of EGRET diffuse Galactic γ-ray emission. *Astronomy and Astrophysics*, 308:L21–L24, April 1996.

E. J. Tasker and J. C. Tan. Star formation in disk galaxies. i. formation and evolution of giant molecular clouds via gravitational instability and cloud collisions. *Astrophysical Journal*, 700:358-375, July 2009.

G. B. Taylor, C. L. Carilli, and R. A. Perley. *Synthesis Imaging in Radio Astronomy II*. 1999.

Y. Terashima, N. Iyomoto, L. C. Ho, and A. F. Ptak. X-Ray Properties of LINERs and Low-Luminosity Seyfert Galaxies Observed with ASCA. I. Observations and Results. *Astrophysical Journal, Supplement*, 139:1–36, March 2002.

A. G. G. M. Tielens and D. Hollenbach. Photodissociation regions. i basic model. *Astrophysical Journal*, 291:722-746, April 1985.

S. Tommasin, L. Spinoglio, M. A. Malkan, and G. Fazio. Spitzer-IRS High-Resolution Spectroscopy of the 12 μm Seyfert Galaxies. II. Results for the Complete Data Set. *Astrophysical Journal*, 709:1257–1283, February 2010.

C. M. Urry and P. Padovani. Unified Schemes for Radio-Loud Active Galactic Nuclei. *Publications of the ASP*, 107:803, September 1995.

L. Vallini, A. Ferrara, A. Pallottini, and S. Gallerani. Molecular clouds photoevaporation and FIR line emission. *Monthly Notices of the RAS*, June 2016.

P. C. van der Kruit. High-resolution Radio Continuum Observations of Bright Spiral Galaxies at 1415 MHz: A General Discussion. *Astronomy and Astrophysics*, 29:263, December 1973.

P. P. van der Werf, K. G. Isaak, R. Meijerink, M. Spaans, A. Rykala, T. Fulton, A. F. Loenen, F. Walter, A. Weiß, L. Armus, J. Fischer, F. P. Israel, A. I. Harris, S. Veilleux, C. Henkel, G. Savini, S. Lord, H. A. Smith, E. González-Alfonso, D. Naylor, S. Aalto, V. Charmandaris, K. M. Dasyra, A. Evans, Y. Gao, T. R. Greve, R. Güsten, C. Kramer, J. Martín-Pintado, J. Mazzarella, P. P. Papadopoulos, D. B. Sanders, L. Spinoglio, G. Stacey, C. Vlahakis, M. C. Wiedner, and E. M. Xilouris. Black hole accretion and star formation as drivers of gas excitation and chemistry in Markarian 231. *Astronomy and Astrophysics*, 518:L42, July 2010.

T.A. van Kempen, R. Kneissl, N. Marcelino, E.B. Fomalont, S.A. Barkats, D. Corder, R. A. Lucas, B. Peck, and R. Hills. Alma memo 599: The alma calibrator database i: Measurements taken during the commissioning phase of alma. 2014.

S. Veilleux. Spectroscopy of Luminous Infrared Galaxies. In J. E. Barnes and D. B. Sanders, editors, *Galaxy Interactions at Low and High Redshift*, volume 186 of *IAU Symposium*, page 295, 1999.

S. Veilleux and D. E. Osterbrock. Spectral classification of emission-line galaxies. *Astrophysical Journal, Supplement*, 63:295–310, February 1987.

M. P. Véron-Cetty and P. Véron. A catalogue of quasars and active nuclei: 12th edition. *Astronomy and Astrophysics*, 455:773–777, August 2006.

B. V. Vilaro and L. Nyman. *ALMA Cycle 0 Technical Handbook*. ALMA Partnership, 2011.

J. P. Williams and C. F. McKee. The galactic distribution of ob associations in molecular clouds. *Astrophysical Journal*, 476:166-183, February 1997.

Y. Z. Wu, E. P. Zhang, Y. C. Liang, C. M. Zhang, and Y.-H. Zhao. The Different Nature of Seyfert 2 Galaxies With and Without Hidden Broad-line Regions. *Astrophysical Journal*, 730: 121, April 2011.

C. K. Xu, C. Cao, N. Lu, Y. Gao, P. van der Werf, A. S. Evans, J. M. Mazzarella, J. Chu, S. Haan, T. Diaz-Santos, R. Meijerink, Y.-H. Zhao, P. Appleton, L. Armus, V. Charmandaris, S. Lord, E. J. Murphy, D. B. Sanders, B. Schulz, and S. Stierwalt. ALMA Observations of Warm Molecular Gas and Cold Dust in NGC 34. *Astrophysical Journal*, 787:48, May 2014.

K. Zhang, T. Wang, X. Dong, and H. Lu. Difference in Narrow-Emission-Line Spectra of Seyfert 1 and 2 Galaxies. *Astrophysical Journal, Letters*, 685:L109, October 2008.

V. Zubko, E. Dwek, and R. G. Arendt. Interstellar Dust Models Consistent with Extinction, Emission, and Abundance Constraints. *Astrophysical Journal, Supplement*, 152:211–249, June 2004.